Exploring Catalytic Systems for Furfural Upgradation to Value-Added Products

A Thesis Submitted in Partial Fulfilment of the Requirements for the Degree of

DOCTOR OF PHILOSOPHY

by

Anurag Jaswal (2019CHZ0003)



DEPARTMENT OF CHEMICAL ENGINEERING INDIAN INSTITUTE OF TECHNOLOGY ROPAR

January, 2025





Declaration of Originality

I hereby declare that the thesis titled 'Exploring Catalytic Systems for Furfural Upgradation to Value-Added Products,' is my original work and has been authored solely by me. It represents the findings of my independent research, conducted between July 2019 and November 2024, under the supervision of Dr. Tarak Mondal, Assistant Professor at the Indian Institute of Technology Ropar. To the best of my knowledge, this thesis is original in both content and narrative, and has not been submitted or accepted, either in whole or in part, for any degree, diploma, fellowship, associateship, or equivalent title at any other institution or university. Appropriate credit has been given to relevant sources and collaborations (where applicable), with proper citations and acknowledgments, adhering to established ethical standards. Furthermore, I confirm that no idea, data, fact, or source in this thesis has been fabricated, falsified, or misrepresented. I have followed all principles of academic honesty and integrity. I understand that if this work is found to be plagiarized, fabricated, or otherwise in violation of academic standards, the Institute reserves the right to withdraw the thesis and revoke the associated degree. Additionally, the Institute reserves the right to inform relevant parties as necessary. If accepted, I consent to my thesis being made available online in the Institute's Open Access repository, interlibrary loan, and for the title and abstract to be shared with external organizations.

Signature: White

Name: Anurag Jaswal

Entry Number: 2019CHZ0003

Department: Chemical Engineering

Indian Institute of Technology Ropar

Rupnagar, Punjab 140001

Date: 20-01-2025

Certificate

This is to certify that the thesis entitled 'Exploring Catalytic Systems for Furfural

Upgradation' submitted by Anurag Jaswal (2019CHZ0003) for the award of the degree of

Doctor of Philosophy of Indian Institute of Technology Ropar, is a record of bonafide

research work carried out under my guidance and supervision. To the best of my knowledge

and belief, the work presented in this thesis is original and has not been submitted, either in

part or full, for the award of any other degree, diploma, fellowship, associateship or similar

title of any university or institution.

In my opinion, the thesis has reached the standard fulfilling the requirements of the regulations

relating to the Degree.

Signature of the Supervisor

Hondey

Name: Dr. Tarak Mondal

Department: Chemical Engineering

Indian Institute of Technology Ropar

Rupnagar, Punjab 140001

Date: 20-01-2025

iii

Acknowledgements

First and foremost, I extend my deepest gratitude to my supervisor, Dr. Tarak Mondal, Principal Investigator of the Catalysis and Sustainable Energy Research Laboratory (CSERL) at IIT Ropar. His unwavering guidance, encouragement, and remarkable research acumen were the pillars that supported this work. Dr. Mondal's ability to motivate and challenge me to strive for excellence played a crucial role in shaping the success of this research. His open-door approach and willingness to discuss every obstacle provided clarity during complex times. I am especially grateful for his mentorship during the challenging period of the COVID-19 pandemic, where his advice helped me navigate uncertainties. His belief in my abilities gave me the confidence to push the boundaries of my work, and it has been a privilege to learn from his vast experience and thoughtful insights. Words fall short of expressing my appreciation for his kindness, generosity, and constant support.

I am also deeply thankful to the members of my Doctoral Committee: Dr. Vishwajeet Mehandia (Chairperson), Dr. Chandi Sasmal, Dr. Neelkanth Nirmalkar, and Prof. Narinder Singh, for their valuable feedback, guidance, and thought-provoking discussions throughout this journey. Special thanks to Dr. Asad Sahir for his inspiring conversations, both academic and personal, that have motivated me to expand my horizons. I also want to acknowledge the faculty and staff of the Chemical Engineering Department for their continuous support.

I extend my sincere appreciation to the Catalysis Research Lab of Prof. Rajendra Srivastava at IIT Ropar, Prof. Prakash Biswas's research group at the IIT Roorkee, and Dr. Omvir Singh at the Rajiv Gandhi Institute of Petroleum Technology for their invaluable support in providing access to essential characterization facilities for my research. My gratitude also goes to Mr. Ravinder Singh from the Research section, Ms. Sunpreet Kaur, Mr. Jagmail Singh, and Mr. Maan Singh from the Chemical Engineering office for their administrative assistance. I would also like to recognize the Central Research Facilities at IIT Ropar, especially Mr. Amit Kaushal (SEM and XRD), Mr. Abhishek Kumar (FESEM), Mr. Manu Thakur (XPS), and Mr. Manish (HRTEM), for their technical support, along with the IIT Ropar Library for providing access to essential resources. Additionally, I extend my gratitude to the Central Research

Facilities at IIT Delhi, particularly Dr. Somendra Singh (TPD), for their invaluable technical support in characterization.

A special mention to my colleagues at CSERL - Dr. Piyush Pratap Singh, Harikiran, Rajat, Ajay, Aamir, Vijay, and Ajeet - for their collaboration and friendship. I would like to extend my heartfelt gratitude to Dr. Piyush for his invaluable support and guidance throughout my Ph.D. journey. Working with him was an enriching experience, and our in-depth discussions on various catalytic biomass conversion processes proved to be highly insightful and instrumental in shaping my research. His mentorship went beyond technical guidance - his encouragement and willingness to offer constructive feedback greatly enhanced my learning experience. His generous sharing of expertise and resources, combined with his unwavering support, played a pivotal role in the successful completion of my research work. I am deeply grateful for his mentorship and for the numerous ways in which he contributed to my academic and professional growth. I also cherish the memorable moments shared with my friends Harsh Sharma, Gaurav Yadav, Dipika, Ganesh More, Atul Tripathi, Arjun Manal, Nilanjan Dutta, Nazim Ali, and Manish Pandey whose companionship brought warmth and laughter throughout my time at IIT Ropar. I am grateful to Mr. Nand Kishore, head of security, and his team for their patience and support, especially during the pandemic. My thanks also go to the cleaning and maintenance staff for their dedicated services.

Finally, I express my deepest love and gratitude to my parents and my brother Aniket, whose unwavering support has been the bedrock of my journey. I would like to honour the memory of my grandfather, the late Mr. Jaswant Singh. Though he is no longer with us, his influence and encouragement continue to inspire me, and his presence is deeply missed. I extend my heartfelt thanks to everyone who has supported me, directly or indirectly, throughout this incredible journey.

Anurag Jaswal

Lay Summary

The world's shift away from fossil fuels has driven the search for renewable alternatives, particularly in producing valuable chemicals. One promising candidate is furfural (FFR), a platform chemical derived from biomass. This thesis focuses on developing and optimizing catalytic systems to efficiently convert FFR into high-value chemicals, specifically furfuryl alcohol (FAL) and 2-methylfuran (2-MeF), which are important intermediates in various industries.

The primary objective of this research was to identify and optimize various catalytic systems using both molecular hydrogen (H₂) and alternative/renewable hydrogen sources. By focusing on the conversion of FFR in continuous vapor-phase reactions, this work seeks to provide foundational knowledge that can guide the future development of more efficient and sustainable catalytic processes for biomass valorization. The experimental investigations spanned several approaches, evaluating different catalytic systems for their ability to transform FFR under diverse reaction conditions. This included the use of bimetallic catalysts (e.g., Cu-Ni) and mixed metal oxides (e.g., Cu-Fe, Mg-Fe) to improve the performance of these systems. Additionally, innovative methods were explored, such as using rice husk ash - a sustainable and costeffective source of silica - as a support for these catalytic systems. Throughout the research, factors such as catalyst composition, temperature, hydrogen availability, and space velocity were critical to achieving high selectivity and conversion rates. The findings revealed that specific combinations of metals and reaction conditions led to significant improvements in selectivity toward FAL and 2-MeF. Moreover, the study provided valuable insights into optimizing process variables, all of which play a key role in enhancing catalyst efficiency. While detailed investigations into catalyst deactivation were not a central focus, the results hinted at potential challenges in longterm catalyst stability. Regeneration studies provided partial recovery of catalytic activity, suggesting areas where future research can address the issue of catalyst longevity.

Overall, this work contributes to the broader field of sustainable chemical production by advancing the understanding of catalytic systems for biomass conversion. It lays the groundwork for future innovations aimed at reducing reliance on fossil fuels and creating more environmentally friendly production methods for essential chemicals.

Abstract

As the world moves toward sustainable and renewable resources, efficient biomass conversion processes have become a key area of focus. Furfural (FFR), a platform chemical derived from lignocellulosic biomass, presents significant potential for replacing fossil-derived products with high-value chemicals and fuels. This thesis explores the design and optimization of catalytic systems for converting FFR into value-added products such as 2-methylfuran (2-MeF) and furfuryl alcohol (FAL), contributing to a greener chemical industry. Both traditional hydrogenation using molecular hydrogen (H₂) and alternative transfer hydrogenation approaches using non-conventional hydrogen sources are examined, aiming to develop more sustainable biomass conversion processes.

A variety of catalytic systems were tested, including bimetallic catalysts, mixed metal oxides, and supported metal-incorporated mesoporous silica, to enhance catalyst performance and selectivity in FFR valorization. Detailed material characterization was carried out using techniques such as X-ray diffraction (XRD), Brunauer-Emmett-Teller surface area analysis (BET), temperature-programmed desorption (TPD), scanning electron microscopy (FESEM), X-ray photoelectron spectroscopy (XPS), and high-resolution transmission electron microscopy (HRTEM). These analyses confirmed the successful synthesis and structural properties of the catalysts.

Optimization of process parameters, such as space-time and reaction temperature, along with time-on-stream (TOS) studies, revealed promising results. TiO₂-supported Cu-Ni bimetallic catalysts exhibited impressive selectivity for converting FFR to 2-MeF, achieving up to 84.5% selectivity at 200 °C using a 10% Cu-10% Ni/TiO₂ catalyst. Additionally, Cu-Fe mixed oxide catalysts with equimolar ratios of Cu and Fe demonstrated excellent performance in FFR hydrodeoxygenation, achieving up to 90% selectivity for 2-MeF at 230 °C under ambient H₂ pressures.

The thesis also highlights the use of mesoporous silica derived from rice husk ash, with metals incorporated to create highly efficient catalysts. The Cu-supported Zr-incorporated mesoporous silica catalyst (Cu@Zr-MS) achieved FFR conversion rates of 90% and maintained FAL yields of approximately 85% over extended reaction periods. Further exploration of transfer hydrogenation using Mg-Fe mixed oxide catalysts showed that the optimal Mg/Fe ratio of 4 delivered a 79.8% selectivity for 2-MeF and 85.2% FFR conversion over a 4-hour reaction time at 400 °C.

This research underscores the potential of innovative catalytic systems for developing more sustainable and efficient biomass conversion processes, offering valuable insights into advancing the green chemical industry

Keywords: Biomass Valorization; Furfural, 2-Methylfuran, Furfuryl Alcohol; Hydrogenation; Transfer Hydrogenation; Sustainable Chemistry

TABLE OF CONTENTS

Declaration of Originality
Certificateiii
Acknowledgmentsi
Lay Summaryiii
Abstractiv
List of figuresxiii
List of tablesxix
List of abbreviationsxxi
Chapter 1: Introduction1
1.1 Chemicals and Fuels: Cornerstones of Technological and Economic Progress 1
1.2 The Dominance of Fossil Fuels and the Imperative for Transition
1.3 Harnessing Biomass: A Pathway to Cleaner Energy and Chemicals2
1.4 Breaking Down Biomass: Understanding Its Composition and Structure3
1.5 Biomass Conversion Strategies: From Raw Material to Valuable Products5
1.6 Reimagining Biomass Valorization: Chemicals over Biofuels
1.7 Biorefineries and Beyond
1.8 Charting the Course: Platform Chemicals and the DOE 'Top 10' Roadmap for Biobased Chemical Production
1.9 Furfural: A Platform Chemical with Diverse Potential9
1.10 Furfural Transformation: Pathways to Valuable Chemicals and Fuels11
References
Chapter 2: Literature Review
2.1 Conventional (Molecular H ₂ -based) FFR HDO to 2-MeF
2.2 Conventional (Molecular H ₂ -based) FFR Hydrogenation to FAL
2.3 Catalytic Transfer Hydrogenation of FAL to 2-MeF24

2.4 Highlights/Observations and Research Gaps	26
2.5 Objectives	30
2.5.1 Main Objective	31
2.5.2 Specific Objectives	31
2.6 Organization of the Thesis	31
Referecnes	34
Chapter 3: Materials and Methods	37
3.1. Catalyst synthesis	37
3.1.1 Materials used	37
3.1.2 Synthesis of TiO ₂ supported monometallic and bimetallic Cu and Ni	catalysts
	37
3.1.3 Synthesis of Cu-Fe mxed oxide catalysts	38
3.1.4 Synthesis of Cu catalysts supported on metal-incorporated rice h	usk ash-
derived mesoporous silica	39
3.1.4.1 Preparation of Rice Husk Ash	39
3.1.4.2 Syntheis of Pristine and Metal Incorporated Mesoporous Silica Supp	ports40
3.1.4.3 Synthesis of Supported Cu catalysts	41
3.1.5 Synthesis of Mg-Fe mixed oxide catalysts	42
3.2 Catalyst Characterization	43
3.2.1 X-ray Diffraction (XRD)	43
3.2.2 N ₂ Physisorption	44
3.2.3 Field Emission Scanning Electron Microscope	44
3.2.4 Energy-dispersive X-ray spectroscopy	45
3.2.5 H ₂ -Temperature Programmed Reduction (H ₂ -TPR)	45
2.2.8 NH ₃ /CO ₂ -Temperature Programmed Desorption (NH ₃ /CO ₂ -TPD)	46
3.2.7 X-ray Photoelectron Spectroscopy (XPS)	46
3.2.8 High Resolution Transmission Electron Microscopy (HRTEM)	47
3.3 Reactions Involved in FFR transformation to FAL and 2-MeF	48

	3.3.1 Main Reactions	48
	3.3.2 Major Side reactions	49
	3.4 Evaluation of Catalytic Activity	50
	3.4.1 For FFR Hydrogenation and HDO using the H ₂	
	3.4.2 For FFR Transfer Hydrogenation	
	3.4.3 Evaluation of Catalytic Performance	
	References	
(Chapter 4: FFR HDO to 2-MeF over TiO2-supported Cu-Ni bimetallic	
		-
	4.1 Catalyst Characterization	55
	4.1.1 XRD	55
	4.1.2 H ₂ -TPR	59
	4.1.3 SEM-EDX	62
	4.1.4 HRTEM	64
	4.1.5 N ₂ Physisorption	65
	4.1.6 XPS	66
	4.1.7 NH ₃ -TPD	69
	4.2 Catalytic Activity in FFR HDO	70
	4.2.1 Initial Catalyst Screening	70
	4.2.1.1 FFR HDO over monometallic Cu catalyst	70
	4.2.1.2 FFR HDO over monometallic Ni catalyst	71
	4.2.1.3 FFR HDO over Cu-Ni bimetallic catalysts	73
	4.2.1.4 Probable Reaction Mechanism	74
	4.2.2 Effect of reaction conditions on FFR HDO over 10%Cu-10%Ni@TiC	₂ catalyst
		76
	4.2.2.1 Effect of reaction temperature	77
	4.2.2.2 Effect of WHSV	78

	4.2.1 Evaluating the possibility of CTH	80
	4.2.4 Catalyst Stability	82
	References	84
(Chapter 5: FFR HDO to 2-MeF over Cu-Fe mixed oxide catalysts	91
	5.1 Catalyst characterization	91
	5.1.1 XRD	91
	5.1.2 H ₂ -TPR	96
	5.1.3 NH ₃ -TPD	98
	5.1.4 XPS	99
	5.1.5 N ₂ Physisorption	. 101
	5.1.6 FESEM	101
	5.1.7 HRTEM	102
	5.2 FFR HDO over Cu-Fe mixed oxide catalysts	103
	5.2.1 Effect of Cu/Fe molar ratio	103
	5.2.2 Effect of reactio conditions on FFR HDO over Cu-Fe mixed oxide catalyst	with
	Cu/Fe= 1	. 106
	5.2.2.1 Effect of reaction temperature	. 106
	5.2.2.2 Effect of WHSV	. 108
	5.2.2.3 Effect of reduction temperature	109
	5.2.2.4 Effect of H ₂ /FFR ratio	112
	5.2.3 Catalyst Stability and Regeneration	. 114
	References	. 117
(Chapter 6: FFR Hydrogenation to FAL over Cu catalysts supported on rice l	husk
a	sh-derived and metal-incorporated mesoporous silica	. 121
	6.1 Catalyst Characterization	. 121
	6.1.1 XRF	. 121
	6.1.2 XRD	122
	6.1.3 FTIR	. 125

6.1.4 N ₂ Physisorption	127
6.1.5 H ₂ -TPR	129
6.1.6 NH ₃ -TPD	129
6.1.7 XPS	133
6.1.7.1 Evalutation of surface states of metal-incorporated supports	133
6.1.7.2 Evaluation of surface states of reduced Cu catalysts supported on n	nixed oxide
supports	135
6.1.7.3 Evaluating Copper Oxidation States	136
6.1.7.4 Evaluating Oxidation States of Incorporated Metals	137
6.1.8 FESEM	139
6.1.9 HRTEM	140
6.2 Evaluation of Catalytic Activity in FFR Hydrogenation	141
6.2.1 Effect of metal incorporation in mesoporous silica support	141
6.2.2 Effect of temperature	144
6.2.3 Effect of WHSV	145
6.2.4 Catalyst Stability and Regeneration	146
6.2.5 Probable Reaction Mechanism	149
References	151
Chapter 7: FFR Transfer Hydrogenation to 2-MeF over Mg-Fe m	ixed oxide
catalysts	157
7.1 Catalyst Characterization	157
7.1.1 XRD	157
7.1.2 N ₂ Physisorption	159
7.1.3 NH ₃ -TPD	160
7.1.4 CO ₂ -TPD	161
7.1.5 FESEM	163
7.1.6 XPS	165
7.1.7 HRTEM	166

7.2 Evaluation of FFR Transfer Hydrogenation Activity	167
7.2.1 Initial Catalyst Screening	167
7.2.1.1 Evaluation of pure Mg and Fe mixed oxide catalysts	167
7.2.1.2 Evaluation of Mg-Fe mixed oxide catalysts	170
7.2.2 Effect of temperature	172
7.2.3 Effect of WHSV	174
7.2.4 Effect of calcination temperature	176
7.2.5 Catalyst Stability and Regeneration	181
7.2.6 Probable Reaction Mechanism	183
References	186
Chapter 8: Conclusion and Future Recommendations	191
8.1 Conclusion	192
8.2 Future Recommendations	195
Appendix	199
Fixed bed reactor unit with GC	199
List of Publications	201
Journal Publications	201
Book Chapter	202
Conference presentation	203
	205

List of figures

Fig. 1.1 Typical sources of biomass
Fig. 1.2 Structure of lignocellulosic biomass
Fig. 1.3 Common thermochemial strategies for lignocellulosic biomass conversion and
their products6
Fig. 1.4 A typical biorefinery featuring biomass conversion to value-added products . 8
Fig. 1.5 List of some of the most relevant FFR derivatives
Fig. 3.1 Schematic Diagram for the synthesis of TiO ₂ -supported bimetallic Cu-Ni
catalysts
Fig. 3.2 Schematic Diagram for the synthesis of Cu-Fe mixed oxide catalysts39
Fig. 3.3 Schematic Diagram for rice husk ash synthesis
Fig. 3.4 Schematic Diagram for metal-incorporated mesoporous silica synthesis from
rice husk ash41
Fig. 3.5 Schematic Diagram for the synthesis of Mg-Fe mixed oxide catalysts43
Fig. 3.6 Conversion Pathways during FFR hydrogenation
Fig. 3.6 Schematic Diagram of experimental setup for FFR transformation
Fig. 4.1 XRD patterns of calcined (a) 10%Cu/TiO ₂ , (b) 10%Cu-2.5%Ni/TiO ₂ , (c)
10%Cu-5%Ni/TiO ₂ , (d) 10%Cu-10%Ni/TiO ₂ , (e) 10%Cu-20%Ni/TiO ₂ , and (f)
10%Ni/TiO ₂ catalysts
Fig. 4.2 XRD patterns of reduced (a) 10%Cu/TiO ₂ , (b) 10%Cu-2.5%Ni/TiO ₂ , (c)
10%Cu-5%Ni/TiO ₂ , (d) 10%Cu-10%Ni/TiO ₂ , (e) 10%Cu-20%Ni/TiO ₂ , and (f)
10%Ni/TiO ₂ catalysts59
Fig. 4.3 H ₂ -TPR reduction profiles of (a) 10%Cu/TiO ₂ , (b) 10%Cu-2.5%Ni/TiO ₂ , (c)
10%Cu-5%Ni/TiO ₂ , (d) 10%Cu-10%Ni/TiO ₂ , and (e) 10%Ni/TiO ₂ catalysts61
Fig. 4.4 SEM images of (a) 10%Cu/TiO ₂ , (b) 10%Cu-2.5%Ni/TiO ₂ , (c) 10%Cu-
5% Ni/TiO ₂ , (d) 10% Cu-10% Ni/TiO ₂ , (e) 10% Cu-20% Ni/TiO ₂ , and (f) 10% Ni/TiO ₂ .
63
Fig. 4.5 FESEM micrograph of calcined 10%Cu-10%Ni/TiO ₂ catalyst
Fig. 4.6 HRTEM images of reduced 10%Cu-10%Ni/TiO ₂ catalyst65

Fig. 4.7 XPS spectra of (a) Cu 2p, (b) Ni 2p, (c) Ti 2p and (d) O 1s of calcined 10% Cu-
10%Ni/TiO ₂
Fig. 4.8 XPS spectra of (a) Cu 2p, and (b) Ni 2p, of reduced 10% Cu- 10% Ni/TiO ₂ 68
Fig. 4.9 NH ₃ -TPD profiles of calcined (a) 10% Cu/TiO ₂ , (b) 10% Cu- 10% Ni/TiO ₂ , and
(c) 10%Ni/TiO ₂ catalysts
Fig. 4.10 Proposed mechanism of FFR HDO over 10%Cu/TiO ₂ catalys
Fig. 4.11 Proposed mechanism of FFR HDO over 10%Ni@TiO ₂ catalyst
Fig. 4.12 Conversion and product selectivities over TiO ₂ supported mono- and
bimetallic Cu-Ni catalysts. Reaction conditions: Feed flowrate = $9.05 \text{ mmol}_{FFR} \text{ h}^{-1}$
H_2/FFR ratio = 15, Temp. = 200 °C, WHSV = 0.87 g_{FFR} h^{-1} $g_{catalayst}^{-1}$, Pressure = 1 atm
Fig. 4.13 Proposed mechanism of FFR HDO over bimetallic Cu-Ni/TiO ₂ catalyst
Fig. 4.14 Effect of reaction temperature on FFR HDO over 10%Cu-10%Ni/TiO ₂
catalysts. Reaction conditions: Feed flowrate = 9.05 mmol _{FFR} h ⁻¹ , H ₂ /FFR ratio = 15
WHSV = $0.87 \text{ g}_{\text{FFR}} \text{ h}^{-1} \text{ g}_{\text{catalayst}}^{-1}$, Pressure = 1 atm
Fig. 4.15 Effect of WHSV on FFR HDO over 10%Cu-10%Ni/TiO ₂ catalysts. Reaction
conditions: Feed flowrate = 9.05 mmol _{FFR} h ⁻¹ , H ₂ /FFR ratio = 15, Temp. = 200 °C
Pressure = 1 atm80
Fig. 4.16 FFR HDO over 10%Cu-10%Ni/TiO ₂ catalysts through CTH using IPA as the
H donor. Reaction conditions: Feed flowrate = 9.05 mmol _{FFR} h ⁻¹ , IPA/FFR ratio = 20
Temp. = 200 °C, WHSV = 0.87 $g_{FFR} h^{-1} g_{catalayst}^{-1}$, Pressure = 1 atm
Fig. 4.17 Time-on-stream (TOS) study on FFR HDO over 10%Cu-10%Ni/TiO ₂
catalysts. Reaction conditions: Feed flowrate = 9.05 mmol _{FFR} h ⁻¹ , H ₂ /FFR ratio = 15
Temp. = 200 °C, WHSV = 0.87 $g_{FFR} h^{-1} g_{catalayst}^{-1}$, Pressure = 1 atm
Fig. 5.1 XRD diffractograms of fresh Cu-Fe oxides with (a) Cu/Fe = 0.5, (b) Cu/Fe =
1, (c) $Cu/Fe = 1.5$ and (d) $Cu/Fe = 2$
Fig. 5.2 XRD diffractograms of reduced Cu-Fe oxides with (a) Cu/Fe = 0.5, (b) Cu/Fe
= 1, (c) Cu/Fe = 1.5 and (d) Cu/Fe = 294

Fig. 5.3 H ₂ -TPR profiles of the synthesized Cu-Fe mixed oxide catalysts with Cu/Fe
ratios of (a) 0.5, (b) 1, (c) 1.5 and (d) 2
$Fig.\ 5.4\ Temperature-programmed\ NH_{3}\ desorption\ profiles\ of\ reduced\ (a)\ Cu/Fe=0.5,$
(b) $Cu/Fe = 1$, (c) $Cu/Fe = 1.5$ and (d) $Cu/Fe = 2$ catalysts
Fig. 5.5 XPS spectra of (a) Cu 2p and (b) Fe 2p for the reduced catalyst with Cu/Fe =
1101
Fig. 5.6 FESEM images of calcined Cu-Fe oxide catalysts with (a) Cu/Fe = 1, (b) Cu/Fe
= 2, (c) Cu/Fe = 3, and (d) Cu/Fe = 4
Fig. 5.7 HRTEM images of the Cu-Fe mixed catalyst with Cu/Fe = 1 and reduced at 350°C
Fig. 5.8 Effect of Cu to Fe molar ratio on conversion and product selectivities during
FFR HDO. Reaction conditions: feed flowrate = $5.43 \text{ mmol}_{FFR} \text{ h}^{-1}$, $\text{H}_2/\text{FFR} = 15$,
$Temperature = 230 ^{\circ}C, WHSV = 0.5 g_{FFR} h^{1} g_{catalyst} ^{1}, Pressure = 1 atm \dots 104 e^{1} g_{catalyst} ^{1}$
Fig. 5.9 Probable FFR HDO to 2-MeF mechanism over Cu-Fe catalyst with $\mbox{Cu/Fe} = 1$
106
Fig. 5.10 Effect of reaction temperature on conversion and product selectivities during
FFR HDO over Cu-Fe mixed oxide catalyst with $\text{Cu/Fe} = 1$. Reaction conditions: feed
$flowrate:~5.43~mmol_{FFR}~h^{1},~H_2/FFR=15,~WHSV=0.5~g_{FFR}~h^{1}~g_{catalyst}~^{1},~Pressure=1$
atm
Fig. 5.11 Effect of WHSV on conversion and product selectivities during FFR HDO
over Cu-Fe mixed oxide catalyst with Cu/Fe = 1. Reaction conditions: $H_2/FFR = 15$,
Temperature = 230 °C, Pressure = 1 atm
Fig. 5.12 Effect of reduction temperature on conversion and product selectivities during
FFR HDO over Cu-Fe mixed oxide catalyst with $\text{Cu/Fe} = 1$. Reaction conditions: feed
$flowrate = 5.43 \ mmol_{FFR} \ h^{1}, \ H_{}/FFR = 15, \ Temperature = 230 \ ^{\circ}C, \ WHSV = 0.5 \ g_{FFR} = 10.000 \ g_{FFR} = 10.000$
h^{-1} $g_{catalyst}$ -1, $Pressure = 1$ atm
Fig. 5.13 XRD diffractograms of Cu-Fe oxide catalyst with Cu/Fe = 1 reduced at (a)
350 °C, (b) 450 °C and (c) 550 °C
Fig. 5.14 Fe $2p$ XPS spectrum of Cu-Fe oxide catalyst with Cu/Fe = 1 reduced at (a)
450 °C, and (b) 550 °C
Fig. 5.15 Effect of H ₂ /FFR molar ratio on conversion and product selectivities during
FFR HDO over Cu-Fe mixed oxide catalyst with Cu/Fe = 1. Reaction conditions: feed
flowrate = 5.43 mmol _{FFR} h^{-1} , Temperature = 230 °C, WHSV = 0.5 $g_{FFR} h^{-1} g_{catalyst}^{-1}$,
Pressure = 1 atm. 114

Fig. 5.16 Time-on-stream (TOS) study for FFR HDO over Cu-Fe mixed oxide cataly with Cu/Fe = 1. Reaction conditions: feed flowrate = $5.43 \text{ mmol}_{\text{FFR}} \text{ h}^{-1}$, H ₂ /FFR = 1 mixed						
Temperature = 230 °C, WHSV = 0.5 $g_{FFR} h^{-1} g_{catalyst}^{-1}$, Pressure = 1 atm, TOS = 24 h.						
Fig. 5.17 Regeneration study for FFR HDO over Cu-Fe mixed oxide catalyst with						
Cu/Fe = 1. Reaction conditions: feed flowrate = 5.43 mmol _{FFR} h ⁻¹ , H ₂ /FFR = 10,						
Temperature = 230 °C, WHSV = 0.5 $g_{FFR} h^{-1} g_{catalyst}^{-1}$, Pressure = 1 atm, TOS = 24 h						
Fig. 6.1 The XRD diffractograms of the calcined (a) Cu@MS, (b) Cu@Al-MS, (c)						
Cu@Sn-MS, (d) Cu@Ti-MS, and (e) Cu@Zr-MS catalysts124						
Fig. 6.2 The XRD diffractograms of the (a) Cu@MS, (b) Cu@Al-MS, (c) Cu@Sn-MS,						
(d) Cu@Ti-MS, and (e) Cu@Zr-MS catalysts reduced at 300 °C						
Fig. 6.3 FTIR spectra of (a) MS, (b) Al-MS, (c) Sn-MS, (d) Ti-MS and (e) Zr-MS						
supports						
Fig. 6.4 N ₂ physisorption-desorption curves for the calcined Cu@M-MS catalysts. 128						
Fig. 6.5 Deconvoluted reduction profiles of the (a) Cu@MS, (b) Cu@Al-MS, (c)						
Cu@Sn-MS, (d) Cu@Ti-MS, and (e) Cu@Zr-MS catalysts131						
Fig. 6.6 Deconvoluted NH ₃ -TPD profiles of the (a) Cu@MS, (b) Cu@Al-MS, (c)						
Cu@Sn-MS, (d) Cu@Ti-MS, and (e) Cu@Zr-MS catalysts						
Fig. 6.7 XPS Spectrum of Si 2p for (a) MS, (b) Al-MS, (c) Sn-MS, (d) Ti-MS, and (e)						
Zr-MS supports						
Fig. 6.8 (i) Reduced XPS Cu 2p spectra of (a) Cu@MS, (b) Cu@Al-MS, (c) Cu@Sn-						
MS, (d) Cu@Ti-MS and (e) Cu@Zr-MS catalysts and (ii) Zr 3d spectra of reduced						
Cu@Zr-MS catalyst. 136						
Fig. 6.9 Cu Auger Spectra for reduced (a) Cu-MS, and (b)Cu@Al-MS, (c) Cu@Sn-MS,						
(d) Cu@Ti-MS, and Cu@Zr-MS catalysts						
Fig. 6.10 XPS spectra of (a) Sn 3d, (b) Ti 2p and (c) Al 2p of reduced Cu@Sn-MS and						
Cu@Ti-MS catalysts, respectively						
Fig. 6.11 FESEM images of the calcined (a) Cu@MS, (b) Cu@Al-MS, (c) Cu@Sn-						
MS, (d) Cu@Ti-MS, and (e) Cu@Zr-MS catalysts						
Fig. 6.12 HRTEM images of the reduced Cu@Zr-MS catalyst						

Fig. 6.13 Effect of Metal Incorporation on the conversion and yield during FFR
hydrogenation over Cu supported on mesoporous silica catalysts. Feed Flowrate = 5.43
$mmol_{FFR} h^{-1}$, $H_2/FFR = 10$, $Temperature = 180 ^{\circ}C$, $WHSV = 1 g_{FFR} h^{-1} g_{catalyst}^{-1}$, $Pressure = 180 ^{\circ}C$
= 1 atm
Fig. 6.14 Effect of reaction temperature on the conversion and yield during FFR
hydrogenation over Cu@Zr-MS catalyst. Feed Flowrate = 5.43 mmol _{FFR} h ⁻¹ , H ₂ /FFR =
10, WHSV = 1 $g_{FFR} h^{-1} g_{catalyst}^{-1}$, Pressure = 1 atm
Fig. 6.15 Effect of WHSV on the conversion and yield during FFR hydrogenation over
Cu@Zr-MS catalyst. H ₂ /FFR = 10, Temperature = 200 °C, Pressure = 1 atm 146
Fig. 6.16 Time-on-Stream (TOS) study for FFR hydrogenation to FAL over Cu@Zr-
MS catalyst. Feed Flowrate = 5.43 mmol _{FFR} h ⁻¹ , H ₂ /FFR = 10, Temperature = 200 °C,
WHSV = 1 $g_{FFR} h^{-1} g_{catalyst}^{-1}$, Pressure = 1 atm, TOS = 30 h
Fig. 6.17 Regeneration study for FFR hydrogenation to FAL over Cu@Zr-MS catalyst.
Feed Flowrate = 5.43 mmol _{FFR} h ⁻¹ , H ₂ /FFR = 10, Temperature = 200 °C, WHSV = 1
$g_{FFR} h^{-1} g_{catalyst}^{-1}$, $Pressure = 1 atm$, $TOS = 24 h$
Fig. 6.18 A schematic representation of possible reaction mechanism of FFR
hydrogenation over Cu@Zr-MS to
FAL150
Fig. 7.1 XRD diffraction patterns of (a) Mg0Fe1 and Mg1Fe0 and (b) Mg-Fe mixed
oxide catalysts with varying Mg/Fe ratios159
Fig. 7.2 NH ₃ -TPD profiles of (a) Mg0Fe1, (b) Mg4Fe1 and (c) Mg1Fe0 catalysts.
4.64
161
Fig. 7.3 CO ₂ -TPD profiles of (a) Mg0Fe1, (b) Mg4Fe1 and (c) Mg1Fe0
Fig. 7.3 CO ₂ -TPD profiles of (a) Mg0Fe1, (b) Mg4Fe1 and (c) Mg1Fe0
Fig. 7.3 CO ₂ -TPD profiles of (a) Mg0Fe1, (b) Mg4Fe1 and (c) Mg1Fe0 catalysts
Fig. 7.3 CO ₂ -TPD profiles of (a) Mg0Fe1, (b) Mg4Fe1 and (c) Mg1Fe0 catalysts
Fig. 7.3 CO ₂ -TPD profiles of (a) Mg0Fe1, (b) Mg4Fe1 and (c) Mg1Fe0 catalysts
Fig. 7.3 CO ₂ -TPD profiles of (a) Mg0Fe1, (b) Mg4Fe1 and (c) Mg1Fe0 catalysts
Fig. 7.3 CO ₂ -TPD profiles of (a) Mg0Fe1, (b) Mg4Fe1 and (c) Mg1Fe0 catalysts
Fig. 7.3 CO ₂ -TPD profiles of (a) Mg0Fe1, (b) Mg4Fe1 and (c) Mg1Fe0 catalysts

mmol _{FFR} h ⁻¹ , Temperature = 300 °C, WHSV = 0.70 g _{FFR} h ⁻¹ g _{catalyst} ⁻¹ , Pressure = 1 atm
Fig. 7.8 (a) FFR conversion, (b) FAL selectivity, and (c) 2-MeF selectivity over Mg-Fe
mixed oxide catalysts with varying Mg/Fe ratios during FFR CTH. Reaction conditions:
feed flowrate = 7.24 mmol _{FFR} h ⁻¹ , Temperature = 300 °C, WHSV = 0.70 g _{FFR} h ⁻¹ g _{catalyst}
⁻¹ , Pressure = 1 atm
Fig. 7.9 (a) FFR conversion, (b) FAL selectivity, and (c) 2-MeF selectivity over Mg-Fe
mixed oxide catalysts with Mg/Fe = 4 during FFR CTH at different temperatures.
Reaction conditions: feed flowrate = $7.24 \text{ mmol}_{FFR} \text{ h}^{-1}$, WHSV = $0.70 \text{ g}_{FFR} \text{ h}^{-1} \text{ g}_{catalyst}^{-1}$,
Pressure = 1 atm
Fig. 7.10 (a) FFR conversion, (b) FAL selectivity, and (c) 2-MeF selectivity over Mg-
Fe mixed oxide catalysts with Mg/Fe = 4 during FFR CTH at different space velocity
values ($g_{FFR} \ g_{catalyst}^{-1} \ h^{-1}$). Reaction conditions: Temperature = 400 °C, Pressure = 1 atm
176
Fig. 7.11 (a) FFR conversion, (b) FAL selectivity, and (c) 2-MeF selectivity over Mg-
Fe mixed oxide catalysts with $Mg/Fe = 4$ calcined at different temperatures during FFR
CTH. Reaction conditions: feed flowrate = $7.24 \text{ mmol}_{FFR} \text{ h}^{-1}$, Temperature = $400 ^{\circ}\text{C}$,
$WHSV = 0.70 \ g_{FFR} \ h^{-1} \ g_{catalyst}^{-1}, \ Pressure = 1 \ atm \ 178$
Fig. 7.12 Diffraction patterns of the Mg-Fe mixed oxide catalysts with $Mg/Fe = 4$
calcined at (a) 400 °C, (b) 600 °C, (c) 700 °C and (d) 800 °C
Fig. 7.13 FESEM images of the Mg-Fe mixed oxide catalysts with $Mg/Fe = 4$ calcined
at (a) 400 °C, (b) 600 °C, (c) 700 °C and (d) 800 °C
Fig. 7.14 Time-on-stream (TOS) study for FFR CTH over Mg-Fe mixed oxide catalysts
with Mg/Fe = 4 calcined at 500 °C. Reaction conditions: feed flowrate = 7.24 mmol $_{\rm FFR}$
$h^{\text{-}1}\text{, Temperature} = 400~^{\circ}\text{C, WHSV} = 0.70~g_{FFR}~h^{\text{-}1}~g_{catalyst}~^{\text{-}1}\text{, Pressure} = 1~atm$
Fig. 7.15 Regeneration study for FFR CTH over Mg-Fe mixed oxide catalysts with
Mg/Fe = 4 calcined at 500 $^{\circ}$ C. Reaction conditions: feed flowrate = 7.24 mmol _{FFR} h ⁻¹ ,
Temperature = 400 °C, WHSV = 0.70 $g_{FFR} h^{-1} g_{catalyst}^{-1}$, Pressure = 1 atm
Fig. 7.16 Probable reaction of FFR CTH to 2-MeF over Mg-Fe mixed catalyst with
Mg/Fe = 4 185

List of tables

Table 2.1 Literature representing studies in vapor-phase hydrodeoxygenation of FFR to
2-MeF using molecular H ₂
Table 2.2 Literature representing studies in vapor-phase hydrogenation of FFR to 2-
FAL using molecular H ₂ 24
Table 2.3 Literature representing studies in vapor-phase transfer hydrogenation of FFR
to 2-MeF
Table 4.1 Physical properties of the calcined mono- and bimetallic Cu-Ni catalysts
57
Table 4.2 Physical properties of the reduced mono- and bimetallic Cu-Ni
catalysts59
Table 4.3 Elementary surface composition of the synthesized mono- and bimetallic Cu-
Ni bimetallic catalysts 64
Table 5.1 Physical properties of the Cu-Fe mixed oxide catalysts
95
Table 5.2 Reduction temperature (°C) and H ₂ Consumption values for Cu-Fe mixed
oxide catalysts with varying Cu/Fe ratios obtained through deconvolution of $H_2\text{-}TPR$
profile98
Table 5.3 Elemental surface composition of the synthesized Cu-Fe mixed oxide
catalysts using EDX analysis
Table 6.1 Metal content of the rice husk ash before and after acid treatment
Till 62 N i l G OMS 1 G OMM 1 C OMM 1
Table 6.2 Physical properties of the Cu@MS and Cu@M-MS catalysts
Table 6.3 Elemental composition of the synthesized Cu supported on pristine and metal-
incorporated mesoporous silica catalysts

Table 7	'.1 Physical	properties of	of the	synthesized	pure	and	mixed	oxide	Mg-Fe
catalysts	S	•••••				•••••			159
Table 7	.2 Elemental	composition	n anal	ysis of the p	oristine	and	Mg-Fe	mixe	d oxide
catalysts	S	•••••				•••••		•••••	164
Table 7	.3 CO ₂ Deso	rption Value	s fron	n CO ₂ -TPD	Analys	is of	Mg-Fe	Mixed	l Oxide
Catalyst	s with Mg/Fe	e = 4 calcined	l at dif	fferent tempe	ratures	• • • • • • • • • • • • • • • • • • • •			181

List of abbreviations

1,5-PDO	1,5-Pentanediol
1-POL	1-Pentanol
2-MeF	2-Methylfuran
2-MeTHF	2-Methyltetrahydrofuran
2-POL	2-Pentanol
2-PON	2-Pentanone
ВЈН	Barrett-Johner-Halenda
BE	Binding Energy
BET	Brunauer-Emmett-Teller
ID	Inner Diameter
FFR	Furfural
FAL	Furfuryl Alcohol
FID	Flame Ionization Detector
FTIR	Fourier Transform Infrared Spectroscopy
GHSV	Gas Hourly Space Velocity
FESEM	Field Emission Scanning Electron Microscopy
GCMS	Gas Chromatography Mass Spectroscopy
HRTEM	High Resolution Transmission Electron Microscopy
SEM	Scanning Electron Microscopy
THFA	Tetrahydrofurfuryl Alcohol
TPD	Temperature Programmed Desorption
TPR	Temperature Programmed Reduction
TOS	Time-on-Stream
WHSV	Weight Hourly Space Velocity
WHST	Weight Hourly Space Time
XRD	X-ray Diffraction
XPS	X-ray Photon Spectroscopy

1.1 Chemicals and Fuels: Cornerstones of Technological and Economic Progress

Chemicals and fuels are the bedrock of contemporary human society, intricately woven into every facet of modern life. Chemicals serve as essential components in our infrastructure, from buildings and vehicles adorned with plastics, rubber, and synthetic textiles, to the ubiquitous items of daily use such as toothbrushes, carrier bags, and food packaging. They are embedded in vital technologies, including mobile phones and computers, and are even present in our furnishings - carpets, clothing, and furniture. Beyond their visible applications, chemicals enhance other materials like metals and wood through protective coatings and decorative finishes. In the digital age, plastics are increasingly supplanting paper for information transmission in electronic devices. Modern agriculture heavily relies on chemical fertilizers and agrochemicals to sustain high productivity levels, while the pharmaceutical industry, pivotal to healthcare advancements, is fundamentally driven by chemical innovations. Equally indispensable are fuels, which power transportation systems, provide energy for heating and electricity generation, and drive industrial processes. Fuels underpin the operation of critical infrastructure and are significant contributors to economic growth, facilitating technological advancements and global interconnectedness. The efficient and innovative use of fuels has enabled increased mobility, enhanced industrial capabilities, and interconnected economies on a global scale. In summary, the omnipresence and indispensability of chemicals and fuels underscore their vital role in sustaining human prosperity. They form the cornerstone of modern infrastructure, products, and services, defining the essence of contemporary life. As we look towards the future, the continued development and efficient utilization of these resources are paramount in addressing the emerging challenges and ensuring a sustainable and prosperous global society.

1.2 The Dominance of Fossil Fuels and the Imperative for Transition

Fossil fuels - coal, oil, and natural gas - have for long been the dominant sources of energy and raw materials for chemicals and fuels [1–3]. They have powered industrialization, driven economic growth, and facilitated technological advancements over the past century and a half. However, this over-dependence on fossil fuels has led to fear of an inevitable exhaustion in the not-so-distant future [4,5], disturbances in

supply chain, price fluctuation and/or market manipulation [3]. Their use also results in the emission of greenhouse gases such as CO₂, responsible for global climate change, in extremely large quantities and widespread environmental degradation in the form of land, air and water pollution [3,5,6]. Besides, the substantial rise in their prices over the last few decades has taken away the competitive edge they have had over other sources such as biomass, resulting in a considerable improvement in competitiveness of renewable sources [5,7,8]. Thus, a shift away from fossil fuels towards renewable sources is a timely and highly desirable step if sustainable development is to be achieved.

1.3 Harnessing Biomass: A Pathway to Cleaner Energy and Chemicals

In recent times, biomass, a renewable energy source available in abundance, has emerged as an excellent alternative to traditional fossil resources. Biomass refers to any organic material with a recent origin that can be replenished in a matter of years or decades [9,10]. These include not just plants, crops, bushes, trees, and plant-based materials such as agricultural wastes, residues from forestry but also waste food, animal by-products and animal and human wastes (Fig. 1.1). Due to shorter replenishment times, they are considered short cycle carbon systems, as opposed to fossil fuels that are regarded as long cycle carbon materials [11]. Moreover, since the plant materials comprising biomass utilize the atmospheric CO₂ released by natural or anthropogenic sources during their growth, it makes biomass a carbon neutral resource [3,10]. Among the various types of biomass feedstocks, lignocellulosic biomass has, in particular, emerged as the most suitable feedstock for producing bulk as well as speciality chemical due to a number of reasons. First, since it is non-edible [12], the competition with food production is avoided, and the food vs fuel debate does not arise [13]. Second, it is the most abundant among all the biomass feedstocks [10], due to which the fluctuations in supply tend to be minimum. Third, lignocellulosic biomass grows much faster and can be obtained at lower costs as compared to agriculturally valuable food crop feedstocks [13]. These factors combined with its significant oxygen content, make lignocellulosic biomass a highly promising green platform for producing an extremely diverse portfolio of both low volume and high value chemicals as well as low value, high volume fuels products along a value chain similar to fossil fuel-based compounds.

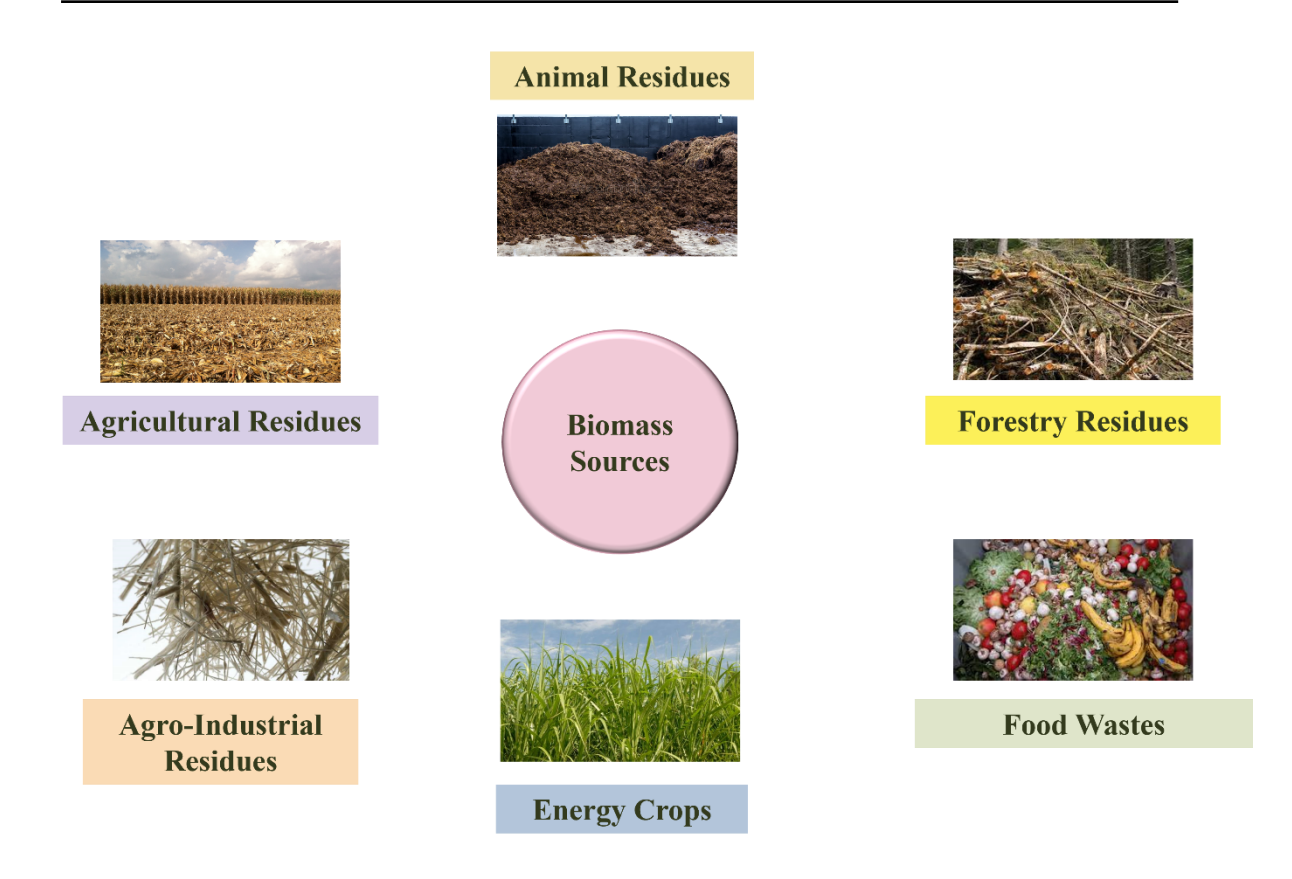


Fig. 1.1 Typical sources of biomass

1.4 Breaking Down Biomass: Understanding Its Composition and Structure

Lignocellulosic biomass is defined by its complex and varied composition, which significantly influences its utility and processing. It is primarily made up of three polymeric fractions - cellulose, hemicellulose and lignin - that together make up nearly 90% of its dry weight (Fig. 1.2) [14]. These three fractions form complex, non-uniform three-dimensional structures that can vary in composition as well as complexity depending on the type of biomass feedstock [10]. A major consequence of this structural complexity is that lignocellulosic biomass is robust and recalcitrant to both chemical as well enzymatic degradation [10,15]. Its recalcitrance is usually ascribed to a combination of the crystalline nature of cellulose, the hydrophobic properties of lignin, and the encapsulation of cellulose by the lignin-hemicellulose matrix [15].

Cellulose is the most abundant among these fractions and constitutes approximately half of the organic carbon in the biosphere [10]. It is made up of repeating _D-glucose units, each forming a six-carbon pyranose ring [14,16,17]. The three hydroxyl groups on each pyranose ring engage in intra- and intermolecular hydrogen bonding [14,16,17], which bestows cellulose with its unique crystalline structure, mechanical

strength, and chemical stability. The pyranose rings are connected by β -1,4-glycosidic linkages [14,16,17], involving the loss of a water molecule, thereby classifying cellulose as a polysaccharide of anhydroglucopyranose. The structure of cellulose includes both crystalline and amorphous regions, which alternate in the form of microfibrils. It possesses a high degree of polymerization [18], which can range to values as high as 10,000 and 15,000 glucopyranose units in materials such as wood and cotton, respectively [17]. When subjected to partial acid hydrolysis, cellulose breaks down into cellobiose (a glucose dimer), cellotriose (a glucose trimer), and cellotetrose (a glucose tetramer). Complete acid hydrolysis further degrades cellulose into glucose, illustrating its complex yet systematically degradable nature [17].

Hemicellulose is the second most prevalent polymer in lignocellulosic biomass. Unlike cellulose, which is a linear chain of glucose units, hemicellulose is a diverse and amorphous polysaccharide composed of various heteropolymers such as xylan, galactomannan, glucuronoxylan, arabinoxylan, glucomannan, and xyloglucan [10,14,16,17]. Its structure integrates a mix of pentose sugars like xylose and arabinose, and hexose sugars including mannose, glucose, and galactose, often with acetyl groups attached [10]. In the plant cell wall, hemicellulose plays a crucial role by forming a network that links cellulose fibers into microfibrils and connects with lignin [10,16], contributing to the overall structural integrity of the plant. Due to its branched, noncrystalline nature and lower degree of polymerization (50 to 200 monomer units) as compared to cellulose (as high as 15000 glucopyranose units for cotton), hemicellulose is more susceptible to hydrolysis and can be easily broken down into its constituent sugars by dilute acids, bases, or hemicellulase enzymes [14,16,17].

Lastly, lignin is a three-dimensional polymer composed of a diverse array of phenylpropane units, including p-coumaryl alcohol, coniferyl alcohol, and sinapyl alcohol, which are linked by a variety of C-O-C and C-C bonds [10,14,16,17]. The phenylpropane units in lignin can be categorized into three primary types: guaiacyl (G), syringyl (S), and p-hydroxyphenyl (H) units [10,14,16,17], with their proportions varying between softwoods and hardwoods. In softwoods, lignin predominantly consists of guaiacyl units, whereas hardwood lignin is a co-polymer of both guaiacyl and syringyl units, reflecting a higher methoxyl content [10,14,16,17]. Lignin's macromolecular structure is characterized by its high molecular weight, averaging around 20,000, with a polydispersity index greater than that of cellulose [14]. This high

molecular weight and its complex bonding network contribute to lignin's limited solubility [14] and its effectiveness in tightly binding cellulose and hemicellulose within the plant cell wall [16]. Lignin's presence provides structural rigidity and stability to plant cell walls and enhances their resistance against insects and pathogens [10]. Additionally, it contributes to challenges in converting lignocellulosic biomass into valuable products, forming compounds such as furans during degradation, that inhibit fermentation and thereby complicating the extraction of fermentable sugars [14].

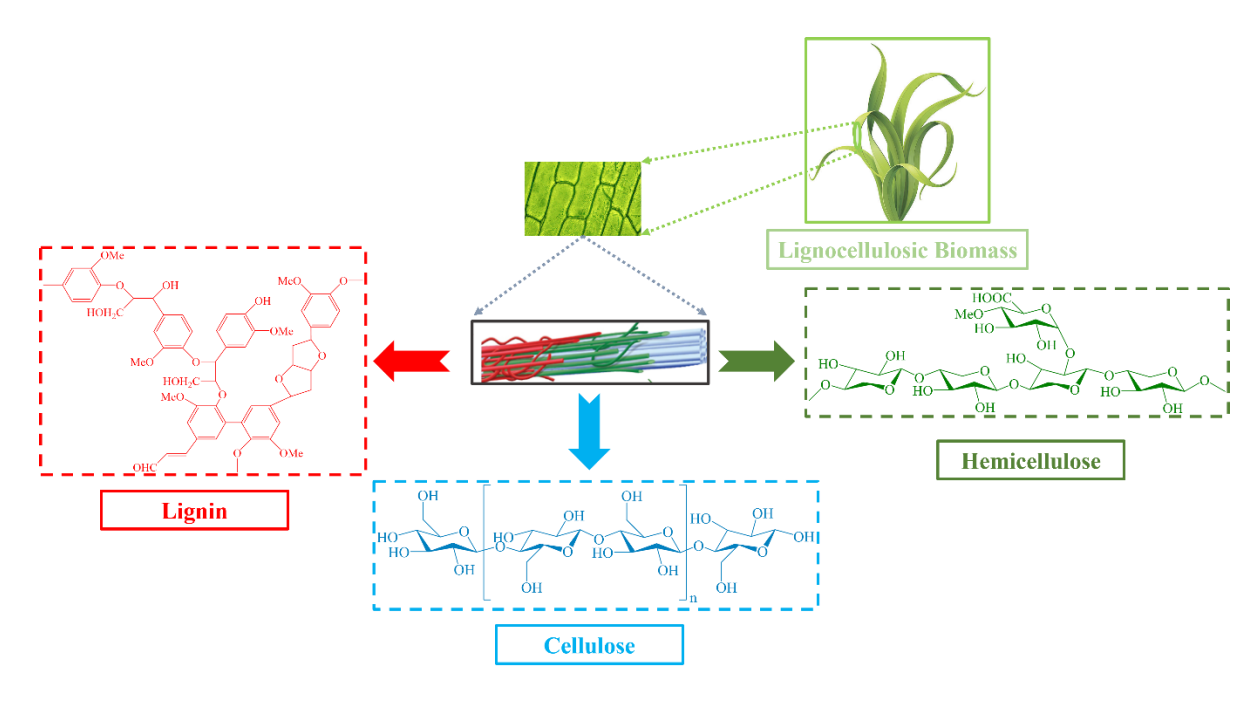


Fig. 1.2 Structure of lignocellulosic biomass.

1.5 Biomass Conversion Strategies: From Raw Material to Valuable Products

Lignocellulosic biomass has traditionally been seen primarily as a potential source of biofuels. Consequently, several strategies have been developed over the course of the past few years for this particular pursuit. Currently, thermochemical methods such as combustion [19], gasification [20], pyrolysis [21], and hydrothermal liquefaction [22] are the predominant techniques for converting biomass into biofuels (Fig. 1.3). These processes involve heating biomass at moderate to high temperatures and, at times, under varying pressures to achieve thermal degradation [23]. However, the multi-scale complexity arising from the complex and rigid structure of polymeric lignocellulose has proven to be a huge and thus far, an unsurmountable challenge in the pursuit of sustainable fuels from biomass. The liquid fuels produced through these thermochemical routes yield are of low quality and low energy content due to their highly acidic nature and presence of large amounts of oxygenated compounds and water

[24]. Further treatment by processes such as hydrodeoxygenation, Fischer-Tropsch synthesis, water-gas shift reaction etc. is required to increase their energy contents and remove the oxygenated compounds before they can be used as transportation fuels [24,25].

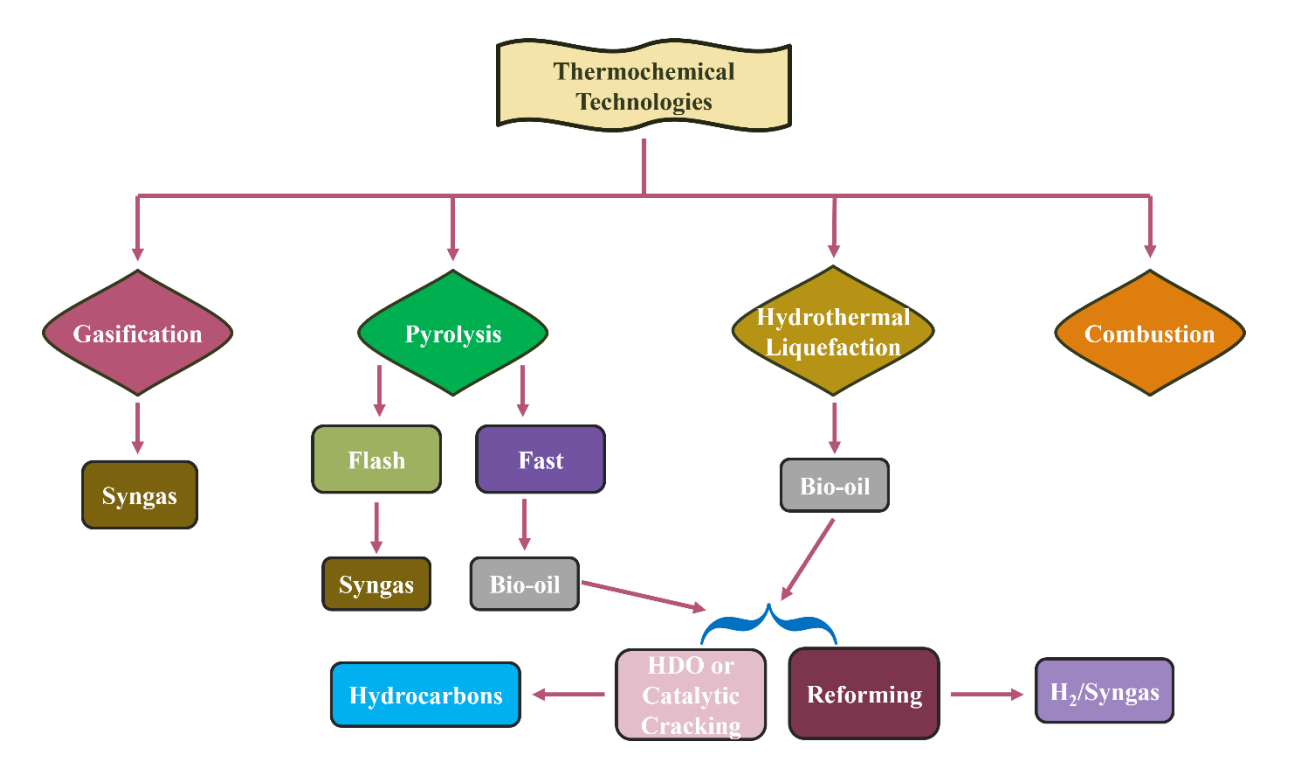


Fig. 1.3 Common thermochemical strategies for lignocellulosic biomass conversion and their products.

1.6 Reimagining Biomass Valorization: Chemicals Over Biofuels

In light of these challenges, there is a growing push to shift the focus of biomass conversion from fuels to chemicals, which could then be further transformed to a wide range of industrially and economically relevant chemicals and fuels. Several factors underpin this strategic shift. Firstly, lignocellulosic biomass contains a significant amount of oxygen - up to 50 wt.%. This high oxygen content enables the production of a diverse array of chemicals that surpass the range typically derived from fossil sources like crude oil. Secondly, while biomass conversion for biofuels produces a broad spectrum of products, concentrating on chemical production allows for more targeted transformations. This selective approach results in fewer products but with higher yields and selectivity. Evidence from mass and energy balance comparisons highlights this advantage: while one kilogram of crude oil yields approximately 0.2 kg of chemicals and 0.8 kg of fuels with a total caloric value of 32 MJ, biomass converted to

ethanol yields only about 6 MJ of energy per kilogram [2]. In contrast, focusing solely on chemical production from biomass can achieve around 0.8 kg of chemicals per kilogram of biomass, reflecting greater efficiency in conversion [2]. Moreover, biomass-derived chemicals present higher valorization opportunities. For instance, specialty aromatic chemicals obtained from lignin via catalytic depolymerization can command prices as high as \$100 per kg for substances like vanillin, compared to around \$1 per kg for petrofuels [2]. Finally, the economic feasibility of biomass-based fuels is increasingly undermined by the efficiency and cost-effectiveness of alternative energy sources such as electricity, hydrogen (H₂), and fuel cells. The availability of low-cost crude oil and shale gas further erodes the competitiveness of biomass-derived fuels. As a result, the production of high-value, low-volume chemicals from biomass offers a more viable and economically sustainable alternative. Given the shift towards electrification and more stringent regulations on combustion engines, focusing on chemical manufacturing from biomass is poised to be a more resilient and profitable pathway for the future.

1.7 Biorefineries and Beyond

Building upon the recognition of biomass as a versatile feedstock beyond traditional biofuels, biorefineries emerge as pivotal facilities for converting biomass into a diverse array of chemicals. Biorefineries represent a paradigm shift in sustainable industrial practices, akin to their petroleum counterparts but tailored to utilize renewable biomass sources. These facilities are envisioned to integrate various conversion processes - thermochemical, chemical, and biological - to extract valuable chemical compounds from biomass (Fig. 1.4) [26]. However, the inherent complexity and variability of biomass composition present notable challenges.

Biomass is a heterogeneous mix of cellulose, hemicellulose, lignin, and other components like proteins, fats, and minerals, with its composition varying by source, location, and season. This variability complicates processing and conversion, necessitating tailored approaches for different biomass types. For instance, lignocellulosic biomass, rich in cellulose and lignin, requires distinct processing methods compared to starch-rich biomass. Efficient chemical production from biomass demands an understanding of the chemical structure of the biomass feedstocks as well as innovations in pretreatment, conversion processes, and catalyst development [27,28].

Moreover, determining the most effective route to convert biomass into a particular biofuel is relatively straightforward since the target product and the feedstock are clearly defined [29]. The structured nature of biofuels production - clear product composition, established price targets, and predictable operational costs - enables focused process analysis and targeted R&D investments. Technologies failing to meet stringent price requirements for fuels are systematically replaced by more economically viable alternatives. In contrast, producing chemicals from biomass presents a far greater challenge. The complexity arises from a myriad of potential chemical products and diverse starting materials, compounded by the absence of standardized conversion technologies [30]. Bozell and Petersen [30] emphasize this intricate landscape, where various reactions and feedstocks offer numerous possibilities for chemical production. Current research in this domain typically employs a unified, versatile technology capable of producing multiple products within a broader family of materials. If a technology proves uneconomical for one application, it may still find viability in others within the same category. This approach allows for a higher-level assessment of energy and economic impacts across families of compounds rather than evaluating each product individually. This facilitates the identification of technology opportunities and promotes efficient and sustainable chemical production from biomass.

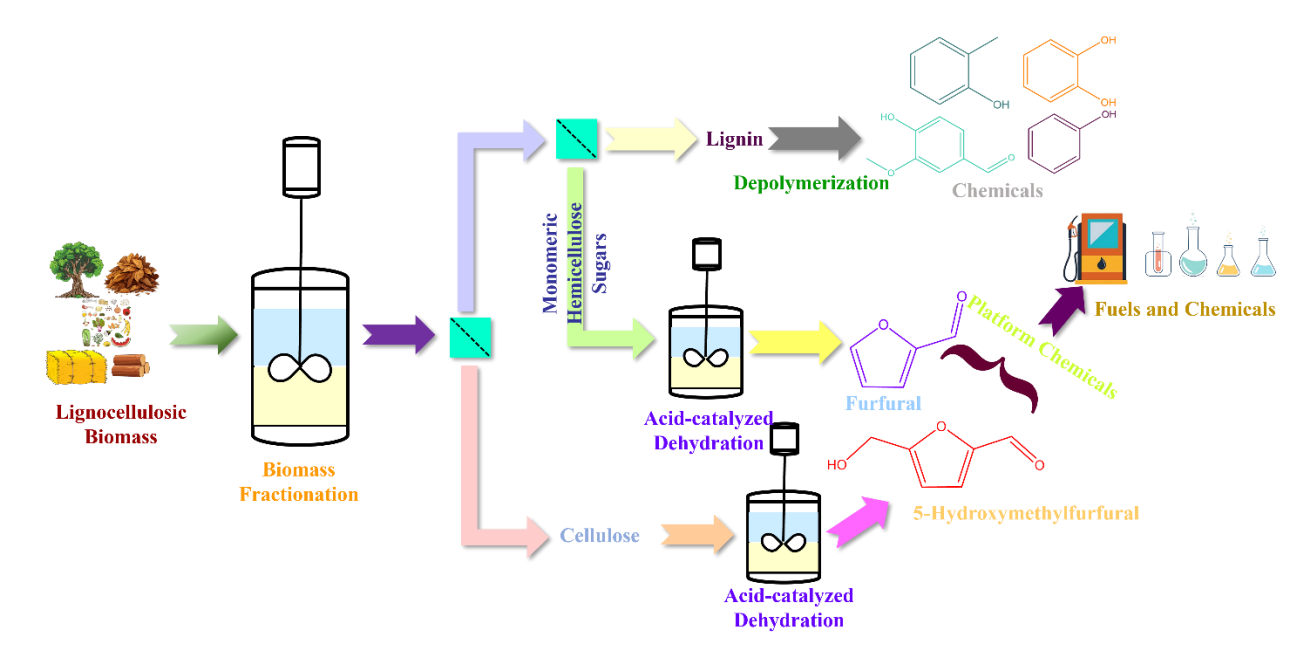


Fig. 1.4 A typical biorefinery featuring biomass conversion to value-added products.

1.8 Charting the Course: Platform Chemicals and the DOE 'Top 10' Roadmap for Biobased Chemical Production

In light of the above discussion, it clear that navigating the strategies for producing chemicals from biomass presents a central challenge: balancing the advancement of fundamental technologies with demonstrating their market potential. This challenge underscores the emergence of platform chemicals as a strategic framework to streamline and enhance chemicals as well as fuels production from biomass. Platform chemicals are intermediate compounds that serve as versatile building blocks for a broad array of end spanning different chemical families [11,31]. Unlike traditional methods focusing on isolated product lines, platform chemicals enable efficient synthesis of multiple high-value chemicals as well as high-volume fuels from a common set of starting materials [11,31].

In this direction, the US Department of Energy (DOE) released a pivotal report in 2004, known as the DOE "Top 10" report, outlining research needs for biobased products [30,32]. This seminal document identified 12 target chemical compounds achievable from biomass carbohydrates from a list of over 300 [30,32], aiming to harmonize broad technology development with targeted product identification. The report emphasized rational selection criteria for selecting biobased compounds and technologies: prioritizing compounds with significant research backing, broad applicability across multiple products akin to petrochemical practices, direct substitution potential for existing petrochemicals, capacity for high-volume production, versatility as starting materials for derivative production, readiness for scale-up, proven commercial presence, suitability as primary building blocks, and production from renewable carbon sources. By specifying chemical targets, the report advocated for using product identification as a guiding principle in research endeavours. This approach was not only aimed to advance technological capabilities but also sought to align biorefinery outputs with market demands.

1.9 Furfural: A Platform Chemical with Diverse Potential

Following the strategic framework for platform chemicals as outlined by the DOE "Top 10" report, furfural (FFR) emerges as a prime example of a versatile platform chemical with significant potential for biomass-derived applications. Recognized in the DOE

report as one of the key target chemicals, FFR is a valuable intermediate compound derived from lignocellulosic biomass, particularly from hemicellulose.

With a worldwide annual production of nearly 652 kilotons [33], FFR is by far the most common chemical of industrial importance that is manufactured exclusively from lignocellulosic biomass. First isolated in a laboratory scale in 1831, the first commercial facility for the production of FFR on a large scale was started by Quaker Oats Company in the year 1921 [33–40]. The current route of FFR production in industries involves the acid catalysed hydrolysis of pentoses present in the biomass to xylose which then yields FFR on dehydration [24,31,34–39,41]. However, the technologies currently in use for FFR production are very inefficient and suffer from a number of limitations such as low yields, undesirable side reactions such as condensation and polymerization, safety issues arising from the use of highly corrosive acids as catalysts, high energy consumption, and generation of large amounts of acidic effluent streams [24,31,42–44]. Efforts have been focused on increasing FFR yields and efficiencies of separations via a number of approaches such as using heterogeneous catalysts, ionic liquids, biphasic processes, supercritical extraction etc. [24,31].

The presence of an aldehyde group and an aromatic furan ring in FFR makes it highly reactive, allowing it to undergo the reactions of both the aromatic ring and the aldehyde functional group [31,41,45]. Due to its chemical reactivity, FFR can be transformed to more than 80 high value-added compounds (Fig. 5), directly or indirectly, through reactions such as selective hydro-deoxygenation, decarbonylation, decarboxylation, hydrogenation, and hydrogenolysis to building blocks, fuels, additives and other industrially important chemicals [31,41]. Fig. 1.5 displays some of the value-added chemicals that can be produced directly from FFR.

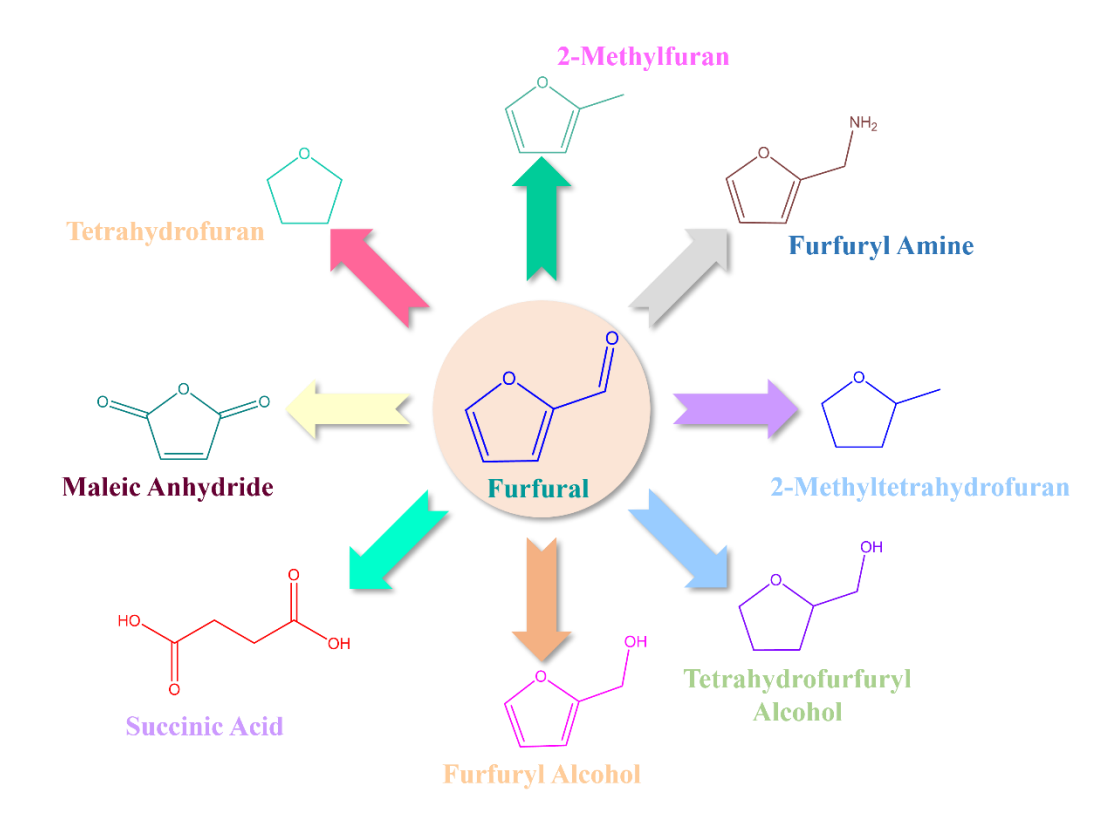


Fig. 1.5 List of some of the most relevant FFR derivatives.

1.10 Furfural Transformation: Pathways to Valuable Chemicals and Fuels

As discussed above, FFR can be transformed into a wide array of high-value chemicals through various catalytic processes such as hydrogenation, hydrodeoxygenation, ring opening, oxidation, and other transformations, each yielding distinct products. Hydrogenation and hydrodeoxygenation (HDO) are, by far, the most explored FFR transformations as they yield a very diverse range of highly valuable compounds such as 2-methylfuran (2-MeF), furfuryl alcohol (FAL), tetrahydrofurfuryl alcohol (THFA), 2-methyltetrahydrofuran (2-MeTHF), furan, and 1,5-pentanediol (1,5-PDO), etc. Among these, 2-MeF and FAL are the two derivatives that have garnered the most attention from the scientific community, which can be seen from the significant amount of work that has been done in the past few years.

1.9.1 2-Methylfuran

2-MeF has emerged as a potential biofuel and fuel additive due to its high research octane number (RON =103) and energy density (28.5 MJ L⁻¹). In addition, it also finds use as a solvent and a raw material in the synthesis of pharmaceutical drugs, pesticides and perfume intermediates, nitrogen and sulphur-containing heterocyclic and functionally substituted aliphatic compounds [41,46–48].

1.9.2 Furfuryl Alcohol

Currently, FAL is the most significant derivative of FFR, accounting for nearly 85% of the global annual FFR production [49] and serving a wide range of applications in the chemical industry. FAL is primarily used in the foundry industry to create resins for high-quality cores and molds for metal casting. It also serves as a reactive solvent for phenolic resins in the refractory industry and as a viscosity reducer for epoxy resins. Additionally, FAL is used in manufacturing polyurethane foams and polyesters and serves as a key building block in the synthesis of THFA, pharmaceuticals like ranitidine, and fragrances. Beyond these uses, FAL can be converted into other valuable chemicals, such as ethyl furfuryl ether (EFE), levulinic acid (LA), and gamma-valerolactone (GVL) [38,39].

References

- [1] British Petroleum, Energy Outlook 2023, 2023.
- [2] V.G. Yadav, G.D. Yadav, S.C. Patankar, The production of fuels and chemicals in the new world: critical analysis of the choice between crude oil and biomass vis-à-vis sustainability and the environment, Clean Technol. Environ. Policy. 22 (2020) 1757–1774. https://doi.org/10.1007/s10098-020-01945-5.
- [3] J.C. Serrano-Ruiz, R.M. West, J.A. Dumesic, Catalytic conversion of renewable biomass resources to fuels and chemicals, Annu. Rev. Chem. Biomol. Eng. 1 (2010) 79–100. https://doi.org/10.1146/annurev-chembioeng-073009-100935.
- [4] A. Cavallo, When the Oil Supply Runs Out, Science (80-.). 317 (2007) 980.
- [5] D.A. Simonetti, J.A. Dumesic, Catalytic strategies for changing the energy content and achieving C-C coupling in biomass-derived oxygenated hydrocarbons, ChemSusChem. 1 (2008) 725–733. https://doi.org/10.1002/cssc.200800105.
- [6] G. Mao, H. Zou, G. Chen, H. Du, J. Zuo, Past, current and future of biomass energy research: A bibliometric analysis, Renew. Sustain. Energy Rev. 52 (2015) 1823–1833. https://doi.org/10.1016/j.rser.2015.07.141.
- [7] M. Patel, A. Kumar, Production of renewable diesel through the hydroprocessing of lignocellulosic biomass-derived bio-oil: A review, Renew. Sustain. Energy Rev. 58 (2016) 1293–1307. https://doi.org/10.1016/j.rser.2015.12.146.
- [8] D.M. Alonso, S.G. Wettstein, J.A. Dumesic, Bimetallic catalysts for upgrading of biomass to fuels and chemicals, Chem. Soc. Rev. 41 (2012) 8075–8098. https://doi.org/10.1039/c2cs35188a.
- [9] A. Demirbaş, Biomass resource facilities and biomass conversion processing for fuels and chemicals, Energy Convers. Manag. 42 (2001) 1357–1378. https://doi.org/10.1016/S0196-8904(00)00137-0.
- [10] F.H. Isikgor, C.R. Becer, Lignocellulosic biomass: a sustainable platform for the production of bio-based chemicals and polymers, Polym. Chem. 6 (2015) 4497–4559. https://doi.org/10.1039/c5py00263j.
- [11] G. Fiorentino, M. Ripa, S. Ulgiati, Chemicals from biomass: technological versus environmental feasibility. A review, Biofuels, Bioprod. Biorefining. 11 (2017) 195–214. https://doi.org/https://doi.org/10.1002/bbb.1729.
- [12] J.C. Serrano-Ruiz, R. Luque, A. Sepúlveda-Escribano, Transformations of biomass-derived platform molecules: From high added-value chemicals to fuels via aqueous-phase processing, Chem. Soc. Rev. 40 (2011) 5266–5281. https://doi.org/10.1039/c1cs15131b.
- [13] National Science Foundation, Breaking the chemical and engineering barriers to lignocellulosic biofuels, Washington D.C., U.S.A., 2008.
- [14] S. Nanda, J. Mohammad, S.N. Reddy, J.A. Kozinski, A.K. Dalai, Pathways of lignocellulosic biomass conversion to renewable fuels, Biomass Convers. Biorefinery. 4 (2014) 157–191. https://doi.org/10.1007/s13399-013-0097-z.

- [15] A. Barakat, H. de Vries, X. Rouau, Dry fractionation process as an important step in current and future lignocellulose biorefineries: A review, Bioresour. Technol. 134 (2013) 362–373. https://doi.org/10.1016/j.biortech.2013.01.169.
- [16] V. Dhyani, T. Bhaskar, A comprehensive review on the pyrolysis of lignocellulosic biomass, Renew. Energy. 129 (2018) 695–716. https://doi.org/10.1016/j.renene.2017.04.035.
- [17] G.W. Huber, S. Iborra, A. Corma, Synthesis of transportation fuels from biomass: Chemistry, catalysts, and engineering, Chem. Rev. 106 (2006) 4044–4098. https://doi.org/10.1021/cr068360d.
- [18] A.J. Ragauskas, C.K. Williams, B.H. Davison, G. Britovsek, J. Cairney, C.A. Eckert, W.J. Frederick, J.P. Hallett, D.J. Leak, C.L. Liotta, J.R. Mielenz, R. Murphy, R. Templer, T. Tschaplinski, The path forward for biofuels and biomaterials, Science (80-.). 311 (2006) 484–489. https://doi.org/10.1126/science.1114736.
- [19] T. Nussbaumer, Combustion and Co-combustion of Biomass: Fundamentals, Technologies, and Primary Measures for Emission Reduction, Energy and Fuels. 17 (2003) 1510–1521. https://doi.org/10.1021/ef030031q.
- [20] S.L. Narnaware, N.L. Panwar, Biomass gasification for climate change mitigation and policy framework in India: A review, Bioresour. Technol. Reports. 17 (2022) 100892. https://doi.org/10.1016/j.biteb.2021.100892.
- [21] G. Wang, Y. Dai, H. Yang, Q. Xiong, K. Wang, J. Zhou, Y. Li, S. Wang, A review of recent advances in biomass pyrolysis, Energy and Fuels. 34 (2020) 15557–15578. https://doi.org/10.1021/acs.energyfuels.0c03107.
- [22] R.K. Mishra, V. kumar, P. Kumar, K. Mohanty, Hydrothermal liquefaction of biomass for bio-crude production: A review on feedstocks, chemical compositions, operating parameters, reaction kinetics, techno-economic study, and life cycle assessment, Fuel. 316 (2022) 123377. https://doi.org/10.1016/j.fuel.2022.123377.
- [23] A.M. Elgarahy, A. Hammad, D.M. El-Sherif, M. Abouzid, M.S. Gaballah, K.Z. Elwakeel, Thermochemical conversion strategies of biomass to biofuels, technoeconomic and bibliometric analysis: A conceptual review, J. Environ. Chem. Eng. 9 (2021) 106503. https://doi.org/10.1016/j.jece.2021.106503.
- [24] X. Li, P. Jia, T. Wang, Furfural: A Promising Platform Compound for Sustainable Production of C4 and C5 Chemicals, ACS Catal. 6 (2016) 7621–7640. https://doi.org/10.1021/acscatal.6b01838.
- [25] R. Kumar, V. Strezov, Thermochemical production of bio-oil: A review of downstream processing technologies for bio-oil upgrading, production of hydrogen and high value-added products, Renew. Sustain. Energy Rev. 135 (2021) 110152. https://doi.org/10.1016/j.rser.2020.110152.
- [26] D. Esposito, M. Antonietti, Redefining biorefinery: the search for unconventional building blocks for materials, Chem. Soc. Rev. 44 (2015) 5821–5835. https://doi.org/10.1039/c4cs00368c.
- [27] P. Gallezot, Direct routes from biomass to end-products, Catal. Today. 167

- (2011) 31–36. https://doi.org/10.1016/j.cattod.2010.11.054.
- [28] P. Gallezot, Process options for converting renewable feedstocks to bioproducts, Green Chem. 9 (2007) 295–30. https://doi.org/10.1039/b615413a.
- [29] J.J. Bozell, Feedstocks for the future Biorefinery production of chemicals from renewable carbon, Clean Soil, Air, Water. 36 (2008) 641–647. https://doi.org/10.1002/clen.200800100.
- [30] J.J. Bozell, G.R. Petersen, Technology development for the production of biobased products from biorefinery carbohydrates—the US Department of Energy's "top 10" revisited, Green Chem. 12 (2010) 539–55. https://doi.org/10.1039/b922014c.
- [31] A. Jaswal, P.P. Singh, T. Mondal, Furfural-a versatile, biomass-derived platform chemical for the production of renewable chemicals, Green Chem. 24 (2022) 510–551. https://doi.org/10.1039/d1gc03278j.
- [32] T. Werpy, G. Petersen, Top Value Added Chemicals from Biomass Volume I, Us Nrel. (2004) Medium: ED; Size: 76 pp. pages. https://doi.org/10.2172/15008859.
- [33] M. Crnomarković, Y. Panchaksharam, J. Spekreijse, C. Vom Berg, Á. Puente, R. Chinthapalli, Case studies on potentially attractive opportunities for bio-based chemicals in Europe Consortium, 2019.
- [34] A.S. Mamman, J.-M. Lee, Y.-C. Kim, I.T. Hwang, N.-J. Park, Y.K. Hwang, J.-S. Chang, J.-S. Hwang, Furfural: Hemicellulose/xylosederived biochemical, Biofuels, Bioprod. Biorefining. 2 (2008) 438–454. https://doi.org/https://doi.org/10.1002/bbb.95.
- [35] S. Dutta, S. De, B. Saha, M.I. Alam, Advances in conversion of hemicellulosic biomass to furfural and upgrading to biofuels, Catal. Sci. Technol. 2 (2012) 2025–2036. https://doi.org/10.1039/C2CY20235B.
- [36] K.J. Zeitsch, Furfural processes, in: Chem. Technol. Furfural Its Many by-Products, Elsevier, 2000: pp. 36–74. https://doi.org/10.1016/S0167-7675(00)80010-X.
- [37] B. Kamm, M. Kamm, P.R. Gruber, S. Kromus, Biorefinery Systems An Overview, in: Biorefineries-Industrial Process. Prod., John Wiley & Sons, Ltd, 2005: pp. 1–40. https://doi.org/https://doi.org/10.1002/9783527619849.ch1.
- [38] R.H. Kottke, Furan derivatives, in: Kirk–Othmer Encycl. Chem. Technol., John Wiley & Sons, Inc., 2000: pp. 259–286. https://doi.org/10.1016/0040-4020(76)85021-1.
- [39] H.E. Hoydonckx, W.M. Van Rhijn, W. Van Rhijn, D.E. De Vos, P.A. Jacobs, Furfural and Derivatives, in: Ullmann's Encycl. Ind. Chem., Wiley-VCH Verlag GmbH & Co. KGaA, Weinheim, 2007: pp. 285–313. https://doi.org/https://doi.org/10.1002/14356007.a12_119.pub2.
- [40] O. Rosales-Calderon, V. Arantes, A review on commercial-scale high-value products that can be produced alongside cellulosic ethanol, Biotechnol. Biofuels. 12 (2019) 240. https://doi.org/10.1186/s13068-019-1529-1.

- [41] R. Mariscal, P. Maireles-Torres, M. Ojeda, I. Sádaba, M. López Granados, Furfural: a renewable and versatile platform molecule for the synthesis of chemicals and fuels, Energy Environ. Sci. 9 (2016) 1144–1189. https://doi.org/10.1039/C5EE02666K.
- [42] S. Czernik, A. V. Bridgwater, Overview of applications of biomass fast pyrolysis oil, Energy and Fuels. 18 (2004) 590–598. https://doi.org/10.1021/ef034067u.
- [43] R. Karinen, K. Vilonen, M. Niemelä, Biorefining: Heterogeneously Catalyzed Reactions of Carbohydrates for the Production of Furfural and Hydroxymethylfurfural, ChemSusChem. 4 (2011) 1002–1016. https://doi.org/https://doi.org/10.1002/cssc.201000375.
- [44] Y. Luo, Z. Li, X. Li, X. Liu, J. Fan, J.H. Clark, C. Hu, The production of furfural directly from hemicellulose in lignocellulosic biomass: A review, Catal. Today. 319 (2019) 14–24. https://doi.org/10.1016/J.CATTOD.2018.06.042.
- [45] J. Hidalgo-Carrillo, A. Marinas, F.J. Urbano, Chemistry of Furfural and Furanic Derivatives, in: Furfural, 2018: pp. 1–30. https://doi.org/10.1142/9781786344878_0001.
- [46] S. Srivastava, G.C. Jadeja, J. Parikh, Synergism studies on alumina-supported copper-nickel catalysts towards furfural and 5-hydroxymethylfurfural hydrogenation, J. Mol. Catal. A Chem. 426 (2017) 244–256. https://doi.org/10.1016/j.molcata.2016.11.023.
- [47] S. Srivastava, G.C. Jadeja, J. Parikh, A versatile bi-metallic copper-cobalt catalyst for liquid phase hydrogenation of furfural to 2-methylfuran, RSC Adv. 6 (2016) 1649–1658. https://doi.org/10.1039/c5ra15048e.
- [48] B. Li, L. Li, H. Sun, C. Zhao, Selective Deoxygenation of Aqueous Furfural to 2-Methylfuran over Cu0/Cu2O·SiO2 Sites via a Copper Phyllosilicate Precursor without Extraneous Gas, ACS Sustain. Chem. Eng. 6 (2018) 12096–12103. https://doi.org/10.1021/acssuschemeng.8b02425.
- [49] R. Gérardy, D. P. Debecker, J. Estager, P. Luis, J.-C. M. Monbaliu, Continuous Flow Upgrading of Selected C2–C6 Platform Chemicals Derived from Biomass, Chem. Rev. 120 (2020) 7219–7347. https://doi.org/10.1021/acs.chemrev.9b00846.

The transformation of FFR into high-value products like 2-MeF and FAL is both a significant challenge and an opportunity within the biomass conversion sector. These compounds are not only valuable in their own right but also serve as key intermediates in the synthesis of many valuable chemicals. Their successful conversion has the potential to enhance the sustainability and efficiency of chemical processes, driving advancements in the development of more sustainable industrial practices.

Research into the hydrogenation of FFR to 2-MeF and FAL has been extensively conducted across both liquid- and vapor-phase systems, utilizing molecular hydrogen and transfer hydrogenation techniques. Liquid-phase processes have provided valuable insights into catalyst design, reaction mechanisms, and process optimization. These studies have significantly advanced the understanding of hydrogenation processes and laid the groundwork for further developments in the field. However, liquid-phase methods also present technical challenges that can limit their broader application. The need for high hydrogen pressures in liquid-phase reactions introduces safety concerns and requires specialized, often expensive, equipment. Moreover, these high-pressure conditions can sometimes lead to the formation of unwanted byproducts, complicating purification. The choice of solvent in liquid-phase hydrogenation can influence reaction pathways, occasionally leading to less favorable outcomes and adding complexity to product separation. Additionally, scalability remains an issue, as maintaining consistent reaction conditions on an industrial scale can be more challenging in liquid-phase systems. On the other hand, vapor-phase hydrogenation offers several advantages, such as greater control over reaction conditions, lower pressure requirements, and easier scalability. Therefore, this literature review will focus specifically on vapor-phase processes, outlining the work that has been done in this area related to the transformation of FFR into 2-MeF and FAL. This focus will allow for a detailed exploration of the advancements and methodologies that have been developed within the context of vapor-phase hydrogenation, reflecting the growing interest and potential of these approaches in biomass conversion to value-added products.

2.1 Conventional (Molecular H₂-based) FFR HDO to 2-MeF

The vapor-phase HDO of FFR to 2-MeF has a rich history, with early studies dating back to the 1920s. Eloi Ricard and Henri Martin Guinot were among the pioneers [1], demonstrating FFR hydrogenation to FAL and 2-MeF using Cu catalysts on supports like asbestos, kaolin and silica. Notably, the catalyst, reduced at temperatures between 140 to 200 °C, initiated reactions as low as 80 °C, with about 10-20% of FAL converting to 2-MeF at 140 °C. Remarkably, the catalyst was able to maintain activity for days without noticeable deactivation, depending on the preparation and reduction methods, as well as the FFR feed rate. Further developments in the mid-20th century saw Johns and Burnette experiment with charcoal-supported copper and copper calcium chromite catalysts [2–4]. Their work identified that operating within a temperature range of 200-230 °C and using an excess of hydrogen were critical for achieving high 2-MeF yields, often exceeding 90%. However, temperatures exceeding 280 °C caused a decline in conversion, with complete loss of activity at 320 °C. Additionally, they found that scaling up the process by 5 to 10 times led to unexpected challenges, reducing both catalyst stability and 2-MeF yield. Wilson later explored FFR hydrodeoxygenation using Co, Cu, Fe, and Ni catalysts [5], identifying copper chromite as the most selective, achieving up to 80% 2-MeF yield at 65% FFR conversion. Nibased catalysts, though offering higher conversions, primarily produced furan. Co and Fe catalysts showed poor FFR conversion; Co favoured furan, while Fe exclusively produced 2-MeF. Further studies found that a Fe-Cu catalyst was more effective for 2-MeF production than Ni-Cu [6], though copper chromite still outperformed both. Despite their initial success, copper chromite catalysts have notable drawbacks, including deactivation over time and the environmental concerns posed by chromium's toxicity. As a result, recent efforts have focused on developing more sustainable alternatives, with Cu catalysts supported on SiO₂ emerging as promising replacements. However, conventional Cu/SiO₂ catalysts - prepared via impregnation method - have faced challenges related to moderate catalytic activity and stability, often due to agglomeration and sintering [7].

To address these issues, researchers have explored various synthesis techniques to enhance the activity and stability of Cu/SiO₂ catalysts. For example, Liu et al. achieved a consistent 2-MeF yield greater than 92% at 200 °C over 150 hours using a Cu/SiO₂ catalyst prepared by the precipitation method [8]. Dong et al. reported complete FFR

conversion with 89.5% 2-MeF selectivity at 220 °C [9], maintained over 210 hours with a similarly prepared catalyst. Notably, the ammonia evaporation method has yielded even more robust catalysts. Dong et al. in another one of their studies achieved a 95.2% 2-MeF yield at 200 °C over 210 hours using this approach [10]. Zhang and colleagues further optimized this method by incorporating hydrothermal crystallization into the synthesis procedure [7], resulting in a catalyst that achieved complete FFR conversion and 86.6% 2-MeF selectivity over 250 hours. Meanwhile, Zong et al. developed a MOF-derived Cu/SiO₂ catalyst that outperformed those synthesized by ammonia evaporation and traditional impregnation methods [11], achieving complete FFR conversion and a 96% 2-MeF yield over 50 hours. Across these studies, the superior activity and stability of the catalysts were attributed to the strong metal-support interactions, which promoted high Cu dispersion and the synergistic presence of both Cu⁰ and Cu⁺ species, contributing to the overall catalytic performance.

Beyond Cu, group VIII metals like Pd [12] and Ni [12,13] supported on silica have also been investigated, though with less success. Pd catalysts tend to favour decarbonylation [12], producing furan as the main product, while Ni catalysts exhibit a more complex selectivity pattern, favouring both FAL and furan at low temperatures and furan and C₄ ring-opening products at higher temperatures [12,13].

Transition metal phosphides (TMPs) and transition metal carbides (TMCs) have garnered attention in the vapor-phase HDO of FFR to 2-MeF, following their promising performance in liquid-phase processes. Lan et al. demonstrated that silica-supported TMPs, particularly Ni₂P and MoP, could achieve high FFR conversion (~90%) and impressive selectivity for 2-MeF (>90%) [14]. A key factor was the P/Ni ratio, which played a crucial role in steering the product distribution. Higher phosphorus content not only enhanced Brønsted acidity but also modulated adsorption behavior on the Ni surface, thus favouring 2-MeF formation. Similarly, TMCs like Mo₂C have shown significant potential. Lee and colleagues highlighted Mo₂C's high selectivity for C=O and C-O bond cleavage in FFR, effectively producing 2-MeF with minimal by-products at a relatively low temperature of 150 °C [15]. However, the challenge of rapid deactivation looms large, as carbonaceous species formation and oxidation of the carbidic phase undermine the catalyst's longevity. Attempts to stabilize the catalyst, such as incorporating Co into Mo₂C, have yielded some improvement, yet the issue of deactivation persists [16], echoing the difficulties faced in similar liquid-phase studies.

Table 2.1 presents the catalysts developed and the reaction conditions employed for the production of 2-MeF from FFR by vapor-phase hydrodeoxygenation using molecular H₂ in the recent years.

Table 2.1 Literature representing studies in vapor-phase hydrodeoxygenation of FFR to 2-MeF using molecular H₂

Catalyst	Space	(H ₂ /	Temp.	TOSf	FFR	2-MeF	Ref.
	Velocity	FFR)e	(K)	(hr)	Conv	Yield/	
					(%)	selectivity	
						(mol%)	
Cu ₂ Cr ₂ O ₅	NAg	NAg	543	NAg	65	80 ^b	5
Cu/SiO ₂	2.3 ^d	10	473	150	> 90	>92 ^b	8
20% Cu/SiO ₂	0.5 ^d	17	493	210	100	89.5ª	9
20%Cu/SiO ₂	0.5 ^d	17	473	210	100	95.5 ^b	10
7%Cu/SiO ₂	1244.4°	15	513	50	100	98.5 ^b	11
5%Ni-	10 ^d	25	523	NA ^g	96.3	39.1ª	13
2%Fe/SiO2							
Ni ₂ P/SiO ₂	3 ^d	74	473	2	90	>90ª	14
MoP/SiO ₂	3 ^d	74	473	2	91	>90ª	14

^a selectivity reported for 2-MeF. ^b yield reported for 2-MeF. ^c LHSV provided. ^d WHSV provided. ^e H₂/FFR molar ratio. ^f Time-on-stream at which catalytic properties were determined. ^g NA - not available

2.2 Conventional (Molecular H₂-based) FFR Hydrogenation to FAL

Like 2-MeF production, FAL production via vapor-phase FFR hydrogenation also dates back to the 1920s, when Eloi Ricard and Henri Martin Guinot first investigated this route using Cu catalysts on supports like asbestos, kaolin and silica [1]. The catalyst showed activity at temperatures as low as 80 °C, with FAL being the major product. The authors noted that the catalyst was able to maintain its activity for days without noticeable deactivation. Du Pont started using copper chromite catalyst in the year 1931 [17]. After a certain time on stream, the catalyst activities were decreased significantly; to circumvent this loss in activity, the catalyst bed temperature had to be raised from 140 °C to around 180 °C. However, the rise in temperature led to the promotion of hydrogenolysis reaction which yielded 2-MeF in significant amounts. Brown and

Hixon investigated a calcium-promoted Cu-Cr catalyst for FFR hydrogenation, exploring temperatures between 100 and 140°C [52]. They observed that using charcoal as a support material unexpectedly led to higher 2-MeF production, likely due to higher temperatures at catalyst surface [52]. They found glass beads to offer several advantages over charcoal as a catalyst support [18]. The researchers identified the temperature range of 130 to 135°C as optimal for FAL production, achieving yields of up to 95%. Quaker Oats circumvented this issue of 2-MeF at higher temperatures over Cu-Cr catalysts by using a Na₂O·xSiO₂ as a support material for the chromite catalysts, which provided 99% yields for FAL at temperatures in the range of 132 to 177 °C [19]. In recent years, concerns over chromium's toxic environmental impact has spurred a shift in focus toward more sustainable alternatives - generally Cu based due to their specificity towards FAL.

One of the early studies in this regard was conducted by Nagaraja et. al., who explored MgO supported Cu catalysts synthesized via co-precipitation, impregnation and solidsolid methods [20]. The sample prepared by co-precipitation method exhibited the best catalytic performance among all the samples, providing FFR conversions and FAL yields of approximately 98% at 180 °C and a low H₂ to FFR ratio of just 2.5 [20]. The catalyst did not exhibit any signs of deactivation during the 5 h period of activity assessment, likely due to the high surface area and larger number of surface active Cu⁰ sites. In another study where they investigated MgO supported Cu catalysts with different Cu loadings [21], the authors achieved optimum FFR conversion and FAL selectivity (98%) at a Cu loading of 16 wt.% under the same reaction conditions. In a similar study, Shirvani and team explored MgO supported Cu catalysts promoted by Ca, Co and Cr [22]. They noted that while the conversion over the bimetallic catalysts followed the trend – Cu-Co > Cu-Cr > Cu-Ca, the FAL selectivity followed a reverse trend. Overall, they found the Co-promoted Cu/MgO to be the best in terms of FFR conversion (75.1%) and FAL selectivity (96.9%) at 180 °C and a much higher H₂/FFR ratio of 10 [22].

Another widely explored support material for Cu catalysts, besides MgO, is SiO₂. While these catalysts are typically prepared using simple methods like wet impregnation, this approach often results in poor activity and stability. To address this, researchers have been exploring alternative synthesis methods. Du et al. compared the performance of various Cu/SiO₂ catalysts for FFR hydrogenation to FAL, focusing on synthesis

techniques like impregnation, ion exchange, ammonia evaporation, and deposition precipitation [23]. At a low space velocity (WHSV = $0.4 \, h^{-1}$), most catalysts performed similarly, except for the impregnation-derived catalyst. When the space velocity increased to 1.8 h⁻¹, the differences became pronounced: the impregnation catalyst's activity plummeted to just 3.1% conversion, whereas the ammonia evaporation-derived catalyst maintained an 85.2% conversion [23]. This catalyst also demonstrated exceptional stability, lasting over 400 hours at 130°C. In another study, the same group investigated Cu supported on ethanolamine-modified SiO₂, prepared by impregnation method, for FFR hydrogenation [24]. They found that the simple Cu on untreated SiO₂ prepared via impregnation had the poorest performance, with FFR conversion dropping from 100% to 84% in 24 hours and by another 44% in just 12 hours at 130°C and a space velocity of 0.4 h⁻¹ [24]. In contrast, ethanolamine-modified SiO₂ supported Cu catalysts showed significantly enhanced stability under similar reaction conditions. For example, with a 1:1 mass ratio of ethanolamine to SiO₂ in the synthesis, the conversion dropped from 99% to 90% over 47 h. Increasing the ratio to 2:1 and 3:1 extended this drop to 135 h and 230 h, respectively, with further increases offering minimal improvement [24]. Notably, this stability surpassed that of their previously studied ammonia evaporation-derived Cu/SiO2 catalyst, which took 110 hours to see a similar drop. Wang et al. reported similar enhancements in activity with their Cu/SiO₂ catalysts [25], which were prepared by reducing lamellar double hydroxy salts synthesized via a combined ammonia evaporation and hydrothermal method. The catalysts with a 25% Cu loading achieved a remarkable FAL selectivity of 97.2% and a 97% FFR conversion at 160°C, H₂/FFR = 15, and a space velocity of 0.45 h⁻¹ [25]. Notably, this catalyst maintained its high performance over 120 hours, nearly seven times longer than the stability of their ammonia evaporation-derived catalyst. The exceptional activity and stability in all of these cases was attributed to the significant presence of Cu⁺ and the synergistic effect between Cu⁰ and Cu⁺ sites.

Besides MgO and SiO₂, other metal oxides such as CeO₂ [26], ZnO [27], mixed oxide supports such as ZnO-Al₂O₃ [28,29] and Fe-Al [30] have also been explored as support materials for Cu catalysts. Jiménez-Gómez and colleagues investigated Cu catalysts supported on CeO₂ and ZnO, exploring various Cu/Ce and Cu/Zn ratios. In the Cu/CeO₂ system [26], all catalysts exhibited noticeable deactivation during a 5-hour test at 190°C, with lower Cu/Ce ratios suffering the most severe deactivation. The best-

performing Cu/CeO₂ catalyst, with a Cu/Ce ratio of 6, achieved 83% FFR conversion and over 80% FAL yield after 5 hours at 190 °C. In the Cu/ZnO system [27], a reverse trend was observed under similar conditions. Lower Cu/Zn ratios resulted in higher conversion and greater stability, attributed to smaller Cu⁰ particle sizes and larger metal surface areas. This was in contrast to the Cu/CeO₂ findings, where metal particles with larger sizes and smaller surface areas led to better performance. The optimal Cu/ZnO catalyst, with a Cu/Zn ratio of 0.2, achieved 93% conversion and 82% FAL selectivity after 5 hours and demonstrated notable stability, maintaining over 60% conversion and approximately 60% FAL yield over a 24-hour period. The same team extended their research to FFR hydrogenation over Cu catalysts supported on ZnO-Al₂O₃, with varying Cu/Zn ratios and a fixed (Cu + Zn)/Al ratio of 3, derived from hydrotalcitetype CuZnAl precursors [28]. While all catalysts were selective towards FAL, they also displayed noticeable deactivation during the 5-hour test period, consistent with their earlier findings on CeO₂ and ZnO supports. The optimal catalyst had a Cu/Zn ratio of 1, achieving a 71% FAL yield at 210°C. In parallel, Venkatesha et al. developed Cu/ZnO-Al₂O₃ catalysts through solid-state grinding of metal nitrate precursors with organic reducing agents like citric acid, formic acid, and hydrazine [29]. The citric acidprepared catalyst stood out, offering superior Cu dispersion and surface area, leading to the best performance: 74% conversion and nearly complete FAL selectivity sustained over 30 hours. Table 2.2 presents the catalysts developed and the reaction conditions employed for the production of FAL from FFR by vapor-phase hydrogenation using molecular H₂ in the recent years.

Table 2.2. Literature representing studies in vapor-phase hydrogenation of FFR to 2-FAL using molecular H₂

Catalyst	Space	(H ₂ /	Temp.	TOSf	FFR	FAL	Ref.
	Velocity	FFR)e	(K)	(hr)	Conv	Yield/	
					(%)	selectivity	
						(mol%)	
Cu/MgO	0.05 ^c	2.5	453	NA ^g	98	98ª	20
16%Cu/MgO	0.05°	2.5	453	NAg	98	98ª	21
Cu-Co/MgO	1.7 ^d	10	453	4	75.1	96.9 ^a	22
20%Cu/SiO ₂	0.4 ^d	12	403	450	>90	~95ª	23
25%Cu/SiO ₂	0.45 ^d	15	433	120	97	97.2ª	25
Cu/CeO ₂	1.47 ^d	11.5	463	5	83	67 ^b	26
Cu/ZnO	1.47 ^d	11.5	463	5	93	82ª	27

^a selectivity reported for FAL. ^b yield reported for FAL. ^c GHSV provided. ^d WHSV provided. ^e H₂/FFR molar ratio. ^f Time-on-stream at which catalytic properties were determined. ^g NA - not available

2.3 Catalytic Transfer Hydrogenation of FFR to 2-MeF

Traditionally, hydrogenation and HDO of biomass-derived oxygenates such as FFR relies on molecular H₂. While H₂ is widely available and easily activated on metallic catalysts, conventional HDO faces challenges such as high H₂-to-substrate ratios and elevated temperatures in vapor-phase processes, or high H₂ pressures in liquid-phase processes. These conditions can lead to oversaturation of the aromatic ring and formation of undesirable by-products like THFA, 2-MeTHF, and ring-opening products such as 1,5-PDO, along with the need for expensive, high-pressure equipment. Catalytic transfer hydrogenation (CTH) offers a promising alternative by using organic molecules like alcohols or formic acid as hydrogen donors, reducing safety concerns and equipment costs associated with high-pressure hydrogen [31–33]. Additionally, the lower hydrogenating capacity of most organic hydrogen donors, compared to molecular H₂, allows for greater control in selective hydrogenation and/or hydrogenolysis, particularly when targeting unsaturated molecules.

The current literature on FFR conversion via transfer hydrogenation to 2-MeF and/or FAL overwhelmingly centres on liquid-phase processes, with just two studies exploring

vapor-phase HDO of FFR to 2-MeF using transfer hydrogenation. This highlights a significant gap in the research, underscoring the need for further exploration and development in vapor-phase approaches. Grazia's study delved into the vapor-phase CTH of FFR to 2-MeF using MgO, Fe₂O₃, and a mixed MgO-Fe₂O₃ catalyst [34,35]. MgO demonstrated strong activity for hydrogenating FFR at lower temperatures, mainly producing FAL at lower temperatures. However, its conversion efficiency was limited, peaking at 35% up to 350°C. As temperatures increased to 400°C and 500°C, the conversion improved to 40% and 59%, respectively. Despite these gains, MgO's capacity to further convert FAL to 2-MeF remained modest, with only a 35% selectivity at 500°C. Higher temperatures also led to more by-products like cyclopentanones and a poorer carbon balance due to heavy compound deposits on the catalyst surface. The game-changer came with the addition of Fe to the MgO catalyst. This modification nearly tripled the 2-MeF yield to 92% and elevated FFR conversion to 93% at 380°C when Fe and Mg were present in a 1:2 ratio. The dramatic boost in performance is attributed to the creation of Lewis acidic sites from Fe₂O₃ within the basic MgO matrix, which enhanced acid-base interactions and facilitated more efficient 2-MeF production. Interestingly, they noted that increasing the Fe/Mg ratio to 10 slightly reduced the 2-MeF yield to 88% [35]. However, these promising results were observed over a very short time-on-stream (TOS) period of just 1 hour. When catalyst stability was tested over extended periods, the Fe-Mg-O catalyst faced rapid deactivation, with conversion dropping to 42% after just 3 hours on stream. The study did not provide data beyond this 3-hour mark, highlighting the need for further investigation into the long-term stability of these catalysts. Table 2.3 presents the catalysts developed and the reaction conditions employed for the production of 2-MeF from FFR by vapor-phase transfer hydrogenation in the recent years.

Table 2.3 Literature representing studies in vapor-phase transfer hydrogenation of FFR to 2-MeF

Catalyst	Space	(Donor/	Temp.	TOSf	FFR	FAL	Ref.
	Velocity	FFR)e	(K)	(hr)	Conv	Yield/	
					(%)	selectivity	
						(mol%)	
Mg/Fe/O	NA ^c	10	653	1	93	79ª	34
MgO	NA ^c	10	653	1	75	5 ^a	35
Al/Mg/O	NA ^c	10	653	1	63	22 ^a	35

^a selectivity reported for 2-MeF. ^b yield reported for 2-MeF. ^c GHSV provided. ^d WHSV provided. ^e Donor/FFR molar ratio. ^f Time-on-stream at which catalytic properties were determined. ^g NA - not available

2.4 Highlights/Observations and Research Gaps

- 1. Historically, the transformation of FFR into valuable products such as FAL and 2-MeF has been carried out using molecular H_2 . This preference is due to the abundant availability of H_2 and its efficient activation on the widely used metallic catalysts, which has made it a go-to choice for these transformations.
- 2. A significant body of research on FFR transformation has centred on liquid-phase processes, driven by the fact that FFR is typically obtained from biomass in a dilute aqueous mixture. This aligns well with liquid-phase processing, simplifying the transformation by avoiding the need for vaporization. Liquid-phase hydrogenation has provided valuable insights into catalyst design, reaction mechanisms, and process optimization, significantly advancing the field. However, this approach has notable challenges. High H₂ pressures are required for ensuring complete reactant conversions, which introduce safety risks and require costly, specialized equipment. These pressures can also promote side reactions, generating unwanted byproducts that complicate purification. The choice of solvent can further influence reaction pathways and separation processes, often leading to less desirable outcomes. Additionally, issues such as metal leaching, low productivity, long downtimes between cycles and difficulties in catalyst recovery and recycling further diminish the practicality and cost-effectiveness of scaling up liquid-phase hydrogenation for FFR transformation

- 3. Vapor-phase FFR transformation offers a host of advantages that make it a compelling alternative for use at industrial scales. This method streamlines the process by removing the need for liquid solvents, thus simplifying operation. By using reactants in vapor phase, vapor-phase processes enable superior interaction between H₂ and FFR, enhancing mixing and mass transfer, which translates into higher conversion rates and faster reaction kinetics. The ability to operate continuously and at low H₂ pressures in vapor-phase systems reduces downtime, lowers operational costs, and boosts productivity. Additionally, the straightforward product separation, due to the gaseous state of primary products, simplifies downstream processing.
- 4. Group VIII metals like Pt, Pd, and Ni are often the go-to choices for any hydrogenation reaction due to their strong ability to activate H₂. However, their exceptional hydrogenation capabilities come at the cost of selectivity when it comes to FFR conversion to value-added products. When FFR interacts with these metals, both its furan ring and carbonyl group bind to the surface, which triggers a range of reactions ranging from hydrogenation, hydrogenolysis, decarbonylation ring saturation and opening, making it difficult to target a specific product like FAL or 2-MeF. Thus, while these metals are highly active catalysts, their high hydrogenation activity makes controlling the selectivity a challenge.
- 5. Cu-based catalysts are highly favoured for converting FFR into FAL and 2-MeF, thanks to their selective interaction with the carbonyl group that allows them to selective activate it over the C=C bonds in furan ring and steer the process towards the desired products. Historically, copper chromite has been the catalyst of choice for FFR conversion to FAL and 2-MeF since the 1920s, underscoring its long-standing effectiveness.
- 6. Despite their historical success, copper chromite catalysts are marred by significant drawbacks, primarily the environmental issues associated with chromium toxicity. This concern has driven a push towards more sustainable alternatives. Among these, Cu catalysts supported on SiO₂ have emerged as promising candidates for both FFR hydrogenation to FAL as well as its HDO to 2-MeF. However, traditional Cu/SiO₂ catalysts, typically prepared through impregnation methods, encounter challenges such as moderate catalytic activity and stability. These issues often arise from problems like agglomeration and sintering, which hinder their performance and longevity.

- 7. Given the potential of Cu/SiO₂ catalysts in FFR hydrogenation and HDO, extensive efforts have been made to enhance their activity through various synthesis methods, including ammonia evaporation, co-precipitation, deposition-precipitation, ion exchange, hydrothermal synthesis, and sol-gel techniques. Among these, the ammonia evaporation and combined ammonia evaporation-hydrothermal synthesis methods have shown exceptional promise, consistently achieving complete FFR conversion and over 90% yield or selectivity toward 2-MeF and FAL, with these values sometimes sustained over reaction periods exceeding 200 hours.
- 8. While advanced synthesis methods have significantly enhanced the performance and stability of Cu/SiO₂ catalysts in FFR hydrogenation and HDO, they also present several challenges. These techniques are often complex, involving multiple precisely controlled steps, and frequently utilize expensive silica sources like colloidal or fumed silica, which can substantially increase production costs. Additionally, reproducibility issues have been observed, with catalysts prepared using identical methods yielding varying results across different research groups, particularly concerning long-term stability. For instance, Du et al. [23] employed the ammonia evaporation method with fumed silica to synthesize Cu/SiO₂ catalysts, achieving impressive results with over 90% FFR conversion and approximately 98% selectivity toward FAL sustained across 400 hours. In contrast, Wang et al. [25], using the same synthesis approach but with silica sol as the silica source, reported rapid catalyst deactivation within 60 hours. Similar discrepancies are evident in studies over Cu/SiO₂ catalysts focused on FFR HDO to 2-MeF as well. Fu et al.'s catalyst [36], prepared via ammonia evaporation, delivered around 80% selectivity to 2-MeF with complete FFR conversion over 25 hours. Conversely, Dong et al., utilizing a different silica source in the same synthesis method [10], achieved a remarkable 95.5% yield to 2-MeF maintained consistently over 215 hours without notable deactivation. Even catalysts derived from the coprecipitation method exhibited variability; Dong et al.'s version provided a steady 89.5% yield to 2-MeF over 210 hours [9], whereas Fu et al.'s counterpart showed lower conversion rates and much higher and fluctuating towards FAL over a shorter assessment period. While differences in reaction conditions might explain some variability, the observed inconsistencies in catalytic performance highlight a broader challenge. These disparities underscore the need to develop more robust and costeffective synthesis methods that can reliably replicate results across diverse conditions.

Achieving this consistency is crucial for advancing the development of catalysts that are both effective and commercially viable.

- 9. While Cu/SiO₂ catalysts have proven highly effective for FFR hydrogenation and HDO to FAL and 2-MeF respectively, they are not the only viable options available. The moderate activity of Cu catalysts towards C-O bond hydrogenolysis highlights the need for alternative strategies to enhance this crucial reaction. One promising direction is the use of different metal oxide supports, such as Al₂O₃, CeO₂, MgO, TiO₂, and ZnO. These materials offer enhanced acidic and basic surface sites, improved metal dispersion, and greater oxygen mobility, addressing some of the key limitations of traditional Cu systems. Initial investigations in both liquid-phase and vapor-phase reactions have demonstrated that these metal oxides can significantly boost the performance of Cu-based catalysts and that they hold the potential to rival or even surpass the efficiency of SiO₂-supported systems. Despite this promise, these alternative supports remain relatively underexplored.
- 10. Beyond exploring alternative metal oxide supports, another effective strategy for improving the performance of Cu-based catalysts involves combining Cu with metals that offer superior hydrogenation or oxophilic properties. Integrating metals like Co, Ni, or Pd with Cu can improve hydrogenation and hydrogenolysis activity by boosting H₂ dissociation. Bimetallic catalysts such as Cu-Co, Cu-Ni, or Cu-Pd leverage this synergy, with Cu providing specificity towards C=O bond activation and the promoter metal enhancing H₂ activation. This combination results in improved FFR conversion and higher selectivity for 2-MeF. Alternatively, pairing Cu with oxophilic metals like Fe, Mo, or W can also enhance oxygen removal. These metals interact strongly with the C=O moiety of FFR, facilitating better oxygen removal while Cu provides the necessary H atoms. Initial bench-scale studies indicate these strategies hold great promise, but further research is needed to optimize these metallic combinations and fully realize their potential for industrial applications.
- 11. So far, the bench-scale FFR hydrogenation and HDO studies have heavily relied on molecular H_2 , which presents significant challenges. Batch processes require high H_2 pressures, often leading to unwanted side reactions, while vapor-phase methods use H_2 in large excess sometimes up to 80 times the FFR amount resulting in inefficient hydrogen use. To address these issues and reduce the carbon footprint associated with

traditional hydrogenation and HDO routes, researchers are investigating renewable organic molecules like formic acid, ethanol, and methanol as alternative hydrogen sources. Although studies in this area - particularly those on vapor-phase FFR HDO to 2-MeF using organic H donors – are scant, the initial results are promising. However, significant gaps remain in this research. Existing studies have not thoroughly examined the active phases of catalysts or their structural changes during transfer hydrogenation. There is also a need to investigate the impact of synthesis conditions on catalyst performance. Furthermore, the catalysts in these studies exhibited rapid deactivation within just one hour, highlighting the need for improved long-term stability.

2.5 Objectives

The objective of this thesis is to develop and optimize catalytic systems for the efficient conversion of FFR - a biomass-derived platform chemical - into high-value chemicals, specifically FAL and 2-MeF, in continuous vapor phase mode. This research emphasizes the initial identification and optimization of various catalytic systems, such as bimetallic catalysts, mixed metal oxides, and metal-incorporated mesoporous silica supports derived from renewable resources, to establish a robust foundation for understanding their performance in FFR conversion processes. This foundational work seeks to address or fill existing knowledge gaps, enhance the understanding of catalyst performance, and guide future research directions in FFR valorization.

By employing both molecular hydrogen (H₂) and alternative hydrogen sources, this thesis seeks to capture a comprehensive range of processes currently trending in FFR valorization. While molecular H₂ processes remain the dominant route for FFR transformation to FAL and 2-MeF, transfer hydrogenation represents an emerging route that offers an innovative and more sustainable, alternative approach. This dual focus not only aims to enhance the understanding of these processes but also provide valuable insights into optimizing catalyst performance, activity, selectivity and/or yield, and stability. Overall, this thesis seeks to advance the sustainable conversion of biomass to valuable products, offering practical insights for improved catalyst design and process optimization.

Detailed studies on catalyst deactivation mechanisms are not included in this thesis, as the primary emphasis at this stage was on the initial identification and optimization of the catalytic systems. The objective was to establish proof of concept and refine the catalytic systems to achieve optimal performance. Considering the novelty and complexity of the developed catalysts, significant effort was devoted to their comprehensive characterization to elucidate their structural and chemical properties. However, insights into potential deactivation mechanisms have been gathered from existing literature to inform future research efforts.

2.5.1 Main Objective:

To develop stable and highly selective catalysts for furfural valorization via hydrogenation to 2-methylfuran and furfuryl alcohol in vapor phase mode.

2.5.2 Specific Objectives:

- 1. Preparation and characterization of metal-based catalysts guided by an extensive review of the existing literature.
- 2. Evaluate the performance of these catalysts to identify an optimal catalyst for the process.
- 3. Analyze the influence of process variables to optimize the yield and selectivity of the target compounds.

2.6 Organization of the thesis

Chapter 1: This chapter sets the stage by exploring the pivotal role that chemicals and fuels play in technological and economic progress, underscoring their integral contribution to modern industries and daily life. It then addresses the dominance of fossil fuels and the urgent need for a transition towards more sustainable sources to mitigate environmental and economic impacts. In response, the chapter introduces biomass as a promising alternative, highlighting its potential for cleaner energy and chemicals. The discussion progresses with an in-depth examination of biomass composition and structure, which is essential for understanding its conversion into valuable products. Various biomass conversion strategies are outlined, detailing methods such as pyrolysis, gasification, and hydrolysis that transform raw biomass into useful chemicals and fuels. Shifting the focus, the chapter reimagines biomass valorization by emphasizing the production of chemicals over traditional biofuels, given the higher value and broader applications of platform chemicals. The concept of biorefineries is then explored, illustrating how they address the complexity of different

feedstocks and enhance conversion efficiency. Further, the chapter charts the importance of platform chemicals within the DOE 'Top 10' roadmap, which guides advancements in biobased chemical production. The discussion narrows to furfural, a key platform chemical with diverse potential, and concludes with an exploration of its transformation into valuable chemicals and fuels through various chemical pathways.

Chapter 2: Chapter 2 offers a thorough review of the existing literature on the hydrogenation and HDO of FFR, with a focus on various catalytic and process methodologies. The chapter begins by exploring the vapor-phase HDO of FFR to 2-MeF using H₂, detailing recent advancements, catalytic performances, and associated challenges. It then transitions to the vapor-phase hydrogenation of FFR to FAL with molecular H₂, examining catalyst efficacy, operational conditions, and improvements in reaction efficiency. The review further encompasses the transfer hydrogenation of FFR to 2-MeF, highlighting the use of alternative hydrogen sources and the development of suitable catalysts for this method. Following these discussions, the chapter presents highlights and observations, summarizing the key findings from the reviewed studies. It also identifies research gaps, providing insight into unresolved issues and areas requiring further investigation. This chapter pinpoints where additional research can contribute to advancing the field and improving catalytic processes for FFR conversion, thereby setting the stage for the experimental chapters that follow.

Chapter 3: Chapter 3 delves into the comprehensive experimental procedures employed in this research. It details the synthesis of catalysts, including the step-by-step methods used to prepare and characterize the catalysts. The chapter also covers the diverse characterization techniques employed to analyze the physical and chemical properties of the synthesized materials. Additionally, this chapter outlines the methodology for catalytic processes, including hydrogenation, hydrodeoxygenation, and transfer hydrogenation. Each process is described in detail, providing insights into the experimental setups, reaction conditions, and analytical methods used to assess catalyst performance

Chapter 4: This chapter discusses the HDO of FFR to 2-MeF over impregnationderived TiO₂ monometallic Cu and Ni catalysts as well as Cu-Ni bimetallic catalysts where the Cu loading was fixed, and the Ni loading was varied. Detailed studies were carried out to evaluate the effect of various process parameters such as Ni content, temperature, and contact time on the selectivity of 2-MeF. The long-term catalytic activity evaluation was also studied.

Chapter 5: This chapter discusses the HDO of FFR to 2-MeF over Cu-Fe mixed oxide catalysts with varying Cu to Fe molar ratios and synthesized via sol-gel method. A comprehensive evaluation of these catalysts was carried out to assess the influence of Cu to Fe ratios, reaction temperatures, weight hourly space velocity and catalyst reduction temperature under atmospheric pressure conditions. Following parameter optimization, long term catalyst stability study and a rigorous regeneration study were conducted.

Chapter 6: This chapter discusses the hydrogenation of FFR to FAL over Cu catalysts supported on metal-incorporated mesoporous silicas derived from rice husk ash, synthesized via a combined hydrothermal-impregnation synthesis method. The changes induced by metal incorporation in the silica matrix were thoroughly evaluated by examining the effects of incorporation with different metal, reaction temperatures, and weight hourly space velocity under atmospheric pressure conditions. Following the initial assessment, the optimized catalyst underwent a rigorous long-term stability study and a regeneration study.

Chapter 7: This chapter discusses the HDO of FFR to 2-MeF via transfer hydrogenation over Mg-Fe mixed oxide catalysts with varying Mg/Fe ratios and calcined at different temperatures after synthesis via co-precipitation method. A comprehensive evaluation of these catalysts was carried out to investigate the influence of Mg to Fe ratios, reaction temperatures, space velocity and calcination temperatures of the catalysts under atmospheric pressure conditions. Following the conclusion of process parameter optimization, the long-term catalytic activity evaluation and regeneration study were also carried out.

Chapter 8: This chapter summarizes the overall conclusion of the thesis.

References

- [1] E. Ricard, H.M. Guinot, Process for the manufacture of furfuryl alcohol and methylfurane, US 1739919, 1929.
- [2] I.B. Johns, L.W. Burnette, Method Of Producing Methylfuran, US 2458857, 1949. https://doi.org/10.17077/0031rd-0360.24332.
- [3] L.W. Burnette, I.B. Johns, Production of 2-Methylfuran by Vapor- Phase Hydrogenation of Furfural, Ind. Eng. Chem. 40 (1948) 502–505.
- [4] R.F. Holdren, Manufacture of methylfuran, US 2445714, 1948.
- [5] C.L. Wilson, Reactions of Furan Compounds. Part V. Formation of Furan from Furfur- aldehyde by the Action of Nickel or Cobalt Catalysts: Importance of Added Hydrogen., J. Chem. Soc. (1945) 61–63.
- [6] R.M. Lukes, C.L. Wilson, Reactions of Furan Compounds. XI. Side Chain Reactions of Furfural and Furfuryl Alcohol over Nickel-Copper and Iron-Copper Catalysts, J. Am. Chem. Soc. 73 (1951) 4790–4794. https://doi.org/10.1021/ja01154a093.
- [7] J. Zhang, G. Ding, Y. Jin, L. Wei, X. Li, D. Wang, Y. Zhu, Y. Li, Stabilizing the interfacial Cu0-Cu+ dual sites toward furfural hydrodeoxygenation to 2-methylfuran via fabricating nest-like copper phyllosilicate precursor, Fuel. 337 (2023) 127212. https://doi.org/10.1016/j.fuel.2022.127212.
- [8] Q. Liu, Q. Liu, X. Hu, Selective conversion of furfural into value-added chemical commodity in successive fixed-bed reactors, Catal. Commun. 135 (2020) 105836. https://doi.org/10.1016/j.catcom.2019.105836.
- [9] F. Dong, Y. Zhu, H. Zheng, Y. Zhu, X. Li, Y. Li, Cr-free Cu-catalysts for the selective hydrogenation of biomass-derived furfural to 2-methylfuran: The synergistic effect of metal and acid sites, J. Mol. Catal. A Chem. 398 (2015) 140–148. https://doi.org/10.1016/j.molcata.2014.12.001.
- [10] F. Dong, G. Ding, H. Zheng, X. Xiang, L. Chen, Y. Zhu, Y. Li, Highly dispersed Cu nanoparticles as an efficient catalyst for the synthesis of the biofuel 2-methylfuran, Catal. Sci. Technol. 6 (2016) 767–779. https://doi.org/10.1039/c5cy00857c.
- [11] Z. Zong, H. Tan, P. Zhang, C. Yuan, R. Zhao, F. Song, W. Yi, F. Zhang, H. Cui, Cu/SiO2 synthesized with HKUST-1 as precursor: high ratio of Cu+/(Cu+ + Cu0) and rich oxygen defects for efficient catalytic hydrogenation of furfural to 2-methyl furan, Phys. Chem. Chem. Phys. 25 (2023) 24377–24385. https://doi.org/10.1039/d3cp02806b.
- [12] S. Sitthisa, D.E. Resasco, Hydrodeoxygenation of Furfural Over Supported Metal Catalysts: A Comparative Study of Cu, Pd and Ni, (n.d.). https://doi.org/10.1007/s10562-011-0581-7.
- [13] S. Sitthisa, W. An, D.E. Resasco, Selective conversion of furfural to methylfuran over silica-supported NiFe bimetallic catalysts, J. Catal. 284 (2011) 90–101. https://doi.org/10.1016/j.jcat.2011.09.005.
- [14] X. Lan, R. Pestman, E.J.M. Hensen, T. Weber, Furfural hydrodeoxygenation

- (HDO) over silica-supported metal phosphides The influence of metal—phosphorus stoichiometry on catalytic properties, J. Catal. 403 (2021) 181–193. https://doi.org/10.1016/j.jcat.2021.01.031.
- [15] W.S. Lee, Z. Wang, W. Zheng, D.G. Vlachos, A. Bhan, Vapor phase hydrodeoxygenation of furfural to 2-methylfuran on molybdenum carbide catalysts, Catal. Sci. Technol. 4 (2014) 2340–2352. https://doi.org/10.1039/c4cy00286e.
- [16] Z. Lin, W. Wan, S. Yao, J.G. Chen, Cobalt-modified molybdenum carbide as a selective catalyst for hydrodeoxygenation of furfural, Appl. Catal. B Environ. 233 (2018) 160–166. https://doi.org/10.1016/j.apcatb.2018.03.113.
- [17] W.A. Lazier, Process for hydrogenating furfural, US 2077422, 1931.
- [18] H.D. Brown, R.M. Hixon, Vapor Phase Hydrogenation of FurFural to FurFuryl Alcohol., Ind. Eng. Chem. 41 (1949) 1382–1385. https://doi.org/10.1021/ie50475a021.
- [19] S. Swadesh, Catalytic production of furfuryl alcohol and catalyst therefor, US 2754304, 1952.
- [20] B.M. Nagaraja, V. Siva Kumar, V. Shasikala, A.H. Padmasri, B. Sreedhar, B. David Raju, K.S. Rama Rao, A highly efficient Cu/MgO catalyst for vapour phase hydrogenation of furfural to furfuryl alcohol, Catal. Commun. 4 (2003) 287–293. https://doi.org/10.1016/S1566-7367(03)00060-8.
- [21] B.M. Nagaraja, A.H. Padmasri, B. David Raju, K.S. Rama Rao, Vapor phase selective hydrogenation of furfural to furfuryl alcohol over Cu-MgO coprecipitated catalysts, J. Mol. Catal. A Chem. 265 (2007) 90–97. https://doi.org/10.1016/j.molcata.2006.09.037.
- [22] S. Shirvani, M. Ghashghaee, V. Farzaneh, S. Sadjadi, Influence of catalyst additives on vapor-phase hydrogenation of furfural to furfuryl alcohol on impregnated copper/magnesia, Biomass Convers. Biorefinery. 8 (2018) 79–86. https://doi.org/10.1007/s13399-017-0244-z.
- [23] H. Du, X. Ma, P. Yan, M. Jiang, Z. Zhao, Z.C. Zhang, Catalytic furfural hydrogenation to furfuryl alcohol over Cu/SiO2 catalysts: A comparative study of the preparation methods, Fuel Process. Technol. 193 (2019) 221–231. https://doi.org/10.1016/j.fuproc.2019.05.003.
- [24] H. Du, X. Ma, M. Jiang, P. Yan, Z. Conrad Zhang, Highly efficient Cu/SiO2 catalyst derived from ethanolamine modification for furfural hydrogenation, Appl. Catal. A Gen. 598 (2020). https://doi.org/10.1016/j.apcata.2020.117598.
- [25] S. Wang, G. Zhao, T. Lan, Z. Ma, H. Wang, Y. Liu, B. Xu, Y. Lu, Gas-phase hydrogenation of furfural to furfuryl alcohol: A promising Cu/SiO2 catalyst derived from lamellar Cu-based hydroxy double salt, Fuel. 372 (2024) 132095. https://doi.org/10.1016/j.fuel.2024.132095.
- [26] C.P. Jiménez-Gómez, J.A. Cecilia, I. Márquez-Rodríguez, R. Moreno-Tost, J. Santamaría-González, J. Mérida-Robles, P. Maireles-Torres, Gas-phase hydrogenation of furfural over Cu/CeO2 catalysts, Catal. Today. 279 (2017) 327–338. https://doi.org/10.1016/j.cattod.2016.02.014.

- [27] C.P. Jiménez-Gómez, J.A. Cecilia, D. Durán-Martín, R. Moreno-Tost, J. Santamaría-González, J. Mérida-Robles, R. Mariscal, P. Maireles-Torres, Gasphase hydrogenation of furfural to furfuryl alcohol over Cu/ZnO catalysts, J. Catal. 336 (2016) 107–115. https://doi.org/10.1016/j.jcat.2016.01.012.
- [28] G.R. Bertolini, C.P. Jiménez-Gómez, J.A. Cecilia, P. Maireles-Torres, Gasphase hydrogenation of furfural to furfuryl alcohol over Cu-ZnO-Al2 O3 catalysts prepared from layered double hydroxides, Catalysts. 10 (2020). https://doi.org/10.3390/catal10050486.
- [29] N.J. Venkatesha, S. Ramesh, Citric Acid-Assisted Synthesis of Nanoparticle Copper Catalyst Supported on an Oxide System for the Reduction of Furfural to Furfuryl Alcohol in the Vapor Phase, Ind. Eng. Chem. Res. 57 (2018) 1506–1515. https://doi.org/10.1021/acs.iecr.7b04701.
- [30] S.A. Selishcheva, A.A. Smirnov, A. V. Fedorov, O.A. Bulavchenko, A.A. Saraev, M.Y. Lebedev, V.A. Yakovlev, Highly active CuFeAl-containing catalysts for selective hydrogenation of furfural to furfuryl alcohol, Catalysts. 9 (2019) 1–20. https://doi.org/10.3390/catal9100816.
- [31] M.J. Gilkey, B. Xu, Heterogeneous Catalytic Transfer Hydrogenation as an Effective Pathway in Biomass Upgrading, ACS Catal. 6 (2016) 1420–1436. https://doi.org/10.1021/acscatal.5b02171.
- [32] W. Fang, A. Riisager, Recent advances in heterogeneous catalytic transfer hydrogenation/hydrogenolysis for valorization of biomass-derived furanic compounds, Green Chem. 23 (2021) 670–688. https://doi.org/10.1039/d0gc03931d.
- [33] D. Banerjee, A.K. Sahu, J.K. Clegg, S. Upadhyayula, Recent advances in 2-methylfuran production via catalytic transfer hydrogenation of biomass-derived furfural, Chem. Eng. J. 493 (2024) 152552. https://doi.org/10.1016/j.cej.2024.152552.
- [34] L. Grazia, A. Lolli, F. Folco, Y. Zhang, S. Albonetti, F. Cavani, Gas-phase cascade upgrading of furfural to 2-methylfuran using methanol as a H-transfer reactant and MgO based catalysts, Catal. Sci. Technol. 6 (2016) 4418–4427. https://doi.org/10.1039/c5cy02021b.
- [35] C. Lucarelli, D. Bonincontro, Y. Zhang, L. Grazia, M. Renom-Carrasco, C. Thieuleux, E.A. Quadrelli, N. Dimitratos, F. Cavani, S. Albonetti, Tandem hydrogenation/hydrogenolysis of furfural to 2-methylfuran over a Fe/Mg/O catalyst: Structure–activity relationship, Catalysts. 9 (2019). https://doi.org/10.3390/catal9110895.
- [36] X. Fu, Y. Liu, Q. Liu, Z. Liu, Z. Peng, Preparation of Highly Active Cu/SiO2 Catalysts for Furfural to 2-Methylfuran by Ammonia Evaporation Method, Catalysts. 12 (2022). https://doi.org/10.3390/catal12030276.

This chapter provides an in-depth account of the experimental protocols used for catalyst synthesis, along with a thorough overview of the characterization techniques applied. Furthermore, it offers a detailed exploration of the methodologies employed in conducting catalytic hydrogenation, hydrodeoxygenation, and transfer hydrogenation reactions.

3.1 Catalyst Synthesis

3.1.1 Materials Used

Aluminium nitrate nonahydrate (Al(NO₃)₃·9H₂O, 98%), copper nitrate trihydrate (Cu(NO)₂·3H₂O (99.5%)), magnesium oxide (MgO, 96%), urea (CO(NH₂)₂, 99%) and zirconyl nitrate hydrate (ZrO(NO₃)₂·xH₂O) were procured from Loba Chemie Pvt. Ltd., Mumbai, India. Cetyltrimethylammonium bromide (C₁₉H₄₂BrN, CTAB, 98%), iron nitrate nonahydrate (Fe(NO₃)₃·9H₂O, 98%), magnesium nitrate hexahydrate (Mg(NO₃)₂·6H₂O, 98%), tin (IV) chloride pentahydrate (SnCl₄·5H₂O), and titanium isopropoxide (Ti[(C₃H₇O)₄], 98%), were procured from Avra Synthesis Pvt. Ltd., Hyderabad, India. Nickel nitrate hexahydrate (Ni(NO)₂·6H₂O, 98-102%) was purchased from Hi-Media Laboratory Pvt. Ltd., Mumbai (India) while citric acid, sodium carbonate (Na₂CO₃, 99.5%), sodium hydroxide (NaOH, 98%), and titanium dioxide (TiO₂, ≥98.5%)) were obtained from Merck Life Sciences Pvt. Ltd., Mumbai. Furfural (99%) was procured from Spectrochem Pvt. Ltd., Mumbai (India). Rice husk used was collected from agricultural fields in the vicinity of Indian Institute of Technology Ropar in the state of Punjab, India. The gases (H₂ and N₂) were sourced from Raj Enterprises, Mohali, with a purity of 99.9999%.

3.1.2 Synthesis of TiO₂ supported monometallic and bimetallic Cu and Ni catalysts

A wet impregnation method [1,2] was used for synthesizing the monometallic catalysts wherein certain amounts of Cu and/or Ni precursors (Cu(NO) $_2$ ·3H $_2$ O and Ni(NO) $_2$ ·6H $_2$ O, respectively) and TiO $_2$ powder were dissolved in 100 mL double distilled water to obtain a 10 weight% loading of each metal in the synthesized monoand bimetallic catalysts (Fig. 1). The resulting solution was then transferred to a 500

mL round bottom flask where it was aged under vigorous stirring at 80 °C for 4 h, followed by the evaporation of water at the same temperature under reduced pressure in a rotary evaporator. The catalysts were collected from the flask, dried in a hot air oven at 100 °C overnight, and finally, calcined in air at 450 °C for 3 h.

The bimetallic Cu-Ni catalysts were synthesized similarly to the monometallic catalysts (Fig. 3.1), wherein certain amounts of Cu and Ni precursors and TiO₂ support were added in 100 mL water to maintain a constant 10 wt.% loading of Cu and 2.5, 5, 10, and 20 wt.% loading of Ni in the synthesized catalysts. The resulting solution was transferred to a round bottom flask and aged at 80 °C for 4 h in a rotary evaporator, followed by the removal of water by evaporation under reduced pressure at the same temperature. The obtained catalyst(s) were then dried at 100 °C overnight and calcined at 450 °C for 3 h in air.

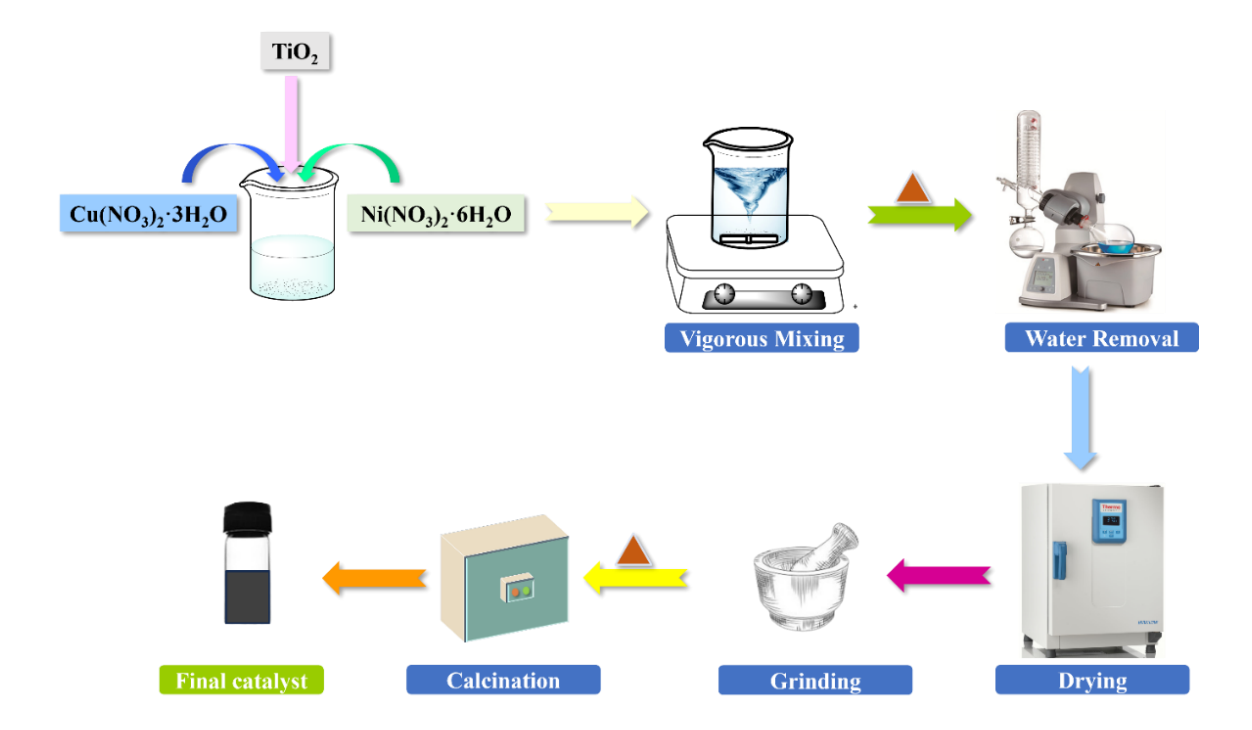


Fig. 3.1 Schematic Diagram for the synthesis of TiO₂-supported bimetallic Cu-Ni catalysts.

3.1.3 Synthesis of Cu-Fe mixed oxide catalysts

Cu-Fe oxide catalysts with varying Cu/Fe ratios (0.5 to 2) were synthesized following a previously reported procedure through a sol-gel route using citric acid as the chelating/gelling agent (Fig. 3.2) [3,4]. In a typical synthesis, x mmol of $Cu(NO_3)_2 \cdot 3H_2O$ and y mmol of $Fe(NO_3)_3 \cdot 9H_2O$ were dissolved in double distilled

water at a temperature of 60 °C for a period of 2 h. Simultaneously, citric acid was dissolved separately in double distilled water in equimolar quantity. Subsequently, the citric acid solution was added to the metal nitrate solution and the resulting solution was heated for 2 h at 60 °C under stirring. Later, the temperature was raised to 80 °C to evaporate the water, yielding a viscous gel. The gel was dried overnight at 120 °C, ground to a fine powder using a mortar and pestle and finally, calcined at 500 °C at a heating rate of 5 °C/min for 4 h.

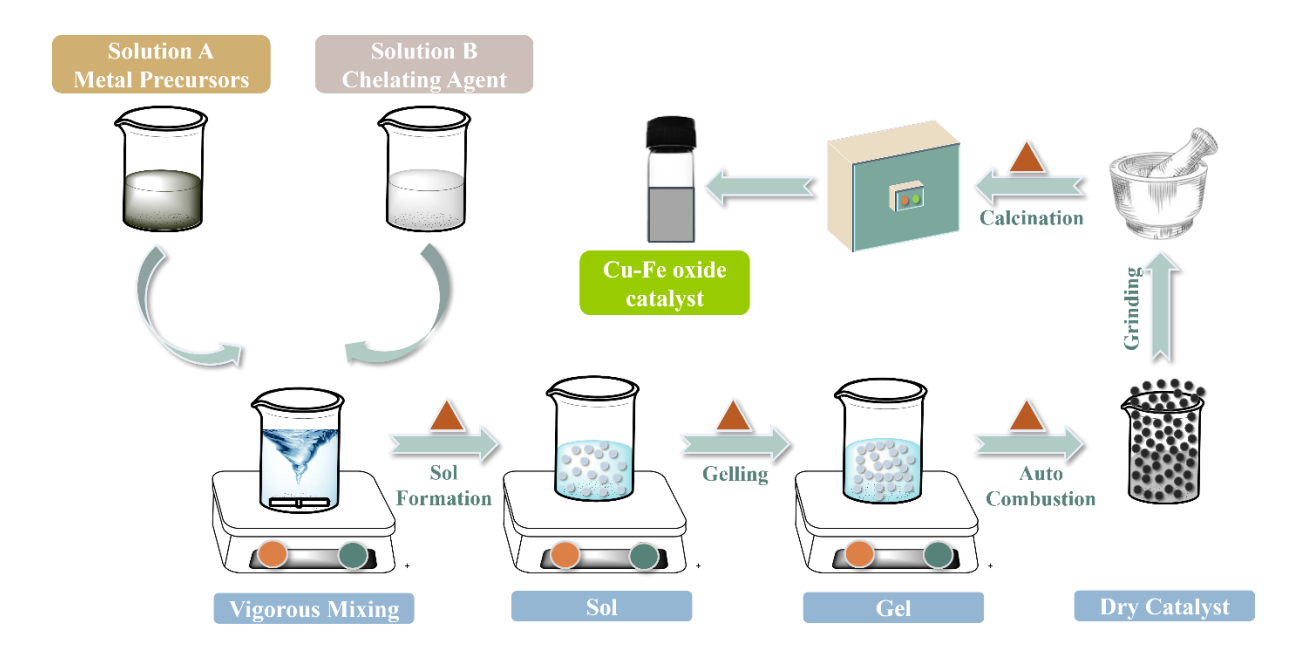


Fig. 3.2 Schematic Diagram for the synthesis of Cu-Fe mixed oxide catalysts.

3.1.4 Synthesis of Cu catalysts supported on metal-incorporated rice husk ashderived mesoporous silica

3.1.4.1 Preparation of Rice Husk Ash

The rice husk collected was washed thoroughly with water to remove any dirt and impurities, followed by drying, crushing, and sieving. Silica-rich rice husk ash then was prepared using the protocol reported in literature [5,6]. In a typical synthesis, 30 g of clean and dried rice husk was added to a 1M solution of HNO₃ (a solid loading of 20 ml g⁻¹) and stirred at 120 °C for 3 h. The acid-treated rice husk was subsequently washed with deionized water until neutralization and dried for approximately 24 h at 100 °C (Fig. 3.3). Finally, the dried material was calcined in a muffle furnace at 600 °C at a ramp rate of 3 °C min⁻¹ for 4 h.

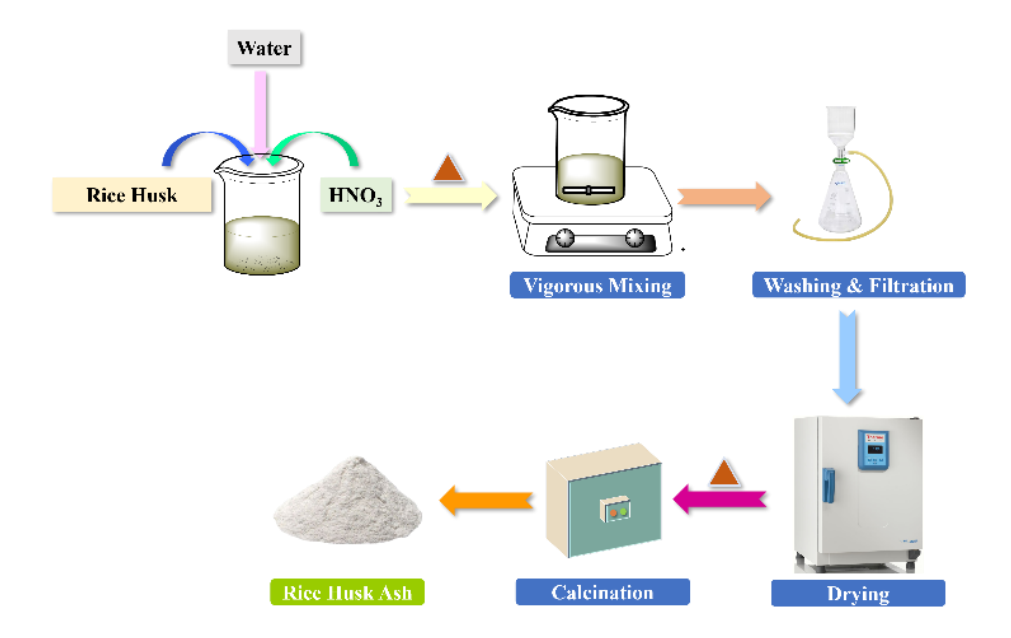


Fig. 3.3 Schematic Diagram for rice husk ash synthesis.

3.1.4.2 Synthesis of Pristine and Metal Incorporated Mesoporous Silica Supports

A mesoporous silica support material was synthesized via a straightforward hydrothermal process [5–7], utilizing the rice husk ash obtained in the previous step as the silica source. In a typical procedure, 10 g each of rice husk ash-derived silica and NaOH (with a NaOH to SiO₂ molar ratio of 1.5) were dissolved in approximately 200 ml of double distilled water and heated at 80 °C for 1 h with stirring. After cooling to room temperature, the mixture was filtered using a Whatman filter paper to obtain a clear sodium silicate solution, labelled as solution I. Simultaneously, a second solution (labelled solution II) was prepared by dissolving 9.1 g CTAB (with a CTAB to SiO₂ molar ratio of 0.15) in 100 ml water and heating at 80 °C for 30 minutes with stirring. Solution II was then cooled to room temperature. Next, the sodium silicate solution (solution I) was added dropwise into the CTAB solution (solution II) under stirring to form solution III. Solution III was heated again at 80 °C for 6 h. Subsequently, the solution was cooled to room temperature, pH adjusted to 10 using a 3M HNO₃ solution, and finally aged for 48 h at 100 °C in a Teflon-lined stainless-steel autoclave. The obtained solid were filtered, washed several times with deionized water and ethanol till neutralization and dried overnight at 80 °C. Finally, the dried solids were calcined at 600 °C at a rate of 3 °C min⁻¹ for 5 h. The obtained mixed supports were labelled as MS.

Mixed oxide supports containing mesoporous silica incorporated with oxides of various metals (Al, Sn, Ti, and Zr) were synthesized using a similar procedure (Fig. 3.4). The only difference was the addition of metal precursor solutions (prepared to maintain a Si to metal molar ratio of 10) to solution III before aging at 80 °C for 6 h, maintaining pH at 10, and aging at 100 °C. The obtained solids were filtered, washed several times with deionized water and ethanol till neutralization and dried overnight at 80 °C. Finally, the dried solids were calcined at 600 °C at a rate of 3 °C min⁻¹ for 5 h. The obtained mixed supports were labelled as Al-MS, Sn-MS, Ti-MS and Zr-MS.

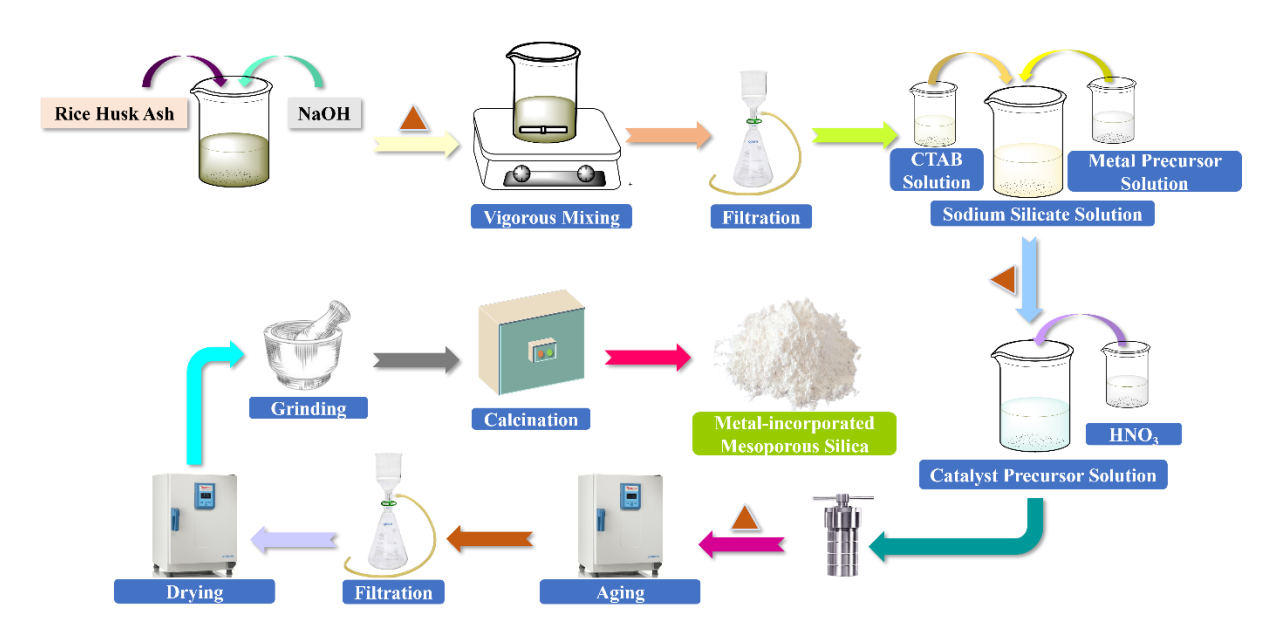


Fig. 3.4 Schematic Diagram for metal-incorporated mesoporous silica synthesis from rice husk ash.

3.1.4.3 Synthesis of Supported Cu catalysts

Catalysts containing Cu supported on pure, and metal-incorporated mesoporous silica were prepared via wet impregnation method wherein a certain amount of Cu precursor and support material were dissolved in 100 mL deionized water to obtain a 5 wt.% loading of Cu metal in the synthesized catalysts. The resulting solution was then transferred to a 500 mL round bottom flask where it was aged under vigorous stirring at 80 °C for 3 h, followed by the evaporation of water at the same temperature under reduced pressure in a rotary evaporator. The catalysts were collected from the flask, dried in a hot air oven at 80 °C overnight, and finally, calcined in air at 500 °C for 4 h at a rate of 3 °C min⁻¹. The final catalysts were labelled as Cu@MS, Cu@Al-MS, Cu@Sn-MS, Cu@Ti-MS and Cu@Zr-MS.

3.1.5 Synthesis of Mg-Fe mixed oxide catalysts

A series of hydrotalcite-type Mg-Fe mixed oxide catalysts with various Mg/Fe molar ratios were synthesized using a co-precipitation method, as described in previous studies (Fig. 3.5) [8,9]. Typically, x millimoles of Mg(NO₃)₂·6H₂O and y millimoles of Fe(NO₃)₃·9H₂O, with x/y ratios ranging from 1 to 5, were dissolved in deionized water to form solution A, which had a metal ion concentration of 0.4M. Concurrently, solution B was prepared by dissolving specific amounts of Na2CO3 and NaOH in deionized water to ensure $n[CO_3^{2-}] = 1 \times n[Mg^{2+} + Fe^{3+}]$ and $[OH^{-}] = 2 \times n[Mg^{2+} + Fe^{3+}]$. Both solution A (the metal nitrate solution) and solution B (the precipitant solution) were added dropwise to a beaker containing distilled water under constant stirring. During this process, the pH of the mixture in the beaker was maintained at 10 ± 0.2 using a Cole-Parmer Oakton PC 2700 benchtop pH meter. After the complete addition of both solutions, the mixture was stirred for 30 minutes at room temperature and then transferred to a Teflon-lined stainless-steel autoclave for hydrothermal treatment at 80 °C for 24 hours. The resulting product was filtered, thoroughly washed to remove excess precipitating agents, dried overnight at 80 °C, crushed, ground, and calcined at 500 °C for 5 hours at a heating rate of 2°C/min under static air in a muffle furnace. The synthesized Mg-Fe mixed oxides with Mg/Fe molar ratios of 1, 2, 3, 4, and 5 were designated as Mg1Fe1, Mg2Fe1, Mg3Fe1, Mg4Fe1, and Mg5Fe1, respectively. Additionally, pure Mg and Fe oxides were synthesized using a similar procedure were labelled Mg1Fe0 and Mg0Fe1 catalysts.

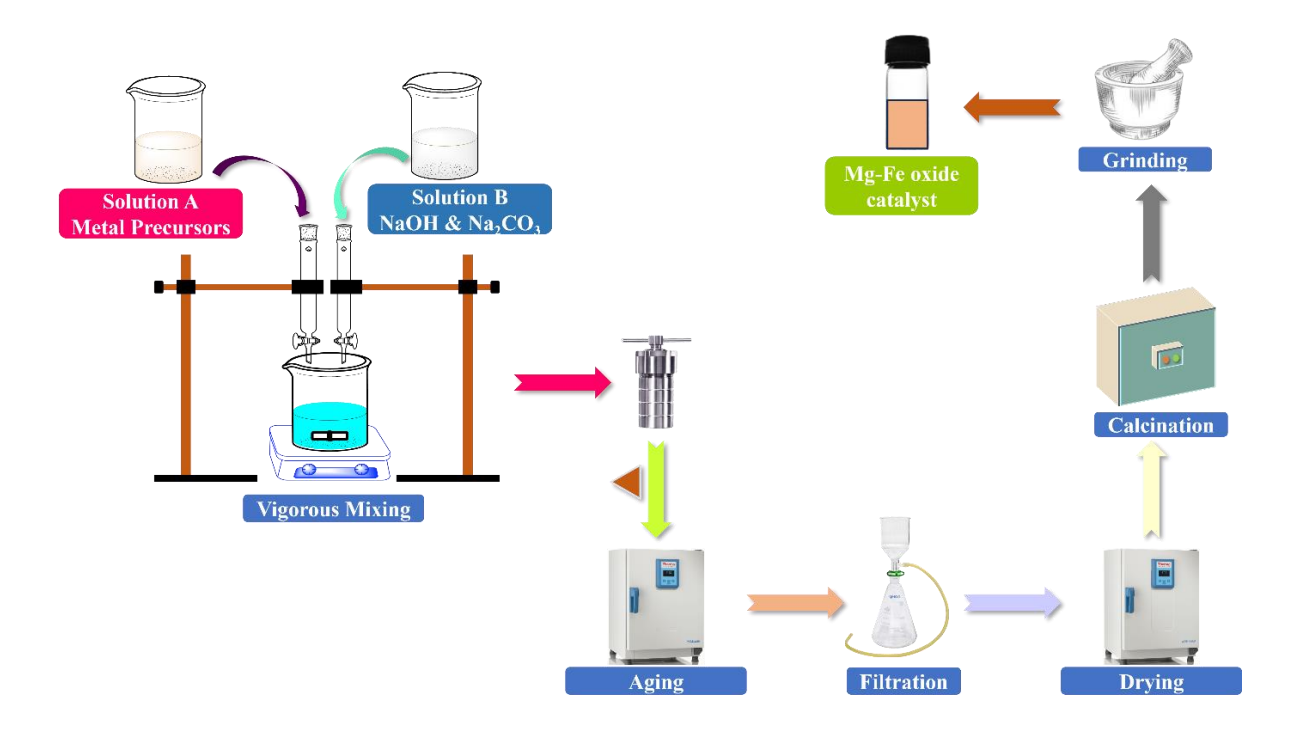


Fig. 3.5 Schematic Diagram for the synthesis of Mg-Fe mixed oxide catalysts.

3.2 Catalyst Characterization

The synthesized fresh catalysts were characterized to evaluate their catalytic properties via different characterization techniques as listed below:

- 1. X-ray diffraction (XRD):
- 2. N₂ Physisorption
- 3. Field emission scanning electron microscopy (FESEM)
- 4. Energy-dispersive X-ray spectroscopy (EDX)
- 5. CO₂- and NH₃-Temperature program desorption (TPD)
- 6. H₂-Temperature program reduction (TPR)
- 7. X-Ray Photon Spectroscopy (XPS)
- 8. Transmission Electron Microscopy (TEM)

3.2.1 X-ray diffraction (XRD)

The crystal structure of the calcined and reduced catalysts was meticulously explored through X-ray diffraction (XRD) using a Rigaku Miniflex 600 diffractometer. Operating under conditions of 30 kV and 10 mA, this instrument harnessed the power of Cu K α radiation (λ = 1.5406 Å) to scan a 2 θ range of 10° to 80° at a speed of 4°/min. The identification of crystalline phases was accomplished by comparing the 2 θ values and d-spacing of characteristic Bragg reflections from our samples to reference data in

the Inorganic Crystal Structure Database (ICSD). Additionally, the average crystallite size (D) of the catalyst samples was calculated using the Scherrer equation, which applied to the full width at half maximum (FWHM) of the X-ray diffraction peaks, correcting for instrumental broadening effects.

$$d = \frac{K*\lambda}{\beta*Cos\theta}$$

Where d is the crystallite size, K is dimensionless shape factor (taken as 0.9, by assuming spherical crystal), λ is wavelength of X-ray, and β represents instrumental broadening of the diffraction line, which corresponds to the Bragg angle (θ), quantitatively represented by the full width at half maximum (FWHM) of the corresponding diffraction peaks.

3.2.2 N₂ Physisorption

The textural properties of the catalysts, including average pore size, pore volume, and BET surface area, were analyzed using N₂ physisorption on Quantachrome Nova 2000e, Quantachrome Autosorb iQ2 or Microtrac BELSORP-mini-X instruments. Prior to the assessment, the catalysts underwent a degassing procedure at 200 °C for 3 hours in a dedicated degassing chamber to effectively eliminate any adsorbed moisture and impurities. The specific surface area and pore size distribution were determined using the Brunauer-Emmett-Teller (BET) equation and the Barrett-Joyner-Halenda (BJH) method, respectively, within a relative pressure range of 0.05 to 1. Additionally, adsorption-desorption isotherms were generated for the catalyst samples, providing comprehensive insights into their textural characteristics.

3.2.3 Field Emission Scanning Electron Microscope (FESEM)

A Field Emission Scanning Electron Microscope (FESEM) analyzes samples by using a highly focused electron beam generated by a field emission source, which operates in an ultra-high vacuum environment to reduce interference. The electron beam is directed toward the surface of the sample, where it interacts with the atoms and produces various signals such as secondary electrons, backscattered electrons, and X-rays. The primary signal used for imaging is the secondary electrons, which are emitted from the sample's surface when the electron beam strikes it. As the beam scans the surface in a raster pattern, these electrons are collected by detectors. The intensity of the secondary

electrons is mapped to create a 2D image of the sample's morphology, revealing fine surface features in extraordinary detail. FESEM stands out for its superior resolution, often reaching 1 nanometer or less. This high resolution is achieved due to the field emission gun (FEG), which generates a highly focused and stable electron beam. Compared to conventional SEMs, the FEG provides a much brighter and coherent electron source, significantly reducing beam spot size and electron scattering. This results in sharper, more detailed images, even at extremely high magnifications - up to 1,000,000X. In the present work, the surface morphology of fresh catalysts was recorded using a JEOL-JSM-7610FPlus field emission scanning electron microscope (FESEM).

3.2.4 Energy-dispersive X-ray spectroscopy (EDX)

Energy Dispersive X-ray Spectroscopy (EDX) is a widely used technique for identifying and mapping the distribution of elements within a sample. The method leverages the unique atomic structure of each element, which produces a characteristic X-ray signal that serves as its "fingerprint" in the EDX spectrum. During analysis, a focused electron beam, generated by an electron gun, is directed at the sample. When this beam strikes the sample, it knocks electrons out of their atomic orbitals. As electrons from higher energy levels fall into the lower energy vacancies, they emit Xrays with specific energies. These emitted X-rays are unique to each element and are captured by a sensitive detector. The detector converts the energy of the X-rays into electrical signals, which are processed by a charge-sensitive preamplifier and a multichannel analyzer. These signals are then interpreted by a computer system, which generates a detailed elemental profile of the sample. This process enables researchers to identify not only the elements present but also their relative abundance and distribution. In this study, a Bruker EDX system integrated with a FESEM (JSM-7610F Plus) was employed to analyze and capture the elemental composition of the catalyst sample, providing critical insights into its makeup.

3.2.5 H₂-Temperature Programmed Reduction (H₂-TPR)

To determine the reduction temperature of the calcined catalyst, Temperature Programmed Reduction (TPR) experiments were performed using a Quantachrome CHEMBETTM TPR/TPD or Micrometrics Pulse Chemisorb 2750 instruments. The process began with the pre-treatment of 50–100 mg of catalyst samples in an argon

atmosphere (Ar flow rate: 30 ml min⁻¹) at 250°C for one hour. Following pre-treatment, the samples were allowed to cool to room temperature. After cooling, the catalyst samples were exposed to a 10% H₂/Ar gas mixture flowing at 30 ml min⁻¹. The temperature was gradually increased from 25°C to 750°C at a controlled ramp rate of 10°C min⁻¹. Throughout this heating process, the amount of hydrogen consumed was continuously measured using a thermal conductivity detector (TCD), providing essential data on the catalyst's reduction behavior.

3.2.6 NH₃-/CO₂-Temperature Programmed Desorption (NH₃- or CO₂-TPD)

The acidity of the catalyst was quantified using Temperature Programmed Desorption (TPD), with ammonia (NH₃) serving as the probe molecule. The analysis was carried out on a Quantachrome CHEMBETTM TPR/TPD, Micrometrics Pulse Chemisorb 2750 and/or MicrotracBEL Corp. BELCAT II instruments. Initially, the catalyst samples were preheated to 300°C at a rate of 10°C min⁻¹ under a continuous flow of helium (He) for 30 minutes to clean the surface. After this step, the sample was cooled to 50°C, and NH₃ (10% in He) was flowed over the catalyst surface at 10 mL min⁻¹ for 1 hour to allow for adsorption. Following NH₃ adsorption, excess or physically adsorbed gas was removed by flushing with helium at 50 mL min⁻¹ for 30 minutes. The desorption process was then monitored as the sample was heated from 50°C to 500°C at a rate of 10°C min⁻¹. The desorbed gases were measured using an in-built thermal conductivity detector (TCD), providing a detailed profile of the catalyst, using carbon dioxide (CO₂) as the probe molecule instead of ammonia.

3.2.7 X-ray Photoelectron Spectroscopy

X-ray Photoelectron Spectroscopy (XPS) is a surface-sensitive analytical technique used to determine the elemental composition, chemical states, and electronic structure of materials. It works by irradiating a sample with X-rays, typically from an aluminum (Al $K\alpha$) or magnesium (Mg $K\alpha$) source, which causes the ejection of photoelectrons from the surface of the material. When X-rays strike the sample, they impart enough energy to eject core-level electrons from atoms on the surface. The kinetic energy of these ejected photoelectrons is measured by an electron detector. Since the energy of the incident X-rays is known, the binding energy of the ejected electrons can be calculated using the equation:

$$E_{binding} = E_{photon} - E_{kinetic} - \phi$$

 $E_{binding}$ is the binding energy, E_{photon} is the energy of the incident X-rays, $E_{kinetic}$ is the measured kinetic energy of the ejected electron, and ϕ is the work function of the spectrometer.

Each element has characteristic binding energies for its electrons, meaning the binding energy serves as a "fingerprint" for identifying elements and their chemical states. The XPS spectrum displays peaks corresponding to the electrons ejected from specific atomic orbitals. By analyzing these peaks, the elemental composition and oxidation states of the surface can be determined, typically within the top 1-10 nanometers of the material. Additionally, the chemical shifts in binding energy help identify different chemical environments or oxidation states of the elements. In the current study, measurements were carried out using the Versaprobe PHI 5000 (Physical Electronics) scanning system and the ESCALAB Xi⁺ (ThermoFisher Scientific), both under an ultrahigh vacuum analysis chamber and using Al Kα X-rays.

3.2.8 High Resolution Transmission Electron Microscopy (HRTEM)

High-Resolution Transmission Electron Microscopy (HRTEM) is a powerful technique that analyzes samples by passing a beam of highly energetic electrons through an ultrathin specimen. The interaction of these electrons with the sample generates signals that are used to produce detailed images at the atomic scale. In HRTEM, an electron gun produces a finely focused beam of electrons that is directed onto the sample. Unlike other electron microscopy techniques, where the electron beam interacts primarily with the surface, HRTEM allows electrons to penetrate the entire sample, providing information about both the internal structure and the surface. The electrons that pass through the sample are scattered according to the arrangement of atoms within the material. These scattered electrons are collected by detectors to form an image. What makes HRTEM unique is its ability to achieve extremely high spatial resolution - often down to the level of individual atoms - due to the very short wavelength of high-energy electrons. To further enhance resolution, HRTEM uses sophisticated electromagnetic lenses to focus the electron beam and minimize aberrations. The interaction between the transmitted electrons and the sample generates phase contrast, which is critical for resolving fine structural details. The resulting image is magnified and recorded on a detector, then processed and analyzed using specialized software. In this

3.3 Reactions Involved in FFR transformation to FAL and 2-MeF

The transformation of FFR to FAL and 2-MeF involves a sequence of key reactions. Initially, the hydrogenation of the carbonyl group in FFR results in the formation of FAL. Subsequently, hydrogenolysis of the hydroxyl group in FAL leads to the production of 2-MeF. However, as highlighted earlier in the introduction and literature review, the unique chemical structure of FFR - characterized by both an aromatic ring and a reactive carbonyl group - renders it highly susceptible to various reactions under hydrogenation conditions. This reactivity can result in the formation of a diverse range of products beyond FAL and 2-MeF, with numerous side reactions occurring concurrently. These competing pathways can yield a complex mixture of by-products, complicating the selective conversion of FFR to the desired products, as seen in Fig. 3.6.

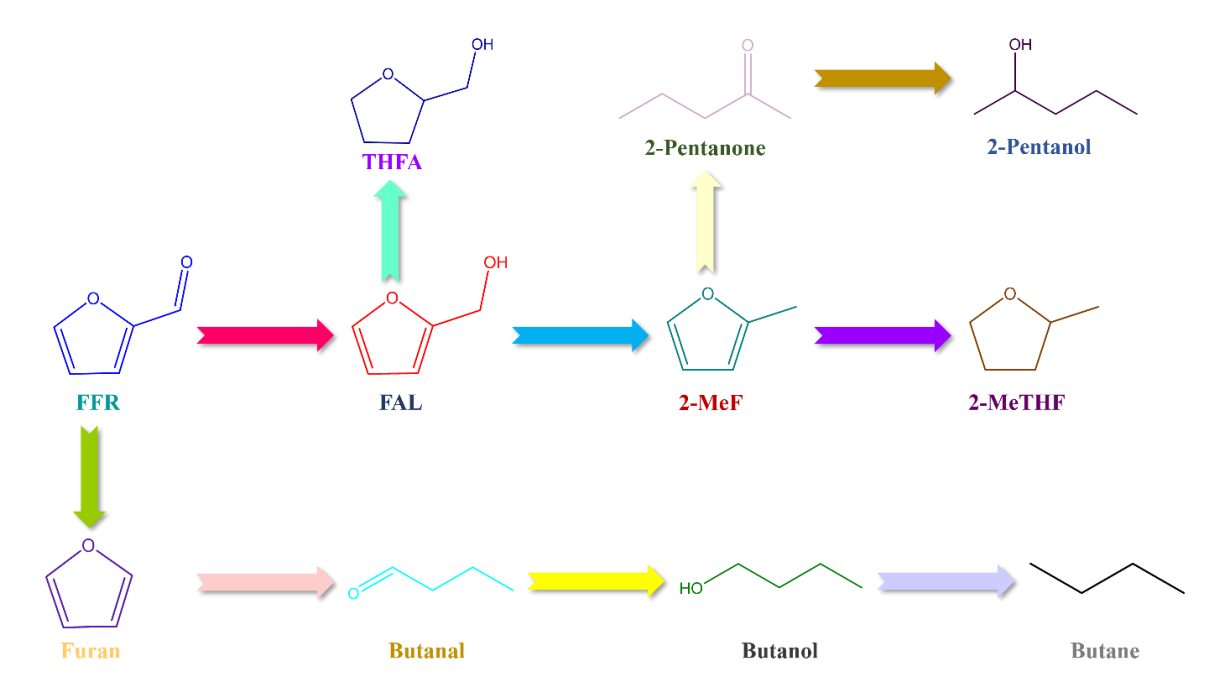


Fig. 6 Conversion Pathways during FFR hydrogenation.

3.3.1 Main Reactions

3.3.1.1 FFR Hydrogenation

$$C_5H_6O_2 + H_2 \rightarrow C_5H_6O + H_2O$$

$$FAL 2-MeF$$
(3.1)

(3.2)

3.3.1.2 FAL Hydrogenolysis

$$C_5H_6O_2 + H_2 \rightarrow C_5H_6O + H_2O$$

FAL 2-MeF

3.3.1.3 Overall FFR HDO

$$C_5H_4O_2 + 2H_2 \rightarrow C_5H_6O + H_2O$$
 (3.3)

FFR 2-MeF

3.3.2 Major Side Reactions

3.3.2.1 FAL Ring Saturation

$$C_5H_6O_2 + 2H_2 \rightarrow C_5H_{10}O_2$$
 (3.4)

FAL THFA

3.3.2.2 FFR Decarbonylation

$$C_5H_4O_2 \rightarrow C_4H_4O + CO \tag{3.5}$$

FFR Furan

3.3.2.3 2-MeF Ring Saturation

$$C_5H_6O + 2H_2 \rightarrow C_5H_{10}O$$
 (3.6)

2-MeF 2-MeTHF

3.3.2.4 2-MeF Ring Opening/Hydrogenolysis

$$C_5H_6O + 2H_2 \rightarrow C_5H_{10}O$$
 (3.7)

2-MeF 2-Pentanone

$$C_5H_{10}O + H_2 \rightarrow C_5H_{12}O$$
 (3.8)

2-Pentanone 2-Pentanol

3.3.2.5 Furan Ring Opening

$$C_4H_4O + 2H_2 \rightarrow C_4H_8O$$
 (3.9)

Furan Butanal

$$C_4H_8O + H_2 \rightarrow C_4H_{10}O$$
 (3.10)

Butanal Butanol

$$C_4H_{10}O + H_2 \rightarrow C_4H_{10} + H_2O$$
 (3.11)

Butanol Butane

3.4 Evaluation of Catalytic Activity

3.4.1 For FFR Hydrogenation and HDO using molecular H₂

The catalytic activity of the synthesized catalysts for FFR hydrogenation and HDO was evaluated at atmospheric pressure in a reactor setup consisting of a feed pump, a preheater mixer, a fixed-bed reactor, a condenser, and a gas-liquid separator for different process parameters such as reaction temperatures and weight hourly space velocities/space times (Fig. 3.7). The fixed-bed reactor comprised a ¼ inch Inconel tube of length 520 mm mounted inside a split-type vertical furnace with two heating zones. Prior to conducting experiments for the evaluation of process parameters, test runs were carried out to ensure that no external and internal mass transfer limitations were present. For this purpose, first the gas hourly space velocity (GHSV) of the carrier gas was varied keeping the reactant space velocity constant and the conversion and product selectivity data were recorded. When the conversion and product selectivity remained constant beyond a certain value of GHSV (4364 h⁻¹ in this case), the external transport resistances were deduced to have vanished and this value was used for conducting further studies. The evaluation of internal resistances to transport was carried out using catalyst particles having average sizes smaller than 2 mm, 1.18 mm, 0.85 mm and 0.500 mm in the external transportation limitation-free regime. It was noted that the values of conversion and product selectivity remained constant at and/for catalyst particles having size smaller than 1.18 mm, signifying the absence of internal resistances. Therefore, for studies involving the evaluation of process parameters, this particle size was selected.

Before each reaction, the reactor tube was loaded with 1 g of the calcined catalyst with inert material SiC, which was mixed to maintain a uniform temperature throughout the bed. All the experiments were carried out by maintaining the plug flow conditions, *i.e.* the ratio of the catalyst bed height to the particle size and the ratio of the internal diameter of the tubular reactor to the particle size of the catalyst was kept at 50 and 30, respectively [10]. The catalyst was placed in the reactor tube between two layers of wool and then reduced at an H₂ flow rate of 50 mL min⁻¹ at a certain reduction temperature (as determined from the TPR analysis) for a period of 2.5 h. Following the reduction step, the temperature was lowered to the desired value (175 to 250 °C) under the same value of H₂ flow rate. Due to its tendency to undergo polymerization and cause a blockage in the pumping lines, FFR was fed in the form of a solution consisting of 5 vol% FFR dissolved in isopropyl alcohol (IPA) was fed to a preheater maintained at 170 °C through a high-pressure liquid chromatography (HPLC) pump at a flow rate of a certain flowrate (mL min⁻¹). Simultaneously, H₂ gas was also introduced into the premixer heater while maintaining a certain H₂ to FFR molar ratio (5 to 15), resulting in its mixing with the vaporized liquid feed; thereafter, this mixed feed was introduced into the fixed bed reactor.

Furthermore, the vapor products leaving the reactor were condensed and the liquid and gaseous products were separated in a gas-liquid separator. The resulting liquid products were identified using an Agilent 7890B gas chromatograph equipped with a 5977GC Mass spectrometer. The liquid products were analysed offline with the same instrument but with a DB-5 capillary column and a flame ionization detector (FID). Similarly, the gaseous products were analysed by sampling the gas stream leaving the gas-liquid separator with a gas-tight syringe and then injecting the sample into an Agilent 7820B gas chromatograph also equipped with a DB-5 capillary column and an FID detector.

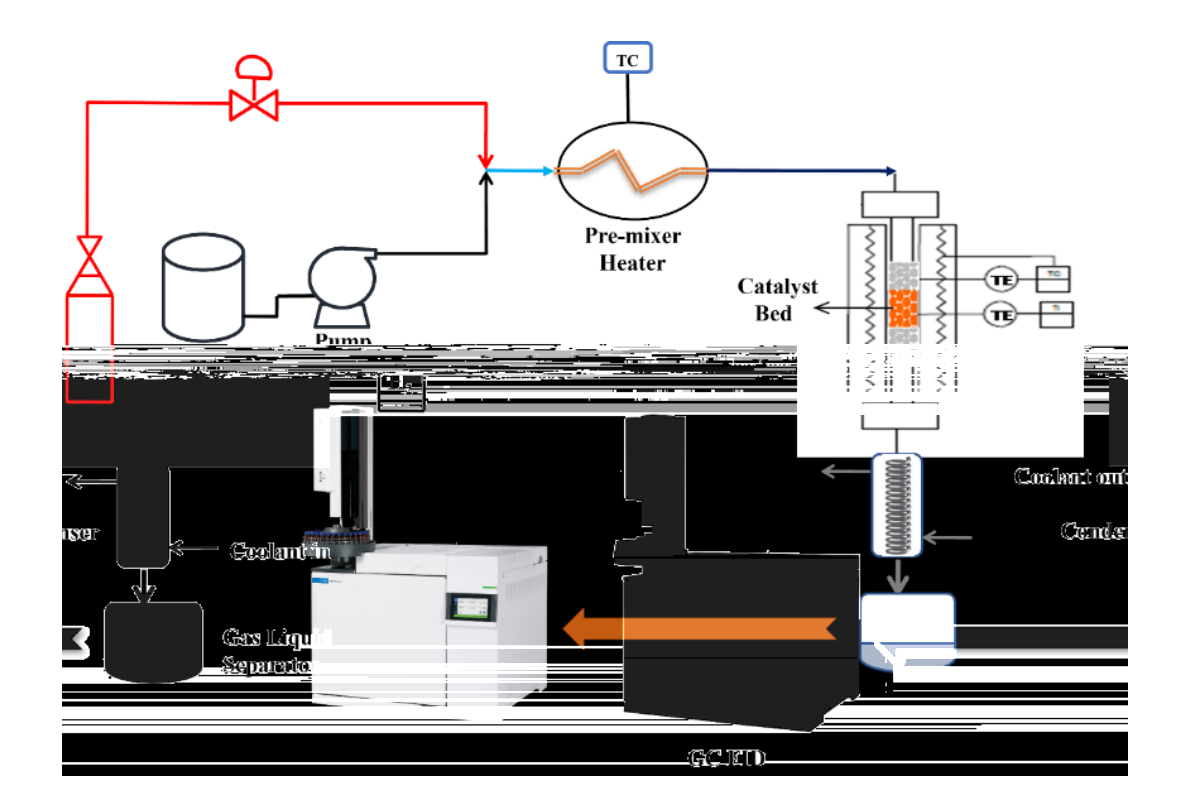


Fig. 3.7 Schematic diagram of experimental setup for FFR transformation

3.4.2 For FFR Transfer Hydrogenation

The catalytic performance of the synthesized catalysts for FFR transfer hydrogenation was evaluated at atmospheric pressure using the same reactor system as mentioned above that included a feed pump, pre-heater mixer, fixed-bed reactor, condenser, and gas-liquid separator. Preliminary tests, as outlined previouslu, were conducted to confirm the absence of external and internal mass transfer limitations. Prior to each reaction, the reactor tube was loaded with 1 g of calcined catalyst mixed with SiC in a 1:1 weight ratio to ensure uniform temperature distribution. Plug flow conditions were maintained with the catalyst bed height to particle size ratio and the internal diameter of the reactor to particle size ratio set at 50 and 30, respectively [10]. The catalyst, positioned between wool layers in the reactor tube, was heated to the desired reaction temperature (250 to 400 °C) under N₂ flow. For the transfer hydrogenation reaction, IPA was used as the hydrogen donor. FFR was fed as a 5 vol% solution in IPA, maintaining a molar ratio of 20:1 (IPA to FFR). This solution was delivered to a premixer heater set at 170 °C using an HPLC pump at a certain flow rate (mL min⁻¹). Simultaneously, N₂ was introduced into the pre-mixer heater at a flow rate of 50 mL min⁻¹, serving as the carrier gas for the vaporized liquid feed. The combined feed was then directed to the reactor for the reaction. The vapor products exiting the reactor were condensed using a chiller maintained at -25 °C. The resulting liquid products were identified using an Agilent 7890B gas chromatograph equipped with a 5977GC Mass spectrometer. The analysis or quantification was carried out using the same instrument but with a DB-5 capillary column and a flame ionization detector.

3.4.3 Evaluation of Catalytic Performance

The catalytic performance was evaluated by determining the FFR conversion and product selectivities and yields defined and determined using the following formulae:

Conversion (%) =
$$\frac{\text{moles of FFR consumed}}{\text{moles of FFR fed}} \times 100$$
 (3.12)

Selectivity of species
$$i$$
 (%) = $\frac{\text{moles of product i formed}}{\text{moles of FFR consumed}} \times 100$ (3.13)

Yield of species
$$i$$
 (%) = $\frac{\text{moles of product i formed}}{\text{moles of FFR fed}} \times 100$ (3.14)

The weight hourly space velocity (WHSV) was calculated as follows:

$$\frac{F_{A0}}{W} = \frac{\text{molar flowrate of FFR into the reactor per hour}}{\text{Weight of the catalyst}} \left(\frac{g_{\text{FFR}} \, h^{-1}}{g_{\text{catalyst}}}\right)$$
(3.15)

The residence time and weight hourly space time (WHST) was calculated as follows:

Residence time =
$$\frac{\text{Weight of the catalyst}}{\text{Molar flowrate of FFR into the reactor}} \left(\frac{g_{\text{catalyst } h}}{g_{\text{FFR}}} \right) h = \text{WHST}$$
 (3.16)

The gas hourly space velocity (GHSV) was calculated as follows:

$$GHSV = \frac{\text{Hydrogen flowrate at STP } (\frac{\text{mL}}{\text{hr}})}{\text{Catalyst Volume (mL)}} \, \text{hr}^{-1}$$
(3.17)

References

- [1] B. Seemala, C.M. Cai, C.E. Wyman, P. Christopher, Support Induced Control of Surface Composition in Cu-Ni/TiO2 Catalysts Enables High Yield Co-Conversion of HMF and Furfural to Methylated Furans, ACS Catal. 7 (2017) 4070–4082. https://doi.org/10.1021/acscatal.7b01095.
- [2] B. Seemala, C.M. Cai, R. Kumar, C.E. Wyman, P. Christopher, Effects of Cu-Ni Bimetallic Catalyst Composition and Support on Activity, Selectivity, and Stability for Furfural Conversion to 2-Methyfuran, ACS Sustain. Chem. Eng. 6 (2018) 2152–2161. https://doi.org/10.1021/acssuschemeng.7b03572.
- [3] R. Srivastava, A. Kumar, Pd-decorated magnetic spinels for selective catalytic reduction of furfural: Interplay of a framework-substituted transition metal and solvent in selective reduction, ACS Appl. Energy Mater. 3 (2020) 9928–9939. https://doi.org/10.1021/acsaem.0c01625.
- [4] G.S. More, A. Shivhare, S.P. Kaur, T.J. Dhilip Kumar, R. Srivastava, Catalytic interplay of metal ions (Cu2+, Ni2+, and Fe2+) in MFe2O4 inverse spinel catalysts for enhancing the activity and selectivity during selective transfer hydrogenation of furfural into 2-methylfuran, Catal. Sci. Technol. 12 (2022) 4857–4870. https://doi.org/10.1039/d2cy00970f.
- [5] S. Steven, E. Restiawaty, P. Pasymi, Y. Bindar, An appropriate acid leaching sequence in rice husk ash extraction to enhance the produced green silica quality for sustainable industrial silica gel purpose, J. Taiwan Inst. Chem. Eng. 122 (2021) 51–57. https://doi.org/10.1016/j.jtice.2021.04.053.
- [6] S. Kamari, F. Ghorbani, Extraction of highly pure silica from rice husk as an agricultural by-product and its application in the production of magnetic mesoporous silica MCM–41, Biomass Convers. Biorefinery. 11 (2021) 3001–3009. https://doi.org/10.1007/s13399-020-00637-w.
- [7] J.A.S. Costa, V.H.V. Sarmento, L.P.C. Romão, C.M. Paranhos, Adsorption of organic compounds on mesoporous material from rice husk ash (RHA), Biomass Convers. Biorefinery. 10 (2020) 1105–1120. https://doi.org/10.1007/s13399-019-00476-4.
- [8] M. V. Bukhtiyarova, A review on effect of synthesis conditions on the formation of layered double hydroxides, J. Solid State Chem. 269 (2019) 494–506. https://doi.org/10.1016/j.jssc.2018.10.018.
- [9] M. Manikandan, A.K. Venugopal, K. Prabu, R.K. Jha, R. Thirumalaiswamy, Role of surface synergistic effect on the performance of Ni-based hydrotalcite catalyst for highly efficient hydrogenation of furfural, J. Mol. Catal. A Chem. 417 (2016) 153–162. https://doi.org/10.1016/j.molcata.2016.03.019.
- [10] P.P. Singh, N. Nirmalkar, T. Mondal, Catalytic steam reforming of simulated bio-oil for green hydrogen production using highly active LaNixCo1-xO3 perovskite catalysts, Sustain. Energy Fuels. 6 (2022) 1063–1074. https://doi.org/10.1039/d1se01786a.

Chapter 4: FFR HDO to 2-MeF over TiO₂-supported Cu-Ni bimetallic catalysts

This work investigates the vapor phase HDO of FFR to 2-MeF over a series of TiO₂-supported mono and bimetallic Cu-Ni catalysts with a fixed Cu content (10 wt.%) and varying Ni content (0-20 wt.%). The catalysts were synthesized through a simple wet impregnation method, and their properties were studied in depth through an array of analytical techniques such as XRD, H₂-TPR, SEM, N₂-physisorption, and NH₃- TPD. Detailed studies were carried out to evaluate the effect of various process parameters such as Ni content, temperature, and contact time on the selectivity of 2-MeF. Following the conclusion of process parameter optimization, the long-term catalytic activity evaluation was also studied.

4.1 Catalyst characterization

4.1.1 XRD

Fig. 4.1 displays the XRD patterns of the synthesized mono- and bimetallic Cu-Ni catalysts supported on TiO2. The diffraction patterns of all the catalysts exhibited diffraction peaks at $2\theta = 25.4^{\circ}$, 37° , 37.8° , 38.6° , 48.1° , 53.9° , 55.1° , 62.7° , 68.8° , 70.3°, 75.1°, and 76.1°, which were ascribed to the (011), (013), (004), (112), (020), (015), (121), (024), (116), (220), (125) and (031) lattice planes of anatase TiO₂ (tetragonal, ICSD collection no. – 202243) [1]. In 10%Cu/TiO₂, a peak belonging to the (002) lattice plane of monoclinic CuO (ICSD collection code – 87123) was observed at $2\theta = 35.4^{\circ}$, confirming the presence of Cu [2]. Similarly, $10\% \text{Ni/TiO}_2$ exhibited a peak at $2\theta = 43.1^{\circ}$, belonging to the (11-1) lattice plane of monoclinic NiO (ICSD collection code – 76670), thereby confirming that Ni is present in the catalyst [2] . In bimetallic catalysts, diffraction peaks at 2θ values of 35.4° and 43.1° confirmed the presence of CuO and NiO [2]. A weak diffraction corresponding to NiO was observed for Ni loading up to 5%, suggesting that at these loading levels, the crystallite size of NiO was quite small (~15 nm). The peak corresponding to NiO at 43.1° grew in intensity with the increment in Ni content to 10% and 20% in the bimetallic catalysts. Also, it was observed that the diffraction peak corresponding to CuO underwent a significant reduction in intensity with the increase in Ni content. The crystallite sizes of CuO and NiO in 10%Cu/TiO2 and 10%Ni/TiO2, calculated using the Scherrer equation at $2\theta = 35.4^{\circ}$ and 43.1° , were found to be 69.5 nm and 29.7 nm, respectively. For the case of bimetallic catalysts, addition of Ni in increasingly larger amounts was noted to have led to a reduction in the crystallite size of CuO, with the size decreasing from 49.6 nm for 10%Cu-2.5%Ni catalyst to 11 nm for 10%Cu-20%Ni catalyst and confirms the observed reduction in the diffraction peak of CuO with increasing Ni content. To summarize, the presence of Ni has a positive effect on CuO, improving its dispersion and leading to a reduction in its crystallite size [3].

Interestingly, a gradual reduction in the intensities of peaks corresponding to TiO₂ support was observed in the diffraction patterns of the bimetallic catalysts with an increase in the Ni content from 2.5% to 20%, with the reduction in intensities being particularly sharp at Ni loadings of 10 and 20%. According to the available literature [1,4,5], the observed reduction in the intensities of peaks corresponding to TiO₂ could correspond to the transformation of TiO₂ from anatase to rutile phase, promoted by NiO [1,4,5]. When present in significant amounts, NiO has been observed to lower the activation energy required for TiO₂ to undergo phase transformation [1,4,5]. Such a transformation is generally accompanied by the appearance of diffraction peaks corresponding to the rutile phase [1,4,5]. In this study, however, no peaks related to this phase were observed in the diffraction patterns of the bimetallic catalysts, even at a Ni content of 20%. Consequently, any contribution of the rutile phase can be ruled out. The addition of Ni has also been associated with inhibiting the growth of grains and particles of TiO₂, which could explain the reduced crystallite size of TiO₂ observed for monometallic Ni catalyst as well as bimetallic Cu-Ni catalysts [6,7]. Table 4.1 displays the crystallite sizes of the synthesized monometallic and bimetallic catalysts.

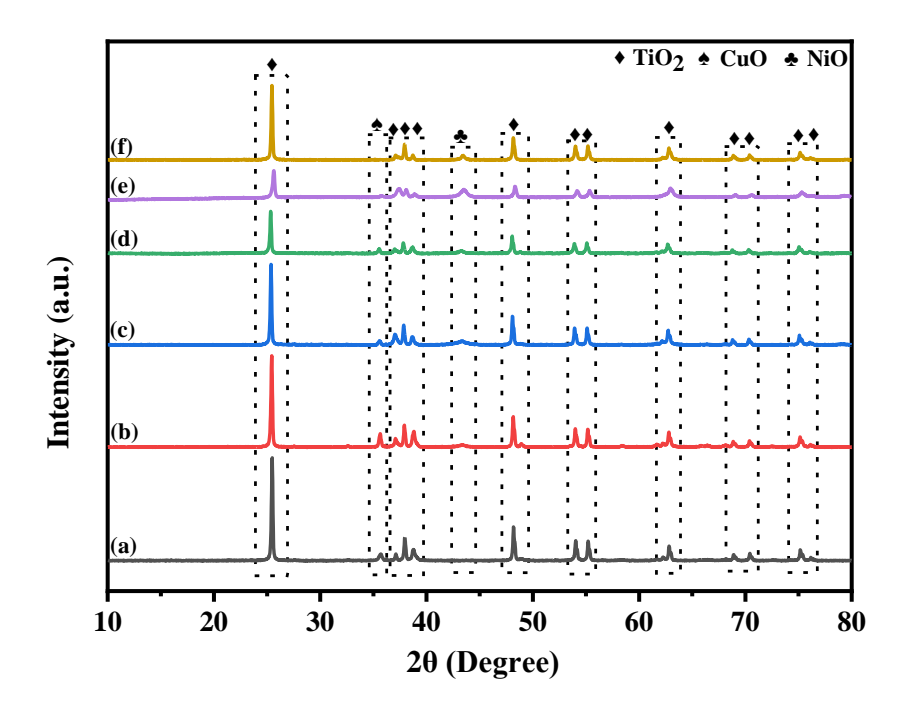


Fig. 4.1 XRD patterns of calcined (a) 10% Cu/TiO₂, (b) 10% Cu-2.5% Ni/TiO₂, (c) 10% Cu-5% Ni/TiO₂, (d) 10% Cu-10% Ni/TiO₂, (e) 10% Cu-20% Ni/TiO₂, and (f) 10% Ni/TiO₂ catalysts

Table 4.1 Physical properties of the calcined mono- and bimetallic Cu-Ni catalysts

Catalyst	Crystallite Size (nm)			Surface Area ^b (m ² g ⁻¹)	Pore Volume ^c (cm ³ g ⁻¹)	Pore Size ^c (nm)
	CuO ^a	NiO ^a	TiO2 ^a			
TiO ₂	-	-	-	9.3	0.0243	10.5
10%Cu/TiO ₂	59.6	-	81.4	9.2	0.020	8.6
10%Cu-2.5%Ni/TiO ₂	49.6	14.3	67.8	8.5	0.016	8.8
10%Cu-5%Ni/TiO2	34.7	18.5	56.5	8.6	0.019	9.2
10%Cu-10%Ni/TiO2	27.8	30.5	48.4	8.8	0.021	9.6
10%Cu-20%Ni/TiO ₂	10.9	43.4	42.4	10.6	0.028	11.2
10%Ni/TiO2	-	29.7	48.5	12.2	0.030	9.8

^aCalculated using Scherrer equation. ^bCalculated using BET method. ^cCalculated using BJH method.

In order to investigate the nature of Cu and Ni species of the catalysts post reduction, XRD analysis was carried out for catalysts after reduction at temperatures determined from H₂-TPR analysis. Fig. 4.2 shows the XRD diffractograms of the reduced catalysts. Diffraction peaks corresponding to the tetragonal anatase TiO₂ phase

at 2θ values = 25.4°, 37°, 37.8°, 38.6°, 48.1°, 53.9°, and 55.1° were observed in the patterns of all the catalysts [1]. The reduced 10%Cu/TiO₂ catalyst exhibited peaks corresponding to the (111) and (200) lattice planes of metallic Cu at 43.3°, and 50.5° [8,9]. Similarly, diffraction peaks corresponding to the (111) and (200) lattice planes of metallic Ni were observed at $2\theta = 44.5^{\circ}$ and 51.9° in the diffractogram of 10% Ni/TiO₂ [8,9]. The peaks corresponding to CuO and NiO, observed previously at $2\theta = 35.4^{\circ}$ and 43.1° respectively in the diffraction patterns of the calcined monometallic catalysts, vanished completely, signifying complete reduction of the oxide phases under the used reduction conditions. Post reduction, the diffractograms of Cu-Ni bimetallic catalysts exhibited peaks corresponding to Cu^0 were observed at $2\theta = 43.3^{\circ}$ and 50.5° but none belonging to CuO were observed, signaling the complete reduction of CuO. Furthermore, the intensity of these reflections was reduced significantly as the Ni content increased from 0 to 10% and completely vanished as Ni content increased further to 20%. This further confirms the conclusion drawn from the XRD diffractograms of calcined bimetallic catalysts that the addition of Ni enhances the dispersion of Cu [10]. The diffraction patterns of the reduced bimetallic catalysts also contained peaks corresponding to Ni⁰ at 44.5° and 51.9°; however, they were found shifted slightly to lower 2θ values (44.1° and 51.6°). The reduction in the intensities of Cu⁰ diffraction peaks and the shifting of Ni⁰ peaks indicates the existence of synergistic interactions between Cu and Ni and the formation of Cu-Ni bimetallic alloys [3,11]. Similar trends have been noted in several reports in literature wherein the formation of Cu-Ni bimetallic alloys was observed at varying Cu/Ni composition, leading to enhancement in dispersion of Cu⁰ species [3,12]. Table 4.2 displays the crystallite sizes of the reduced monometallic and bimetallic catalysts

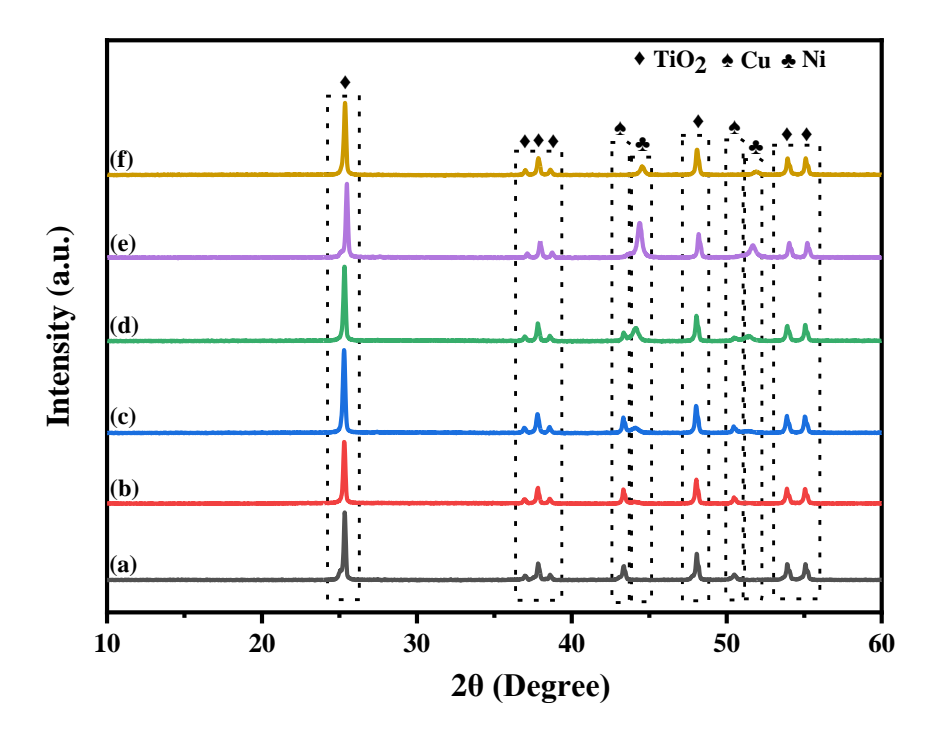


Fig. 4.2 XRD patterns of reduced (a) 10%Cu/TiO₂, (b) 10%Cu-2.5%Ni/TiO₂, (c) 10%Cu-5%Ni/TiO₂, (d) 10%Cu-10%Ni/TiO₂, (e) 10%Cu-20%Ni/TiO₂, and (f) 10%Ni/TiO₂ catalysts

Table 4.2 Physical properties of the reduced mono- and bimetallic Cu-Ni catalysts

Catalyst	Crystallite	Crystallite	
	Size (Cu) ^a	Size (Ni)b	
	(nm)	(nm)	
10%Cu/TiO2	50.9	-	
10%Cu-2.5%Ni/TiO ₂	39.5	17.8	
10%Cu-5%Ni/TiO2	29.6	29.7	
10%Cu-10%Ni/TiO2	17.8	35.7	
10%Cu-20%Ni/TiO2	-	51	
10%Ni/TiO2	-	39	

^a Calculated at $2\theta = 43.3^{\circ}$. ^b Calculated at $2\theta = 44.1^{\circ}$

4.1.2 H₂-TPR

Fig. 4.3 displays the H_2 -TPR profiles of the synthesized TiO_2 mono- 10% Cu and 10% Ni and bimetallic 10% Cu-(2.5, 5, 10, 20) % Ni catalysts. The 10% Cu/ TiO_2 catalyst exhibited a small peak at 227 $^{\circ}$ C and a strong, sharp peak centered at 280 $^{\circ}$ C, corresponding to the reduction of Cu^{2+} species to metallic Cu^{0} species and signaling the presence of different Cu^{2+} species and/or CuO particles of different sizes [13–16].

Several reports available in the literature have described more than one reduction peak in the TPR profiles of Cu catalysts supported on oxide supports [13–16]. The consensus in such cases is that the peak at lower temperatures corresponds to the reduction of CuO particles of smaller size or the finely dispersed Cu²⁺ species with little to no interaction with the support, while the peak at higher temperatures corresponds to the reduction of larger-sized or bulk CuO species interacting relatively strongly with the support [13–16]. Accordingly, the first peak can be attributed to the reduction of smaller-sized CuO particles and/or dispersed Cu²⁺ species and the intense second peak at 280 °C can be ascribed to the reduction of bulk CuO particles [13–16]. Similarly, the TPR profile of 10%Ni/TiO₂ also exhibited a multipeak reduction profile with an intense peak maximum at 373 °C and a small shoulder at 440 °C. The major reduction peak corresponds to the reduction of NiO from Ni²⁺ to Ni⁰, exhibiting weaker interaction with the oxide support, and the small shoulder at 440 °C could be attributed to the reduction of Ni²⁺ species interacting strongly with TiO₂ support [17–21].

The TPR profiles of 10%Cu-(2.5, 5, 10, and 20) %Ni bimetallic catalysts also exhibited two reduction peaks. However, it was observed that the addition of Ni had resulted in the major reduction peak of the bimetallic catalysts shifting towards lower temperatures. With the addition of Ni to the extent of 2.5 wt.%, a strong peak was observed at 236 °C, with a slightly smaller peak at 287 °C. With further increase in the Ni content of the synthesized bimetallic catalysts to 5 and 10 wt.%, the maxima shifted further lower to 227 °C, while the peak at 287 °C was reduced further in intensity to almost a shoulder and shifted to 272 °C. In these profiles, the reduction peak at a lower temperature can be ascribed to the reduction of highly dispersed Cu²⁺ species with little to no interaction with the supporting metal oxide or small-sized CuO particles [13–16], while the peak at a higher temperature could be attributed to the reduction of either the amorphous NiO interacting with the support or bulk CuO species or mixed Cu-Ni oxide species [8,17,22]. The observed shift in the reduction temperatures of CuO and NiO from higher to lower temperatures in the synthesized Cu-Ni bimetallic catalysts is indicative of an enhancement in the reducibility of the catalysts, which could be attributed to a strong synergistic interaction between Cu and Ni, resulting in a reduced crystallite size which was also confirmed with the XRD analysis. This conclusion is in line with the observations made in several reports, where it has been noted that the reduction of CuO to Cu metal enhances and/or catalyzes the reduction of NiO to Ni via spillover mechanism, wherein CuO first undergoes reduction to Cu, which dissociates H₂ that spills over onto NiO resulting in its reduction [2,3,10,11,22–24]. Some studies suggest that the enhanced reducibility could also possibly be attributed, to some extent, to the segregation of Cu and Ni metals where the catalyst surface is enriched in Cu due to the tendency of Ni to occupy bulk or subsurface sites, as a result of which it moves towards the bulk of the catalyst [10,11,25]. To summarize, the addition of Ni led to the formation of supported bimetallic catalysts where the Cu and Ni metals interact synergistically with each other. This interaction grew stronger as the Ni content was increased, resulting in increased reducibility of the synthesized catalysts and reduced crystallite size. Such a change in the reduction behavior of CuO and NiO species in the bimetallic catalysts after the addition of Ni has been reported by numerous studies in literature and is thought to arise from the strong interactions among the Cu and Ni species and is an evidence of the formation of a bimetallic alloy during reduction [11,26]. Therefore, it can be concluded that the observed shifts in reduction temperatures towards lower temperatures in the TPR analysis, combined with the results of XRD analysis post reduction, point towards the formation of Cu-Ni bimetallic alloys.

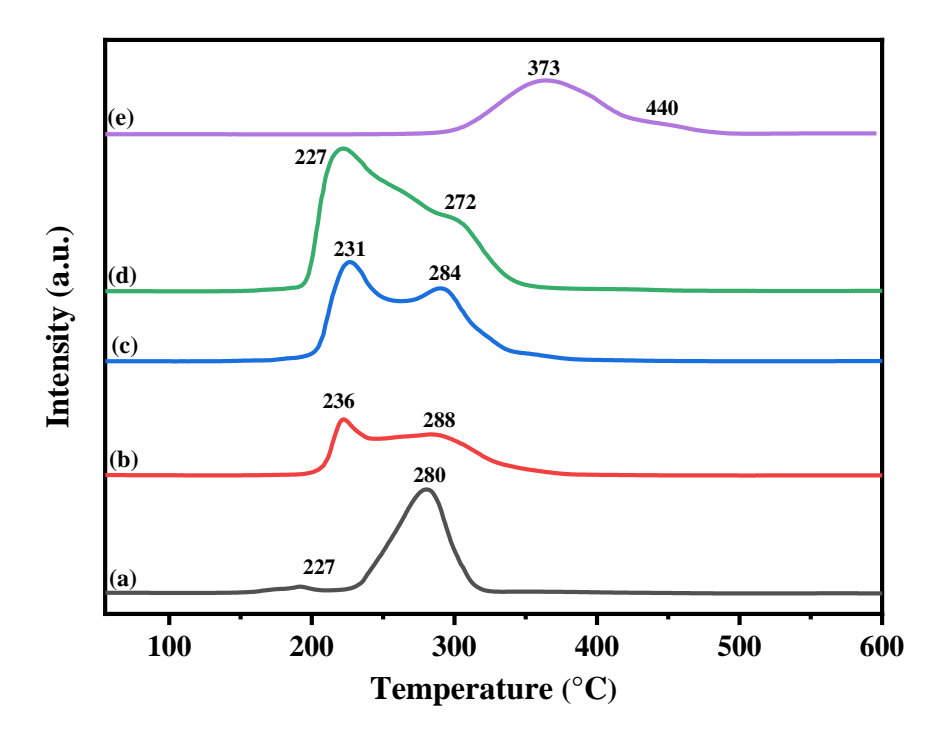


Fig. 4.3 H₂-TPR reduction profiles of (a) 10% Cu/TiO₂, (b) 10% Cu-2.5%Ni/TiO₂, (c) 10% Cu-5%Ni/TiO₂, (d) 10% Cu-10%Ni/TiO₂, and (e) 10% Ni/TiO₂ catalysts

4.1.3 SEM-EDX

Fig. 4.4 displays the SEM images of the synthesized TiO₂-supported mono- and bimetallic Cu-Ni catalysts. The monometallic 10%Cu/TiO₂ exhibited large. irregularly-shaped particles with considerable agglomeration, which is in line with the observations made in the literature for TiO₂-supported copper catalysts (Fig. 4.4a) [15,16,27]. From the SEM micrographs (Fig. 4.4b to 4.4e) of the synthesized bimetallic catalysts, it can be seen that the addition of Ni resulted in reduced particle sizes which could be attributed to the reduction in the crystallite size of TiO₂, which is line with the results of the XRD analysis (Fig. 4.1 and Table 1). In addition to reduced sizes of particles, agglomeration of the metal oxide particles also seemed to have reduced significantly with an increase in Ni loading. A similar conclusion can be drawn from the FESEM image of 10%Cu-10%Ni/TiO₂ catalyst (Fig. 4.5), where small, irregularshaped particles with relatively low levels of agglomeration can be clearly seen. The findings are consistent with the XRD results, where it was observed that the addition of Ni in gradually larger amounts from 2.5% to 20% led to a reduction in the size of both CuO and TiO₂ (Tables 1 and 2). The results are also in agreement with the literature available for Cu-Ni bimetallic catalysts, where a similar reduction in particle size and improved dispersion of metal oxide species was observed with the addition of Ni [3,9,11,28]. In addition, the surface composition of the synthesized mono and bimetallic catalysts was investigated using EDX analysis. The atomic weight percentage of metals obtained from the analysis was found to be nearly consistent with their intended loading amounts. Table 4.3 summarizes the elemental composition (weight %) of the elements in mono and bimetallic catalysts determined using EDX analysis.

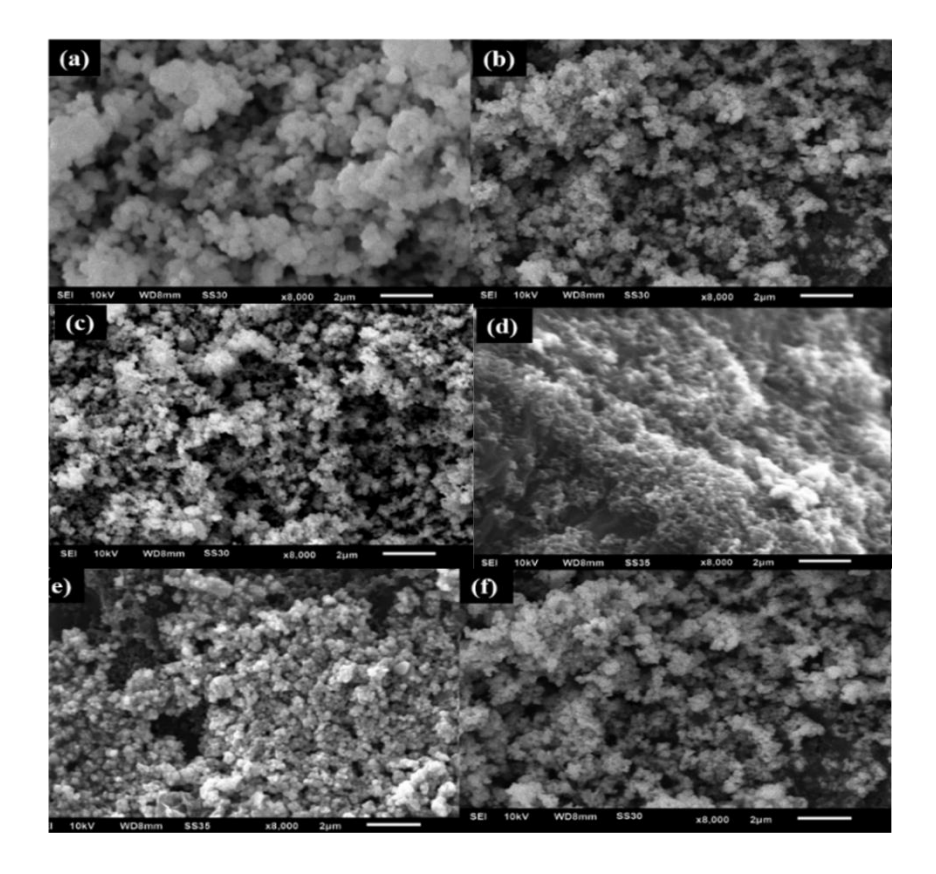


Fig. 4.4 SEM images of (a) 10%Cu/TiO₂, (b) 10%Cu-2.5%Ni/TiO₂, (c) 10%Cu-5%Ni/TiO₂, (d) 10%Cu-10%Ni/TiO₂, (e) 10%Cu-20%Ni/TiO₂, and (f) 10%Ni/TiO₂.

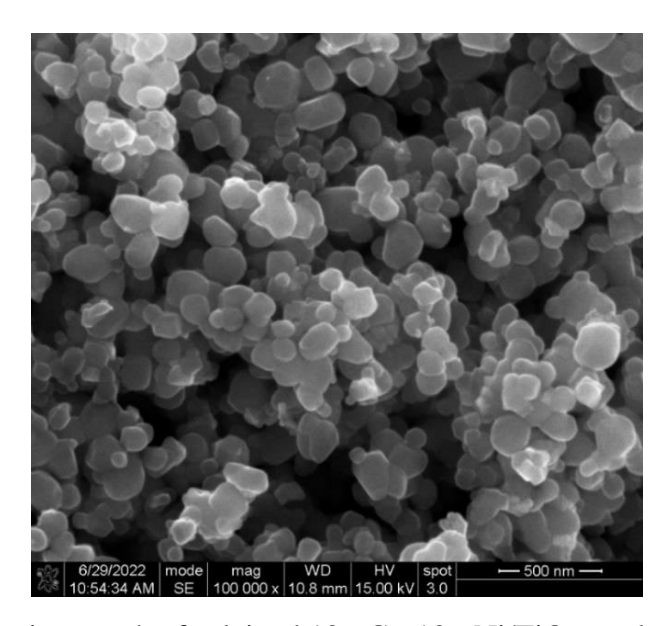


Fig. 4.5 FESEM micrograph of calcined 10%Cu-10%Ni/TiO₂ catalyst.

Table 4.3 Elemental surface composition of the synthesized mono- and bimetallic Cu-Ni catalysts using EDX analysis

	Atom				
Catalyst	Ti	0	Cu	Ni	Cu/Ni
10%Cu/TiO ₂	50.62	36.89	12.49	0	-
10%Cu-2.5%Ni/TiO2	49.2	36.47	11.6	2.72	4.26
10%Cu-5%Ni/TiO2	48.37	36.23	10.30	5.10	2.02
10%Cu-10%Ni/TiO2	44.25	34.95	10.66	10.13	1.05
10%Cu-20%Ni/TiO ₂	34.65	31.97	10.92	22.46	0.48
10%Ni/TiO2	52.17	37.58	0	10.25	-

4.1.4 HRTEM

Fig. 4.6 displays the HRTEM images of 10%Cu-10%Ni/TiO₂ catalyst after reduction. Distinct dark and light colored regions can be observed in the high resolution TEM micrographs which could probably be attributed to metal particles and TiO₂ support, respectively [11,29]. Highly dispersed and small sized metal particles, roughly spherical in shape, were observed in the recorded images (Fig. 6b-d), which is in good agreement with the results of XRD, TPR and SEM analyses that adding Ni enhances the dispersion of Cu species in the bimetallic catalysts. Lattice fringes with d-spacing of about 0.204 nm and 0.35 nm were observed (Fig. 6e), which correspond to the (111) and (011) lattice planes of Cu-Ni alloy and anatase TiO₂, respectively [29,30]. The same was also confirmed from the selected area electron diffraction pattern (SAED), displayed in Fig. 6f. The confirmation of Cu-Ni alloy formation explains the shifting of Ni^0 diffraction peaks towards lower 2θ values observed in the diffractograms of reduced bimetallic catalysts [11]. In order to determine the elemental distribution in the reduced sample, EDS mapping was utilized. Fig. S2 displays the bright field scanning transmission electron microscopy (STEM-BF) and the corresponding elemental maps for Cu, Ni, Ti and O. The elemental map clearly shows that the particles contain Cu and Ni, confirming the formation of Cu-Ni bimetallic alloys. Additionally, the signal corresponding to Ni appeared to be weaker in intensity as compared to that of Cu, which could possibly be pointing to segregation of Cu and Ni and/or enrichment of catalyst surface with Cu, as previously noted by Seemala [8]. Overall, the results of HR-TEM and EDS imaging are consistent with the XRD results and point towards successful formation of bimetallic alloy after reduction.

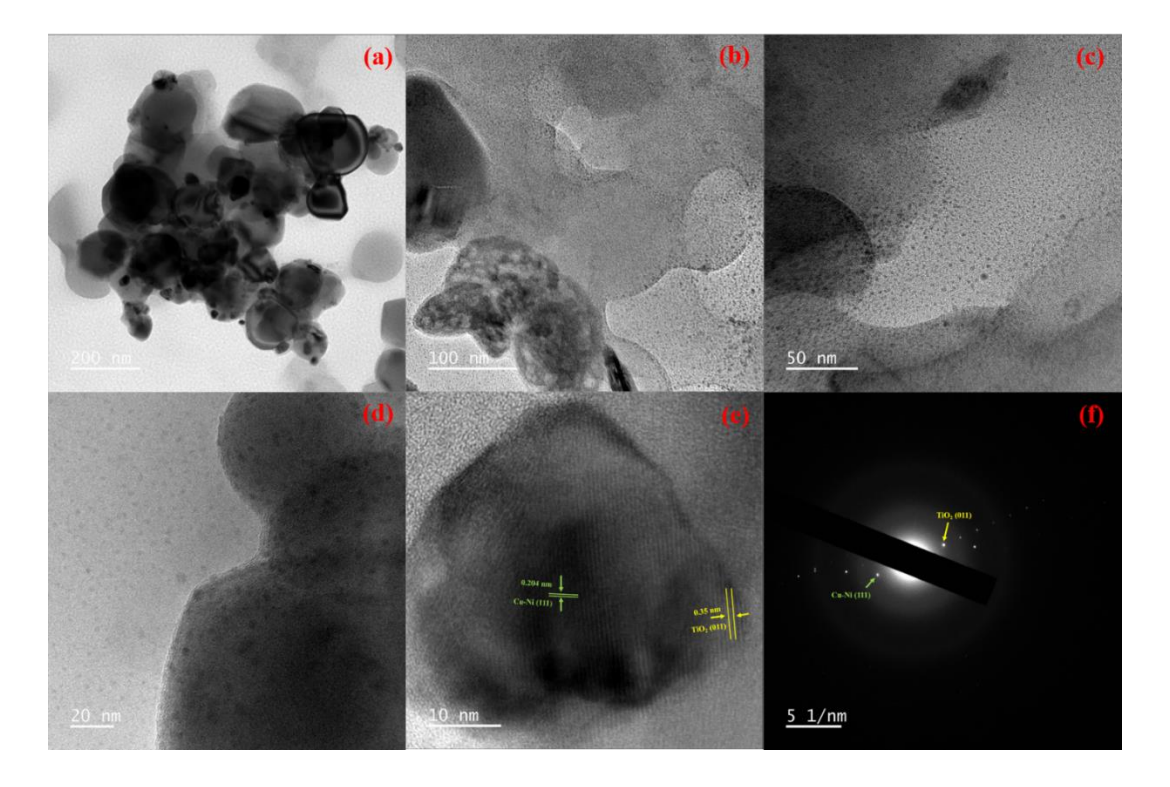


Fig. 4.6 HRTEM images of reduced 10%Cu-10%Ni/TiO₂ catalyst.

4.1.5 N₂ physisorption

Table 1 displays the surface area, pore size, and pore volume of the synthesized mono and bimetallic Cu-Ni catalysts. Among the monometallic catalysts, 10%Ni/TiO₂ catalyst had a higher surface area than its Cu-based counterpart. It also had a larger pore volume and pore size than the monometallic Cu catalyst. It can be ascribed to the fact that the monometallic Ni catalyst had a smaller crystallite size than the Cu catalyst. Adding Ni was observed to have a positive effect on Cu species, and the surface area, pore size, and pore volume for the bimetallic catalysts increased to some extent as the Ni content gradually rose to 20%. The observations are in agreement with the results obtained from XRD analysis and SEM analysis, and therefore, it could be postulated that a strong interaction between Cu and Ni might be responsible for these results. The existence of such interaction can be observed from the reduction in the diffraction peak of CuO and its crystallite size as the Ni loading in the synthesized bimetallic catalysts gradually increased to 20%. As a result, it could be concluded that the addition of Ni

has a positive, stabilizing role on Cu species, preventing its agglomeration and thereby resulting in a slightly increased surface area and porosity [3,12,31].

4.1.6 XPS

Fig. 4.7 displays the XPS spectra of calcined 10%Cu-10%Ni/TiO₂ catalyst. The spectrum for Cu 2p exhibited two major peaks at ~933 eV and 953 eV that can be indexed to Cu 2p_{3/2} and Cu 2p_{1/2} energy levels, respectively, (Fig. 4.7(a)). The deconvolution of the peak at 933 eV revealed a two-peak fit with peaks at 932.5 and 933.8 eV. A similar two-peak fit was observed on the deconvolution of the peak at 953 eV, revealing peaks at 952.2 and 954.2 eV. The peaks observed at 933.6 and 954.2 eV, along with the broad satellite shake-up peaks observed between 938 and 945 eV, and around 964 eV are all characteristic of Cu²⁺ species. [32–34]. Meanwhile, the peaks at 932.5 and 952.2 eV can be ascribed to the presence of reduced Cu⁰ or Cu⁺ species, arising from the reduction of Cu²⁺ species during the analysis [34]. A similar deconvolution of the Ni 2p XPS spectrum yielded four peaks at binding energy values of 853.5, 855.4, 860.8, 863.8 and 872.6 eV (Fig. 4.7(b)). The peaks at 853.5 and 855.4 eV can be ascribed to the doublet for Ni 2p_{3/2} and Ni 2p_{1/2} energy levels, while those at 860.8, 863.8 and 872.6 eV are satellite peaks attributed to Ni²⁺ species [35,36]. These peaks are characteristic of Ni²⁺ species and indicate the NiO on the surface [35,36]. The spectrum of Ti 2p, shown in Fig. 4.7(c), exhibited only two peaks at 458.3 eV and 464.1 eV belonging to the Ti $2p_{3/2}$ and $2p_{1/2}$ energy levels of Ti⁴⁺ species, respectively, thereby confirming the presence of Ti in the form of Ti⁴⁺ species on the catalyst surface [1,34]. The O 1s was also observed to contain only two peaks: an intense peak at 529.5 eV attributed to lattice oxygen (O²-) and a small shoulder at 530.8 eV ascribed to the presence of adsorbed oxygen species [37]. Even though no diffraction peaks corresponding to either Cu₂O or Cu⁰ were observed in the diffractogram of calcined 10%Cu-10%Ni/TiO₂ catalyst, the XPS spectrum of Cu recorded for this catalyst exhibited peaks corresponding to both Cu⁺² and Cu⁺/Cu⁰ species. The existence of peaks belonging to reduced Cu species in the XPS spectrum of unreduced/calcined Cu based catalysts has been reported by a number of reports available in literature and is ascribed to the easy reduction of the Cu⁺² species during XPS analysis [34,38]. However, the intensity of peaks corresponding to the reduced species in this study was noted to be significantly than that of the peaks of Cu⁺² species, signaling the higher concentration of reduced species as compared to the CuO species. The presence of

Cu⁺/Cu⁰ species could possibly be attributed to the fact that the presence of Ni further enhanced the reducibility of Cu. A similar pattern was observed by Li et. al. [38] for the case of Ce doped Cu/TiO₂ catalysts, where they noted that increasing the Ce content led to an increase in the intensity of peaks belonging to Cu⁺ in the Cu 2p spectrum of calcined catalysts. The result of XPS analysis are also consistent with those obtained from XRD, TPR and SEM analyses in this study, all of which suggest an improvement in dispersion and a reduction in crystallite size of Cu with the addition of Ni. The formation of smaller sized Cu particles would not only improve stability against sintering but also provides greater number of active sites [8,10], which in turn would lead to increased activity towards hydrodeoxygenation of furfural to 2-methylfuran. This was observed to be the case by Srivastava et. al. [3] and Seemala et. al. [39] who reported an increase in FFR conversion and 2-MeF selectivity with increased loading of Ni in bimetallic catalysts.

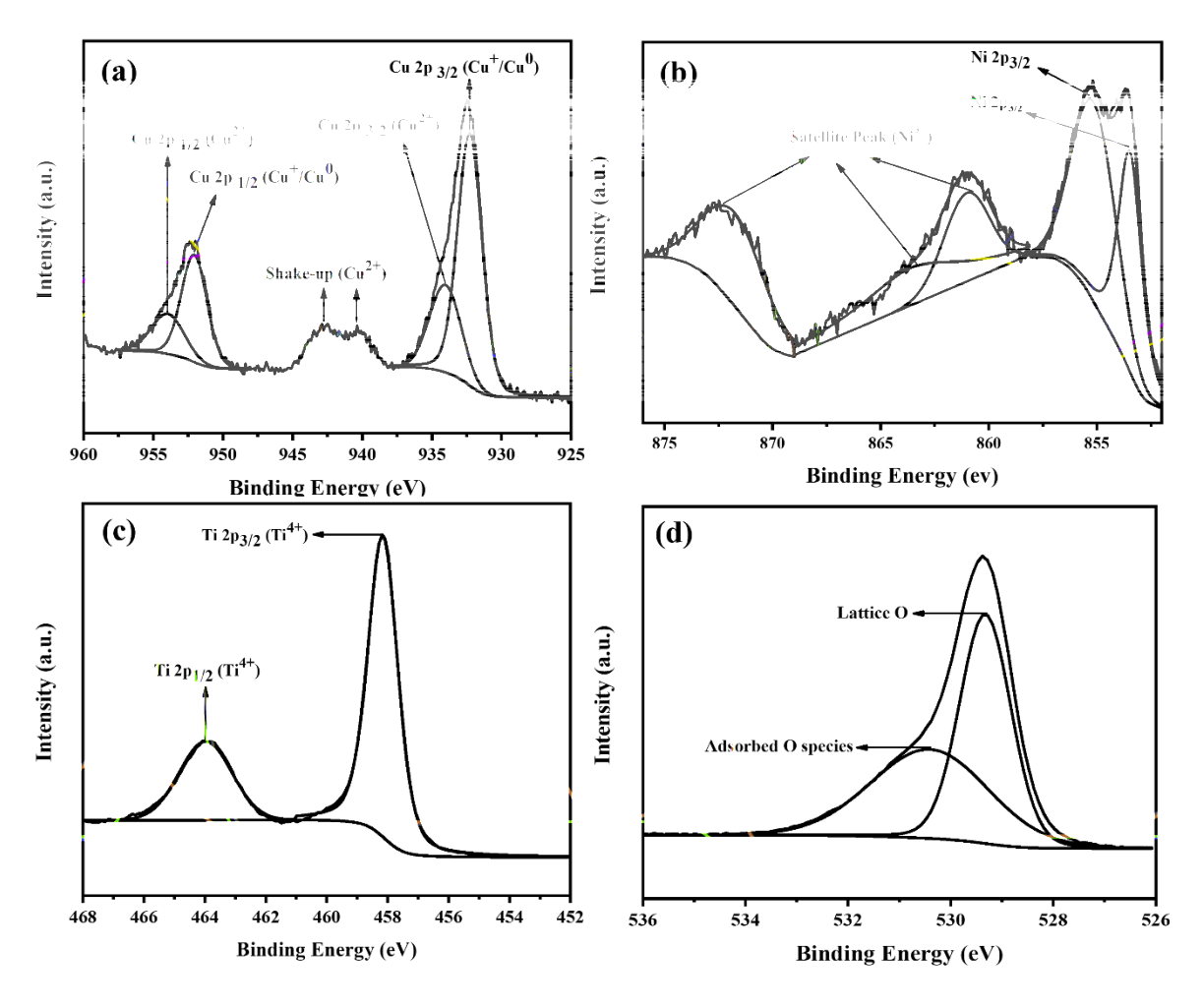


Fig. 4.7 XPS spectra of (a) Cu 2p, (b) Ni 2p, (c) Ti 2p and (d) O 1s of calcined 10%Cu-10%Ni/TiO₂.

In order to further examine the chemical states of the catalyst in the reaction environment, XPS analysis was also carried out for reduced 10%Cu-10%Ni/TiO₂ catalyst, the results of which are shown in Fig. 4.8. The spectrum of Cu 2p exhibited two peaks at binding energy values of 932 eV and 951 eV which correspond to the Cu 2p_{3/2} and Cu 2p_{1/2} energy levels of Cu⁰ species [8,40,41]. No characteristic peaks corresponding to Cu²⁺ species were observed; only a very slight broad hump that corresponds to the shake-up satellite peaks of Cu²⁺ species was noted, though its intensity was much lower than that noted for the calcined sample (Fig. 4.8). Combined with the results obtained from XRD analysis of reduced catalysts, it can be concluded that the oxide phase has a very low concentration and most of the Cu exists in the form of Cu⁰ species. Meanwhile, Ni2p XPS spectrum exhibited multiple peaks belonging to both reduced Ni metal (Ni⁰) as well as Ni²⁺ species. Peaks corresponding to Ni⁰ were observed at binding energy values of 852, 861 and 869.5 eV [8,19,35,41] while those observed at 854.5 and 872 eV belong to the Ni²⁺ species [35,36,41]. The presence of peaks corresponding to oxides phases of Ni points towards the existence of oxide surface layers. The XPS spectrum obtained for Ni is in line with that reported by several studies in literature where Ni has often been observed to be present in both Ni²⁺ as well as Ni⁰ states even after reduction [8,19,35,36,41]. The appearance of peaks corresponding to Cu²⁺ and Ni²⁺ species is due to inevitable partial oxidation resulting from the exposure to air while transferring the sample from the reduction reactor to the XPS chamber.

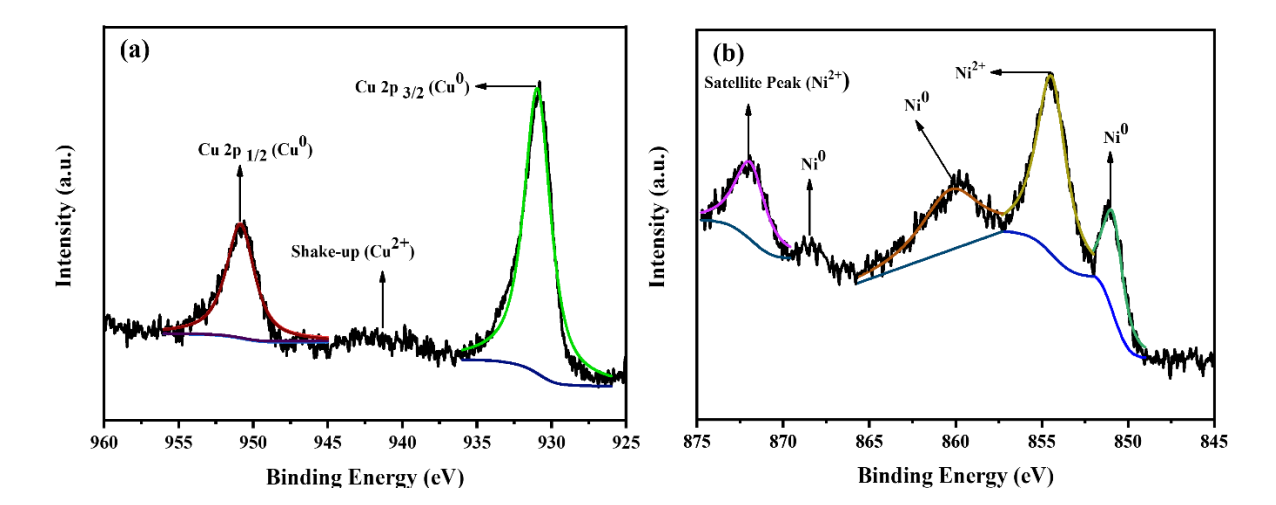


Fig. 4.8 XPS spectra of (a) Cu 2p, and (b) Ni 2p, of reduced 10%Cu-10%Ni/TiO₂.

4.1.7 NH₃-TPD

Fig. 4.9 exhibits the temperature programmed desorption profiles of NH₃ (NH₃-TPD) over 10%Cu/TiO₂, 10%Cu-10%Ni/TiO₂, and 10%Ni/TiO₂. Depending upon the temperature at which NH₃ gets desorbed, a surface acidic site can be decided into three categories: weak (150-350 °C), medium (350-550 °C), and strong (550-850 °C) [35]. Monometallic catalysts and the Cu-Ni bimetallic catalyst exhibited a broad peak between 100 and 200 °C, indicating weak acidic sites. A similar broad but faint peak was observed between 350-500 °C in the desorption profiles of 10%Cu and 10%Cu-10%Ni catalysts, signifying the medium-strength acidic sites. 10%Ni catalyst exhibited a significant sharper peak centered at around 450 °C, indicating that it had a greater number of medium-strength active sites. In addition, the desorption profile of 10%Ni catalyst also exhibited a peak centered at around 610 °C, signifying the strong acidic sites. No such peak was, however, observed for 10%Cu catalyst. It can be seen from the results that while monometallic Cu catalyst exhibited mostly weak acidic sites, its Ni counterpart exhibited medium and strongly acidic sites. The 10%Cu-10%Ni catalyst, like 10%Cu/TiO₂ catalyst, also exhibited weak and medium-strength acidic sites.

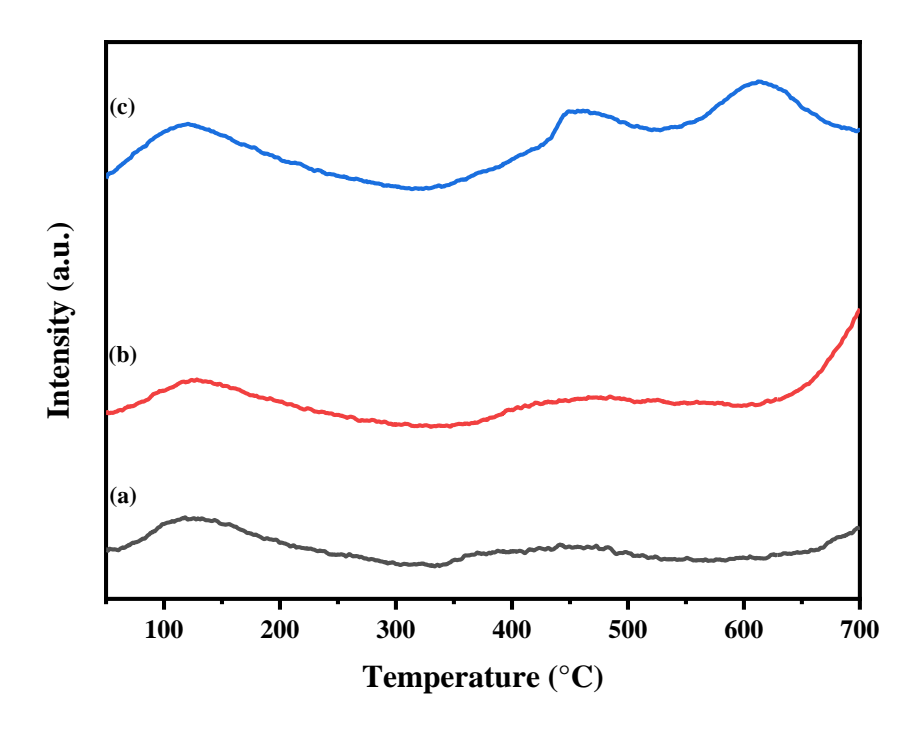


Fig. 4.9 NH₃-TPD profiles of calcined (a) 10%Cu/TiO₂, (b) 10%Cu-10%Ni/TiO₂, and (c) 10%Ni/TiO₂ catalysts.

4.2 Catalytic activity in FFR HDO

4.2.1 Initial catalyst screening

FFR can be hydrogenated to yield a wide variety of valuable products such as FAL, 2-MeF, 2-MeTHF, THFA, furan, CPO, and 1,5-PDO, depending upon the type of catalyst and reaction conditions. FFR HDO to 2-MeF occurs in a sequential manner wherein it first undergoes hydrogenation at the carbonyl moiety to form FAL, which then undergoes hydrogenolysis at the alcohol group to form 2-MeF. However, both FAL and 2-MeF can simultaneously undergo ring hydrogenation, resulting in the formation of THFA and 2-MeTHF, respectively; the latter can also be formed from THFA by the hydrogenolysis of its alcohol group. Besides these, FFR may undergo decarbonylation, resulting in the formation of furan. Therefore, the process requires the use of a catalyst that is capable of interacting, with a high degree of specificity, with the carbonyl moiety of FFR, while minimizing any interaction with the furan ring. In this context, FFR HDO was first carried out over TiO₂-supported monometallic Cu and Ni catalysts and then over the Cu-Ni bimetallic catalysts containing varying Ni contents at 200 °C, an H₂ to FFR molar ratio of 15, and a WHST of 1.15 g_{catalyst} h g_{FFR} -1 (WHSV = 0.87 g_{FFR} h⁻¹ g_{catalyst} -1) to evaluate their catalytic activity and selectivity towards 2-MeF.

4.2.1.1 FFR HDO over monometallic Cu catalyst

Over 10%Cu/TiO₂ catalyst, 2-MeF and FAL were obtained as the major products with selectivity values of 55.2% and 40.2%, respectively and a FFR conversion of 92%. It has previously been reported that FFR interacts with Cu catalysts through the O atom of the carbonyl group via $\eta^I(O)$ binding mode, while its furan ring lies perpendicular to the surface owing to a strong force of repulsion arising from an overlap between the 3d orbital of Cu and the antibonding orbital of the ring (Fig. 4.10) [42–47]. As a result, Cu-based catalysts have been observed to exhibit greater selectivity toward the activation of C=O bond in organic molecules containing both C=C as well as C=O functionalities. In terms of product selectivity, it has been observed that FAL is the major product over these catalysts at low temperatures while 2-MeF is the dominant product at higher temperatures [42–47]. The results obtained here are in good agreement with previously available reports on FFR hydrogenation on supported monometallic Cu catalysts where 2-MeF was observed to be the main product at temperatures \geq 200 °C [3,8,39,48,49]. Other products such as CPO, GVL, and 2-

MeTHF were observed but only in very small amounts. In addition, neither acetone nor any products arising from the etherification of FFR such as furfuryl ethyl ether, furfuryl acetate and/or (2-isopropoxymethyl)furan were observed in the reaction products, signifying that the solvent IPA did not undergo degradation and/or react with FFR under the prevailing reaction conditions.

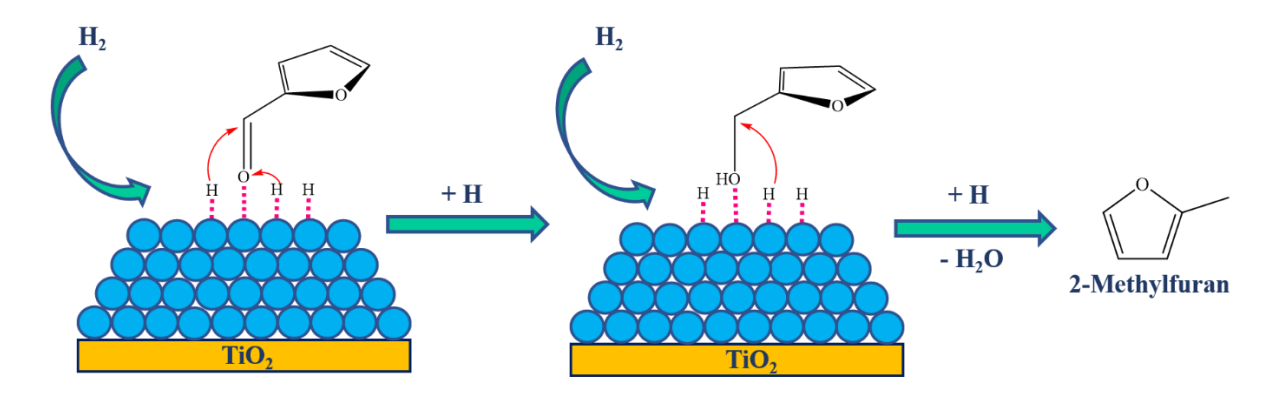


Fig. 4.10 Proposed mechanism of FFR HDO over 10%Cu/TiO₂ catalyst

4.2.1.2 FFR HDO over monometallic Ni catalyst

The product distribution over 10%Ni/TiO₂ catalyst was observed to be markedly different from that of the monometallic Cu catalyst, yielding FAL and furan as the major products with selectivity values of 48.7% and 38.2%, respectively, at an FFR conversion of 95%. Besides FAL and furan, THFA was observed as one of the reaction products with a selectivity value of 4.5%, while the selectivities towards C₄ ring opening products such as butanal and butanol were less than 5%. 2-MeF, the target product, was only observed in very small amounts, with a selectivity value of 2.5%. Similar trends for production distribution were observed by Sitthisa et. al. [50,51] and MacIntosh et. al. [52] for FFR hydrogenation over metal oxide supported monometallic Ni catalysts under similar reaction conditions. To understand the results obtained in the present work, it is important to consider the role of H coverage and the adsorbateadsorbate interactions arising from this coverage on the product distribution over Ni catalysts. It is commonly understood that at a low H coverage, Ni, like other group VIII metals such as Pd, Pt and Ru, interacts with FFR through both the C as well as O atoms of its carbonyl group via a $\eta^2(C,O)$ binding mode, where both the carbonyl group and the furan ring lie parallel to the surface metal atoms [42,46,50,53–56]. This flat adsorption geometry allows Ni catalysts to activate both the C=O bond as well as the C=C bonds of the aromatic ring and, depending upon the reaction temperature, results

in the formation of a variety of products such as FAL, 2-MeF, 2-MeTHF, THFA, pentanediols (1,5-PDO and 1,2-PDO), furan and C₄ ring opening products [42,50,53– 56]. However, FFR HDO reactions are generally carried out in the presence of excess amounts of H₂, with the molar ratio of H₂ to FFR being greater than 10 [47,50,51,57]. Under these conditions, the metal atoms on the catalyst surface are very likely to be saturated with H atoms, resulting in a significant H coverage. As a result, the interactions between the adsorbate molecules adsorbed on these surface atoms can be expected to become influential, particularly at high adsorbate coverages, resulting in a reversal in product selectivity [58,59]. Banerjee et. al. [54] conducted a mechanistic study on FFR hydrogenation over Ni(111) to investigate the various plausible reaction pathways and reported that the product distribution indeed had a large dependence on surface H coverage, which itself was found to be a strong function of reaction temperature. They observed that at low temperatures (227 °C), H adsorbed strongly and spontaneously on Ni surface, resulting in a high H coverage. This resulted in a change in the adsorption geometry of FFR on the Ni from the commonly observed $\eta^2(C,O)$ mode to the bent $\eta^{l}(O)$ binding mode, where it is bonded to Ni atoms through the carbonyl O atom. Under such conditions, reaction pathways for FAL and furan were found to be equally favorable kinetically and, therefore, likely to be the dominant products [54]. The activation barrier for ring saturation was observed to be slightly higher than that for FAL and furan formation pathways; the activation barrier for 2-MeF formation was by far the highest among all pathways. The formation of C₄ ring opening products was also found to be much less favorable kinetically due to higher activation barriers [54]. It was also reported that at temperatures below 227 °C, the reaction pathway for furan formation would become less favorable; on the other hand, THFA would be likely formed in increasingly larger amounts as FAL would adsorb more strongly on Ni surface and undergo ring saturation [54]. Similar results were obtained by Wang et. al. [53] in the mechanistic investigation of FFR HDO over Pd(111) in excess of H₂, wherein they reported a reversal of selectivity from furan towards FAL at high coverage of H and FFR itself. Fig. 4.11 displays the proposed reaction mechanism over 10%Ni/TiO₂ catalyst.

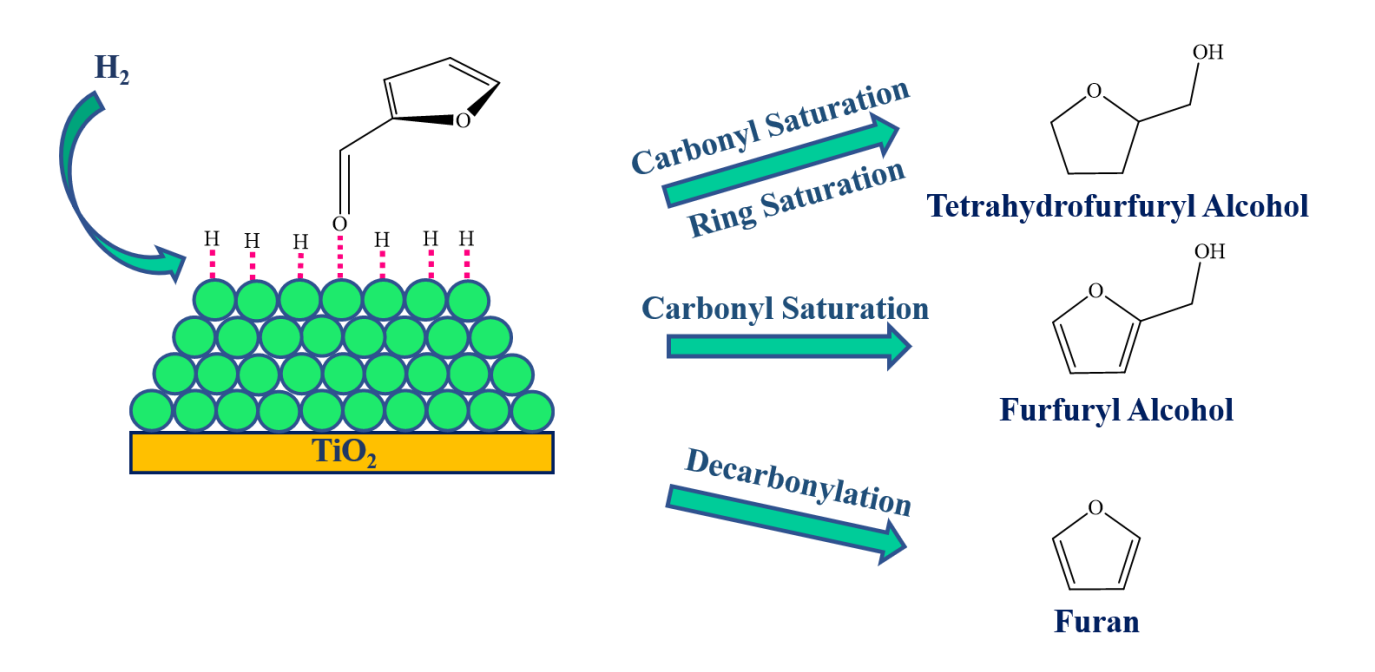


Fig. 4.11 Proposed mechanism of FFR HDO over 10%Ni@TiO2 catalyst.

4.2.1.3 FFR HDO over bimetallic Cu-Ni catalysts

To evaluate the effect of Ni addition on FFR conversion and 2-MeF selectivity, the Ni content in bimetallic Cu-Ni catalyst varied from 2.5 wt.% to 20 wt.%, while the Cu content was kept fixed at 10 wt.% (Fig. 4.12). Even at a low loading of 2.5%, the addition of Ni resulted in a Cu-Ni bimetallic catalyst that yielded higher FFR conversion and 2-MeF selectivity than those obtained with the monometallic Cu catalyst, with conversion increased from 92% to 97.1% and 2-MeF selectivity raise from 55.2% to 68.7%. The selectivity towards FAL, on the other hand, witnessed a decline from 40.2% to 25.7%. In addition, ring saturation products such as 2-MeTHF and THFA were observed in small amounts, while furan and C₄ ring opening products such as butanal and butanol were observed in trace amounts. However, the combined selectivity towards the by-products remained low (3.2%). A further increase in Ni content of the bimetallic catalyst to 5% resulted in a similar increase in FFR conversion and 2-MeF selectivity to 98.7%, and 78.7%, respectively; meanwhile, FAL selectivity fell sharply from 26.2% to 11.5%. The increased Ni content also led to an increased selectivity towards by-products, the most notable among them being 2-MeTHF and THFA, whose selectivities were observed to be 3.5% and 1.5%, respectively, and the overall selectivity towards all the by-products rose to 7%. Increasing the Ni content to 10% led to only a tiny increase in FFR conversion to 100%; 2-MeF selectivity also rose only by a relatively small amount than previous loadings to 84.5%, while FAL selectivity reduced to 1%. The presence of Ni in such amounts accelerated the formation of by-products, with selectivity towards 2-MeTHF raise sharply to 9% and that of THFA rising to 2.5%. Selectivity towards furan and C₄ and C₅ ring opening products such as butanal, butanol, 2-pentanone (2-PON), 2-pentanol (2-POL), and methyl isobutyl ketone remained low (~2%) even as the Ni content increased from 2.5% to 10%. Further increasing the Ni content to 20% did not produce any appreciable change in FFR conversion. However, the selectivity towards 2-MeF witnessed a significant decline, falling to 66.2%, while that of 2-MeTHF and THFA increased to 19% and 4.5%, respectively. Besides these, selectivities of other side products were also observed to have increased. Interestingly, FAL selectivity was also observed to have risen to 2.9%. Also, neither any of the products possible from FFR etherification nor acetone, a possible product of IPA decomposition, were observed in the reaction products for any of the bimetallic compositions, ruling out the degradation of IPA.

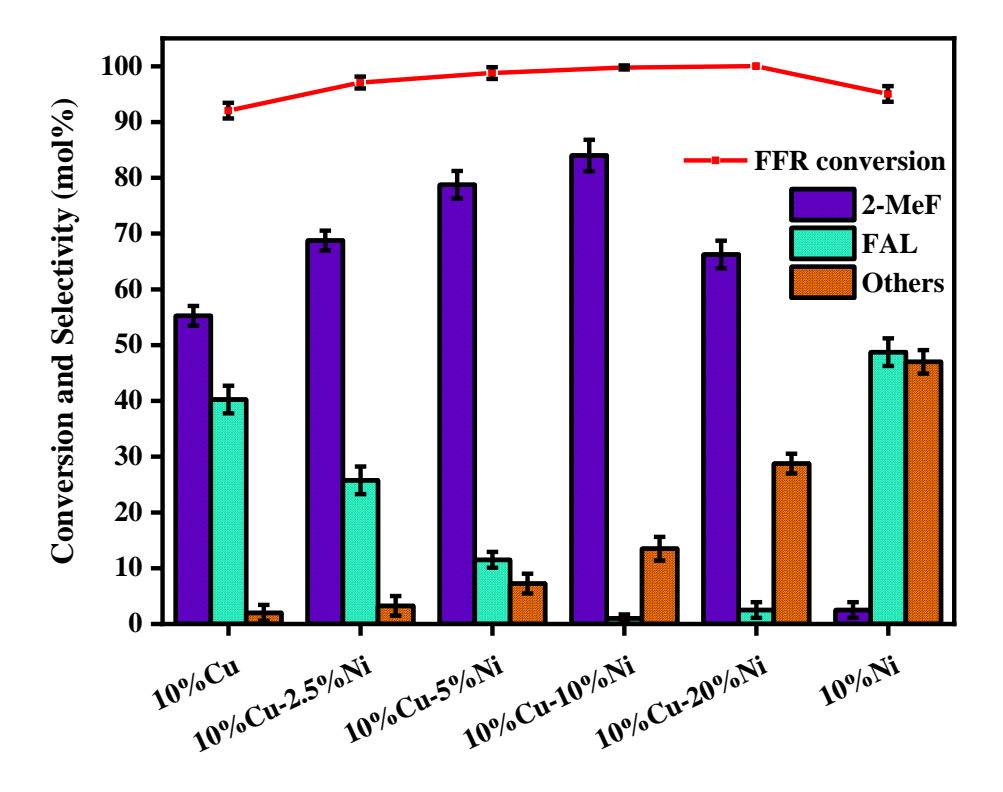


Fig. 4.12 Conversion and product selectivities over TiO_2 supported mono- and bimetallic Cu-Ni catalysts. Reaction conditions: Feed flowrate = 9.05 mmol_{FFR} h⁻¹, H_2/FFR ratio = 15, Temp. = 200 °C, WHSV = 0.87 g_{FFR} h⁻¹ g_{catalayst}⁻¹, Pressure = 1 atm.

4.2.1.4 Probable Reaction Mechanism

From the above discussion, it is clear that the bimetallic Cu-Ni catalysts exhibited higher selectivity towards 2-MeF than monometallic Cu catalyst. Such a remarkable

change in the product selectivity over those observed for Cu catalyst can be explained by the structural changes brought about by Ni addition. Detailed characterization analyses revealed that the monometallic Cu catalyst exhibited poorer CuO dispersion and larger crystallite size than the bimetallic catalysts. The increased dispersion and reduced crystallite sizes of CuO in bimetallic catalysts can be attributed to the stronger interactions between the CuO and NiO species as the Ni content was increased. Furthermore, the reduction temperature of the resulting bimetallic catalysts was observed to have shifted to lower temperatures, and the surface area and porosity increased with increasing Ni content. The Cu catalysts, while being selective towards C=O bond activation, possess low activity towards hydrogenolysis of C-O bond due to lower H₂ activation and/or dissociation activity and (ii) much stronger interactions with FFR and H₂ than FAL. As a result, they require higher reaction temperatures to carry out the hydrogenolysis of the C-O bond of FAL to yield 2-MeF. By combining Cu with more reactive metals possessing greater activity towards H₂ activation and dissociation such as Ni, Pd, Pt etc. to form Cu-M bimetallic catalysts can help achieve the desired balance between catalytic activity and target product selectivity by a combination of electronic and structural modifications [8,39,42,46]. In such bimetallic combinations, the second metal, most often a noble or transition metal, acts as a promoter through a phenomenon called spillover [46,60], wherein it activates and dissociates H₂, which then diffuses/migrates to the nearby Cu atom and reacts with the adsorbed reactant [23,46,61–64]. Interestingly, for the case of C-Ni bimetallic combinations supported on metal oxides, various studies available in literature by Seemala et. al. [8,39], Alstrup et. al. [65], Brongersma et. al. [66], Kitla et. al. [67] and Yao et. al. [68] over metal oxide supported Cu-Ni bimetallic catalysts point significant towards enrichment/segregation of Cu on the surface of these catalysts due to the strong interactions between the Ni atoms and the metal oxide supports [69]. The strong metalsupport interactions result in the movement of Ni atoms to the support interface and that of Cu atoms to the surface, thereby resulting in the segregation of the two metals. Given the known interactions between certain metals and reducible metal oxide supports such as TiO₂ [69], such a segregation of metals in reducible metal oxide supported bimetallic catalysts could in fact, be quite general.

As a result, the observed enhancement in selectivity towards 2-MeF on Ni addition could be attributed to a combination of factors: better Cu dispersion and

smaller crystallite size, and increased reducibility of the bimetallic catalysts, as well as H_2 spillover and possible segregation of Cu and Ni atoms (Fig. 4.13). Such a segregation of Cu and Ni, if possible, would yield a bimetallic catalyst with Cu rich surface domains that would provide the required specificity towards the target compound (2-MeF) by selectively interacting with FFR in the $\eta^I(O)$ mode. The Ni atoms, present in lower concentrations on the surface as isolated domains, would be responsible for supplying the required hydrogen by acting as sites for H_2 activation and dissociation, which then moves on to the Cu atoms for hydrogenation and HDO [8,39]. Due to the lower surface concentration of Ni atoms under such conditions, the interaction between them and FFR molecules will be minimal, which in turn would limit the formation of by-products. Moreover, the increased dispersion, reducibility, and decreased crystallite size of Cu species would provide an additional boost through increased C-O hydrogenolysis rates [3].

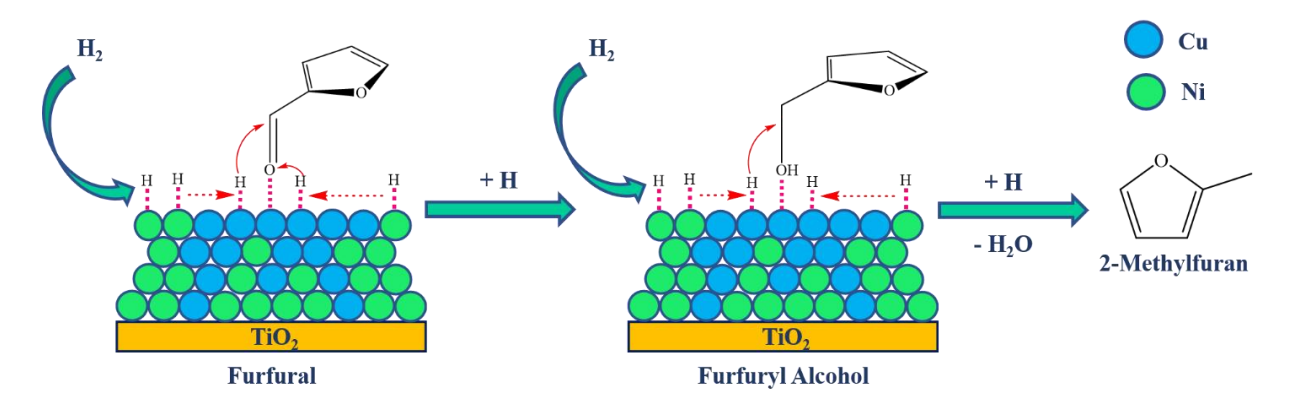


Fig. 4.13 Proposed mechanism of FFR HDO over bimetallic Cu-Ni/TiO₂ catalyst

4.2.2 Effect of reaction conditions on FFR HDO over 10%Cu-10%Ni@TiO2 catalyst

In the initial screening of the synthesized catalysts, 10%Cu-10%Ni/TiO₂ catalyst was observed to display the highest selectivity towards 2-MeF selectivity among the synthesized monometallic Cu and Ni catalysts as well as the Cu-Ni bimetallic ones with different Ni contents under the initial reaction conditions. As a result, it was selected for further investigations on the effect of reaction parameters on target product selectivity.

4.2.2.1 Effect of reaction temperature

Fig. 4.14 displays the results obtained for the influence of reaction temperature on 2-MeF selectivity over 10%Cu-10%Ni/TiO₂ catalyst. When the reaction temperature was 175 °C, FAL and THFA were observed in significant amounts, with their selectivities of 20.8% and 11%, respectively. 2-MeF selectivity was a moderate 59.5%, and the selectivity towards 2-MeTHF was quite low at 4.7%. Reducing the temperature from 200 °C to 175 °C resulted in a small decline in FFR conversion from 100% to 91%, while the 2-MeF selectivity witnessed a steep fall from 84.5% to 59.5%. As the reaction temperature was increased to 200 °C, FFR conversion increased from 91% to 100%, while 2-MeF selectivity increased to 84.5%. Simultaneously, an increase in 2-MeTHF selectivity (9%) and a reduction in those towards FAL and THFA 1 and 2.5%, respectively, were observed. The sizeable FAL and THFA selectivities and moderate 2-MeF selectivity at 175 °C may be ascribed to the fact that at such low temperatures, Cu-based catalysts have considerable activity towards the hydrogenation of C=O bond than the hydrogenolysis of C-O bond, as a result of which FAL was formed as the major product, and 2-MeF selectivity witnessed a fall [40,43,44]. Under similar conditions, Ni-based catalysts have been reported to be active towards the hydrogenation of both the C=O bond and the C=C bonds of the furan ring, yielding THFA as the major product with FAL as the minor product [54,70]. As a result, the domains of Ni atoms present on the surface and in contact with FFR are most likely to hydrogenate its C=O bond and convert it to FAL, which would then itself undergo ring hydrogenation to form THFA, thereby explaining the formation THFA in substantial amounts in the products. Therefore, the optimum value of 2-MeF selectivity observed at 200 °C can possibly be attributed to the increased rates of C-O bond hydrogenolysis of FAL and decreased favorability of the saturation of its furan ring at higher temperatures [40,43,44,54,70]. However, on further increasing the reaction temperature above 200 °C, FFR conversion remained constant at 100%; 2-MeF selectivity, on the other hand, dropped substantially to 68.5% and 42.7% as the temperature was raised to 225 °C and 250 °C, respectively. A similar reduction was observed in the selectivities of FAL, THFA, and 2-MeTHF, with their values dropping to 0.3%, 0.5% and 3.5% as the temperature reached 250 °C. Simultaneously, 2-PON and 2-POL, ring opening products formed by 2-MeF hydrogenolysis, were observed to have been formed in large amounts, with their selectivity values reaching 36% and 6%, respectively at 250 °C. In addition, butanal and butanol, two C₄ ring opening products, were also formed in significant amounts, with their combined selectivity reaching ~7% at 250 °C. The observed reduction in 2-MeF selectivity and enhancement in the formation of C₄ and C₅ ring opening products could be attributed to the fact that at high reaction temperatures, Cu becomes highly active toward C-O bond hydrogenolysis, boosting 2-MeF formation and reducing FAL selectivity [40,42,71]. This enhancement in target product selectivity at increasingly higher temperatures is accompanied by its over-hydrogenolysis to C₅ ring opening products such as 2-PON, 2-POL, and 1-POL [40,42,71]. As a result, the selectivity of 2-MeF decreased and the above-mentioned ring opening products selectivity increased [40,42,71]. Ni catalysts are also known to exhibit a somewhat similar trend in product selectivities, wherein at high temperatures, they favor decarbonylation and ring opening over the hydrogenation of C=O and C=C bonds, thereby resulting in the formation of furan, butanal, butanol and butane [40,42,50,51,54,55].

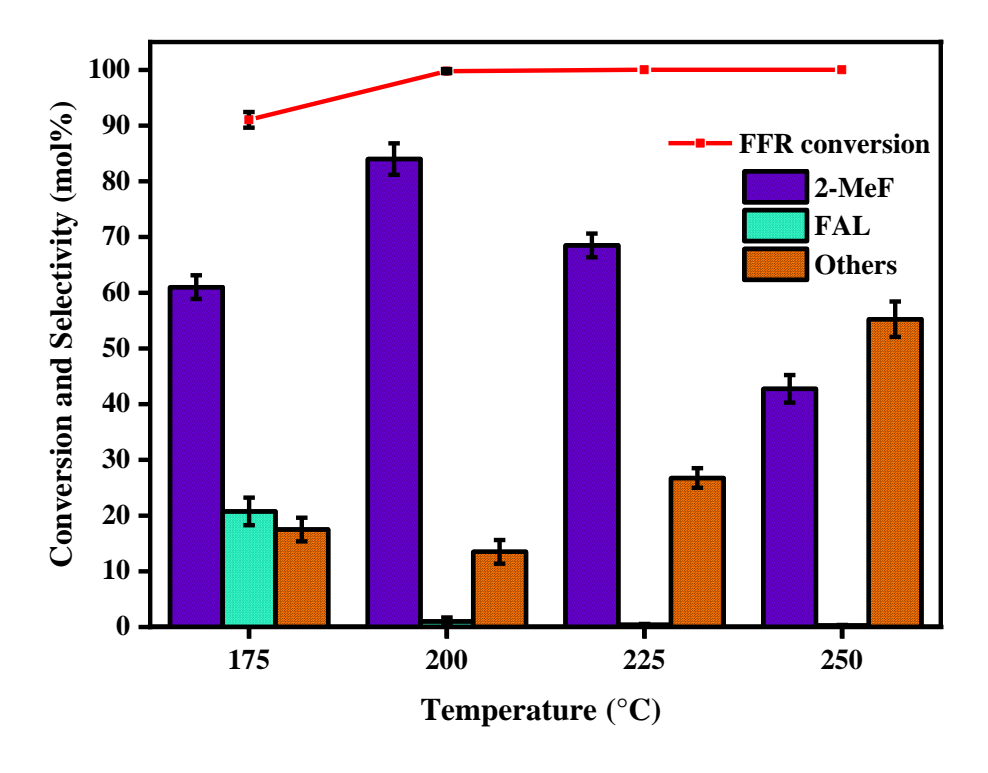


Fig. 4.14 Effect of reaction temperature on FFR HDO over 10% Cu-10% Ni/TiO₂ catalysts. Reaction conditions: Feed flowrate = 9.05 mmol_{FFR} h⁻¹, H₂/FFR ratio = 15, WHSV = 0.87 g_{FFR} h⁻¹ g_{catalayst}⁻¹, Pressure = 1 atm.

4.2.2.2 Effect of WHSV

Fig. 4.15 displays the results obtained for the influence of WHSV on 2-MeF selectivity over 10%Cu-10%Ni/TiO₂ catalyst at 200 °C. An optimum 2-MeF selectivity of 84.5% was observed at a temperature of 200 °C and WHSV value of 0.87 g_{FFR} h⁻¹ g_{catalayst}⁻¹. In

order to study the effect of contact time on product distribution, WHSV varied from 0.58 to 1.74 g_{FFR} h⁻¹ g_{catalayst}⁻¹. Reducing the WHSV to 0.58 g_{FFR} h⁻¹ g_{catalayst}⁻¹, did not bring about any change in FFR conversion, which remained fixed at 100%; however, the selectivity of 2-MeF was observed to have fallen to 76%. A similar reduction in FAL selectivity was also noted, which decreased to around 0.5%. 2-MeTHF selectivity, meanwhile, jumped to nearly 17%, and that of THFA fell slightly to 1.5%. A small increase was also observed in the selectivities of 2-PON and 2-POL; however, no change was observed in the selectivities of furan or C₄ ring opening products. The reduction in 2-MeF and THFA selectivity could be explained by the fact that reducing the WHSV brings about an increase in the contact time, allowing the reactant and the products to remain in contact with the catalyst for a longer period. The increased contact time allowed them to further undergo ring hydrogenation and hydrogenolysis reactions, respectively, thereby yielding 2-MeTHF in large amounts. In addition, it is possible that under such conditions, 2-MeF underwent further hydrogenolysis reaction, which explains the slightly increased formation of 2-PON and 2-POL. A similar trend was observed for 2-MeF selectivity when the WHSV was increased from 0.87 to 1.74 g_{FFR} h⁻¹ g_{catalayst}⁻¹, with the 2-MeF selectivity falling to 72%. The selectivities of 2-MeTHF and THFA also witnessed a fall, dropping to ~4 and 1 %, respectively, as the WHSV was doubled. On the other hand, FAL selectivity was observed to have increased significantly to 18.5%, which could be attributed to the fact that with the reduction in contact time, FAL did not get enough time to undergo further conversion to 2-MeF or THFA. It can therefore be concluded that longer residence times favor the formation of 2-MeF by allowing sufficient time for FAL to undergo hydrogenolysis. However, at longer residence times, there exists a possibility of 2-MeF undergoing ring hydrogenation, as evidenced by the increased 2-MeTHF selectivity at larger contact times.

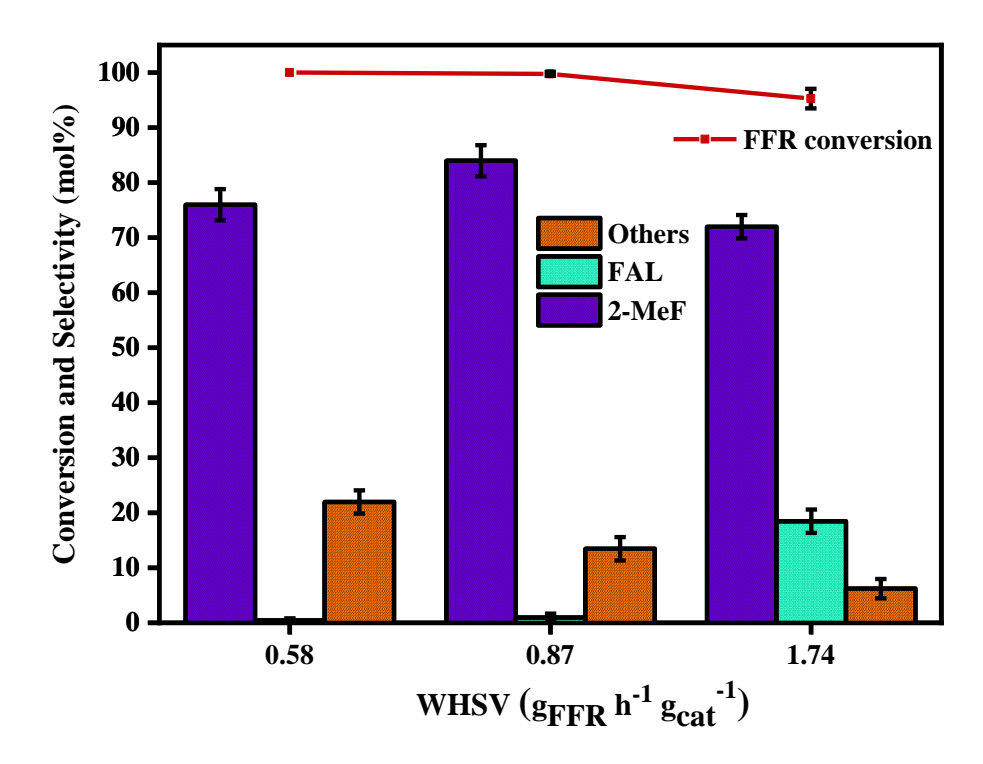


Fig. 4.15 Effect of WHSV on FFR HDO over 10%Cu-10%Ni/TiO₂ catalysts. Reaction conditions: Feed flowrate = 9.05 mmol_{FFR} h⁻¹, H₂/FFR ratio = 15, Temp. = 200 °C, Pressure = 1 atm.

4.2.3 Evaluating the possibility of CTH

Traditionally, hydrogenation and HDO processes at both bench and industrial scales have been carried out using molecular H₂ due to its widespread availability and easy activation on the surfaces of metal-based catalysts [72–74]. However, current hydrogen production processes almost entirely utilize fossil fuels such as natural gas and coal as feedstocks [75], which can threaten the sustainability of biofuels production from biomass-derived platforms such as FFR and HMF. As a result, in the past few decades, catalytic transfer hydrogenation (CTH) has been increasingly seen as an efficient and sustainable alternative strategy for the selective hydrogenation and HDO of biomass-derived furanic compounds. In this process, simple organic molecules such as formic acid and alcohols such as methanol, IPA etc. serve as H donors, donating the H₂ required for the hydrogenation and/or HDO process. The hydrogenation ability of these donors is markedly lower than that of molecular H₂, granting better control over the selective hydrogenation and/or HDO of organic compounds such as FFR and HMF that contain multiple functional groups [72–74]. Furthermore, using organic compounds as H donors would prove advantageous in alleviating the safety hazard posed by the use

of high-pressure H₂ in most bench scales and lowering the overall cost and complexity of the process [72–74].

In this context, it was considered worthwhile to evaluate the possibility of carrying out the selective FFR HDO to 2-MeF using an H donor instead of molecular H₂ at the optimized reaction conditions (200 °C and 0.87 g_{FFR} h⁻¹ g_{catalayst}⁻¹) over 10%Cu-10%Ni/TiO2 catalyst as it exhibited the highest selectivity towards target compound. For this purpose, a set of experiment was carried out by using IPA as the H donor; the feed composition was similar to that used for the sets of experiments carried out in the previous sections, wherein the feed mixture consisted of 5% (v/v) FFR dissolved in IPA. Before the CTH reaction, the catalyst was first reduced in H₂ flow as done previously for experimental runs carried out with molecular H₂, following which it was then cooled down to the reaction temperature. Simultaneously, the gas flow was switched from H₂ to N₂ while the catalyst was being cooled down to the desired temperature and the whole system was purged with N₂ at a flow rate of 200 mL min⁻¹. Once the reaction temperature (200 °C) was achieved, N₂ flow was set to 50 mL min⁻¹. The analysis of the liquid products collected revealed that the FFR conversion was fairly consistent at ~22% throughout the time period of the CTH study (Fig. 4.16). With regard to the product distribution, FAL was observed to be the major product, with a selectivity of ~95%. 2-MeF selectivity was observed to be constant at ~2% during the course of reaction. By-products such as 2-MeTHF and THFA were observed in trace amounts, while ring opening products such as 2-PON and 2-POL were not observed at all. The obtained results are in good agreement with the observations made by Grazia et. al. [76], who reported an FFR conversion of around 20% and a 100% selectivity towards FAL at 200 °C in the vapor phase HDO of FFR to 2-MeF over MgO catalysts using methanol as the H donor. Similarly, in an investigation of the vapor phase CTH of levulinic acid (LAc) to γ-valerolactone (GVL) over Cu@SiO₂ catalyst with formic acid as the H donor, Lomate et. al.[33] noted that only 14% of the LAc fed could be converted at a temperature of 200 °C. The poor FFR conversion observed for the case of CTH in the present study. Moreover, it can be ascribed to the fact that the dehydrogenation of alcohols such as IPA is not thermodynamically favorable at low temperatures, limiting the production of H₂. With increasing temperature, the Gibbs free energy ΔG becomes increasingly less positive, becoming negative at temperatures above ~229 °C for IPA [33]. Grazia et. al. [76] noted a similar trend in FFR conversion,

wherein they noted that both FFR conversion and 2-MeF selectivity increased rapidly as the reaction temperature was increased above 250 °C. Therefore, it can be concluded that CTH with common organic donors is not an efficient strategy for carrying out the hydrogenation or HDO of organic compounds such as FFR at low reaction temperatures, since at such temperatures, the dehydrogenation of these donors is not favorable. It is necessary to use higher temperatures if high conversions and target product selectivities are desired.

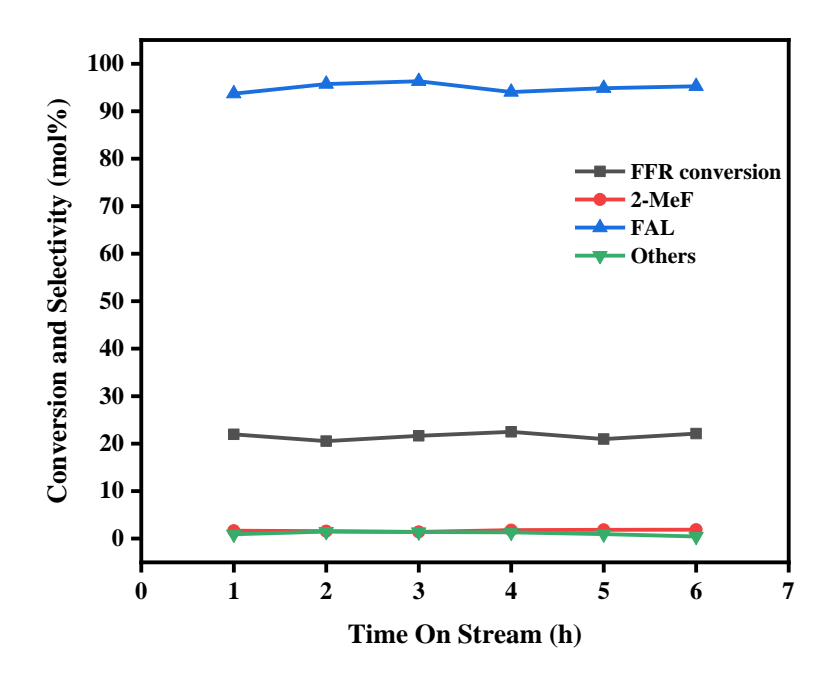


Fig. 4.16 FFR HDO over 10% Cu-10% Ni/TiO₂ catalysts through CTH using IPA as the H donor. Reaction conditions: Feed flowrate = 9.05 mmol_{FFR} h⁻¹, IPA/FFR ratio = 20, Temp. = 200 °C, WHSV = 0.87 g_{FFR} h⁻¹ g_{catalayst} ⁻¹, Pressure = 1 atm.

4.2.4 Catalyst Stability

Fig. 4.17 displays the results from the catalytic stability test over 10%Cu-10%Ni@TiO₂ catalyst for FFR HDO. The catalyst exhibited an FFR conversion close to 100% for 9 h, following which a slight reduction in conversion was observed. As a result, at the end of 15 h FFR conversion was observed to have dropped to 94%. In the context of products, the catalyst selectivity towards 2-MeF was nearly constant at 85% up to 12 h, after which it decreased and dropped to 72% at the end of 15 h. A similar decreasing trend in selectivity was also observed for 2-MeTHF, a ring saturation product of 2-MeF, wherein its selectivity hovered around 8.5% for the first 6 h and then steadily decreased to 1.5% at the end of the stability test. The selectivity towards FAL was low in the initial 6 h (~1%); however, as the time progressed and the catalyst began undergoing

deactivation, its selectivity began rising gradually and reached a value of 22% at the end of this study. The observed reduction in 2-MeF selectivity and the corresponding rise in that of FAL could be attributed to the progressive deactivation suffered by the catalyst along the TOS study, which diminishes the hydrogenation activity of its active sites, which in turn reduces their ability to carry out the hydrogenolysis of C-O bond of FAL to 2-MeF.

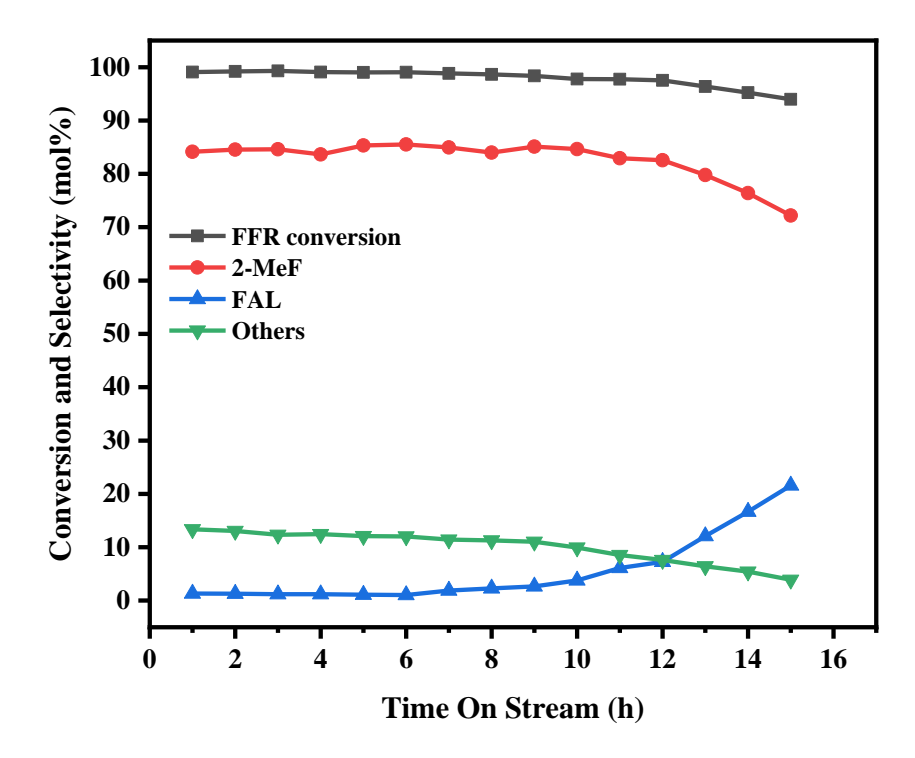


Fig. 4.17 Time-on-stream (TOS) study on FFR HDO over 10% Cu-10% Ni/TiO₂ catalysts. Reaction conditions: Feed flowrate = 9.05 mmol_{FFR} h⁻¹, H₂/FFR ratio = 15, Temp. = 200 °C, WHSV = 0.87 g_{FFR} h⁻¹ g_{catalayst} ⁻¹, Pressure = 1 atm.

References

- [1] M.A. Mannaa, K.F. Qasim, F.T. Alshorifi, S.M. El-Bahy, R.S. Salama, Role of NiO Nanoparticles in Enhancing Structure Properties of TiO2 and Its Applications in Photodegradation and Hydrogen Evolution, ACS Omega. 6 (2021) 30386–30400. https://doi.org/10.1021/acsomega.1c03693.
- [2] J.H. Lin, P. Biswas, V. V. Guliants, S. Misture, Hydrogen production by water-gas shift reaction over bimetallic Cu-Ni catalysts supported on La-doped mesoporous ceria, Appl. Catal. A Gen. 387 (2010) 87–94. https://doi.org/10.1016/j.apcata.2010.08.003.
- [3] S. Srivastava, G.C. Jadeja, J. Parikh, Synergism studies on alumina-supported coppernickel catalysts towards furfural and 5-hydroxymethylfurfural hydrogenation, J. Mol. Catal. A Chem. 426 (2017) 244–256. https://doi.org/10.1016/j.molcata.2016.11.023.
- [4] J. Tian, H. Gao, H. Deng, L. Sun, H. Kong, P. Yang, J. Chu, Structural, magnetic and optical properties of Ni-doped TiO2 thin films deposited on silicon(100) substrates by sol-gel process, J. Alloys Compd. 581 (2013) 318–323. https://doi.org/10.1016/j.jallcom.2013.07.105.
- [5] A. Barmeh, M.R. Nilforoushan, S. Otroj, Wetting and photocatalytic properties of Nidoped TiO2 coating on glazed ceramic tiles under visible light, Thin Solid Films. 666 (2018) 137–142. https://doi.org/10.1016/j.tsf.2018.09.007.
- [6] K. Karthik, S.K. Pandian, N.V. Jaya, Effect of nickel doping on structural, optical and electrical properties of TiO 2 nanoparticles by sol-gel method, Appl. Surf. Sci. 256 (2010) 6829–6833. https://doi.org/10.1016/j.apsusc.2010.04.096.
- [7] Y. Huang, W. Ho, Z. Ai, X. Song, L. Zhang, S. Lee, Aerosol-assisted flow synthesis of B-doped, Ni-doped and B-Ni-codoped TiO2 solid and hollow microspheres for photocatalytic removal of NO, Appl. Catal. B Environ. 89 (2009) 398–405. https://doi.org/10.1016/j.apcatb.2008.12.020.
- [8] B. Seemala, C.M. Cai, C.E. Wyman, P. Christopher, Support Induced Control of Surface Composition in Cu-Ni/TiO2 Catalysts Enables High Yield Co-Conversion of HMF and Furfural to Methylated Furans, ACS Catal. 7 (2017) 4070–4082. https://doi.org/10.1021/acscatal.7b01095.
- [9] T. Lu, Z. Du, J. Liu, C. Chen, J. Xu, Dehydrogenation of primary aliphatic alcohols to aldehydes over Cu-Ni bimetallic catalysts, Cuihua Xuebao/Chinese J. Catal. 35 (2014) 1911–1916. https://doi.org/10.1016/S1872-2067(14)60208-4.
- [10] X. Wang, X. Pan, R. Lin, S. Kou, W. Zou, J.X. Ma, Steam reforming of dimethyl ether over Cu-Ni/γ-Al2O3 bi-functional catalyst prepared by deposition-precipitation method, Int. J. Hydrogen Energy. 35 (2010) 4060–4068. https://doi.org/10.1016/j.ijhydene.2010.01.142.
- [11] F. Chen, Y. Tao, H. Ling, C. Zhou, Z. Liu, J. Huang, A. Yu, Ni-Cu bimetallic catalysts on Yttria-stabilized zirconia for hydrogen production from ethanol steam reforming, Fuel. 280 (2020) 118612. https://doi.org/10.1016/j.fuel.2020.118612.
- [12] A. Yin, C. Wen, X. Guo, W.L. Dai, K. Fan, Influence of Ni species on the structural evolution of Cu/SiO2 catalyst for the chemoselective hydrogenation of dimethyl oxalate, J. Catal. 280 (2011) 77–88. https://doi.org/10.1016/j.jcat.2011.03.006.
- [13] F. Boccuzzi, A. Chiorino, G. Martra, M. Gargano, N. Ravasio, B. Carrozzini, Preparation, characterization, and activity of Cu/TiO2 catalysts: I. Influence of the preparation method on the dispersion of copper in Cu/TiO2, J. Catal. 165 (1997) 129–139. https://doi.org/10.1006/jcat.1997.1475.

- [14] Z. Wang, D. Brouri, S. Casale, L. Delannoy, C. Louis, Exploration of the preparation of Cu/TiO2 catalysts by deposition-precipitation with urea for selective hydrogenation of unsaturated hydrocarbons, J. Catal. 340 (2016) 95–106. https://doi.org/10.1016/j.jcat.2016.05.011.
- [15] L.S. Yoong, F.K. Chong, B.K. Dutta, Development of copper-doped TiO2 photocatalyst for hydrogen production under visible light, Energy. 34 (2009) 1652–1661. https://doi.org/10.1016/j.energy.2009.07.024.
- [16] N. Riaz, F.K. Chong, B.K. Dutta, Z.B. Man, M.S. Khan, E. Nurlaela, Photodegradation of Orange II under visible light using Cu-Ni/TiO 2: Effect of calcination temperature, Chem. Eng. J. 185–186 (2012) 108–119. https://doi.org/10.1016/j.cej.2012.01.052.
- [17] Y. Qian-Gu, L. Chun-Rong, W. Wei-Zheng, Y. Le-Fu, W. Hui-Lin, W. Ting-Hua, Activation of Methane over Ni/TiO₂ Catalyst, Acta Physico-Chimica Sin. 17 (2001) 733–738. https://doi.org/10.3866/pku.whxb20010813.
- [18] E.T. Kho, J. Scott, R. Amal, Ni/TiO2 for low temperature steam reforming of methane, Chem. Eng. Sci. 140 (2016) 161–170. https://doi.org/10.1016/j.ces.2015.10.021.
- [19] W. Lin, H. Cheng, L. He, Y. Yu, F. Zhao, High performance of Ir-promoted Ni/TiO2 catalyst toward the selective hydrogenation of cinnamaldehyde, J. Catal. 303 (2013) 110–116. https://doi.org/10.1016/j.jcat.2013.03.002.
- [20] S. Ashokkumar, V. Ganesan, K.K. Ramaswamy, V. Balasubramanian, Bimetallic Co-Ni/TiO2 catalysts for selective hydrogenation of cinnamaldehyde, Res. Chem. Intermed. 44 (2018) 6703–6720. https://doi.org/10.1007/s11164-018-3517-7.
- [21] M. Varkolu, V. Velpula, R. Pochamoni, A.R. Muppala, D.R. Burri, S.R.R. Kamaraju, Nitrobenzene hydrogenation over Ni/TiO2 catalyst in vapour phase at atmospheric pressure: influence of preparation method, Appl. Petrochemical Res. 6 (2016) 15–23. https://doi.org/10.1007/s13203-015-0115-0.
- [22] A.J. Vizcaíno, A. Carrero, J.A. Calles, Hydrogen production by ethanol steam reforming over Cu-Ni supported catalysts, Int. J. Hydrogen Energy. 32 (2007) 1450–1461. https://doi.org/10.1016/j.ijhydene.2006.10.024.
- [23] Y. Yao, D.W. Goodman, Direct evidence of hydrogen spillover from Ni to Cu on Ni-Cu bimetallic catalysts, J. Mol. Catal. A Chem. 383–384 (2014) 239–242. https://doi.org/10.1016/j.molcata.2013.12.013.
- [24] H.P. Reddy Kannapu, C.A. Mullen, Y. Elkasabi, A.A. Boateng, Catalytic transfer hydrogenation for stabilization of bio-oil oxygenates: Reduction of p-cresol and furfural over bimetallic Ni-Cu catalysts using isopropanol, Fuel Process. Technol. 137 (2015) 220–228. https://doi.org/10.1016/j.fuproc.2015.04.023.
- [25] R. Hierl, H. Knözinger, H.P. Urbach, Surface properties and reduction behavior of calcined CuO Al2O3 and CuO-NiO Al2O3 catalysts, J. Catal. 69 (1981) 475–486. https://doi.org/10.1016/0021-9517(81)90183-4.
- [26] A.G.S. Hussien, C.M. Damaskinos, A. Dabbawala, D.H. Anjun, M.A. Vasiliades, M.T.A. Khaleel, N. Wehbe, A.M. Efstathiou, K. Polychronopoulou, Elucidating the role of La3+/Sm3+ in the carbon paths of dry reforming of methane over Ni/Ce-La(Sm)-Cu-O using transient kinetics and isotopic techniques, Appl. Catal. B Environ. 304 (2022) 121015. https://doi.org/10.1016/j.apcatb.2021.121015.
- [27] N. Riaz, F.K. Chong, Z.B. Man, M.S. Khan, B.K. Dutta, Photodegradation of Orange II under Visible Light Using Cu–Ni/TiO2: Influence of Cu:Ni Mass Composition, Preparation, and Calcination Temperature, Ind. Eng. Chem. Res. 52 (2013) 4491–4503.

- [28] M.M. Ambursa, T.H. Ali, H.V. Lee, P. Sudarsanam, S.K. Bhargava, S.B.A. Hamid, Hydrodeoxygenation of dibenzofuran to bicyclic hydrocarbons using bimetallic Cu-Ni catalysts supported on metal oxides, Fuel. 180 (2016) 767–776. https://doi.org/10.1016/j.fuel.2016.04.045.
- [29] K.K. M., G. Naresh, V.K. V., S.V. B., B. Sasikumar, A. Venugopal, Improved H2 yields over Cu-Ni-TiO2 under solar light irradiation: Behaviour of alloy nano particles on photocatalytic H2O splitting, Appl. Catal. B Environ. 299 (2021) 120654. https://doi.org/10.1016/j.apcatb.2021.120654.
- [30] B. Gao, J. Zhang, J.H. Yang, Bimetallic Cu-Ni/MCM-41 catalyst for efficiently selective transfer hydrogenation of furfural into furfural alcohol, Mol. Catal. 517 (2022) 112065. https://doi.org/10.1016/j.mcat.2021.112065.
- [31] L.C. Chen, S.D. Lin, The ethanol steam reforming over Cu-Ni/SiO2 catalysts: Effect of Cu/Ni ratio, Appl. Catal. B Environ. 106 (2011) 639–649. https://doi.org/10.1016/j.apcatb.2011.06.028.
- [32] R. Camposeco, R. Zanella, Multifunctional Pt-Cu/TiO2 nanostructures and their performance in oxidation of soot, formaldehyde, and carbon monoxide reactions, Catal. Today. 392–393 (2022) 23–30. https://doi.org/10.1016/j.cattod.2021.06.025.
- [33] S. Lomate, A. Sultana, T. Fujitani, Vapor Phase Catalytic Transfer Hydrogenation (CTH) of Levulinic Acid to γ-Valerolactone Over Copper Supported Catalysts Using Formic Acid as Hydrogen Source, Catal. Letters. 148 (2018) 348–358. https://doi.org/10.1007/s10562-017-2241-z.
- [34] J.L. Cao, G.S. Shao, T.Y. Ma, Y. Wang, T.Z. Ren, S.H. Wu, Z.Y. Yuan, Hierarchical meso-macroporous titania-supported CuO nanocatalysts: Preparation, characterization and catalytic CO oxidation, J. Mater. Sci. 44 (2009) 6717–6726. https://doi.org/10.1007/s10853-009-3583-8.
- [35] W. Huo, C. Zhang, H. Yuan, M. Jia, C. Ning, Y. Tang, Y. Zhang, J. Luo, Z. Wang, W. Zhang, Vapor-phase selective hydrogenation of maleic anhydride to succinic anhydride over Ni/TiO2 catalysts, J. Ind. Eng. Chem. 20 (2014) 4140–4145. https://doi.org/10.1016/j.jiec.2014.01.012.
- [36] D. Messou, V. Bernardin, F. Meunier, M.B. Ordoño, A. Urakawa, B.F. Machado, V. Collière, R. Philippe, P. Serp, C. Le Berre, Origin of the synergistic effect between TiO2 crystalline phases in the Ni/TiO2-catalyzed CO2 methanation reaction, J. Catal. 398 (2021) 14–28. https://doi.org/10.1016/j.jcat.2021.04.004.
- [37] C. Liu, D. Chen, J. Ashok, P. Hongmanorom, W. Wang, T. Li, Z. Wang, S. Kawi, Chemical looping steam reforming of bio-oil for hydrogen-rich syngas production: Effect of doping on LaNi0.8Fe0.2O3 perovskite, Int. J. Hydrogen Energy. 45 (2020) 21123–21137. https://doi.org/10.1016/j.ijhydene.2020.05.186.
- [38] C. Li, Y. Yang, W. Ren, J. Wang, T. Zhu, W. Xu, Effect of Ce Doping on Catalytic Performance of Cu/TiO2 for CO Oxidation, Catal. Letters. 150 (2020) 2045–2055. https://doi.org/10.1007/s10562-020-03130-1.
- [39] B. Seemala, C.M. Cai, R. Kumar, C.E. Wyman, P. Christopher, Effects of Cu-Ni Bimetallic Catalyst Composition and Support on Activity, Selectivity, and Stability for Furfural Conversion to 2-Methyfuran, ACS Sustain. Chem. Eng. 6 (2018) 2152–2161. https://doi.org/10.1021/acssuschemeng.7b03572.
- [40] G. Singh, T.S. Khan, C. Samanta, R. Bal, A. Bordoloi, Single-step synthesis of 2-pentanone from furfural over Cu–Ni @SBA-15, Biomass and Bioenergy. 156 (2022) 106321. https://doi.org/10.1016/j.biombioe.2021.106321.

- [41] M. Kalong, P. Hongmanorom, S. Ratchahat, W. Koo-amornpattana, K. Faungnawakij, S. Assabumrungrat, A. Srifa, S. Kawi, Hydrogen-free hydrogenation of furfural to furfuryl alcohol and 2-methylfuran over Ni and Co-promoted Cu/γ-Al2O3 catalysts, Fuel Process. Technol. 214 (2021) 106721. https://doi.org/10.1016/j.fuproc.2020.106721.
- [42] S. Chen, R. Wojcieszak, F. Dumeignil, E. Marceau, S. Royer, How Catalysts and Experimental Conditions Determine the Selective Hydroconversion of Furfural and 5-Hydroxymethylfurfural, Chem. Rev. 118 (2018) 11023–11117. https://doi.org/10.1021/acs.chemrev.8b00134.
- [43] Y. Shi, Y. Zhu, Y. Yang, Y.W. Li, H. Jiao, Exploring Furfural Catalytic Conversion on Cu(111) from Computation, ACS Catal. 5 (2015) 4020–4032. https://doi.org/10.1021/acscatal.5b00303.
- [44] G. Ren, G. Wang, H. Mei, Y. Xu, L. Huang, Reaction mechanism investigation of furfural conversion to 2-methylfuran on Cu(1 1 1) surface, Chem. Phys. Lett. 703 (2018) 1–7. https://doi.org/10.1016/j.cplett.2018.04.029.
- [45] K. Xiong, W. Wan, J.G. Chen, Reaction pathways of furfural, furfuryl alcohol and 2-methylfuran on Cu(111) and NiCu bimetallic surfaces, Surf. Sci. 652 (2016) 91–97. https://doi.org/10.1016/j.susc.2016.02.011.
- [46] M. Luneau, J.S. Lim, D.A. Patel, E.C.H. Sykes, C.M. Friend, P. Sautet, Guidelines to Achieving High Selectivity for the Hydrogenation of α,β-Unsaturated Aldehydes with Bimetallic and Dilute Alloy Catalysts: A Review, Chem. Rev. 120 (2020) 12834–12872. https://doi.org/10.1021/acs.chemrev.0c00582.
- [47] S. Sitthisa, T. Sooknoi, Y. Ma, P.B. Balbuena, D.E. Resasco, Kinetics and mechanism of hydrogenation of furfural on Cu/SiO2 catalysts, J. Catal. 277 (2011) 1–13. https://doi.org/10.1016/j.jcat.2010.10.005.
- [48] S. Srivastava, G.C. Jadeja, J. Parikh, A versatile bi-metallic copper-cobalt catalyst for liquid phase hydrogenation of furfural to 2-methylfuran, RSC Adv. 6 (2016) 1649–1658. https://doi.org/10.1039/c5ra15048e.
- [49] B. Seemala, R. Kumar, C.M. Cai, C.E. Wyman, P. Christopher, Single-step catalytic conversion of furfural to 2-pentanol over bimetallic Co-Cu catalysts, React. Chem. Eng. 4 (2019) 261–267. https://doi.org/10.1039/c8re00195b.
- [50] S. Sitthisa, W. An, D.E. Resasco, Selective conversion of furfural to methylfuran over silica-supported NiFe bimetallic catalysts, J. Catal. 284 (2011) 90–101. https://doi.org/10.1016/J.JCAT.2011.09.005.
- [51] S. Sitthisa, D.E. Resasco, Hydrodeoxygenation of furfural over supported metal catalysts: A comparative study of Cu, Pd and Ni, Catal. Letters. 141 (2011) 784–791. https://doi.org/10.1007/s10562-011-0581-7.
- [52] K.L. MacIntosh, S.K. Beaumont, Nickel-Catalysed Vapour-Phase Hydrogenation of Furfural, Insights into Reactivity and Deactivation, Top. Catal. 63 (2020) 1446–1462. https://doi.org/10.1007/s11244-020-01341-9.
- [53] S. Wang, V. Vorotnikov, D.G. Vlachos, Coverage-Induced Conformational Effects on Activity and Selectivity: Hydrogenation and Decarbonylation of Furfural on Pd(111), ACS Catal. 5 (2015) 104–112. https://doi.org/10.1021/cs5015145.
- [54] A. Banerjee, S.H. Mushrif, Investigating Reaction Mechanisms for Furfural Hydrodeoxygenation on Ni and the Effect of Boron Doping on the Activity and Selectivity of the Catalyst, J. Phys. Chem. C. 122 (2018) 18383–18394.

- https://doi.org/10.1021/acs.jpcc.8b01301.
- [55] G. Ren, G. Wang, H. Mei, Y. Xu, L. Huang, A theoretical insight into furfural conversion catalyzed on the Ni(111) surface, Phys. Chem. Chem. Phys. 21 (2019) 23685–23696. https://doi.org/10.1039/c9cp03245b.
- [56] N. Shan, M.K. Hanchett, B. Liu, Mechanistic Insights Evaluating Ag, Pb, and Ni as Electrocatalysts for Furfural Reduction from First-Principles Methods, J. Phys. Chem. C. 121 (2017) 25768–25777. https://doi.org/10.1021/acs.jpcc.7b06778.
- [57] S. Sitthisa, T. Pham, T. Prasomsri, T. Sooknoi, R.G. Mallinson, D.E. Resasco, Conversion of furfural and 2-methylpentanal on Pd/SiO2 and Pd-Cu/SiO2 catalysts, J. Catal. 280 (2011) 17–27. https://doi.org/10.1016/j.jcat.2011.02.006.
- [58] L.C. Grabow, B. Hvolbæk, J.K. Nørskov, Understanding trends in catalytic activity: The effect of adsorbate-adsorbate interactions for Co oxidation over transition metals, Top. Catal. 53 (2010) 298–310. https://doi.org/10.1007/s11244-010-9455-2.
- [59] A.C. Lausche, A.J. Medford, T.S. Khan, Y. Xu, T. Bligaard, F. Abild-Pedersen, J.K. Nørskov, F. Studt, On the effect of coverage-dependent adsorbate-adsorbate interactions for CO methanation on transition metal surfaces, J. Catal. 307 (2013) 275–282. https://doi.org/10.1016/j.jcat.2013.08.002.
- [60] W.C. Conner, J.L. Falconer, Spillover in Heterogeneous Catalysis, Chem. Rev. 95 (1995) 759–788. https://doi.org/10.1021/cr00035a014.
- [61] A. Crucq, L. Degols, G. Lienard, A. Frennet, Hydrogen Spillover from Ni to CuNi Alloys, Elsevier Science Publishers B.V., 1983. https://doi.org/10.1016/S0167-2991(08)64668-6.
- [62] E.A. Lewis, M.D. Marcinkowski, C.J. Murphy, M.L. Liriano, E.C.H. Sykes, Hydrogen dissociation, spillover, and desorption from cu-supported co nanoparticles, J. Phys. Chem. Lett. 5 (2014) 3380–3385. https://doi.org/10.1021/jz5016789.
- [63] K. Fulajtárova, T. Soták, M. Hronec, I. Vávra, E. Dobročka, M. Omastová, Aqueous phase hydrogenation of furfural to furfuryl alcohol over Pd–Cu catalysts, Appl. Catal. A Gen. 502 (2015) 78–85. https://doi.org/10.1016/J.APCATA.2015.05.031.
- [64] G. Kyriakou, M.B. Boucher, A.D. Jewell, E.A. Lewis, T.J. Lawton, A.E. Baber, H.L. Tierney, M. Flytzani-Stephanopoulos, E.C.H. Sykes, Isolated metal atom geometries as a strategy for selective heterogeneous hydrogenations, Science (80-.). 335 (2012) 1209–1212. https://doi.org/10.1126/science.1215864.
- [65] I. Alstrup, U.E. Petersen, J.R. Rostrup-Nielsen, Propane hydrogenolysis on sulfur- and copper-modified nickel catalysts, J. Catal. 191 (2000) 401–408. https://doi.org/10.1006/jcat.1999.2812.
- [66] H.H. Brongersma, M.J. Sparnaay, T.M. Buck, Surface segregation in Cu-Ni and Cu-Pt alloys; A comparison of low-energy ion-scattering results with theory, Surf. Sci. 71 (1978) 657–678. https://doi.org/10.1016/0039-6028(78)90453-3.
- [67] A. Kitla, O. V. Safonova, K. Föttinger, Infrared studies on bimetallic copper/nickel catalysts supported on zirconia and ceria/zirconia, Catal. Letters. 143 (2013) 517–530. https://doi.org/10.1007/s10562-013-1001-y.
- [68] Y. Yao, D.W. Goodman, In situ IR spectroscopic studies of Ni surface segregation induced by CO adsorption on Cu-Ni/SiO2 bimetallic catalysts, Phys. Chem. Chem. Phys. 16 (2014) 3823–3829. https://doi.org/10.1039/c3cp54997f.
- [69] N.J. O'Connor, A.S.M. Jonayat, M.J. Janik, T.P. Senftle, Interaction trends between

- single metal atoms and oxide supports identified with density functional theory and statistical learning, Nat. Catal. 1 (2018) 531–539. https://doi.org/10.1038/s41929-018-0094-5.
- [70] Y. Nakagawa, H. Nakazawa, H. Watanabe, K. Tomishige, Total Hydrogenation of Furfural over a Silica-Supported Nickel Catalyst Prepared by the Reduction of a Nickel Nitrate Precursor, ChemCatChem. 4 (2012) 1791–1797. https://doi.org/10.1002/cctc.201200218.
- [71] H.Y. Zheng, Y.L. Zhu, B.T. Teng, Z.Q. Bai, C.H. Zhang, H.W. Xiang, Y.W. Li, Towards understanding the reaction pathway in vapour phase hydrogenation of furfural to 2-methylfuran, J. Mol. Catal. A Chem. 246 (2006) 18–23. https://doi.org/10.1016/j.molcata.2005.10.003.
- [72] M.J. Gilkey, B. Xu, Heterogeneous Catalytic Transfer Hydrogenation as an Effective Pathway in Biomass Upgrading, ACS Catal. 6 (2016) 1420–1436. https://doi.org/10.1021/acscatal.5b02171.
- [73] W. Fang, A. Riisager, Recent advances in heterogeneous catalytic transfer hydrogenation/hydrogenolysis for valorization of biomass-derived furanic compounds, Green Chem. 23 (2021) 670–688. https://doi.org/10.1039/d0gc03931d.
- [74] X. Jin, B. Yin, Q. Xia, T. Fang, J. Shen, L. Kuang, C. Yang, Catalytic Transfer Hydrogenation of Biomass-Derived Substrates to Value-Added Chemicals on Dual-Function Catalysts: Opportunities and Challenges, ChemSusChem. 12 (2019) 71–92. https://doi.org/10.1002/cssc.201801620.
- [75] P.P. Singh, N. Nirmalkar, T. Mondal, Catalytic steam reforming of simulated bio-oil for green hydrogen production using highly active LaNixCo1–xO3 perovskite catalysts, Sustain. Energy Fuels. 6 (2022) 1063–1074. https://doi.org/10.1039/d1se01786a.
- [76] L. Grazia, A. Lolli, F. Folco, Y. Zhang, S. Albonetti, F. Cavani, Gas-phase cascade upgrading of furfural to 2-methylfuran using methanol as a H-transfer reactant and MgO based catalysts, Catal. Sci. Technol. 6 (2016) 4418–4427. https://doi.org/10.1039/c5cy02021b.
- [77] X. Yang, X. Xiang, H. Chen, H. Zheng, Y.W. Li, Y. Zhu, Efficient Synthesis of Furfuryl Alcohol and 2-Methylfuran from Furfural over Mineral-Derived Cu/ZnO Catalysts, ChemCatChem. 9 (2017) 3023–3030. https://doi.org/10.1002/cctc.201700279.
- [78] C.P. Jiménez-Gómez, J.A. Cecilia, R. Moreno-Tost, P. Maireles-Torres, Selective Production of 2-Methylfuran by Gas-Phase Hydrogenation of Furfural on Copper Incorporated by Complexation in Mesoporous Silica Catalysts, ChemSusChem. 10 (2017) 1448–1459. https://doi.org/10.1002/cssc.201700086.
- [79] C.P. Jiménez-Gómez, J.A. Cecilia, R. Moreno-Tost, P. Maireles-Torres, Nickel Phosphide/Silica Catalysts for the Gas-Phase Hydrogenation of Furfural to High–Added–Value Chemicals, ChemCatChem. 9 (2017) 2881–2889. https://doi.org/10.1002/cctc.201700312.
- [80] X. Lan, R. Pestman, E.J.M. Hensen, T. Weber, Furfural hydrodeoxygenation (HDO) over silica-supported metal phosphides The influence of metal–phosphorus stoichiometry on catalytic properties, J. Catal. 403 (2021) 181–193. https://doi.org/10.1016/j.jcat.2021.01.031.

hapter 4 FFR HDO to 2-MeF over TiO2-supported Cu-Ni bimetallic catalysts					

Chapter 5: FFR HDO to 2-MeF over Cu-Fe mixed oxide catalysts

This chapter investigates Cu-Fe mixed oxide catalysts with varying Cu/Fe molar ratios (0.5 to 2) synthesized via a sol-gel method for vapor-phase FFR HDO. The catalysts were characterized using XRD, H₂-TPR, NH₃-TPD, N₂ physisorption, FESEM and XPS to gain sights into their properties. Subsequently, a comprehensive evaluation of these catalysts was carried out to assess their catalytic efficacy in the FFR HDO process. This investigation explored the influence of Cu to Fe ratios, reaction temperatures, and weight hourly space velocity under atmospheric pressure conditions. It goes beyond routine optimization methodology by thoroughly examining additional key factors: (i) the role of reduction temperature of the catalysts, (ii) the influence of H₂ to FFR molar ratio on the HDO process, and (iii) a rigorous regeneration study, where the catalyst was regenerated after an initial cycle of extended time-on-stream reactions (24 h). Here, the catalyst was first calcined at 500 °C in air, followed by re-activation in H₂ atmosphere, both inside the reactor. Finally, the regenerated catalyst underwent a second 24 h cycle of TOS reactions. Here, the idea was to gauge the catalyst's resilience and potential for sustained catalytic performance.

5.1 Characterization

5.1.1 XRD

Fig. 5.1 shows the XRD patterns of the fresh Cu-Fe oxide catalysts with varying Cu to Fe molar ratios calcined at 500 °C. All the diffractograms exhibit peaks at 2θ values of 18.4° , 30.1° , 35.6° , 43.2° , 53.8° , 57.3° , and 62.5° , which may be ascribed to the (111), (220), (311), (400), (422), (511), and (440) lattice planes of cubic CuFe₂O₄ spinel phase [1,2]. However, it must be noted that the peaks at $2\theta = 35.6^{\circ}$, 43.1° , 53.8° , 57.3° , and 62.5° can also correspond to the lattice planes of CuO and Fe₂O₃ [1,3,4]. As a consequence, the diffractograms in Fig. 5.1 represent an intriguing ambiguity in the assignment of the diffraction peaks, the resolution of which hinges on taking into consideration the influence of calcination temperature. While some studies available in literature suggest that the spinel CuFe₂O₄ phase can indeed be formed at relatively lower calcination temperatures such as $400 \, ^{\circ}$ C [5], other studies suggest that at moderate calcination temperatures (typically between 400 and 600 °C), CuO and Fe₂O₃

are the dominant species in the calcined catalysts, and the spinel phase is either non-existent or makes up a small fraction [3,6,7]. With increasing temperatures (generally greater than 600 °C), the peaks corresponding to the spinel structure begin to emerge; however, those corresponding to Cu and Fe oxides still remain noticeable. It is only when the calcination temperatures become very high (800 °C or more) that the spinel CuFe₂O₄ emerges as the main phase [3,6–8]. Nevertheless, it is worth noting that CuO and/or Fe₂O₃ phases may still be present, albeit in trace amounts, even after calcination at such elevated temperatures. In light of the above discussion, it is more appropriate to infer that the catalyst synthesized here is a mixed-oxide phase predominantly made up of CuO and Fe₂O₃ while also containing some spinel CuFe₂O₄.

In addition to the above-mentioned peaks, additional peaks were observed in the diffraction pattern of the catalyst with Cu/Fe = 0.5 at 38.7°, which corresponds to CuO and at 33.2° and 49.3° which can be assigned to Fe₂O₃. Increasing the Cu to Fe molar ratio from 0.5 to 2 led to a sharp increase in the intensities of peaks at 35.6°, 38.6° and 48.8°. Additionally, several new peaks belonging to CuO appeared at 66.2°, 68.2° and 75.2°. Subtle changes can also be noted for the peaks at 57.5° and 62.4°, both of which split into two peaks as the Cu to Fe molar ratios increased to 2. The changes observed in the diffractograms upon increasing Cu/Fe ratios are consistent with the observations made in existing published reports and signify that when the metal ratios are greater than the stoichiometric ratio required for the formation of the spinel phase (Cu:Fe = 1:2), the calcined Cu-Fe catalysts will always contain the oxide species of the metal present in excess, in this case CuO, regardless of the calcination temperature [6– 8]. Interestingly, it was observed that at low Cu to Fe ratios, CuO had comparatively lower crystallite sizes (Table 5.1). Even more interesting is the fact that the crystallite size was the smallest at a Cu/Fe ratio of 1, perhaps signifying the presence of synergistic interaction between Cu and Fe at this ratio that promoted the dispersion of Cu.[9] This is in line with observations made in previous reports where Fe has been known to inhibit the agglomeration of Cu [9]. However, such a promotional role is possible when the proportion of Fe is significant; at high Cu content, Fe is no longer able to influence Cu's dispersion, explaining the larger crystallite size observed when Cu is in excess. As we will see later, this synergistic interaction and improved dispersion will prove beneficial during the assessment catalytic performance.

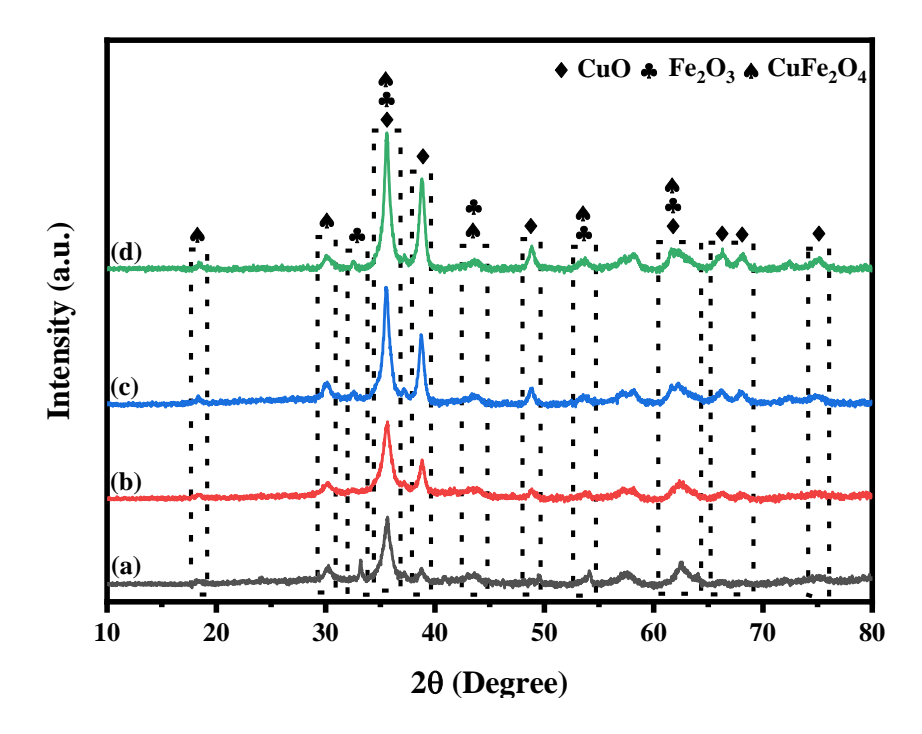


Fig. 5.1 XRD diffractograms of fresh Cu-Fe oxides with (a) Cu/Fe = 0.5, (b) Cu/Fe = 1, (c) Cu/Fe = 1.5 and (d) Cu/Fe = 2.

To understand the nature of Cu and Fe species under the reaction conditions, XRD analysis was carried out for the catalysts following reduction at 350 °C, as shown in Fig. 5.2. The catalyst with the Cu to Fe molar ratio of 0.5 had diffraction peaks corresponding to the (111), (200) and (220) lattice planes of metallic Cu at 43.4°, 50.5° and 74.2°[3,10], and no discernable peaks associated with CuO, signaling the complete reduction of Cu. Simultaneously, multiple peaks corresponding to Fe₂O₃ were noted at 2θ values of 24.2°, 33.3°, 35.8°, 40.6°, 49.6°, 54.1°, and 64.1° [3,11], along with peaks corresponding to Fe₃O₄ at 30.2°, 57° and 62.4°. The presence of numerous peaks attributed to Fe₂O₃ and Fe₃O₄ in the diffraction pattern signifies that the former was only partially reduced under these conditions [11,12]. Upon examining the catalyst with Cu/Fe ratio equal to 1, it was noted that the peaks belonging to Fe₂O₃ had disappeared, replaced by intense peaks corresponding to the cubic Fe₃O₄ phase (ICSD collection code: 158741) at $2\theta = 30.1^{\circ}$, 35.4°, 37.05°, 57°, and 62.6° [13], signaling that Fe₂O₃ had been reduced to Fe₃O₄. Notably, the peaks at 50.4°, and 74.2°, which belong to metallic Cu, exhibited a sharp rise in intensity, suggesting a substantial enhancement in the amount of metallic Cu present. Especially striking was the pronounced increase in intensity observed for the peak at 43.3°, possibly arising from an overlap between the (111) lattice plane of Cu and (004) lattice plane of Fe₃O₄, pointing towards the existence of a probable strong interaction between Cu and Fe₃O₄. As the Cu to Fe ratio increased to 1.5, the intensity of the diffraction peaks for Cu and Fe₃O₄ was somewhat reduced. Concomitantly, new peaks emerged at 36.3°, 42.3° and 61.2°, which could be ascribed to the presence of Cu₂O [13] (ICSD collection code: 172174), indicating that due to the substantial excess of Cu in the catalyst, CuO was not completely reduced to metallic Cu. Additionally, a small peak at 38.6°, corresponding to CuO, further confirmed that the excessive presence of Cu was hindering its complete reduction. Moving to an even higher Cu to Fe molar ratio of 2, a significant reduction in the intensities of peaks corresponding to metallic Cu at 43.4°, 50.6° and 74.2°, signifying that the formation of metallic Cu had fallen substantially. Simultaneously, the peaks corresponding to Cu₂O and CuO, highlighting their increased presence of these phases. Additionally, a very small peak at 40.6°, corresponding to Fe₂O₃, further confirmed that the excessive presence of Cu was not only hindering its own complete reduction but also that of Fe.

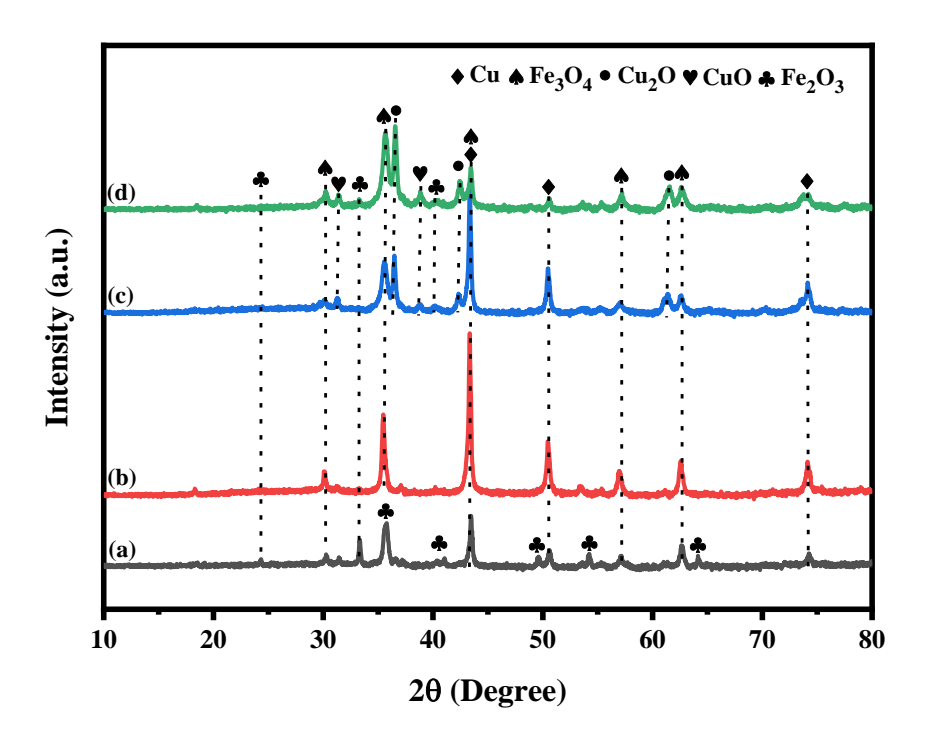


Fig. 5.2 XRD diffractograms of reduced Cu-Fe oxides with (a) Cu/Fe = 0.5, (b) Cu/Fe = 1, (c) Cu/Fe = 1.5 and (d) Cu/Fe = 2.

The XRD analysis of reduced Cu-Fe oxide catalysts reveals a subtle correlation between the Cu to Fe molar ratio and the resultant phase formations. The reduction of Fe₂O₃ under hydrogen atmosphere has generally been postulated to occur over a wide range of temperature (~400 to 700-800 °C) in three steps: Fe₂O₃ \rightarrow Fe₃O₄ \rightarrow FeO \rightarrow Fe [11,12,14]. However, the presence of metals such as Cu greatly enhances the reducibility of Fe, as a result of which the reduction of Fe begins at substantially lower

temperatures [11,12,14]. As such, this reduction behaviour has been attributed to the promotional role played by Cu, wherein it is the first to undergo reduction from Cu²⁺ to Cu⁰ and subsequently, facilitates the reduction of Fe by providing the requisite hydrogen through spillover [11,12,14]. In fact, such a synergistic effect was also noted in a previous study of ours for the case of Cu-Ni bimetallic catalysts, where the presence of Cu led to a drastic reduction in the reduction temperature of Ni²⁺ species [15]. Initially, at a lower Cu to Fe ratio of 0.5, Cu was noted to have undergone complete reduction to its metallic form (Cu⁰); however, the reduction of Fe₂O₃ to Fe₃O₄ was not complete. The incomplete reduction of Fe₂O₃ to Fe₃O₄ suggests that the available Cu species may not be present in a quantity sufficient to effectively promote the reduction of Fe₂O₃. At a Cu to Fe ratio of 1, the observed formation of Cu⁰ and Fe₃O₄ phases indicates an optimum outcome that is a result of a delicate balance: the Cu content is sufficiently high to effectively catalyze the complete reduction of Fe₂O₃ to Fe₃O₄, yet not so high as to hinder its own reduction. As the Cu to Fe ratios increase beyond 1 to 1.5 and 2, an interesting interplay is observed. The excessive presence of Cu appears to hinder its own reduction, as indicated by the significant reduction in the intensities of peaks corresponding to metallic Cu and the appearance of peaks belonging to Cu₂O and CuO. The incomplete reduction of Cu may stem from an overwhelming amount of Cu being present in the catalyst, leading to the formation of bulk oxide phases, which are inherently more difficult to reduce. The formation of these tough-to-reduce bulk oxides also leads to a drop in the amount of hydrogen available through spillover, which negatively affects the reduction of Fe species, as witnessed from the formation of Fe₂O₃.

Table 5.1 Physical properties of the Cu-Fe mixed oxide catalysts

Catalyst	Crystallite Size	Crystallite	Surface Area ^c	Pore	Pore
	(CuO) ^a	Size (Cu) ^b	$(m^2 g^{-1})$	Volume ^d	Size ^d
	(nm)	(nm)		$(cm^3 g^{-1})$	(nm)
Cu/Fe = 0.5	21.9	15.2	8.6	0.031	3.06
Cu/Fe = 1	17.5	18.3	6.9	0.027	3.08
Cu/Fe = 1.5	25.04	22.8	6.1	0.025	3.18
Cu/Fe = 2	35.1	25.8	5.9	0.022	3.26

^a Calculated using Scherrer equation at $2\theta = 38.6^{\circ}$. ^b Calculated using Scherrer equation at $2\theta = 50.3^{\circ}$ ^c Calculated using BET method. ^d Calculated using BJH method

5.1.2 H₂-TPR

H₂-TPR analysis was carried out to systematically investigate the effect of varying Cu to Fe ratios on the reduction behaviour of Cu-Fe mixed oxide catalysts, as shown in Fig. 5.3. At a Cu to Fe ratio of 0.5, the deconvolution of the H2-TPR profile unveiled two distinct reduction peaks occurring at 251.2 °C and 293.5 °C. These peaks correspond to the reduction of CuO to Cu, consistent with the existing literature, which suggests the presence of two CuO species: easily reducible dispersed particles and a tougher-to-reduce bulk phase [4,10]. Upon increasing the Cu to Fe ratio to 1, a notable shift in the reduction peaks towards lower temperatures was observed (234.2 °C and 281.2 °C). This shift was accompanied by a substantial increase in the proportion of H₂ consumed by the dispersed phase, which reached 62% of the total H₂ consumed during CuO reduction (Table 5.2). These findings suggest a synergistic effect between Cu and Fe, resulting in the formation of more easily reducible CuO particles. At a Cu to Fe ratio of 1.5, a faint reduction peak at 216.8 °C indicated the presence of highly dispersed CuO species with small particle size. Additionally, the reduction temperatures exhibited an increase compared to the Cu/Fe = 1 catalyst, potentially attributable to Cu hindering its own reduction through the formation of bulk oxides. Further increasing the Cu to Fe ratio to 2 resulted in both reduction peaks shifting towards further higher temperatures (264.3 °C and 302.5 °C). Deconvolution of the reduction profile revealed a doubling in the proportion of H₂ consumed by the bulk phase compared to the Cu to Fe ratio of 1.5. This suggests that excess Cu may impede its own reduction, leading to the formation of bulk oxide species requiring higher temperatures for reduction. The shift in the reduction temperatures of Cu towards higher temperatures for the case of Cu/Fe = 1.5 and 2 suggests that the large excess of Cu in the catalyst could be playing a negative role, forming bulk oxide species with larger particle sizes and interacting comparatively more strongly with the support, hindering their reducibility. The results obtained here are in good agreement with those obtained from the XRD analysis which also suggested that beyond a certain Cu to Fe ratio, the excess Cu starts to impede its own reduction due to the formation of agglomerated species – as Fe is no longer to inhibit aggregation - that require higher temperatures for reduction. In summary, the detailed analysis provided by H₂-TPR offers valuable insights into the intricate interplay between Cu and Fe in mixed oxide catalysts and their effects on reduction behavior.

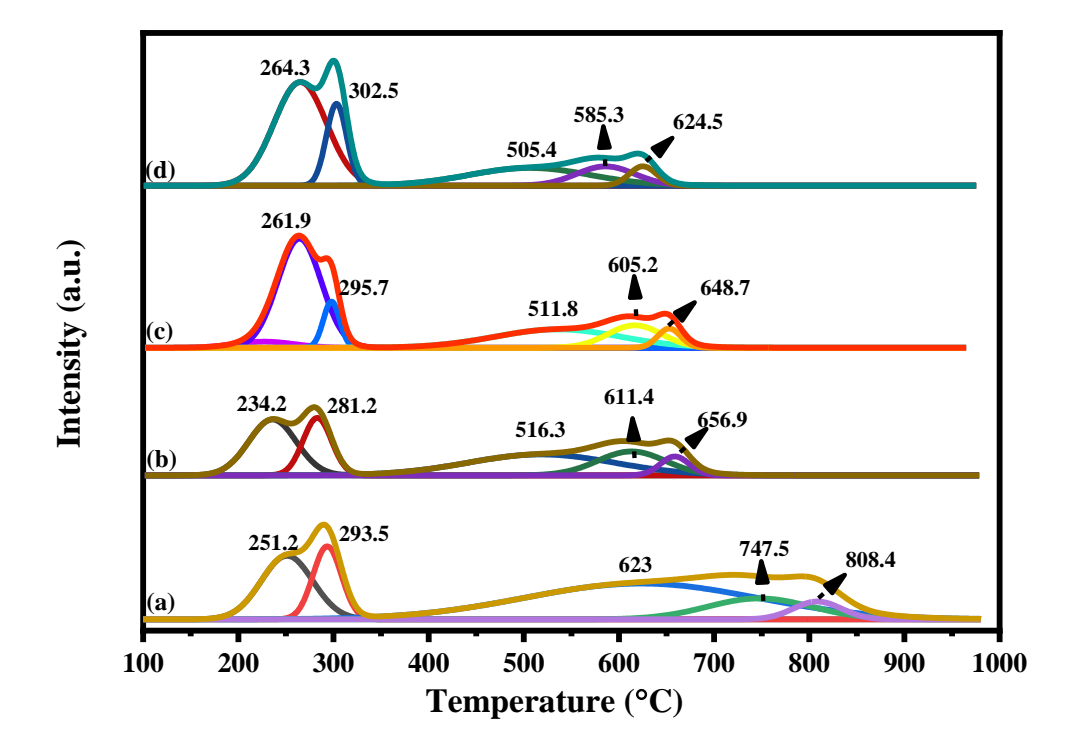


Fig. 5.3 H₂-TPR profiles of the synthesized Cu-Fe mixed oxide catalysts with Cu/Fe ratios of (a) 0.5, (b) 1, (c) 1.5 and (d) 2.

Analyzing the reduction behaviour of Fe across the varying Cu to Fe molar ratios revealed three distinct peaks, aligning with the established consensus of three-staged reduction process for Fe reduction: $Fe_2O_3 \rightarrow Fe_3O_4 \rightarrow FeO \rightarrow Fe$ [11,12,14]. For the catalyst with Cu/Fe = 0.5, reduction peaks corresponding to three stages were observed at 623 °C, 747.5 °C and 808.4 °C, with the H₂ consumption percentages of 73.2%, 19.2% and 7.6%, respectively. The extraordinarily high H₂ consumption during stage 1 as compared to stages 2 and 3, which correspond to the reduction of the in-situ generated Fe₃O₄ and FeO species respectively, could be attributed to Cu's promotional role, influencing the reduction kinetics of Fe and enhancing the reducibility of Fe. Increasing the Cu to Fe ratio to 1 further enhanced the reducibility of Fe, which was reflected in the fact that the three reduction peaks now appeared at much lower temperatures (516.3 °C, 611.4 °C and 656.9 °C). Intriguingly, the H₂ consumption pattern also underwent drastic changes. The percentage H₂ consumption for Fe₂O₃ reduction to Fe₃O₄ dropped substantially, while the consumption in reduction of in-situ generated Fe₃O₄ and FeO rose (Table 2). Increased H₂ consumption in the 2nd and 3rd stages suggests a pronounced promotional effect of the metallic Cu that is now present in higher abundance due to its greater loading. The presence of metallic Cu in higher amounts, as seen from reduced XRD analysis, would result in ample amount of H₂ being available for the reduction of iron oxides through spillover, thereby explaining the observed consumption trend. As the Cu to Fe ratio exceeds 1 (Cu/Fe = 1.5 and 2), the reduction temperature for Fe_2O_3 shifts slightly leftward but the percentage H_2 consumption for this stage is reduced. The peaks corresponding to the reduction of the in-situ formed Fe_3O_4 and FeO, on the other hand, exhibited a comparatively larger shift towards lower temperatures. The percentage H_2 consumption for the reduction of Fe_3O_4 to FeO and FeO to Fe continued to increase as the Cu/Fe ratio rose to 2. These observations are well in agreement with the existing consensus that the presence of Cu greatly enhances the reducibility of Fe through strong interactions among them.

Table 5.2 Reduction temperature (°C) and H₂ Consumption values for Cu-Fe mixed oxide catalysts with varying Cu/Fe ratios obtained through deconvolution of H₂-TPR profile.

Percentage H ₂ Consumption						H ₂	
Catalyst	Cu			Fe		Consumption (mmol H ₂	
	Peak 1	Peak 2	Peak 3	Peak 1	Peak 2	Peak 3	gcat ⁻¹)
Cu/Fe = 0.5	-	46.9	53.9	73.2	19.2	7.6	23.1
Cu/Fe = 1	-	61.8	38.2	58.5	31.1	10.4	18.6
Cu/Fe = 1.5	1.4	82.3	16.3	52.9	33.4	13.8	18.1
Cu/Fe = 2	0.3	75.6	24.1	45.4	37.5	17.1	17.8

5.1.3 NH₃-TPD

In NH₃-TPD analysis which characterizes a catalyst's acidic sites, distinct trends were once again noted across varying Cu to Fe molar ratios, as can be seen in Fig. 5.4. Based on the temperature at which the adsorbed NH₃ desorbs from the catalyst surface, the strength of the surface acid sites can be categorized as weak (< 300 °C), medium (~300 to 500 °C) and strong (> 500 °C) [16]. In the catalyst with Cu/Fe = 0.5, a very intense peak at approximately 122 °C, suggesting a significant presence of weak acidic sites. Additionally, a broad and faint peak centered at around 500 °C indicates the existence of some medium-strength sites. The predominance of weak sites can be explained by the presence of Cu⁰ and unreduced Fe₂O₃ species, both of which exhibit weak Lewis acidity. Upon increasing the Cu/Fe ratio to 1, two peaks were observed at 91 °C and

195 °C that point to the continued presence of weak acidic sites, though it is notable that their intensity is much weaker than the intensity of the peak observed for Cu/Fe = 0.5. Concurrently, the intensity of the peaks around 410 °C and 505 °C increased substantially, signifying an increase in medium-strength sites, perhaps due to the presence of more Lewis acidic Fe₃O₄ formed by the reduction of Fe₂O₃. A faint peak observed at 600 °C indicated that the catalyst contained fewer strong acidic sites. As the Cu/Fe rose further to 1.5 and 2, the peak corresponding to the medium-strength acidic sites grew further in intensity, as did the peak assigned to strong sites (Fig. 5.4). Simultaneously, a reduction in the number of weak acid sites was noted with increasing Cu to Fe molar ratios. The rise in the concentration of medium- and strong-strength sites for this catalyst may be linked to the emergence of Cu₂O and CuO formation for catalysts with Cu/Fe = 1.5 and 2, as seen from reduced XRD analysis.

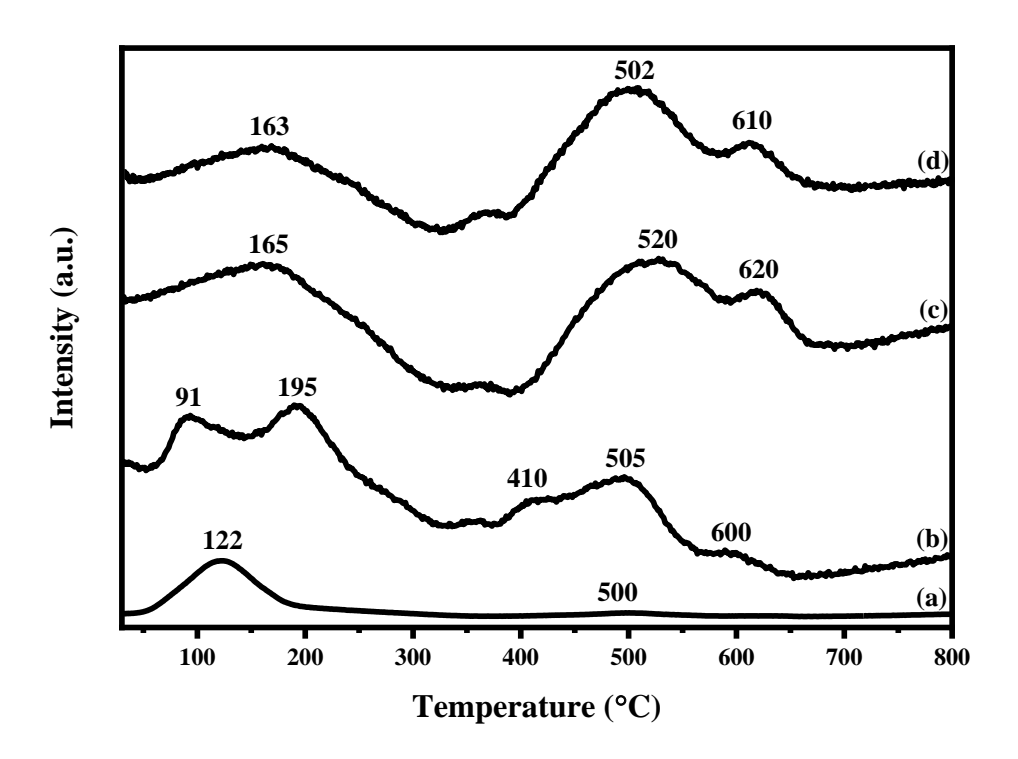


Fig. 5.4 Temperature-programmed NH₃ desorption profiles of reduced (a) Cu/Fe = 0.5, (b) Cu/Fe = 1, (c) Cu/Fe = 1.5 and (d) Cu/Fe = 2 catalysts.

5.1.4 XPS

In order to further investigate the surface oxidation states of Cu and Fe, XPS analysis was carried with the catalyst with Cu/Fe = 1, reduced at 350 °C (Fig. 5.5). The Cu 2p spectral profile revealed two peaks at 932 and 952 eV that can be ascribed to the $2p_{3/2}$ and $2p_{1/2}$ energy levels of metallic Cu, respectively [13,15,17]. Additionally, a broad and faint hump, associated with the shake-up satellite peaks of Cu²⁺ species,

concomitantly appear between 940 and 946 eV [15]. These results, coupled with those obtained from reduced XRD analysis, confirm that Cu predominantly exists in the form of metallic Cu species. The Fe 2p spectrum (shown in Fig. 5.5(b)), upon deconvolution, revealed peaks corresponding to Fe 2p_{3/2} and Fe 2p_{1/2} energy levels as well as two satellite peaks. Three peaks were observed corresponding to the Fe 2p_{3/2} energy level at 709.9, 711.3 and 713.6 eV, ascribed to the Fe²⁺ species present in octahedral sites, Fe³⁺ species present in octahedral sites and Fe³⁺ present in tetrahedral sites, respectively [5,18–20]. Similarly, three peaks were noted for the Fe 2p_{1/2} energy level as well at binding energy values of 723.2, 725.2 and 727.3 eV, ascribed to the Fe²⁺ species in octahedral sites, Fe³⁺ species in octahedral sites and Fe³⁺ species in tetrahedral sites, respectively [5,18–20]. The existing literature suggests that Fe₃O₄ has an inverse spinel structure, wherein the Fe2+ ions occupy the octahedral sites while the Fe3+ ions are present in both octahedral and tetrahedral sites [19,20]. The ratio of Fe³⁺ to Fe²⁺ species. determined through peak integration, was calculated to be 1.88, which is close to the experimentally predicted value of 2 for the inverse structure [5]. In addition to these peaks, satellite peaks ascribed to Fe³⁺ species were noted at binding energy values of 718.5 eV and 732.8 eV. The overall spectral profile, featuring distinct peaks corresponding to both Fe²⁺ and Fe³⁺ species, aligns well with the expected features of an inverse spinel phase characteristic of Fe₃O₄ and therefore, support the conclusion that the obtained results are consistent with the formation of Fe₃O₄ in the catalyst. This finding is further corroborated by concurrent evidence from reduced XRD analysis, which independently confirms the presence of Fe₃O₄ in the catalyst.

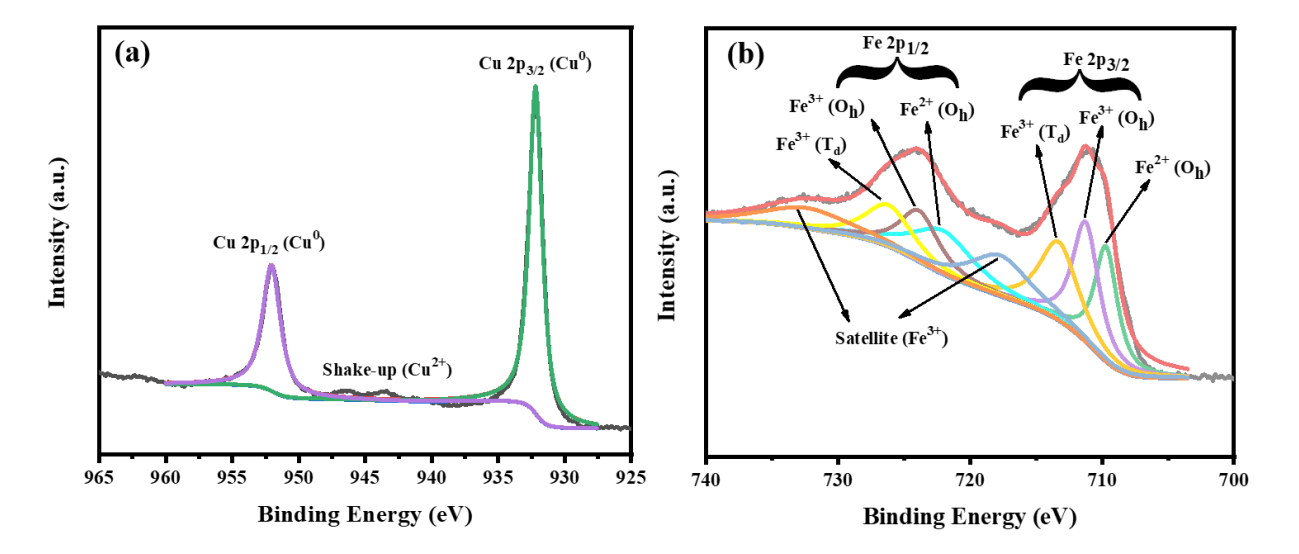


Fig. 5.5 XPS spectra of (a) Cu 2p and (b) Fe 2p for the reduced catalyst with Cu/Fe = 1.

5.1.5 N₂ physisorption

Table 4 shows the results of the N₂ physisorption analysis for the determination of specific surface, pore volume and pore size distribution. As the Cu to Fe ratio increased from 0.5 to 2, a consistent reduction was noted in both surface area as well as pore volume. This could be attributed to the high Cu loading, which leads to agglomeration and the formation of large particles of bulk oxides, particularly when Cu is in large excess as evidenced from XRD and H₂-TPR analyses. The presence of large particles would result in a partial coverage of the surface of iron oxide and/or pore blockage, thereby diminishing the surface area and pore volume [21].

5.1.6 FESEM

Fig. 5.6 presents the FESEM images of the synthesized Cu-Fe mixed oxide catalysts. It is clear from the images that all the catalysts exhibited large particles. Shafaei et. al. [22], Gao et al.[23], and More et. al.[5] have all previously reported the formation of large sized particles in Cu-Fe oxide catalysts synthesized through sol-gel method. Additionally, it appears that as the Cu/Fe molar ratios increases, the shape of the particles changes from looking somewhat cubical to largely irregular, and non-uniform. In addition, the surface composition of the synthesized mixed oxide catalysts was investigated using EDX analysis. The atomic weight percentage of metals obtained from the analysis was found to be nearly consistent with their intended Cu/Fe molar

ratios. Table 5.3 summarizes the elemental composition (weight %) of the elements in Cu-Fe mixed oxide catalysts determined using EDX analysis.

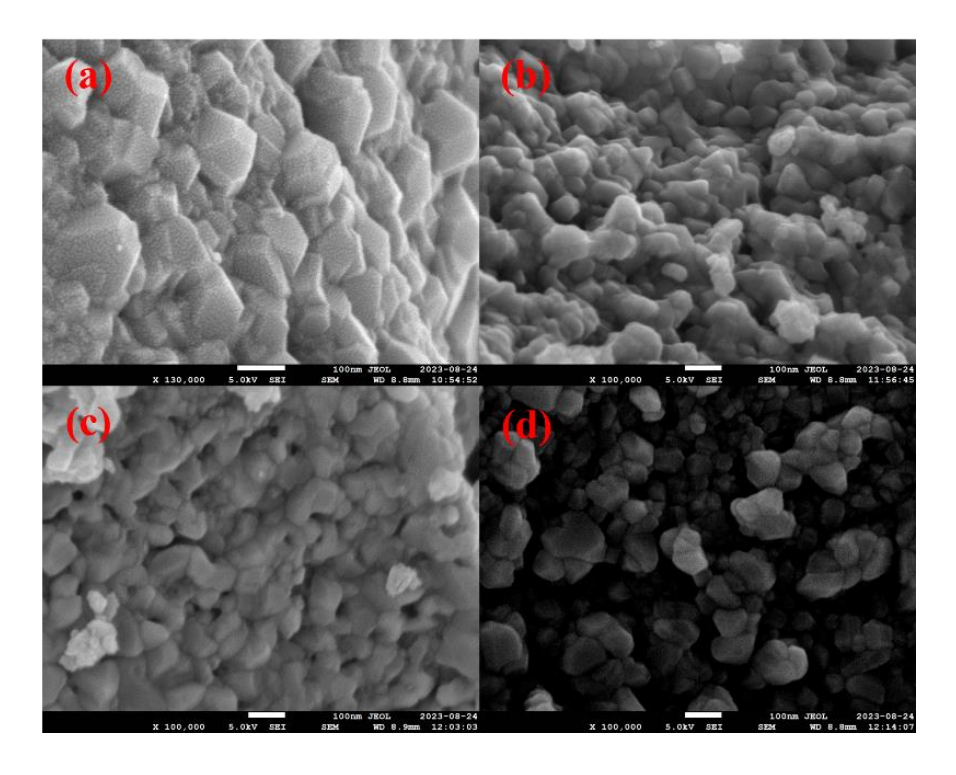


Fig. 5.6 FESEM images of calcined Cu-Fe oxide catalysts with (a) Cu/Fe = 1, (b) Cu/Fe = 2, (c) Cu/Fe = 3, and (d) Cu/Fe = 4.

Table 5.3 Elemental surface composition of the synthesized Cu-Fe mixed oxide catalysts using EDX analysis

Catalyst	Atomic weight % from EDX						
	Fe	0	Cu	Cu/Fe Molar Ratio			
Cu/Fe = 0.5	46.4	26.9	26.5	0.5			
Cu/Fe = 1	34	25.7	40.3	1.04			
Cu/Fe = 1.5	27.5	23.7	48.8	1.56			
Cu/Fe = 2	24.3	23.1	52.6	1.90			

5.1.7 HRTEM

Further investigation into the morphological structure of the Cu-Fe mixed oxide catalyst, with a Cu/Fe ratio of 1 and reduced at 350 °C, through HRTEM revealed intriguing insights (Fig. 5.7). The analysis indicated a diverse range of particle shapes; some particles exhibited a roughly rectangular morphology, while others were more elongated or displayed a near-spherical form. This variety in morphology is consistent with the findings from the FESEM analysis, which similarly identified larger-sized particles. Importantly, the HRTEM images showcased distinct fringes corresponding to

the Cu (111) plane and the (004), (022), and (044) planes of Fe₃O₄. These observations suggest that the reduction process of the mixed oxide catalyst effectively facilitated the formation of Cu₀ and Fe₃O₄ phases, aligning well with the results obtained from XRD and XPS analyses.

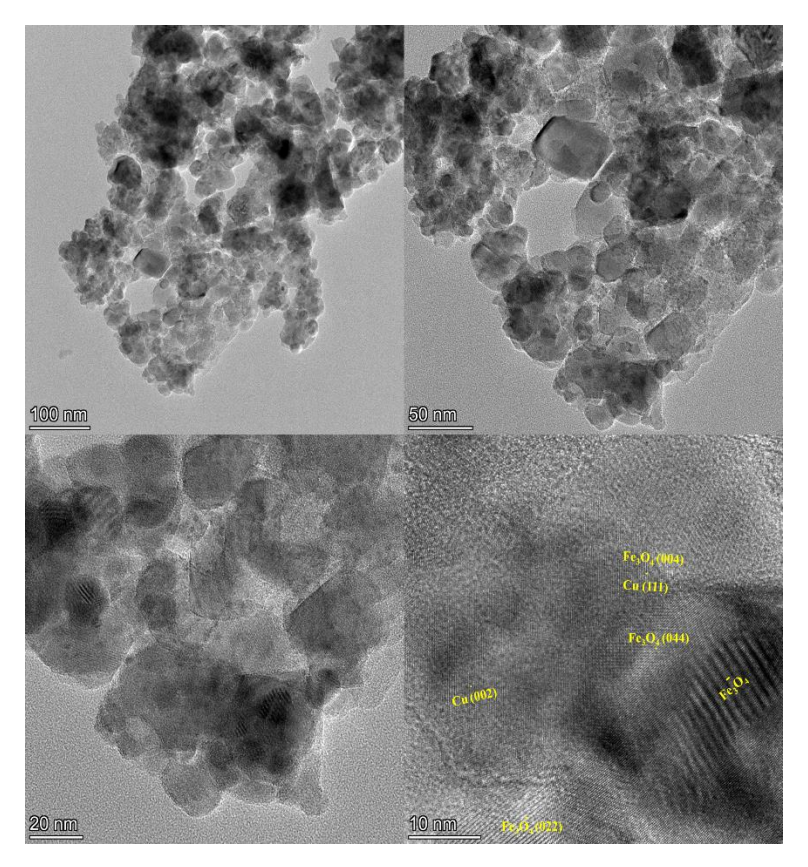


Fig. 5.7 HRTEM images of the Cu-Fe mixed catalyst with Cu/Fe = 1 and reduced at 350 °C.

5.2 FFR HDO over Cu-Fe mixed oxide catalysts

5.2.1 Effect of Cu/Fe molar ratio

The evaluation of the catalytic performance of the synthesized Cu-Fe mixed oxide catalysts was started by assessing the role of varying Cu to Fe molar ratios on FFR HDO to 2-MeF at 230 °C, an H₂ to FFR molar ratio of 15, and a WHST of 1.92 g_{catalyst} h g_{FFR} ⁻¹ (WHSV = 0.5 g_{FFR} h⁻¹ g_{catalyst} ⁻¹), as shown in Fig. 5.8. At the lower end of the investigated range, where the Cu to Fe was 0.5, the observed FFR conversion and 2-MeF selectivity were moderately high at 82% and 73.8%, respectively. Meanwhile, the selectivity towards FAL, an intermediate formed through the hydrogenation of FFR's carbonyl moiety, was notably elevated at 20.6%. By-products such as 2-PON and 2-POL were also detected, albeit with low selectivity (3.2%). As the Cu to Fe increased

to 1, the catalyst's activity and selectivity towards 2-MeF both improved significantly, reaching nearly 100% and 90%, respectively. Simultaneously, the selectivity towards FAL decreased substantially to 6% and by-products selectivity only showed a minor increase to 3.8%. As the Cu to Fe ratio further increased to 1.5 and subsequently 2, the conversion first dropped to 92.5 and then to 78%. The 2-MeF selectivity exhibited a similar trend, falling off to 81.5% and then 64.2% as the Cu/Fe ratio rose to 1.5 and 2, respectively. Conversely, the selectivity to FAL shot up rapidly, reaching a value of 34.3% at Cu/Fe = 2. Like 2-MeF, formation of by-products also fell with increasing Cu to Fe ratios.

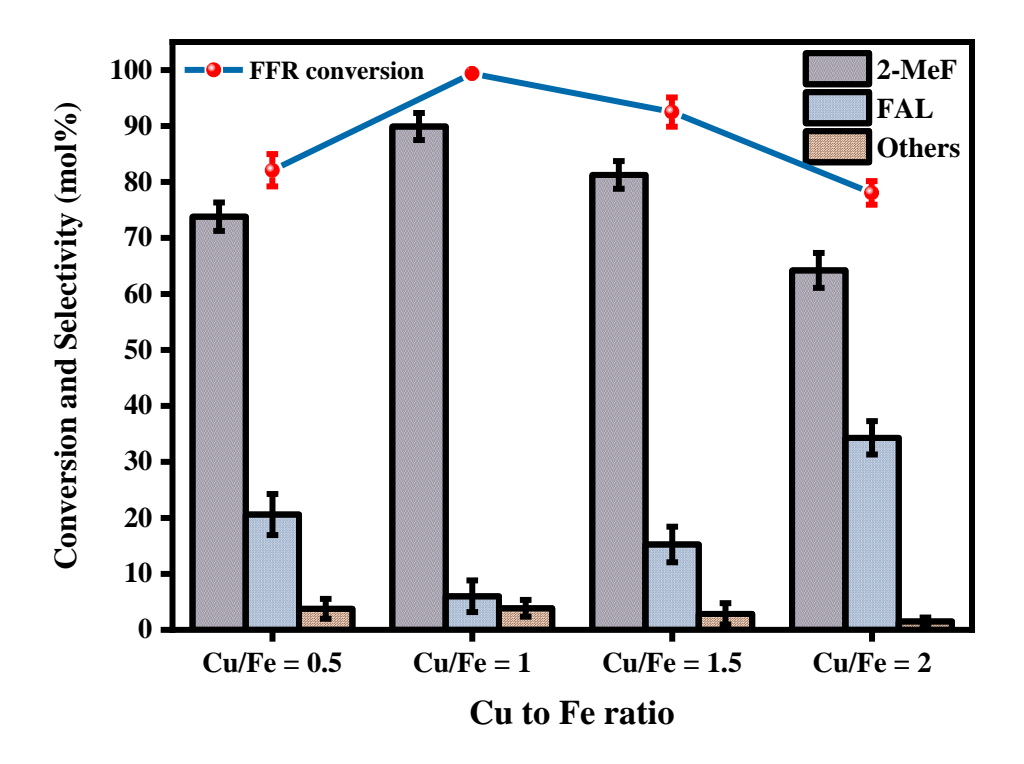


Fig. 5.8 Effect of Cu to Fe molar ratio on conversion and product selectivities during FFR HDO. Reaction conditions: feed flowrate = $5.43 \text{ mmol}_{FFR} \text{ h}^{-1}$, $\text{H}_2/\text{FFR} = 15$, Temperature = $230 \, ^{\circ}\text{C}$, WHSV = $0.5 \, \text{g}_{FFR} \, \text{h}^{-1} \, \text{g}_{catalyst}^{-1}$, Pressure = 1 atm.

From the above results, it is clear that the Cu to Fe molar ratio has a significant bearing on the activity as well as selectivity of the synthesized catalysts. In order to understand the observed trends, it is crucial to explore the insights gained from the characterization analyses. The combination of weak acidic sites and limited H₂ availability owing to lower Cu loading in the catalyst with Cu to Fe ratio of 0.5 resulted in insufficiently strong binding of the FFR molecule and incomplete deoxygenation, respectively, explaining the moderate conversion and selectivity to 2-MeF, along with the substantial selectivity of FAL.

In contrast, when the Cu and Fe were in equimolar amounts, Fe was seen to have a promotional role on Cu dispersion, giving rise to more dispersed CuO as seem from XRD and TPR analysis. Additionally, the TPR analysis also revealed a dramatic increase in the reducibility of Fe, leading to the formation of the Fe₃O₄, as confirmed by reduced XRD analysis. Consequently, the catalyst now boasted markedly higher acidic sites of medium-strength along with some strong sites, enabling the stronger binding of the FFR molecule. Moreover, there was increased availability of H₂ from spillover due to the higher amount of Cu⁰ species at this Cu/Fe ratio, facilitating both increased conversion and improved selectivity to 2-MeF. However, in the presence of excess Cu (when Cu/Fe = 1.5 and 2), there was a noticeable decrease in the reducibility of Cu itself, evident from the results of the H₂-TPR analysis. This finding was further validated by the appearance of peaks corresponding to Cu₂O and CuO in the diffraction patterns of these peaks. The incomplete reduction of Cu oxides resulted in a heightened presence of medium- and strong-strength acidic sites. This increase in acidity could lead to overly strong binding of reactant and product molecules to the active sites, hindering their easy desorption. This phenomenon also has the potential to accelerate catalyst deactivation over extended reaction periods or convert the desired product into undesired by-products. Notably, the intensity of peaks corresponding to Cu⁰ also decreased substantially, indicating a reduction in the quantity of Cu⁰ species responsible for activating and supplying the H₂ required for FFR deoxygenation. Despite the continued presence of the active Fe₃O₄ phase in the catalysts, the combined effect of increased acidity and reduced H₂ availability contributed to significant reduction in reactant conversion and target product selectivity. To conclude, the optimum values of conversion and 2-MeF selectivity over the catalyst with Cu/Fe = 1 could be assigned to comparatively better Cu dispersion, presence of ample number of acidic sites of appropriate strength, along with sufficient H atoms on the surface through spillover and lastly, strong synergistic interaction between the in-situ generated Cu⁰ and Fe₃O₄, as represented in Fig. 5.9.

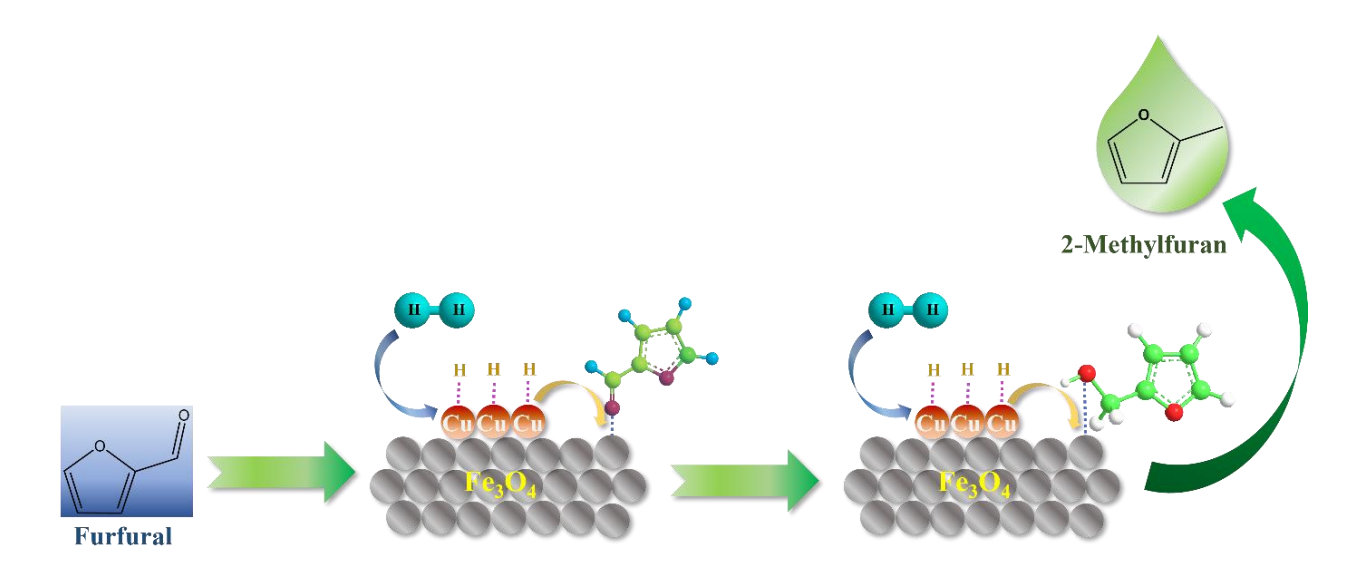


Fig. 5.9 Probable FFR HDO to 2-MeF mechanism over Cu-Fe catalyst with Cu/Fe = 1.

5.2.2 Effect of reaction conditions on FFR HDO over Cu-Fe mixed oxide catalyst with Cu/Fe = 1

During the initial evaluation of the prepared catalysts, it was noted the Cu-Fe mixed oxide catalyst featuring a Cu/Fe ratio of 1 exhibited the highest selectivity of 2-MeF among the various catalysts under the initial reaction conditions. Consequently, this particular catalyst was chosen for subsequent investigations into the impact of reaction parameters on the selectivity of the target compound.

5.2.2.1 Effect of reaction temperature

Fig. 5.10 illustrates the impact of temperature on FFR conversion and 2-MeF selectivity over the catalyst with Cu/Fe = 1. Decreasing the temperature from 230 °C to 210 °C resulted in a minimal change in conversion, which remained above 99%. However, product selectivities exhibited variation, with 2-MeF selectivity dropping to 84.2% and FAL selectivity rising to 11%. By-product selectivity also decreased slightly to 3%. Further reduction in reaction temperature to 190 °C and 170 °C led to noticeable declines in conversion to 95.3% and 88%, respectively. Simultaneously, 2-MeF selectivity decreased to 76% and 62.4%, while FAL selectivity increased to 19.3% and 34% as the temperature dropped to 190 and 170 °C, respectively. By-product selectivity mimicked the trend of 2-MeF selectivity, decreasing as the evaluation was carried out at lower temperatures. The reduced conversion and 2-MeF selectivity at low reaction temperatures can be attributed to Cu's poor hydrogen activation/dissociation ability, and weaker binding with the activated H atoms adsorbed on the surface, allowing for

their easy desorption [24–27]. Furthermore, Cu has been known to interact more strongly with FFR in comparison to FAL. Therefore, despite their specificity towards the C=O bond, Cu-based catalysts are unable to completely deoxygenate it at low reaction temperatures, leading to incomplete conversion, reduced 2-MeF selectivity and elevated FAL selectivity.[16,28] Meanwhile, when the reaction was carried out at an elevated temperature of 250 °C, the reactant was completely converted. However, at this temperature, the selectivity towards both 2-MeF and FAL decreased sharply to 77% and 0.6%, respectively. Instead, by-products such as 2-PON, 2-POL and 1-POL were formed in a much higher amount with a combined selectivity of 20.3%. The reduction in 2-MeF selectivity at this temperature can be ascribed to Cu becoming increasingly active not only towards H₂ activation and hydrogenolysis of C-O bond in FAL but also the over-hydrogenolysis of 2-MeF itself [16,17,29]. Consequently, at such elevated reaction temperatures, C₅ ring opening products such as 2-POL and 1- and 2-POL are formed from 2-MeF hydrogenolysis in larger amounts [16,17,29]. In the light of these trends, the optimum selectivity observed at 230 °C points towards a delicate balance being achieved at this temperature - the catalyst was quite active towards the hydrogenolysis of C-O bond of FAL but not too active to cause the over-hydrogenolysis of 2-MeF. Overall, the results obtained here highlight the crucial role of temperature in influencing and/or optimizing selectivity towards 2-MeF.

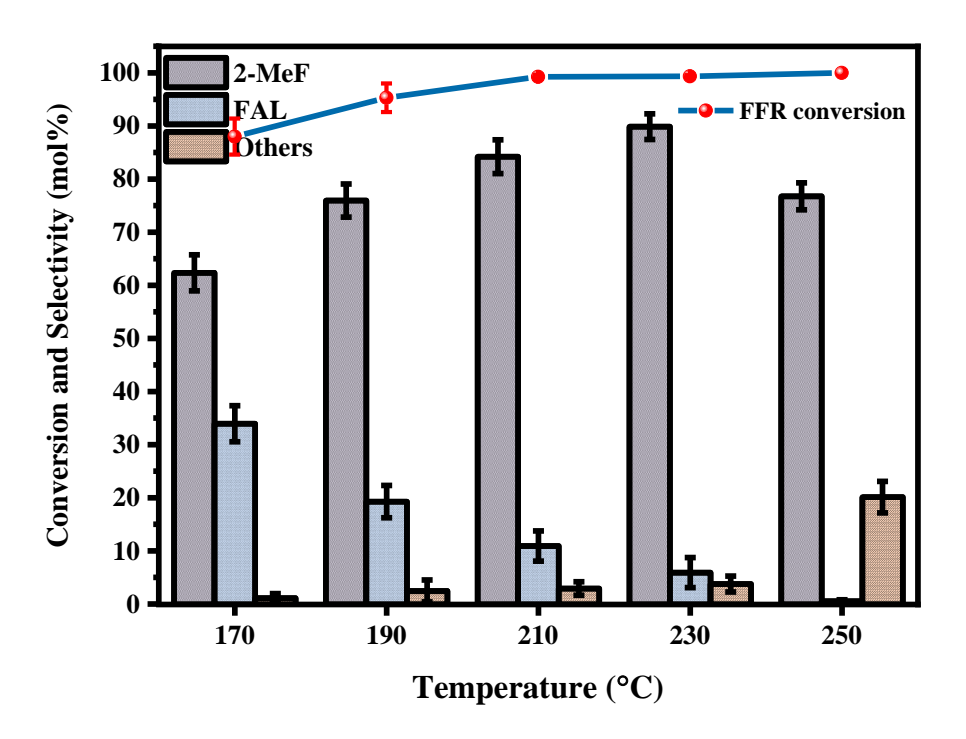


Fig. 5.10 Effect of reaction temperature on conversion and product selectivities during FFR HDO over Cu-Fe mixed oxide catalyst with Cu/Fe = 1. Reaction conditions: feed

flowrate: $5.43 \text{ mmol}_{FFR} \text{ h}^{-1}$, $H_2/FFR = 15$, $WHSV = 0.5 \text{ g}_{FFR} \text{ h}^{-1} \text{ g}_{catalyst}^{-1}$, Pressure = 1 atm.

5.2.2.2 Effect of WHSV

Fig. 5.11 presents the results of investigating the influence of varying space velocity (WHSV) on the selectivity towards 2-MeF over Cu-Fe oxide catalyst with Cu/Fe = 1. Previously during the investigation on the effect of temperature, an optimum selectivity of 90% was observed at 230 °C while the space velocity was maintained at 0.52 g_{FFR} h⁻ ¹ g_{catalyst} ⁻¹. Now, in order to explore the role of WHSV, additional investigations were carried out at increased space velocity values of 1, 2 and 3 g_{FFR} h⁻¹ g_{catalyst} -1. With increase in WHSV from 0.5 to 1 g_{FFR} h⁻¹ g_{catalyst} -1 led to a 10% drop in FFR conversion; the reduction for 2-MeF selectivity, on the other hand, was comparatively lower at 5.5%, resulting in a selectivity of 84.5%. Further increases in space velocity to 2 and 3 g_{FFR} h⁻¹ g_{catalyst} ⁻¹ led to the conversion dropping to 79.3% and 62% respectively. 2-MeF selectivity followed a similar trend, declining sharply to 55% as the space velocity increased to 3 g_{FFR} h⁻¹ g_{catalyst} -1. The selectivity of by-products, once again mirrored the trend of 2-MeF, reaching a very low value of 0.7% at a WHSV value of 3 g_{FFR} h⁻¹ g_{catalyst} ⁻¹. Concurrently, FAL selectively rose rapidly, reaching a high value of 42.4% at a space velocity of 3 g_{FFR} h⁻¹ g_{catalyst} -1. The increase in space velocity resulted in a reduction in residence/contact time, limiting the time available for FFR and FAL, the key intermediate in the process, to undergo further conversion [16,28]. Consequently, not only was FFR partially converted but the selectivity to 2-MeF also decreased, while the selectivity to FAL became considerably higher.

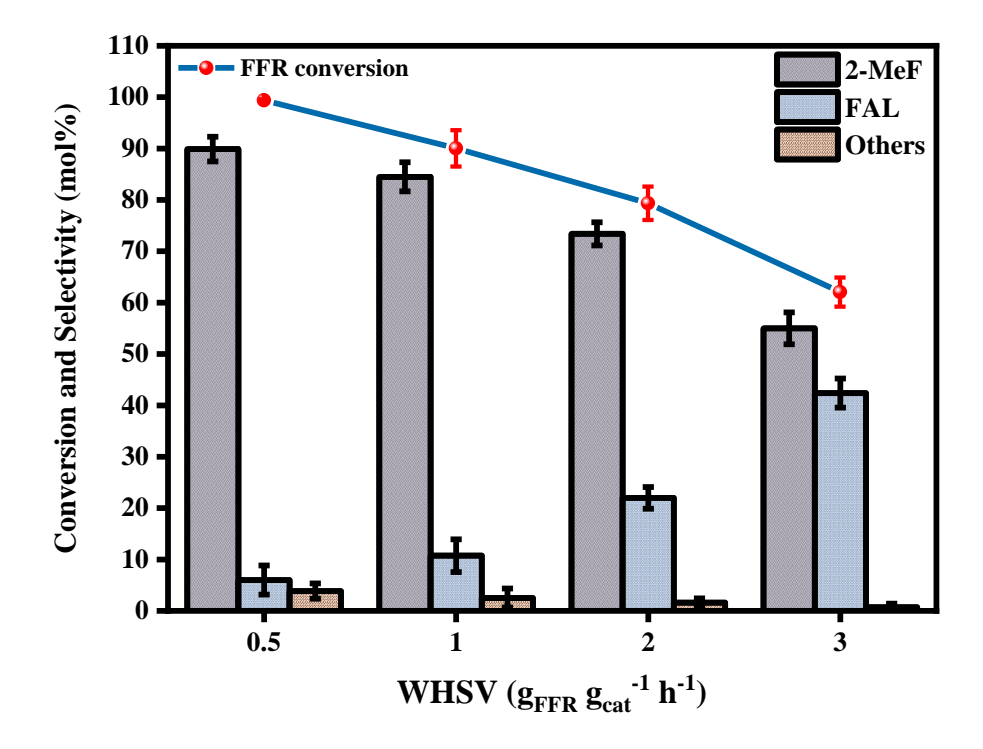


Fig. 5.11 Effect of WHSV on conversion and product selectivities during FFR HDO over Cu-Fe mixed oxide catalyst with Cu/Fe = 1. Reaction conditions: $H_2/FFR = 15$, Temperature = 230 °C, Pressure = 1 atm.

5.2.2.3 Effect of reduction temperature

The reducibility of Fe introduces complexity, as it can exist in multiple oxidation states (Fe³⁺, Fe²⁺ and Fe⁰) depending upon the reduction temperature, as seen in Fig. 5.2 (reduced XRD). Notably, the available literature points towards a catalytic significance of Fe₃O₄ in FFR HDO. The presence of Cu, however, further complicates this scenario as it is known to significantly influence the reducibility of Fe. Therefore, exploring the impact of reduction temperature becomes crucial to elucidate the role of different Fe species in shaping the catalyst's activity. With this in mind, the catalytic activity of the Cu-Fe mixed oxide catalyst with Cu/Fe = 1 was evaluated at two additional reduction temperatures: 450 °C and 550 °C (Fig. 5.12). Previously when the investigation was carried out with the catalyst reduced at 350 °C, near complete FFR conversion and a 90% selectivity to 2-MeF were noted, which could be ascribed to the synergistic interaction between Cu and Fe₃O₄. When the reduction temperature was raised to 450 °C, a massive drop was observed in FFR conversion and 2-MeF selectivity, which fell to 50.8% and 38.3%, respectively. FAL selectivity, meanwhile, surged to 58.8%. Increasing the reduction temperature further to 550 °C caused the conversion to fall to an even lower value of 21.2%. The 2-MeF selectivity followed a similar trend, plummeting to just 4% while FAL selectivity soared to 92%.

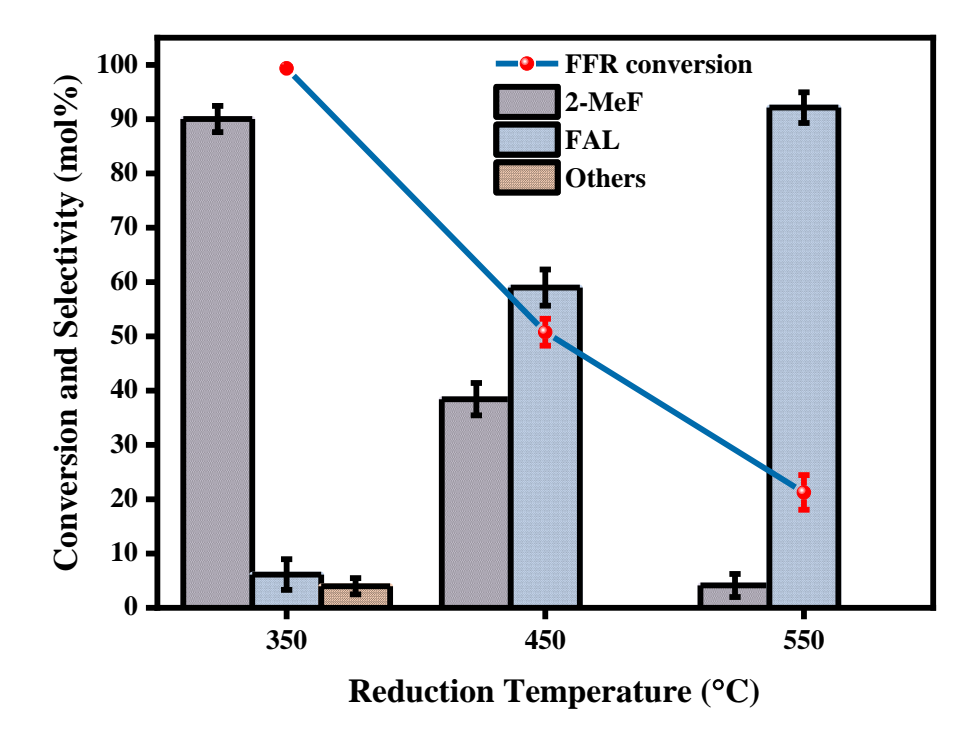


Fig. 5.12 Effect of reduction temperature on conversion and product selectivities during FFR HDO over Cu-Fe mixed oxide catalyst with Cu/Fe = 1. Reaction conditions: feed flowrate = $5.43 \text{ mmol}_{FFR} \text{ h}^{-1}$, $\text{H}_2/\text{FFR} = 15$, Temperature = $230 \, ^{\circ}\text{C}$, WHSV = $0.5 \, \text{g}_{FFR} \, \text{h}^{-1} \, \text{g}_{\text{catalyst}}^{-1}$, Pressure = 1 atm.

To gain a comprehensive understanding of these drastic changes in conversion and product selectivity, it is once again imperative to closely examine the insights from characterization analyses. The XRD analysis of the catalysts (Fig. 5.13) divulged a significant transformation: when subjected to reduction at 450 °C, the active Fe₃O₄ phase was entirely reduced, evident from the disappearance of its peaks. In its stead, peaks corresponding to (110) and (220) lattice planes of Fe⁰ emerged at 44.7° and 65°[30], intensifying as the reduction temperature further increased to 550 °C. XPS analysis of the reduced samples, shown in Fig. 14, showcased peaks indicative of metallic Fe at 707 and 720 eV [31], affirming the formation of Fe⁰ through reduction at 450 and 550 °C. However, it is worth noting here that the XPS analysis also included peaks attributed to Fe²⁺ and Fe³⁺ species, signifying the presence of some Fe in an oxidized form possibility due to potential surface oxidation associated with ex-situ XPS analysis. Arias and team [30], in their investigation on selective hydrogenation of biomass-based platform chemicals, with Cu-Fe bimetallic catalysts, reported similar results where the XRD analysis only revealed the presence of metallic Cu and Fe while XPS analysis pointed towards the presence of some Fe²⁺ and Fe³⁺ species when the reduction temperature was 450 °C. It is also equally crucial to note that during the entire

duration of the catalytic activity evaluation – encompassing both reduction and reaction – the catalyst is consistently in a reductive environment. As a consequence, the existence of these oxides species is unlikely. Even if, by any chance, they did exist, their presence would in exceedingly minute quantities. Therefore, it is reasonable to conclude that after reduction at 450 and 550 °C, the catalyst would consist predominantly of metallic Cu and Fe, with a very small amount of oxide species. With the oxide species now completely reduced, the acidity of the catalyst would essentially plummet to near zero. This loss of essential acidic sites hampers the catalyst's ability to bind FFR and FAL molecules, explaining the drastic reduction in conversion and selectivity to the target product. It is therefore clear that 350 °C is the optimum reduction temperature for the catalyst to achieve the highest conversion and 2-MeF selectivity.

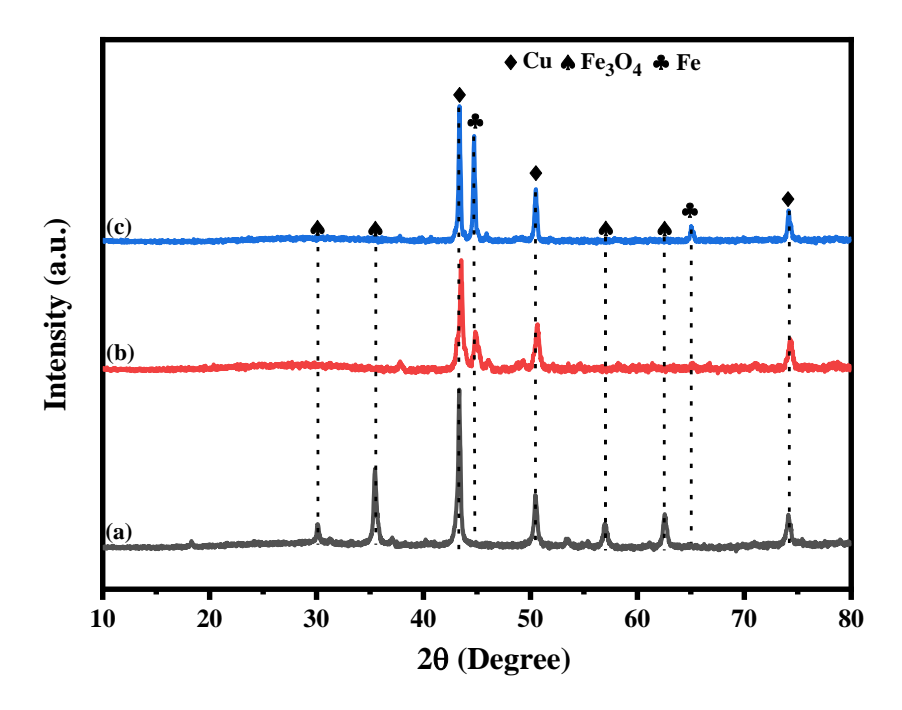


Fig. 5.13 XRD diffractograms of Cu-Fe oxide catalyst with Cu/Fe = 1 reduced at (a) 350 °C, (b) 450 °C and (c) 550 °C.

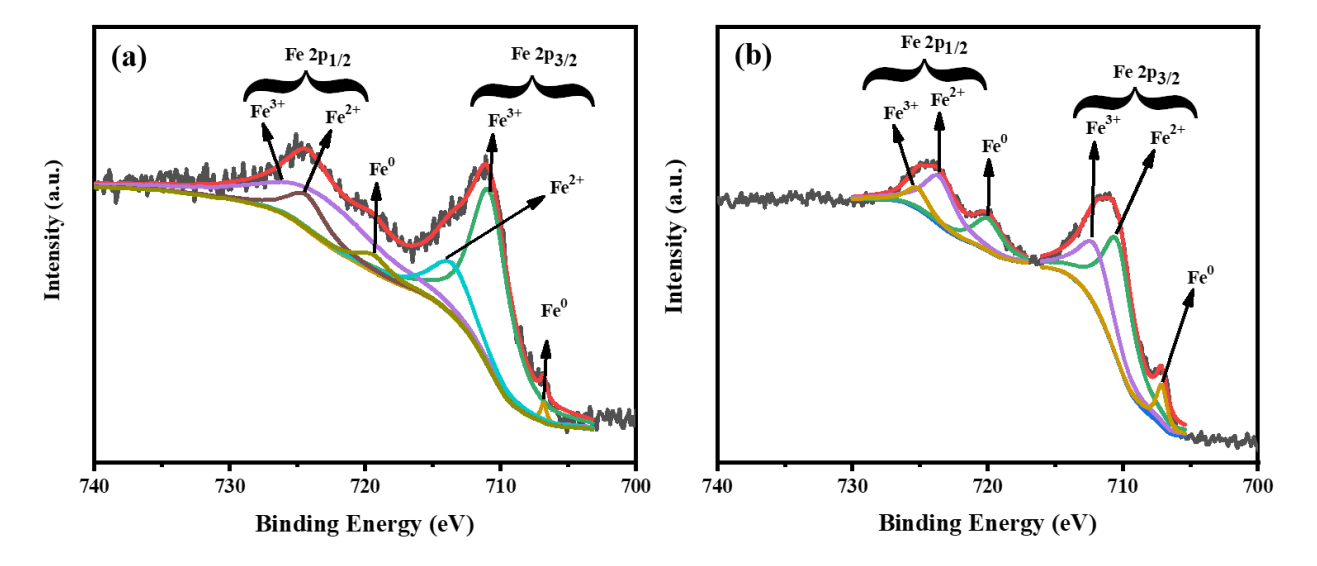


Fig. 5.14 Fe 2p XPS spectrum of Cu-Fe oxide catalyst with Cu/Fe = 1 reduced at (a) $450 \,^{\circ}$ C, and (b) $550 \,^{\circ}$ C.

5.2.2.4 Effect of H₂/FFR ratio

Vapor phase reactions for HDO of biomass-derived platform chemicals and/or oxygenates such as FFR, guaiacol, phenol, etc. are commonly carried out in the presence of excess amount of H₂, with the H₂ to oxygenate molar ratio lying between 20 and 50 [32–34]. There are various strategic reasons behind the usage of H₂ in such large excesses in HDO reactions. To begin with, surplus of H₂ ensures a continuous and ample supply of H atoms, which is pivotal for the hydrogenation integral to HDO. These hydrogenation reactions are essentially eliminating oxygen from the biomass oxygenates, transforming them into valuable compounds. Additionally, the presence of excess H₂ promotes the activation of oxygen-containing functional groups, [34]. Furthermore, H₂ often functions as a carrier gas in vapor-phase reactions [35], but also helps prevent or mitigate catalyst deactivation when present in excess [35–37]. While utilizing excess H₂ in vapor-phase HDO reactions offers various advantages, there are also notable disadvantages associated with this approach. The use of excess H₂ can contribute to higher operational expenses, increased energy consumption during the separation and recovery processes, and can lead to the overreduction of crucial intermediate species as well as the target production, altering the selectivity and leading to the formation of numerous undesired by-products. [36] Hence, optimization of H₂ usage in HDO reactions becomes a very critical aspect of process design.

Considering these factors, the H₂/FFR molar ratios was varied from 5 to 15 to explore its impact on FFR conversion and 2-MeF selectivity over Cu-Fe mixed catalyst

with Cu/Fe = 1, at optimized reactions conditions of 230 °C and 0.5 g_{FFR} h⁻¹ g_{catalyst} -1 (Fig. 5.15). Under these optimized conditions and a H₂/FFR molar ratio of 15, FFR was almost completely converted while the selectivity was 90%. Lowering the H₂/FFR molar ratio to 10 showed no change in either conversion or 2-MeF selectivity values, which aligns with expectations given that H₂ is still in quite a large excess and high activity of Cu towards hydrogenolysis at elevated temperatures. However, with further reduction in the H₂/FFR ratio to 5, changes in conversion and product selectivity become apparent. The conversion decreased by around 19%, reaching a value of 81%. The reduction in 2-MeF selectivity was more pronounced, dropping to 59% while the FAL selectivity soared up to nearly 38%. By-product formation also slows down, evident from a very low selectivity value of 0.6%. The results suggest that dropping down the H₂/FFR value due to 5 significantly reduced the amount of H atoms available on the surface, not only slowing down the conversion of FFR but also the hydrogenolysis of FAL. This aligns with findings reported by Taylor et. al. [38] in their study on FFR hydrodeoxygenation over Pt(111), where a high H₂/FFR ratio at the surface promotes FFR hydrogenation to FAL and FAL hydrogenolysis to 2-MeF while suppressing carbon deposition. Pourzolfaghar et. al. [34], in their investigation on phenol hydrodeoxygenation, also reported that a high H₂ to phenol not only increased phenol conversion but also increased the degree of deoxygenation. In conclusion, the investigation into varying H₂/FFR molar ratios revealed that maintaining a ratio of 10 or higher provided optimal FFR conversion and 2-MeF selectivity. However, a ratio below 10 led to noticeable decline in both conversion and selectivity, emphasizing the important role of hydrogen availability.

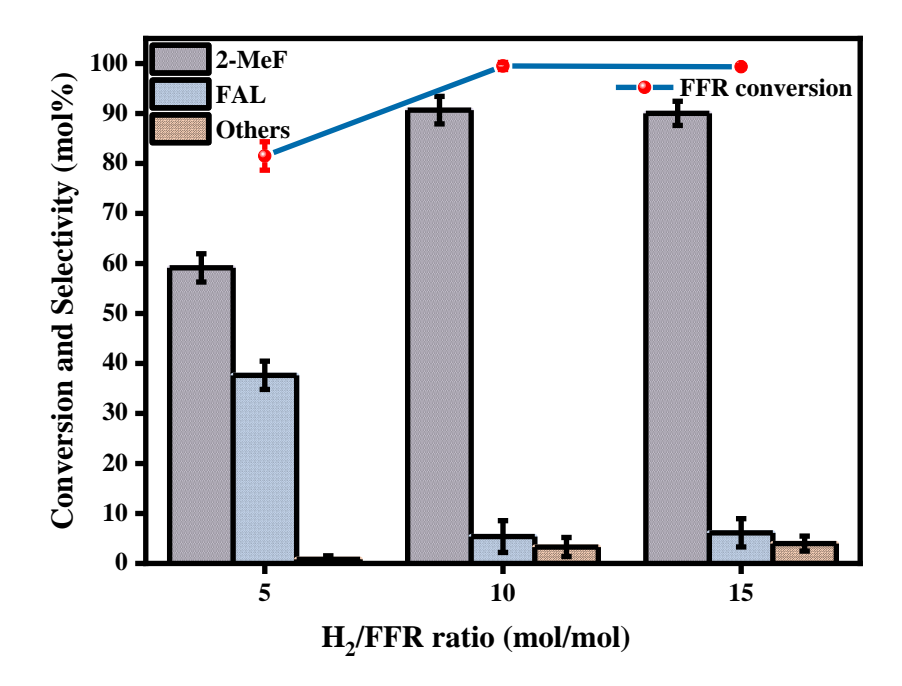


Fig. 5.15 Effect of H₂/FFR molar ratio on conversion and product selectivities during FFR HDO over Cu-Fe mixed oxide catalyst with Cu/Fe = 1. Reaction conditions: feed flowrate = $5.43 \text{ mmol}_{\text{FFR}} \text{ h}^{-1}$, Temperature = $230 \, ^{\circ}\text{C}$, WHSV = $0.5 \, \text{g}_{\text{FFR}} \text{ h}^{-1} \, \text{g}_{\text{catalyst}}^{-1}$, Pressure = $1 \, \text{atm.}$

5.2.3 Catalyst Stability and Regeneration

To assess catalyst stability over prolonged operation, a 24-h time-on-stream (TOS) study was conducted (Fig. 5.16). During the initial 12 h, the catalyst maintained a consistent conversion rate above 99%, after which a gradual decline ensued. Even at the end of 24 h period, the conversion remained robust at 93.7%, which can possibly be attributed to the high activity of Cu towards the activation of both C=O and C-O bonds at higher reaction temperatures and presence of large excess of H₂. The trend observed in 2-MeF selectivity mirrored that of conversion, remaining stable around 90% for the first 12 h before experiencing a gradual decline. However, after the 16 h mark, the decline became more pronounced, reaching 55% by the end of the TOS study. FAL selectivity, initially steady at 6.5%, began to rise steadily as deactivation set in. Notably, the increase in FAL selectivity became more prominent after 16 h, nearly tripling over the course of the next 8 h and reaching a final value of 43.8%.

While catalyst deactivation was not explicitly studied in this study, the changes observed in conversion and product selectivity here can still be explained by drawing upon the insights previously reported in published literature. In a study by MacIntosh and Beaumont on FFR hydrogenation over supported Ni metal catalysts, deactivation

was linked to the formation of oligomeric and/or polymeric condensation compounds originating from FFR and FAL [39]. Similarly, Du and colleagues, exploring FFR hydrogenation to FAL over silica supported Cu catalysts, associated deactivation with carbon deposition resulting from the polymerization products of FFR and FAL [40]. The investigation of Jiménez-Gómez et. al.[28] supports these findings, linking the deactivation of their mesoporous silica supported Cu catalyst to the formation of carbonaceous deposits resulting from the formation of oligomeric compounds. In addition, they noted that stronger adsorption of FFR and FAL may also contribute to deactivation via site blocking [28]. In the light of this understanding, the likely cause of catalyst deactivation in this study involves strong adsorption of FFR and FAL, along with the formation of their oligomerization products, leading in site and/or pore blockage.

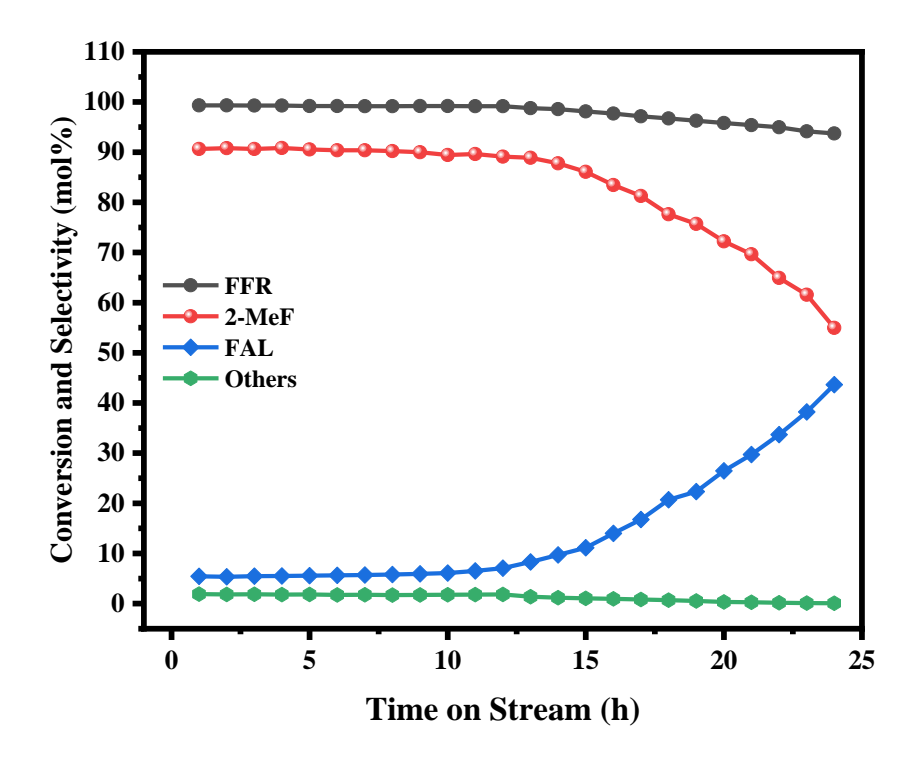


Fig. 5.16 Time-on-stream (TOS) study for FFR HDO over Cu-Fe mixed oxide catalyst with Cu/Fe = 1. Reaction conditions: feed flowrate = $5.43 \text{ mmol}_{FFR} \text{ h}^{-1}$, H₂/FFR = 10, Temperature = $230 \, ^{\circ}\text{C}$, WHSV = $0.5 \, \text{g}_{FFR} \, \text{h}^{-1} \, \text{g}_{catalyst}^{-1}$, Pressure = 1 atm, TOS = $24 \, \text{h}$.

To assess the catalyst's resilience and its potential for sustained catalytic performance, a regeneration study was conducted after the initial cycle of extended TOS reactions lasting 24 h. This involved a sequential process, beginning with calcination at 500 °C in air, followed by reactivation in an H₂ atmosphere, both performed within the fixed-bed reactor unit. Subsequently, the regenerated catalyst underwent a second 24 h TOS

cycle, aiming to provide insights into the catalyst's stability and its capacity to maintain effectiveness over multiple reaction cycles. Fig. 5.17 illustrates the results of the regeneration study, indicating a partial recovery of catalytic activity after the regeneration process. The catalyst maintained a consistent conversion of 85% for approximately 10 h, after which a gradual decline ensured, accelerating over time and leading to a final value of 68%. While product selectivity did not exhibit drastic changes, some variations were observed. 2-MeF was still the major product, with a nearly constant selectivity of about 86% in the initial 10 h. However, its selectivity began declining rapidly after 14 h, dropping to 46.5% at the end of 24 h period. Initially stable at 9.5%, FAL selectivity rose rapidly after 14 h on stream, more than tripling to 52% at the end of 24 h period. The observed changes in catalytic performance could be attributed to sintering resulting from extended exposure to elevated temperatures during the reduction, TOS and calcination steps, affecting the catalyst's morphology and influencing its stability over time.

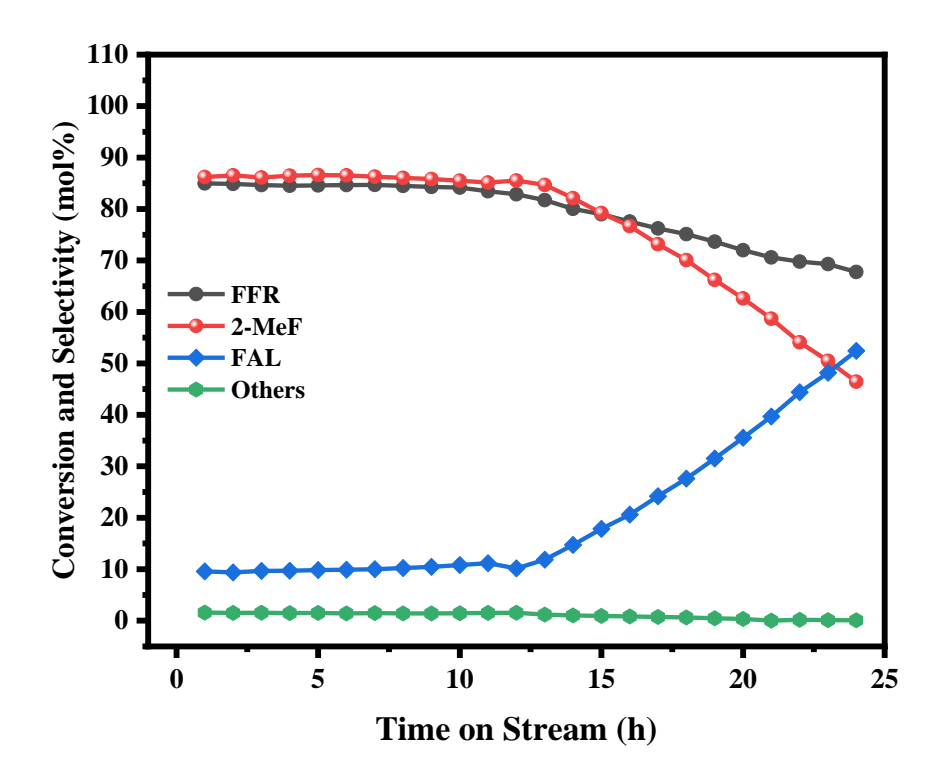


Fig. 5.17 Regeneration study for FFR HDO over Cu-Fe mixed oxide catalyst with Cu/Fe = 1. Reaction conditions: feed flowrate = $5.43 \text{ mmol}_{FFR} \text{ h}^{-1}$, $\text{H}_2/\text{FFR} = 10$, Temperature = $230 \, ^{\circ}\text{C}$, WHSV = $0.5 \, \text{g}_{FFR} \, \text{h}^{-1} \, \text{g}_{catalyst}^{-1}$, Pressure = 1 atm, TOS = $24 \, \text{h}$.

References

- [1] G. Wang, W. An, Y. Zhang, Z. Liu, S. Yang, P. Jin, D. Ding, Mesoporous carbon framework supported Cu-Fe oxides as efficient peroxymonosulfate catalyst for sustained water remediation, Chem. Eng. J. 430 (2022) 133060. https://doi.org/10.1016/j.cej.2021.133060.
- [2] H. Zheng, J. Huang, T. Zhou, Y. Jiang, Y. Jiang, M. Gao, Y. Liu, Recyclable magnetic Cu/CuFe2O4 nanocomposites for the rapid degradation of 4-NP, Catalysts. 10 (2020) 1–11. https://doi.org/10.3390/catal10121437.
- [3] M. Kalong, A. Srifa, P. Hongmanorom, C. Cholsuk, W. Klysubun, S. Ratchahat, W. Koo-amornpattana, P. Khemthong, S. Assabumrungrat, S. Kawi, Catalytic transfer hydrogenation of furfural to furfuryl alcohol and 2-methylfuran over CuFe catalysts: Ex situ observation of simultaneous structural phase transformation, Fuel Process. Technol. 231 (2022). https://doi.org/10.1016/j.fuproc.2022.107256.
- [4] V.D.B.C. Dasireddy, K. Bharuth-Ram, D. Hanzel, B. Likozar, Heterogeneous Cu-Fe oxide catalysts for preferential CO oxidation (PROX) in H2-rich process streams, RSC Adv. 10 (2020) 35792–35802. https://doi.org/10.1039/d0ra06969h.
- [5] G.S. More, A. Shivhare, S.P. Kaur, T.J. Dhilip Kumar, R. Srivastava, Catalytic interplay of metal ions (Cu2+, Ni2+, and Fe2+) in MFe2O4 inverse spinel catalysts for enhancing the activity and selectivity during selective transfer hydrogenation of furfural into 2-methylfuran, Catal. Sci. Technol. 12 (2022) 4857–4870. https://doi.org/10.1039/d2cy00970f.
- [6] S.C. Yang, W.N. Su, S.D. Lin, J. Rick, J.H. Cheng, J.Y. Liu, C.J. Pan, D.G. Liu, J.F. Lee, T.S. Chan, H.S. Sheu, B.J. Hwang, Preparation of nano-sized Cu from a rod-like CuFe2O4: Suitable for high performance catalytic applications, Appl. Catal. B Environ. 106 (2011) 650–656. https://doi.org/10.1016/j.apcatb.2011.06.030.
- [7] H. Abdelli, H.I. Hamoud, J.P. Bolletta, A. Paecklar, A. Bardaoui, K.L. Kostov, E. Szaniawska, A. Maignan, C. Martin, M. El-Roz, H2 production from formic acid over highly stable and efficient Cu-Fe-O spinel based photocatalysts under flow, visible-light and at room temperature conditions, Appl. Mater. Today. 31 (2023) 101771. https://doi.org/10.1016/j.apmt.2023.101771.
- [8] K. Yan, A. Chen, Selective hydrogenation of furfural and levulinic acid to biofuels on the ecofriendly Cu-Fe catalyst, Fuel. 115 (2014) 101–108. https://doi.org/10.1016/j.fuel.2013.06.042.
- [9] Y. Zhu, L. Jin, Y. Wang, B. Hu, J. Li, B. Hu, X. Liu, Selective catalytic oxidation of phenylcarbinol with Fe-doped Cu/SBA-15 catalyst: A study on the synergistic effect of Cu-Fe metals, Mol. Catal. 551 (2023). https://doi.org/10.1016/j.mcat.2023.113649.
- [10] J. Luo, Y. Cheng, H. Niu, T. Wang, C. Liang, Efficient Cu/FeOx catalyst with developed structure for catalytic transfer hydrogenation of furfural, J. Catal. 413 (2022) 575–587. https://doi.org/10.1016/j.jcat.2022.07.013.
- [11] O.A. Bulavchenko, Z.S. Vinokurov, A.A. Saraev, A.M. Tsapina, A.L. Trigub,

- E.Y. Gerasimov, A.Y. Gladky, A. V. Fedorov, V.A. Yakovlev, V. V. Kaichev, The Influence of Cu and Al Additives on Reduction of Iron(III) Oxide: In Situ XRD and XANES Study, Inorg. Chem. 58 (2019) 4842–4850. https://doi.org/10.1021/acs.inorgchem.8b03403.
- [12] Y. Zhou, S. Wang, M. Xiao, D. Han, Y. Lu, Y. Meng, Novel Cu-Fe bimetal catalyst for the formation of dimethyl carbonate from carbon dioxide and methanol, RSC Adv. 2 (2012) 6831–6837. https://doi.org/10.1039/c2ra20359f.
- [13] S. He, W. Wang, Z. Shen, G. Li, J. Kang, Z. Liu, G.C. Wang, Q. Zhang, Y. Wang, Carbon nanotube-supported bimetallic Cu-Fe catalysts for syngas conversion to higher alcohols, Mol. Catal. 479 (2019) 110610. https://doi.org/10.1016/j.mcat.2019.110610.
- [14] J. Zieliński, I. Zglinicka, L. Znak, Z. Kaszkur, Reduction of Fe2O3 with hydrogen, Appl. Catal. A Gen. 381 (2010) 191–196. https://doi.org/10.1016/j.apcata.2010.04.003.
- [15] A. Jaswal, P.P. Singh, A.K. Kar, T. Mondal, R. Srivastava, Production of 2-methyl furan, a promising 2nd generation biofuel, by the vapor phase hydrodeoxygenation of biomass-derived furfural over TiO2 supported Cu[sbnd]Ni bimetallic catalysts, Fuel Process. Technol. 245 (2023) 107726. https://doi.org/10.1016/j.fuproc.2023.107726.
- [16] F. Dong, Y. Zhu, H. Zheng, Y. Zhu, X. Li, Y. Li, Cr-free Cu-catalysts for the selective hydrogenation of biomass-derived furfural to 2-methylfuran: The synergistic effect of metal and acid sites, J. Mol. Catal. A Chem. 398 (2015) 140–148. https://doi.org/10.1016/J.MOLCATA.2014.12.001.
- [17] G. Singh, T.S. Khan, C. Samanta, R. Bal, A. Bordoloi, Single-step synthesis of 2-pentanone from furfural over Cu–Ni @SBA-15, Biomass and Bioenergy. 156 (2022) 106321. https://doi.org/10.1016/j.biombioe.2021.106321.
- [18] M.O. Amin, B. D'Cruz, M. Madkour, E. Al-Hetlani, Magnetic nanocomposite-based SELDI probe for extraction and detection of drugs, amino acids and fatty acids, Microchim. Acta. 186 (2019). https://doi.org/10.1007/s00604-019-3623-2.
- [19] S. Poulin, R. França, L. Moreau-Bélanger, E. Sacher, Confirmation of X-ray photoelectron spectroscopy peak attributions of nanoparticulate iron oxides, using symmetric peak component line shapes, J. Phys. Chem. C. 114 (2010) 10711–10718. https://doi.org/10.1021/jp100964x.
- [20] D. Wilson, M.A. Langell, XPS analysis of oleylamine/oleic acid capped Fe 3 O 4 nanoparticles as a function of temperature, Appl. Surf. Sci. 303 (2014) 6–13. https://doi.org/10.1016/j.apsusc.2014.02.006.
- [21] L. Zhang, J.M.M. Millet, U.S. Ozkan, Effect of Cu loading on the catalytic performance of Fe-Al-Cu for water-gas shift reaction, Appl. Catal. A Gen. 357 (2009) 66–72. https://doi.org/10.1016/j.apcata.2009.01.011.
- [22] A. Shafaei, A. Irankhah, Evaluation of Co-Fe, Cu-Fe, Ni-Al and Ni-Fe mixed oxides in catalytic combustion of methane: Comparison study and investigating the effect of preparation method, Mol. Catal. 538 (2023) 112989. https://doi.org/10.1016/j.mcat.2023.112989.

- [23] W. Gao, S. Li, H. Huo, F. Li, Y. Yang, X. Li, X. Wang, Y. Tang, R. Li, Investigation of the crystal structure of Cu-Fe bimetal oxide and their catalytic activity for the Baeyer–Villiger oxidation reaction, Mol. Catal. 439 (2017) 108–117. https://doi.org/10.1016/j.mcat.2017.06.027.
- [24] M. Luneau, J.S. Lim, D.A. Patel, E.C.H. Sykes, C.M. Friend, P. Sautet, Guidelines to Achieving High Selectivity for the Hydrogenation of α,β-Unsaturated Aldehydes with Bimetallic and Dilute Alloy Catalysts: A Review, Chem. Rev. 120 (2020) 12834–12872. https://doi.org/10.1021/acs.chemrev.0c00582.
- [25] S. Chen, R. Wojcieszak, F. Dumeignil, E. Marceau, S. Royer, How Catalysts and Experimental Conditions Determine the Selective Hydroconversion of Furfural and 5-Hydroxymethylfurfural, Chem. Rev. 118 (2018) 11023–11117. https://doi.org/10.1021/acs.chemrev.8b00134.
- [26] B. Seemala, C.M. Cai, C.E. Wyman, P. Christopher, Support Induced Control of Surface Composition in Cu-Ni/TiO2 Catalysts Enables High Yield Co-Conversion of HMF and Furfural to Methylated Furans, ACS Catal. 7 (2017) 4070–4082. https://doi.org/10.1021/acscatal.7b01095.
- [27] B. Seemala, C.M. Cai, R. Kumar, C.E. Wyman, P. Christopher, Effects of Cu-Ni Bimetallic Catalyst Composition and Support on Activity, Selectivity, and Stability for Furfural Conversion to 2-Methyfuran, ACS Sustain. Chem. Eng. 6 (2018) 2152–2161. https://doi.org/10.1021/acssuschemeng.7b03572.
- [28] C.P. Jiménez-Gómez, J.A. Cecilia, R. Moreno-Tost, P. Maireles-Torres, Selective Production of 2-Methylfuran by Gas-Phase Hydrogenation of Furfural on Copper Incorporated by Complexation in Mesoporous Silica Catalysts, ChemSusChem. 10 (2017) 1448–1459. https://doi.org/10.1002/cssc.201700086.
- [29] H.Y. Zheng, Y.L. Zhu, B.T. Teng, Z.Q. Bai, C.H. Zhang, H.W. Xiang, Y.W. Li, Towards understanding the reaction pathway in vapour phase hydrogenation of furfural to 2-methylfuran, J. Mol. Catal. A Chem. 246 (2006) 18–23. https://doi.org/10.1016/j.molcata.2005.10.003.
- [30] K.S. Arias, L. Liu, A. Garcia-Ortiz, M.J. Climent, P. Concepcion, S. Iborra, A. Corma, Bimetallic CuFe nanoparticles as active and stable catalysts for chemoselective hydrogenation of biomass-derived platform molecules, Catal. Sci. Technol. 11 (2021) 3353–3363. https://doi.org/10.1039/d1cy00339a.
- [31] Q. Xia, D. Zhang, Z. Yao, Z. Jiang, Investigation of Cu heteroatoms and Cu clusters in Fe-Cu alloy and their special effect mechanisms on the Fenton-like catalytic activity and reusability, Appl. Catal. B Environ. 299 (2021) 120662. https://doi.org/10.1016/j.apcatb.2021.120662.
- [32] S. Sitthisa, T. Sooknoi, Y. Ma, P.B. Balbuena, D.E. Resasco, Kinetics and mechanism of hydrogenation of furfural on Cu/SiO2 catalysts, J. Catal. 277 (2011) 1–13. https://doi.org/10.1016/j.jcat.2010.10.005.
- [33] L. Nie, B. Peng, X. Zhu, Vapor-Phase Hydrodeoxygenation of Guaiacol to Aromatics over Pt/HBeta: Identification of the Role of Acid Sites and Metal Sites on the Reaction Pathway, ChemCatChem. 10 (2018) 1064–1074. https://doi.org/10.1002/cctc.201701413.

- [34] H. Pourzolfaghar, F. Abnisa, W.M.A. Wan Daud, M.K. Aroua, Gas-phase hydrodeoxygenation of phenol over Zn/SiO2 catalysts: Effects of zinc load, temperature, weight hourly space velocity, and H2 volumetric flow rate, Biomass and Bioenergy. 138 (2020) 105556. https://doi.org/10.1016/j.biombioe.2020.105556.
- [35] M.S. Zanuttini, M. Gross, G. Marchetti, C. Querini, Furfural hydrodeoxygenation on iron and platinum catalysts, Appl. Catal. A Gen. 587 (2019). https://doi.org/10.1016/j.apcata.2019.117217.
- [36] W. Zhang, Y. Zhu, S. Niu, Y. Li, A study of furfural decarbonylation on K-doped Pd/Al2O 3 catalysts, J. Mol. Catal. A Chem. 335 (2011) 71–81. https://doi.org/10.1016/j.molcata.2010.11.016.
- [37] M.S. Zanuttini, M.A. Peralta, C.A. Querini, Deoxygenation of m-Cresol: Deactivation and Regeneration of Pt/γ-Al2O3 Catalysts, Ind. Eng. Chem. Res. 54 (2015) 4929–4939. https://doi.org/10.1021/acs.iecr.5b00305.
- [38] M.J. Taylor, L. Jiang, J. Reichert, A.C. Papageorgiou, S.K. Beaumont, K. Wilson, A.F. Lee, J. V. Barth, G. Kyriakou, Catalytic Hydrogenation and Hydrodeoxygenation of Furfural over Pt(111): A Model System for the Rational Design and Operation of Practical Biomass Conversion Catalysts, J. Phys. Chem. C. 121 (2017) 8490–8497. https://doi.org/10.1021/acs.jpcc.7b01744.
- [39] K.L. MacIntosh, S.K. Beaumont, Nickel-Catalysed Vapour-Phase Hydrogenation of Furfural, Insights into Reactivity and Deactivation, Top. Catal. 63 (2020) 1446–1462. https://doi.org/10.1007/s11244-020-01341-9.
- [40] H. Du, X. Ma, P. Yan, M. Jiang, Z. Zhao, Z.C. Zhang, Catalytic furfural hydrogenation to furfuryl alcohol over Cu/SiO2 catalysts: A comparative study of the preparation methods, Fuel Process. Technol. 193 (2019) 221–231. https://doi.org/10.1016/j.fuproc.2019.05.003.

This chapter investigates the catalytic performance of low loading Cu catalysts supported on rice husk-ash derived mesoporous silica support modified with metals (Al, Sn, Ti and Zr) for the vapor-phase transformation of FFR to FAL. The catalysts underwent thorough characterization employing XRD, H₂-TPR, NH₃-TPD, FTIR, N₂ physisorption, XPS, and FESEM techniques, providing comprehensive insights into their properties. The changes induced by metal incorporation in the silica matrix were thoroughly evaluated by examining the effects of incorporation with different metal, reaction temperatures, and weight hourly space velocity under atmospheric pressure conditions, providing valuable insights into the catalytic performance of these advanced materials. Following the initial assessment, the optimized catalyst underwent a rigorous long-term stability study to assess its durability under extended reaction conditions. After the first cycle of TOS reactions, the spent catalyst was first calcined at 500 °C in air, followed by re-activation in H₂ atmosphere, both inside the reactor. Finally, the regenerated catalyst underwent a second 24 h cycle of TOS reactions.

6.1 Catalyst Characterization

6.1.1 XRF

Rice husk, an agricultural byproduct produced in enormous amounts globally, is inherently rich in SiO₂, as confirmed by the XRF analysis shown in Table 6.1. The XRF results of the ash produced from untreated rice husk reveal a significant presence of metal oxides (such as K₂O, CaO, etc.) alongside silica. To enhance the silica content and remove impurities, the rice husk was treated with a 1M HNO₃ solution. This acid treatment effectively removed the metal oxides, resulting in a purified rice husk ash possessing a SiO₂ content of ~99% (table 1). Consequently, the ash produced from acid-treated rice husk can serve as an ideal source of high-purity silica for catalyst preparation, demonstrating the efficacy of the purification process.

Table 6.1 Metal content of the rice husk ash before and after acid treatment

Metal Oxides	Content (Wt.%)			
	Before Treatment	After Treatment		
Na ₂ O	0.7	0.11		
MgO	0.9	0.09		
Al ₂ O ₃	0.9	0.27		
SiO_2	88.4	98.91		
P_2O_5	1.3	0.11		
SO_3	1.8	0.04		
Cl	0.3	0.03		
K_2O	3.2	0.07		
CaO	2.4	0.07		
TiO_2	1.3	0		
Fe ₂ O ₃	1.3	0.20		

6.1.2 XRD

Fig. 6.1 displays the X-ray diffraction patterns of the calcined Cu catalysts supported on pure and metal-incorporated mesoporous silica materials. Low-angle X-ray diffraction (XRD) analysis was performed to investigate the structural properties of the synthesized mesoporous silica support material derived from rice husk. Although not depicted here, the XRD patterns exhibited faint peaks at 2θ values of 2° , 4° , and 4.6° , which are typically indicative of the highly ordered hexagonal MCM-41 structure [1]. Although the presence of these peaks hints at the potential formation of a hexagonal mesoporous framework, their faint intensity suggests a modest degree of crystallinity or order within the structure. However, with the addition of these metals, the peaks corresponding to the ordered MCM-41 structure became almost negligible. This change in peak intensity indicates a loss of order within the framework and could be attributed to the disruption to the formation of ordered structure induced by the incorporation with metals. Given the very faint peaks corresponding to the MCM-41 framework, it is more appropriate to refer to the synthesized materials as mesoporous silicas. This terminology better reflects the reduced structural order in the silica framework. In wideangle XRD analysis, a broad peak between ~20 and 35° was observed, typically associated with the amorphous silica [2]. Notably, this peak was only observed for the mesoporous silica incorporated with Al and Ti, However, this peak was notably absent in the wide-angle XRD patterns of the other three samples. One possible reason for this observation could be variations in the interaction between the incorporated metals and silica matrix, potentially altering the structural properties of the silica framework and leading to the observed differences in the XRD patterns. Additionally, the diffraction patterns of all the catalysts exhibited peaks at 20 values of 35.5°, 38.6°, 48.7°, 53.2°, 58.1°, 61.4, 66.1, 68.1°, and 74.9°, which can be ascribed to the (11 -1), (111), (20 -2), (020), (202), (11 -3), (31 -1), (220) and (004) lattice planes of monoclinic CuO (ICSD collection code: 67850) [2]. Interestingly, no diffraction peaks that may correspond to the presence of metal oxides (Al₂O₃, SnO₂, TiO₂ and ZrO₂) were observed, indicating that the added metals were perhaps either incorporated or present as amorphous and/or well-dispersed oxides on the surface of mesoporous silica [3]. Upon examination of the crystallite size (Table 8), it becomes evident that CuO species with the smallest Cu@MS. crystallite size are present on However, with the incorporation/incorporation/incorporation of metal, the crystallite size of CuO species increased slightly, with the size generally aligning with the density and size of the incorporated metal (Sn > Zr > Ti > Al). The observed increase in crystallite size in catalysts with Cu supported on metal-incorporated mesoporous silica supports could be attributed to either the formation of larger metal oxide particles or enhanced crystallinity following metal modification. As discussed later in the FESEM analysis (section 6.1.7), the incorporation of Sn and Ti resulted in a significant reduction in particle size, whereas no such change was observed for Cu@Al-MS and Cu@Zr-MS catalysts, whose particle sizes remained similar to that of the Cu@MS catalyst. Therefore, the increase in crystallite size does not appear to indicate larger particle size but is more likely due to higher crystallinity.

To gain insights into the nature of the Cu species under reaction conditions, XRD analysis was conducted on the catalysts post-reduction at 300 °C, as depicted in Fig. 6.2. The reduced Cu@MS catalyst did not show any peaks corresponding to the Cu⁰ phase, implying that the formed Cu⁰ species were likely very small and/or well-dispersed. This behavior could be attributed to the exceptionally high surface area of the pure mesoporous silica support, coupled with the strong interactions between Cu

metal particles and the support. In contrast, all the metal-incorporated mesoporous silica-supported Cu catalysts exhibited pronounced peaks corresponding to the metallic Cu phase at 43.3°, 50.6°, and 74.1° [4]. No peaks indicative of CuO or Cu₂O were observed in the diffraction patterns, suggesting that CuO was either completely reduced to Cu⁰ or that the remaining oxide phases were highly dispersed.

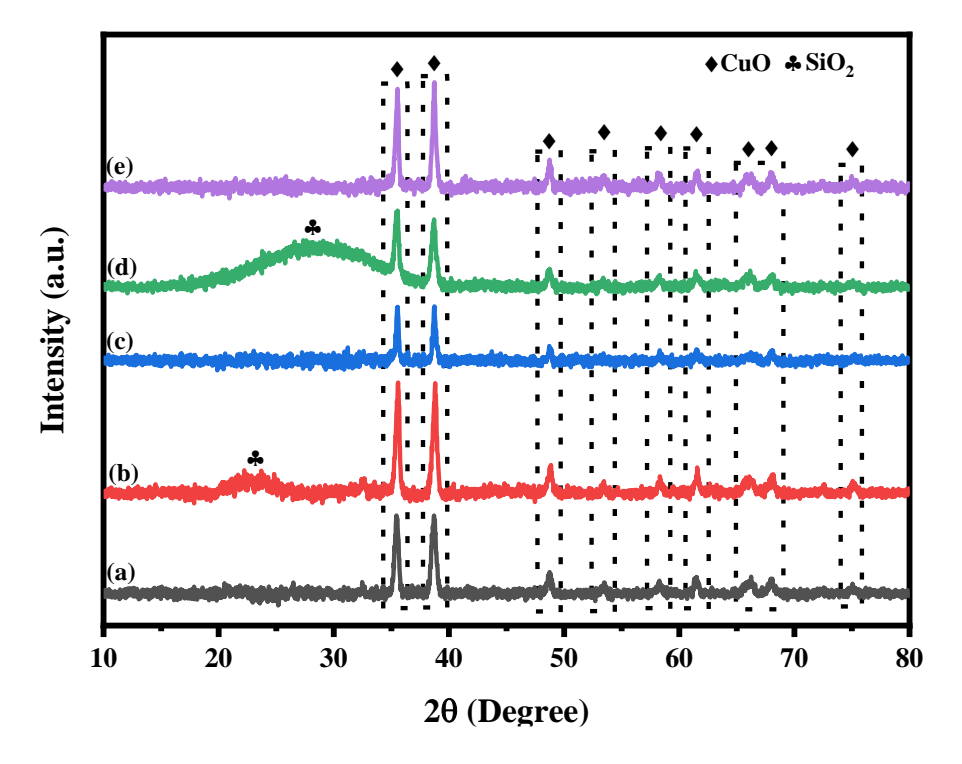


Fig. 6.1 The XRD diffractograms of the calcined (a) Cu@MS, (b) Cu@Al-MS, (c) Cu@Sn-MS, (d) Cu@Ti-MS, and (e) Cu@Zr-MS catalysts

Interestingly, the crystallite size of Cu increased after reduction in all the metal-incorporated silica-supported catalysts compared to their pre-reduction values (Table 6.2). This suggests that, despite the incorporation with metals, which typically enhances interaction between Cu and the support, some degree of sintering occurred during reduction or perhaps higher crystallinity.

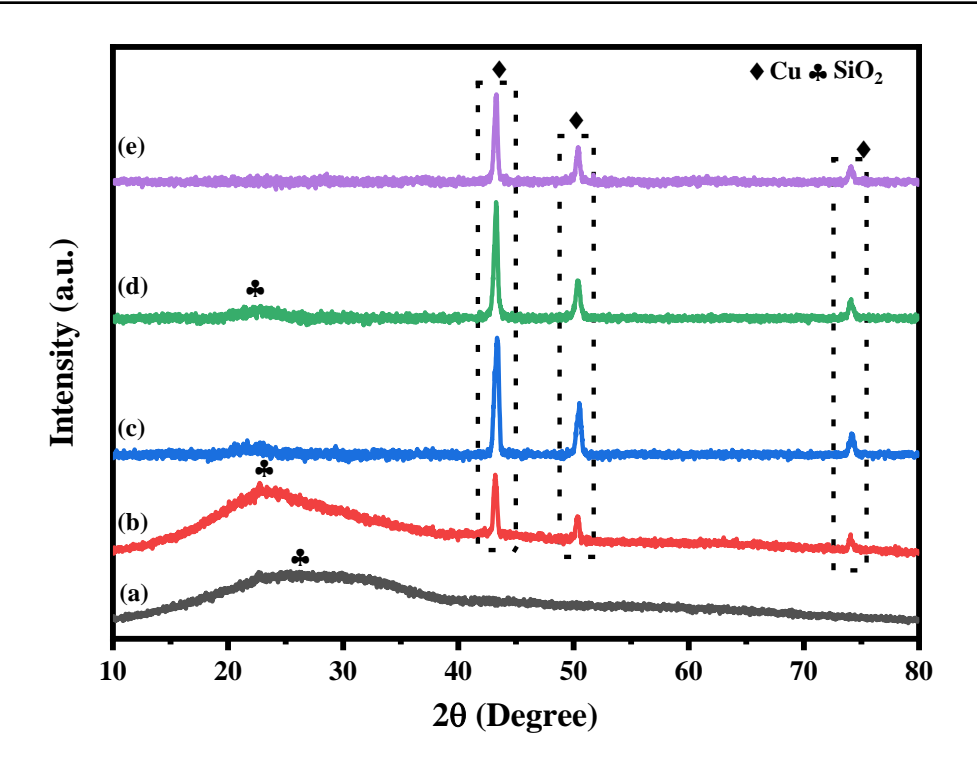


Fig. 6.2 The XRD diffractograms of the (a) Cu@MS, (b) Cu@Al-MS, (c) Cu@Sn-MS, (d) Cu@Ti-MS, and (e) Cu@Zr-MS catalysts reduced at 300 °C.

Table 6.2 Physical properties of the Cu@MS and Cu@M-MS catalysts

Catalyst	Crystallite	Crystallite	Surface	Pore	Pore
	Size	Size (Cu) ^b	Areac	Volume ^d	Size ^d
	$(CuO)^a$	(nm)	$(m^2 g^{-1})$	$(cm^3 g^{-1})$	(nm)
	(nm)				
Cu@MS	10.96	-	870.7	1.16	5.3
Cu@Al-MS	12.52	14.61	687.3	1.03	5.9
Cu@Sn-MS	21.91	25	164.4	0.38	11.5
Cu@Ti-MS	14.61	17.5	419.6	0.70	6.6
Cu@Zr-MS	17.5	22	377.8	0.47	7.03

^a Calculated using Scherrer equation at $2\theta = 38.6^{\circ}$. ^b Calculated using Scherrer equation at $2\theta = 43.4^{\circ}$ ^c Calculated using BET method. ^d Calculated using BJH method

6.1.3 FTIR

To assess the structural changes induced by metals, FTIR spectroscopy was conducted on mesoporous silica samples modified with metals (Fig. 6.3). The FTIR spectra of pure mesoporous silica support exhibited an absorption band at approximately 1060

cm⁻¹, along with the smaller shoulder band at around 1250 cm⁻¹, both of which can be ascribed to the asymmetric stretching vibrations of the Si-O-Si bonds [5–7]. A weak band was noted at ~960 cm⁻¹, ascribed to the symmetric stretching vibrations of the Si-OH group [8]. Lastly, the two bands at ~800 cm⁻¹ and ~450 cm⁻¹ correspond to the symmetric stretching and bending vibrations of Si-O-Si linkages, respectively [8]. Upon modification with metals, the absorption band at 1060 cm⁻¹ shifted to lower wavenumbers, accompanied by a decrease in intensity, indicating structural alterations in the silica framework due to interaction with the metal species. This shift and intensity reduction suggest the formation of Si-O-M (M = metal) bonds [6], confirming the incorporation of the metal species into the silica framework. Specifically, for the Snmodified mesoporous silica, this band broadened significantly, indicating much more extensive structural alteration following Sn incorporation. Similar shifts and intensity reductions were observed in other bands as well, with the reduction in intensity generally being commensurate with the size of the incorporated metal. Another approach to assess the formation of Si-O-M bonds could be through monitoring the silanol and the ring-structural Si-O bands in FTIR spectra. The silanol band predominantly represents surface Si-OH groups, with bulk Si atoms exist in forms including Si-O-Si and M-O-Si linkages [6,9]. Increasing M-O-Si linkages reduce the availability of Si atoms in Si-O-Si linkages, thereby decreasing the intensity of the silanol band in the mixed oxide structure [6,9]. Our study shows a decrease in the intensity of the silanol band with metal modification, suggesting the formation of M-O-Si bonds. Similarly, changes in the intensities of ring-structural Si-O bands observed here at 815 and 445 cm⁻¹ for pure mesoporous silica can also be correlated with the formation of M-O-Si -linkages in the mixed oxides [6]. A reduction in these band intensities after modification with metals is generally known to indicate a reduction in ring-structural Si-O bonds and the potential formation of M-O-Si linkages [6]. As was the case with the silanol band, the bands corresponds to the ring-structural Si-O bonds were also noted to have reduced in intensity following the addition of metals, further implying that the added metals had been incorporated into the silica matrix. In summary, FTIR analysis of the mixed oxide supports confirms the formation of Si-O-M bonds upon metal incorporation into mesoporous silica, evidenced by shifts in absorption bands and changes in intensity, reflecting structural alterations and the incorporation of metal species into the silica framework.

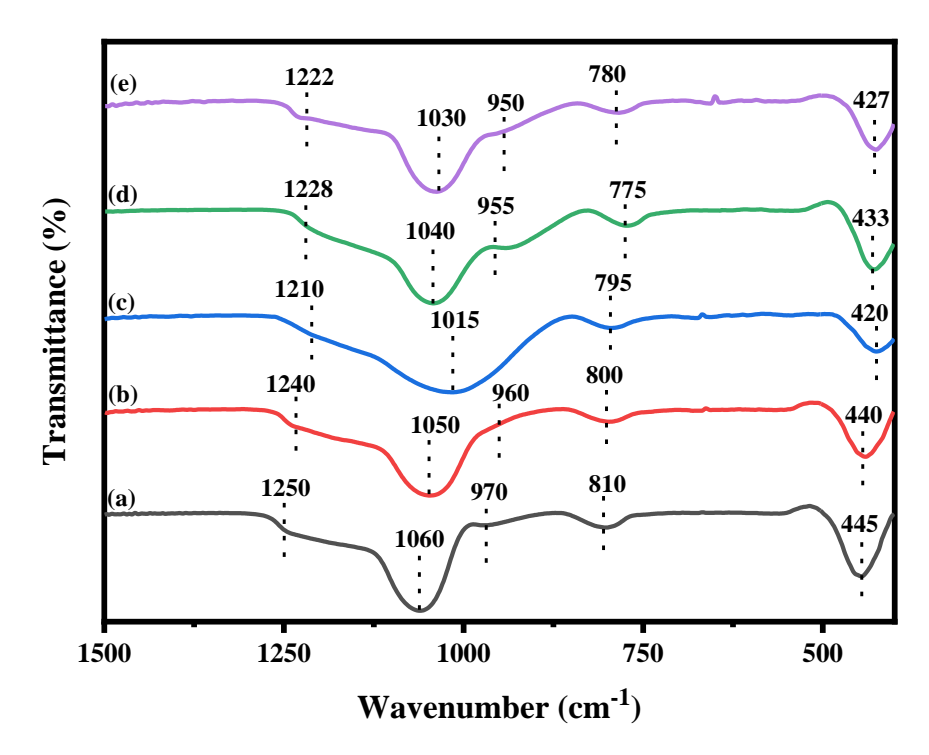


Fig. 6.3 FTIR spectra of (a) MS, (b) Al-MS, (c) Sn-MS, (d) Ti-MS and (e) Zr-MS supports.

6.1.4 N₂ physisorption

N₂ physisorption analysis was conducted to characterize the surface area, pore volume, and pore size distribution of the synthesized catalysts, the results of which are presented in Table 2. The N₂ adsorption-desorption curves (Fig. 6.4) of the catalysts displayed a type IV isotherm, which as per the IUPAC classification is a characteristic of ordered mesoporous materials [10]. The point of inflection can be observed at a relative pressure (P/P_o) of ~0.2, which marks the completion of monolayer coverage by N₂ adsorbate on the walls of the mesopores [11]. The subsequent uptake in N₂ adsorption between P/P₀ values of ~0.2 and 0.4 corresponds to N₂ condensation within the ordered mesopores of the silica framework [1,5]. The steepness of this step highlights the narrow and welldefined pore size distribution characteristic of mesoporous materials such as MCM-41. It is noteworthy that the steepness decreases upon the incorporation of metals (Al, Sn, Ti and Zr), indicating loss of the ordered structure following metal addition [5], which is in agreement with the results of XRD analysis. Additionally, the inflection point moved somewhat to the right with the metal loading, hinting to an enlargement of the pores [11]. In some of the catalysts (Cu@Sn-MS, Cu@Ti-MS and Cu@Zr-MS), a plateau was observed at P/Po values between 0.4 and 0.8, which can be attributed to multilayer N₂ adsorption [5]. Finally, a sharp increase in N₂ adsorption at higher relative pressures ($P/P_o > 0.8$), accompanied by a hysteresis loop, is typically ascribed to N_2 condensation in the interparticle pores [12].

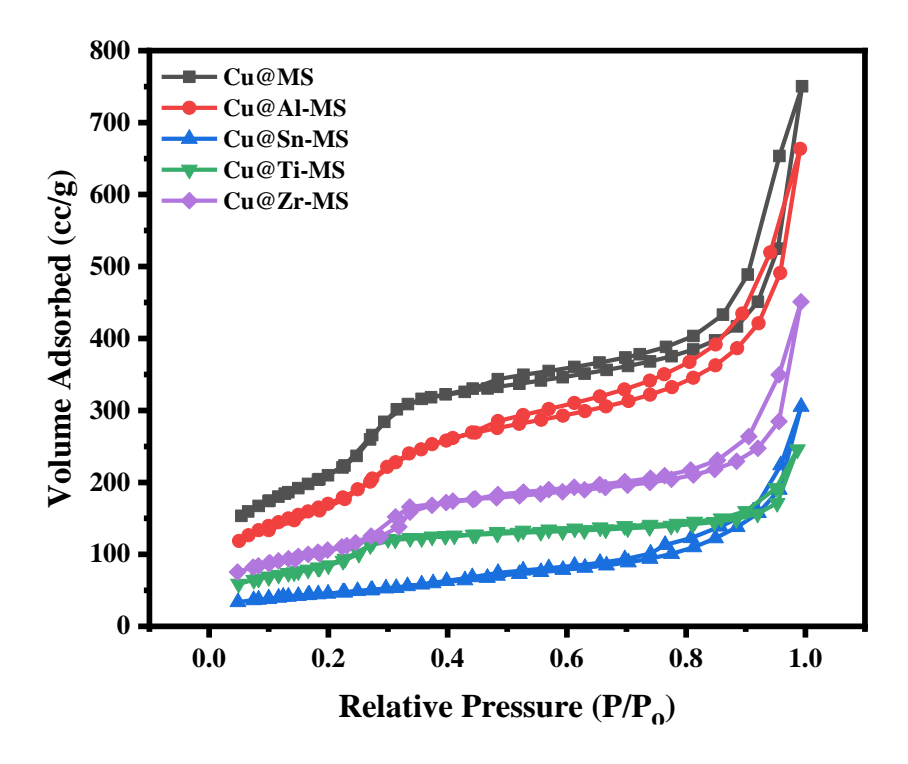


Fig. 6.4 N₂ physisorption-desorption curves for the calcined Cu@M-MS catalysts.

Surface area and pore size distribution analyses (Table 8) revealed that the Cu@MS catalyst boasted the highest surface area and pore volume at 870.7 m²/g and 1.16 cm³/g. However, with the incorporation of metals, both surface area and pore volume experienced significant reduction. This decline in surface area and pore volume in catalysts with metal oxides incorporated on mesoporous silica can be attributed to the structural alterations induced by the loading of these metals during the one-pot synthesis process. These alterations can disrupt the regular arrangement of pores, leading to pore blockage or constriction [5], thereby diminishing both surface area and pore volume. Additionally, the subsequent deposition of Cu during impregnation steps may exacerbate pore occlusion and decrease accessible pore volume. Furthermore, the presence of metals could induce particle aggregation or clustering, diminishing the effective surface area available for adsorption. The disruption of the regular pore structure, combined with the aggregation induced by the presence of metals, may lead to pore widening, thus explaining the observed increase in pore size.

6.1.5 H₂-TPR

Temperature programmed reduction (TPR) is a highly effective technique for assessing how supported metal oxide catalysts undergo reduction. The ease with which metalbased catalysts are reduced is a critical factor in determining their catalytic activity. Fig. 6.5 presents the raw and deconvoluted H₂-TPR profiles of the pure and metalincorporated mesoporous silicas impregnated with Cu, respectively. The Cu@MS catalyst displayed distinct features in its profile: a sharp peak centred at 273.2 °C and a broad hump-shaped peak at 584.5 °C. The presence of two peaks in the H₂-TPR profile of Cu catalysts suggests the coexistence of CuO species with different sizes and/or interactions with the support. Typically, peaks occurring below 250 °C are attributed to well-dispersed Cu²⁺ species with small particle sizes and/or weak interactions with the support, while those between 250 and 300 °C or higher are associated with the reduction of larger-sized or bulk CuO species interacting more strongly with the support [13–16]. However, peak positions may shift, depending on the Cu-support interaction strength. Weak interactions are known to facilitate CuO reduction to metallic copper, whereas strong interactions lead to higher reduction temperatures.

Given the observed small crystallite size of Cu (~11 nm) in this catalyst, the low-temperature peak is most likely due to reduction of well-dispersed and small-sized Cu²⁺ species with weak interactions. The high-temperature peak may be attributed to the reduction of Cu²⁺ species interacting strongly with the support through Cu-O-Si bonds formed by the interaction of Cu with the surface hydroxyl groups [17]. The high surface area and porosity of the silica support also contribute by providing numerous sites for the dispersion and interaction of Cu, leading to stronger interactions. Notably, the findings align well with those from XPS and Auger analysis, which revealed a significant presence of Cu²⁺ species, most likely the CuO species that maintain strong interactions with the support. Shen et. al. [11] observed similar trends for their Co-MCM-41 catalyst, where higher temperatures for Co²⁺ reduction compared to supported Co catalysts was attributed to strong Co and Si interactions resulting from a Co-O-Si bond.

The low-temperature reduction peak remained largely unchanged when SiO₂ was incorporated with Al and Zr, consistent with minimal alterations in crystallite size. However, the high-temperature peak, previously observed at 584.5 °C, shifted to lower

temperatures for Cu@Al-MS (480 °C) and Cu@Zr-MS (554.2 °C), with significantly reduced intensity. This suggests that the incorporation of Al and Zr enhanced the reducibility of Cu. The XPS analysis (section 3.6.1.4 and Fig. S3) of both the catalysts also indicated substantial presence of Cu⁺ and/or Cu⁰ species, corroborating the findings and confirming that both Al and Zr facilitated the reduction of Cu species, albeit to different extents.

Conversely, the addition of Ti and Sn appeared to influence the reducibility of Cu in a distinct manner. The reduction profile of Cu@Sn-MS exhibited a broad, significant peak at 360 °C, which sharpened and slightly shifted to 370 °C for Cu@Ti-MS. According to literature, bulk CuO typically undergoes reduction around 350 °C, suggesting the observed peaks could correspond to the formation and reduction of bulk CuO species on the surfaces of SnO₂-SiO₂ and TiO₂-SiO₂ mixed oxide supports. Alternatively, the observed peaks may also signify that CuO species is strongly interacting with the support materials, leading to a two-stage reduction process. Rajendran et al. [18], investigating ethylene oxidation over TiO₂-supported Cu catalysts, reported Cu²⁺ to Cu⁺ reduction occurring up to 550 K (277 °C), followed by Cu⁺ to Cu⁰ reduction up to 650 K (377 °C). In this scenario, the lower temperature peaks (275.1 °C for Cu@Sn-MS and 295.3 °C for Cu@Ti-MS) could be assigned to Cu²⁺ to Cu⁺ step and the higher temperature peaks (360 °C for Cu@Sn-MS and 370 °C for Cu@Ti-MS) could be assigned to the Cu⁺ to Cu⁰ step, respectively. The findings from Auger analysis (section 3.6.1.4 and Fig. S3) reinforce the two-step reduction mechanism, revealing only Cu⁺ species in both Cu@Sn-MS and Cu@Ti-MS catalysts. This indicates that while the incorporation of Sn and Ti aids in the reduction from Cu²⁺ to Cu⁺, it does not facilitate the complete reduction to Cu⁰. A possible reason for this could be the interaction of Cu with the incorporated metals through the formation of Cu⁺-O-M^{δ+} bonds [19]. Overall, the results of H₂-TPR analysis point towards an improvement in Cu reducibility post metal-incorporation in mesoporous silica, most probably due to the formation of more reducible Cu^{2+} -O- $M^{\delta+}$ (Al^{3+} , Sn^{4+} , Ti^{4+} or Zr^{4+}) bonds at the interface of Cu and metal-incorporated silica supports [19].

The interaction of Cu species with the support material is also evident from additional peaks in the reduction profiles of Cu@Sn-MS and Cu@Ti-MS catalysts. Cu@Sn-MS exhibited intense peaks at 646 °C and 665 °C, which align with reports

indicating pure SnO₂ reduction to metallic Sn around 680 to 700 °C [20]. These peaks likely denote reduction of amorphous and bulk SnO₂ phases, respectively [21]. Similarly, Cu@Ti-MS showed small, hump-shaped peaks at 456.5 °C and 482.3 °C as well as 697.7 °C. Zhu et al. [22] reported that TiO₂ reduction typically yields very weak and poorly identifiable peaks above 550 °C, which aligns with the findings of Cordoba et al. [23] and Rajendran et al. [18]. They noted that Cu addition facilitated easier reduction of Ti⁴⁺ to Ti³⁺, evidenced by shifts in reduction peaks to lower temperatures. Therefore, the peaks observed here at 456.5 °C, 482.3 °C, and 697.7 °C for Cu@Ti-MS likely indicate reduction of Ti⁴⁺ to Ti³⁺ species. The XPS analysis (section 3.1.6.4) revealed the formation of reduced Ti (Ti³⁺) and Sn (Sn²⁺ and Sn⁰) species, confirming Cu's promotional role in aiding the reduction of Sn⁴⁺ and Ti⁴⁺ species through spillover, which further underscores the existence of strong metal-support interactions. In conclusion, the interaction between the metal and support material significantly influences the reduction temperatures in the synthesized catalyts.

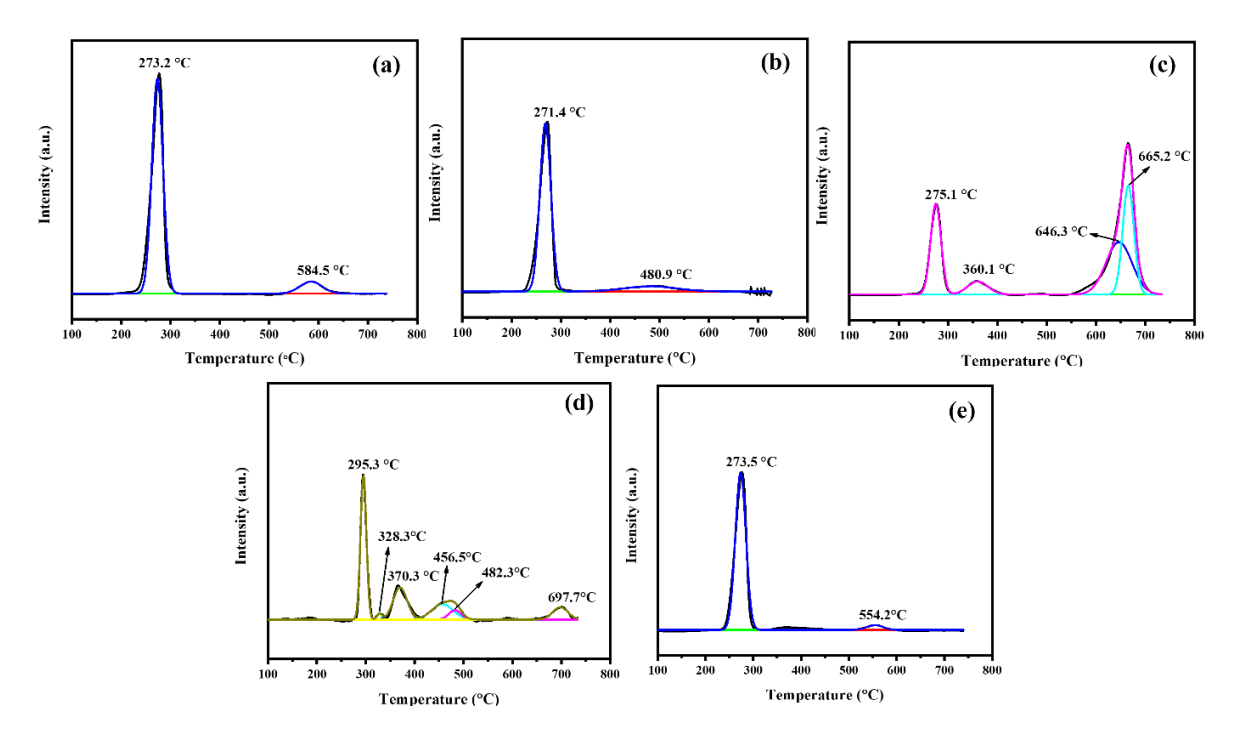


Fig. 6.5 Deconvoluted reduction profiles of the (a) Cu@MS, (b) Cu@Al-MS, (c) Cu@Sn-MS, (d) Cu@Ti-MS, and (e) Cu@Zr-MS catalysts.

6.1.6 NH₃-TPD

NH₃-TPD is a valuable technique for investigating the surface acidity of catalysts, offering crucial insights into their interaction with adsorbates. Fig. 6.6 presents the NH₃-TPD profiles of calcined pure and metal-incorporated mesoporous silicas

impregnated with Cu. Based on the desorption temperature of NH₃ from the catalyst surface, the strength of the surface acid sites can be categorized as weak (<300 °C), medium (300-500 °C), and strong (>500 °C) [24]. The TPD profile of Cu@MS features an intense and broad peak between ~100 and 350 °C, which, on deconvolution, reveals two peaks at 184.8 °C and 254.5 °C. A fainter peak centered at 437.4 °C, likely from hydroxyl groups on the silica surface, is also noted. These results indicate the presence of weak acidic sites, consistent with literature noting the weak acidity of CuO and SiO₂ [25,26].

The Al-incorporated catalyst exhibits a sharp and broad peak between 100 and 400 °C, with deconvolution revealing peaks in the low-temperature range (<300 °C). Additionally, significant peaks at 334.2 and 480.2 °C indicate medium-strength acid sites. The increased acidity likely arises from Si-O-Al bridging sites, where the charge imbalance between Si⁴⁺ and Al³⁺ creates acid sites [27]. Both Sn and Zr-incorporated samples have peaks in the 100 to 300 °C range, slightly shifted to higher temperatures compared to Cu@MS, indicating stronger weak acidic sites. The Cu@Sn-MS profile only has a faint hump-shaped peak in the 300 to 500 °C range, with no peaks above 500 °C, indicating that Sn addition did not significantly change the strength of the acidic sites. This aligns with literature stating that SnO₂-SiO₂ mixed oxides generally feature weak acid sites. In addition to the weak sites, the Zr-incorporated catalyst exhibits a sizeable peak centered at 314.5 °C and two small peaks above 500 °C, indicating the presence of medium and strong acidic sites. The higher strength of surface acidic sites in Cu@Zr-MS could be attributed to the formation of Zr-O-Si bonds. Studies have noted that in ZrO₂-SiO₂ mixed oxides, ZrO₂ forms Lewis acid sites due to the higher ionic nature of Zr-O bonds present near the more covalent Si-O bonds [28–30]. The Cu@Ti-MS catalyst also has three peaks below 300 °C, indicating numerous weak sites. This catalyst differs in having significant NH₃ desorption above 600 °C. Though SiO₂ and TiO₂ both possess weak acid sites, combining them greatly increases the acidic strength of SiO₂ and the total number of acidic sites for TiO₂ [31–33], explaining the observed increase.

While the strength of acidic sites in Cu catalysts increased with metal incorporation, the total acidic strength (determined by the amount of NH₃ desorbed) did not follow the same trend. Instead, it correlated with surface area: the Cu@MS catalyst had the highest

number of acidic sites, while Cu@Sn-MS had the lowest. This seemingly contradictory result agrees with observations by Itoh et al. [33], who also noted a correlation between total acidic strength and surface area.

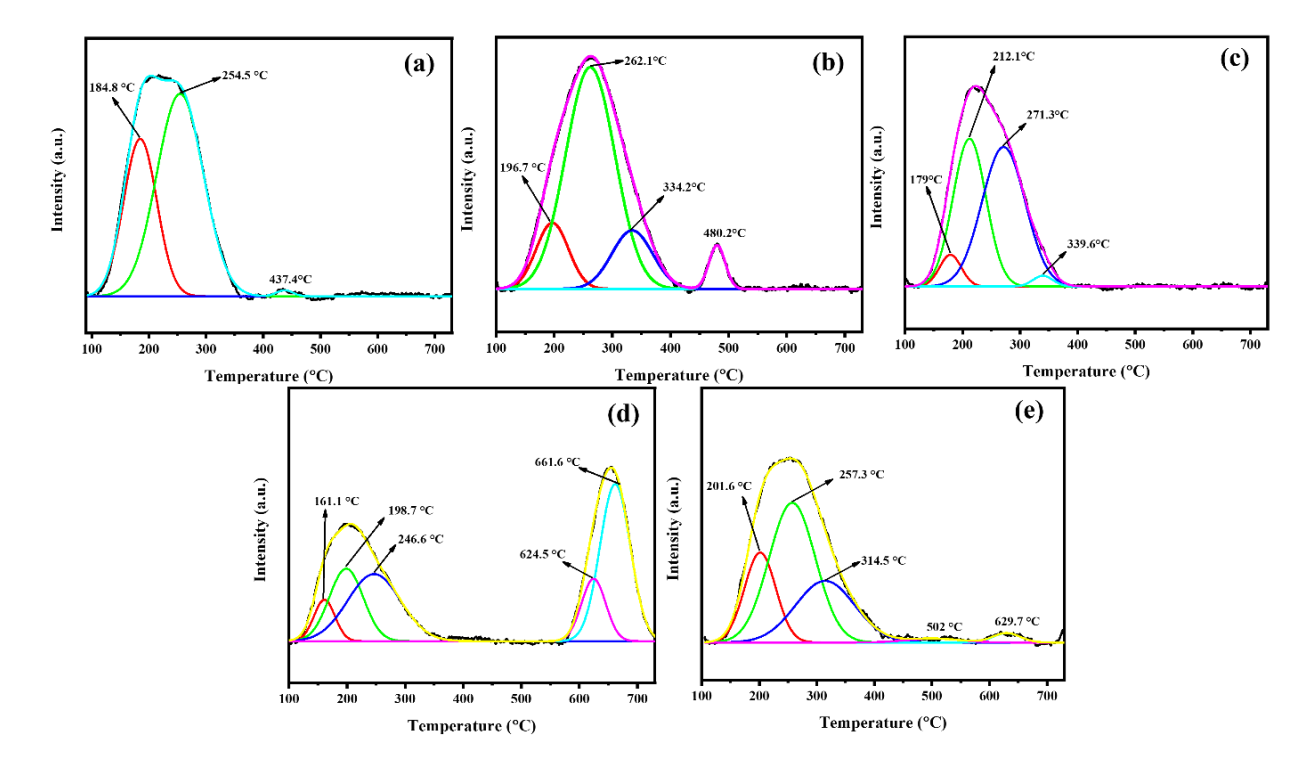


Fig. 6.6 Deconvoluted NH₃-TPD profiles of the (a) Cu@MS, (b) Cu@Al-MS, (c) Cu@Sn-MS, (d) Cu@Ti-MS, and (e) Cu@Zr-MS catalysts

6.1.7 XPS

6.1.7.1 Evaluation of surface states of metal-incorporated oxide supports

To further elucidate the structural modifications resulting from metal integration into the mixed oxide support, XPS analysis was conducted on both the pristine mesoporous silica and the metal-incorporated mesoporous silica samples. As shown in Fig. 6.7, the XPS spectra of Si 2p for all the supports displayed asymmetry and broadening, suggestive of Si existing in varied oxidation states or environments. In the literature, multiple peaks in the Si 2p spectrum are commonly reported for silica materials, particularly those derived from carbonaceous sources such as rice husk [34–37]. Upon deconvolution, the Si 2p spectrum of pure mesoporous silica revealed six distinct peaks with binding energy values at approximately 101, 101.6, 102.1, 102.8, 103.7, and 104.5 eV. In the literature, Si-O-Si linkages typically manifest at binding energy values around 103.8 eV, with Si³⁺ at approximately 103.2 eV, Si²⁺ at 102.6 eV, and Si⁺ at 102.1 eV [34,35]. Additionally, peaks indicating elemental silicon (Si⁰) appear at lower

binding energies, approximately 100.4 eV and 99.6 eV [38]. In this study, these values align with literature in terms of peak positions but are slightly shifted to higher binding energies, possibly due to differences in local environments within the mesoporous silica matrix, such as variations in surface interactions or electronic effects induced by synthesis conditions. The presence of these sub-oxide states can be attributed to several factors. Incomplete combustion of acid-treated rice husk under static air conditions can sometimes lead to residual carbon in the resulting rice husk ash that may persist through subsequent processing steps. The combustion of the residual carbon as well as the organic template (CTAB) in the calcination step can release gases like CO that can react with SiO₂, inducing reduction reactions and further contributing to the formation of Si suboxide states. These findings align with literature reports that attribute the multifarious silicon valences observed in XPS spectra to thermal reduction reactions between carbon and SiO₂ [34,35]. Factors influencing this phenomenon include the porous structure of the material and its specific surface area, which affect the release of CO gas during combustion. This accelerates the reduction reaction of SiO₂ and enhances the presence of Si suboxides in the final material. Furthermore, in the context of materials synthesis involving silica and carbonaceous materials, such as in the case of rice husk and its ash, interactions between carbon and SiO₂ can lead to the formation of pores or voids within the material [34]. This phenomenon occurs when several carbon atoms around SiO₂ particles are consumed with the formation of pores, which weakens the reduction degree of SiO₂ [39]. This would potentially lead to uneven reduction across the material surface and the formation of diverse silicon valence states, as observed in XPS spectrum. After examining the Si 2p spectra of metal-modified mesoporous silica supports, it is evident that the peaks are similar in nature to those observed in pristine mesoporous silica and appear at comparatively lower binding energy values. These shifts suggest alterations in the bonding environments of Si within the material and could potentially indicate the formation of Si-O-M bonds through electron transfer from the metals to the Si atoms, likely facilitated by the lower electronegativity of metals like Al, Ti, Sn, and Zr compared to Si. These findings suggest significant interactions between Si and the metals, indicative of successful metal incorporation into the silica framework.

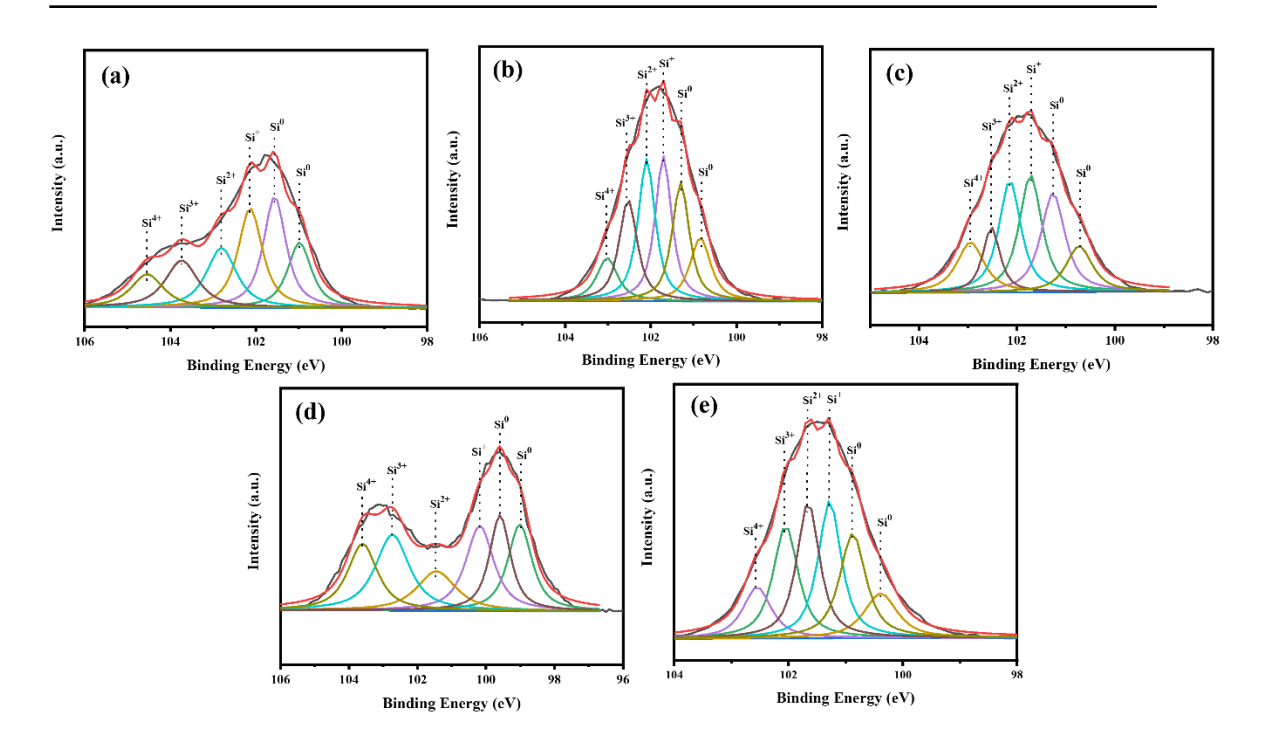


Fig. 6.7 XPS Spectrum of Si 2p for (a) MS, (b) Al-MS, (c) Sn-MS, (d) Ti-MS, and (e) Zr-MS supports

6.1.7.2 Evaluation of surface states of reduced Cu catalysts supported on mixed oxide supports

Besides the supports oxides, XPS analysis was also carried out for the synthesized supported Cu catalysts to investigate the surface oxidation states under dynamic reaction conditions, after reduction at 300 °C (Fig. 6.8). The deconvoluted Cu 2p spectral profile for Cu@MS catalyst showed two peaks at 932.6 eV and 952.3 eV corresponding to the 2p_{3/2} and 2p_{1/2} energy levels of metallic Cu and/or Cu⁺, respectively [16,40]. Additionally, despite reduction, the Cu 2p spectrum still retained peaks corresponding to the Cu 2p_{3/2} and Cu 2p_{1/2} energy levels of Cu²⁺ species at 933.4 eV and 953.4 eV, respectively (Fig. 6) [16,40,41]. This persistence of Cu²⁺ species, even after reduction, is noteworthy. The H₂-TPR profile of this catalyst had revealed a particularly strong interaction between Cu and SiO₂, evidenced from the existence of a high temperature reduction peak. This strong interaction could enhance the stabilization of Cu²⁺, through the formation of Cu²⁺-O-Si⁴⁺ bonds, impeding the reduction process and hindering the complete reduction of CuO species to Cu⁰ or Cu⁺.

Upon the incorporation of metals in the mesoporous silica framework, the peaks corresponding to Cu²⁺ species disappeared for all the catalyst, and the peaks

corresponding to the Cu⁰/Cu⁺ species moved to higher binding energy values. Only the Cu@Zr-MS catalyst exhibited a broad, faint hump associated with the shake-up satellite peaks of Cu²⁺ species between 940 and 946 eV [16]. The shifting of the Cu⁰/Cu⁺ peaks to higher binding energy values is indicative of an electron transfer from Cu to the incorporated metal at the interfaces, leaving the Cu atoms electron deficient. This phenomenon can be attributed to the strong interactions between Cu and the incorporated metals, which enhanced the reducibility of the Cu²⁺ species and has the potential to stabilize the Cu⁺ species at the catalyst surface [42]. The same was also evidenced by the H₂-TPR analysis.

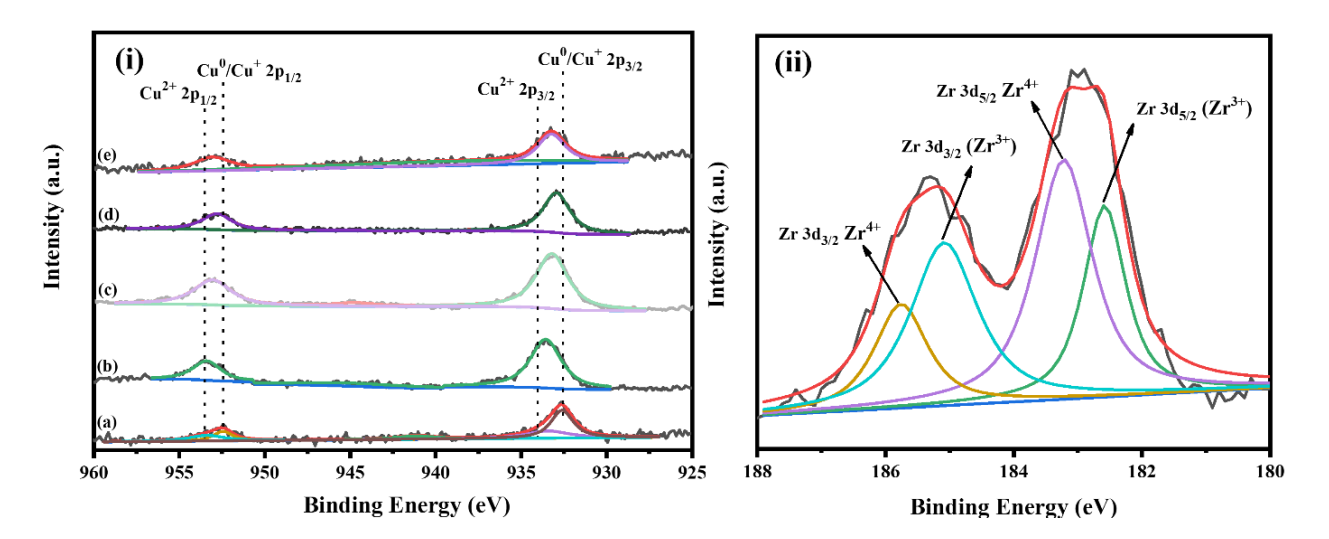


Fig. 6.8 (i) Reduced XPS Cu 2p spectra of (a) Cu@MS, (b) Cu@Al-MS, (c) Cu@Sn-MS, (d) Cu@Ti-MS and (e) Cu@Zr-MS catalysts and (ii) Zr 3d spectra of reduced Cu@Zr-MS catalyst.

6.1.7.3 Evaluating Copper Oxidation States

Both Cu⁰ and Cu⁺ species are known to be essential for effective furfural hydrogenation in Cu-based catalysts, making it vital to assess their relative proportions. However, conventional XPS is limited in its ability to distinguish between Cu⁰ and Cu⁺, so Auger analysis is often employed to distinguish between these two species. The Auger analysis results (Fig. 6.9) show that the Cu@MS catalyst has significant amounts of Cu²⁺ (46.5%), along with 22.4% Cu⁰ and 31.1% Cu⁺. This indicates a strong stabilization of Cu²⁺ due to interactions with the support, which is also evident in the H₂-TPR as well as XPS findings, even though Cu²⁺ species was not detected in reduced XRD. In contrast, the Cu@Al-MS catalyst exhibits no Cu²⁺, containing 8.7% Cu⁰ and 91.3% Cu⁺. This indicates improved reducibility due to the incorporation of Al. However, the

high proportion of Cu⁺ suggests that this oxidation state is effectively stabilized, likely due to the strong interactions with the support material. Meanwhile, the Cu@Sn-MS and Cu@Ti-MS catalysts contained only Cu⁺ species, signifying that the Sn and Ti-incorporated mesoporous silica supports promoted the stabilization of this oxidation state at the catalyst surface. This observation aligns with the two-step reduction process seen in their H₂-TPR profiles, where Cu²⁺ is first reduced to Cu⁺ before being further converted to Cu⁰. The stabilization of Cu⁺ indicates that rather than quickly reducing Cu²⁺ directly to Cu⁰, the reduction occurs stepwise: first to Cu⁺, which can persist due to the support's influence. Lastly, Meanwhile, the Cu@Zr-MS catalyst shows a more balanced composition of 29.5% Cu⁰, 57.6% Cu⁺, and 12.9% Cu²⁺, reflecting a moderate interaction between Cu and Zr, which facilitates a more favourable reduction environment compared to the other supports. As we will see further in the experimental results section, the amount of Cu⁰ and Cu⁺ will prove crucial in the hydrogenation of FFR.

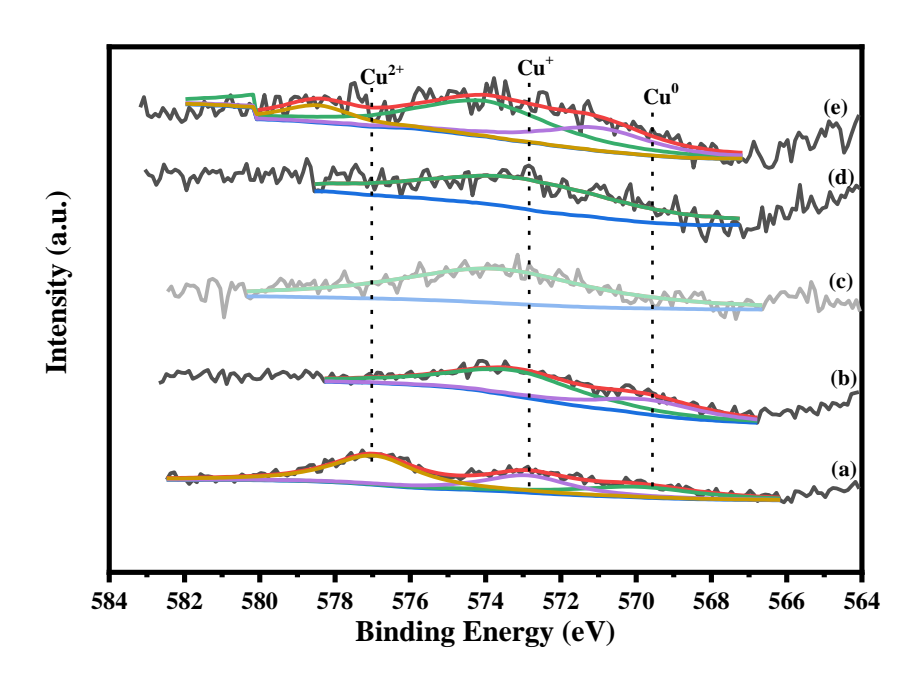


Fig. 6.9 Cu Auger Spectra for reduced (a) Cu-MS, and (b) Cu@Al-MS, (c) Cu@Sn-MS, (d) Cu@Ti-MS, and Cu@Zr-MS catalysts.

6.1.7.4 Evaluating Oxidation States of Incorporated Metals

The Zr 3d spectral profile showed two doublets after deconvolution, indicating the presence of two types of Zr species in the reduced catalyst (Fig. 6.8). The peaks at 182.4 eV and 184.8 eV correspond to the Zr 3d5/2 and Zr 3d3/2 doublets, characteristic of

Zr³⁺ species, suggesting the presence of partially reduced Zr (Zr³⁺) species and indicating that oxygen vacancies may also be present in the reduced catalyst. Additionally, peaks at 183.2 eV and 185.6 eV suggest the presence of Zr as Zr⁴⁺ in the synthesized catalyst [43–45]. In the Sn 3d spectra (Fig. S4), peaks at 487.7 eV, 495.1 eV, and 497.7 eV were observed. Deconvolution of these peaks revealed doublets corresponding to Sn⁰ at 486 and 494.6 eV, Sn²⁺ species (SnO) at 486.9 and 495.2 eV, and Sn⁴⁺ (SnO₂) at 487.6 and 497.6 eV [46]. The Ti 2p spectral profile also displayed two peaks at 459.4 eV and 465.2 eV (Fig. 6.10). Deconvolution further revealed peaks corresponding to Ti³⁺ at 458.8 eV and 464.6 eV, as well as peaks corresponding to Ti⁴⁺ at 459.6 and 465.5 eV [19]. Like the case for Cu@Zr-MS catalyst, the presence of the partially reduced Ti³⁺ species points towards the presence of oxygen vacancies [19]. Lastly, the deconvoluted Al 2p spectral profile exhibited peaks corresponding to Al-O, Al-OH and Al-O-Si bonds at binding energy values of 74.2 eV, 75 eV and 77 eV, respectively [47].

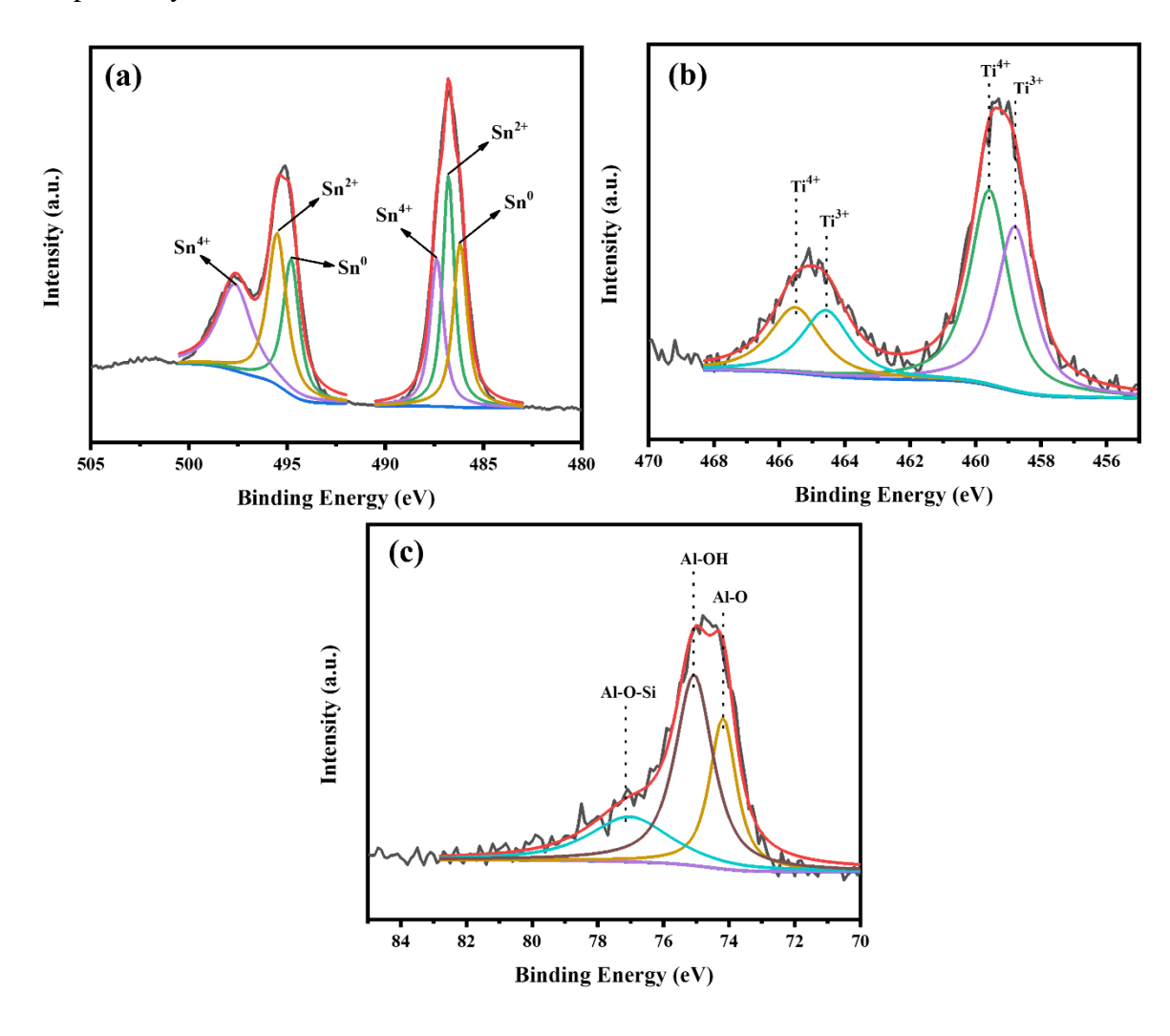


Fig. 6.10 XPS spectra of (a) Sn 3d, (b) Ti 2p and (c) Al 2p of reduced Cu@Sn-MS and Cu@Ti-MS catalysts, respectively

6.1.8 FESEM

Figure 6.11 presents the FESEM images of the calcined Cu catalysts supported on pure and metal-modified mesoporous silica supports. The pure mesoporous silica-supported catalyst (Cu@MS) displayed large, irregularly shaped particles, consistent with observations made in literature [5,48]. Similarly, the Al and Zr-incorporated catalysts (Cu@Al-MS and Cu@Zr-MS) exhibited large particles with no uniform shape or size. This outcome was expected for the Cu@Zr-MS catalyst due to its low surface area. However, it was surprising for the Cu@Al-MS catalyst, given its relatively high surface area. The H₂-TPR analysis explained this anomaly by showing that metal-support interactions weakened after loading Al and Zr, which hindered the improvement of dispersion in the Cu@Al-MS catalyst. In contrast, the Cu@Sn-MS and Cu@Ti-MS catalysts exhibited much smaller and more uniformly distributed particles. This observation aligns with the TPR analysis, which indicated that modification with Sn and Ti significantly increased metal-support interactions. These stronger interactions likely stabilized the CuO species, enhancing their dispersion and resulting in smaller, well-distributed particles. In addition, the surface composition of the synthesized supported Cu catalysts was investigated using EDX analysis. The atomic weight percentage of metals obtained from the analysis was found to be nearly consistent with their intended loading amounts. Table 6.3 summarizes the elemental composition (weight %) of the elements in pristine and metal-incorporated mesoporous silica supported Cu catalysts determined using EDX analysis.

Chapter 6 FFR Hydrogenation to FAL over Cu catalysts supported on rice husk ash-derived and metal-incorporated mesoporous silica

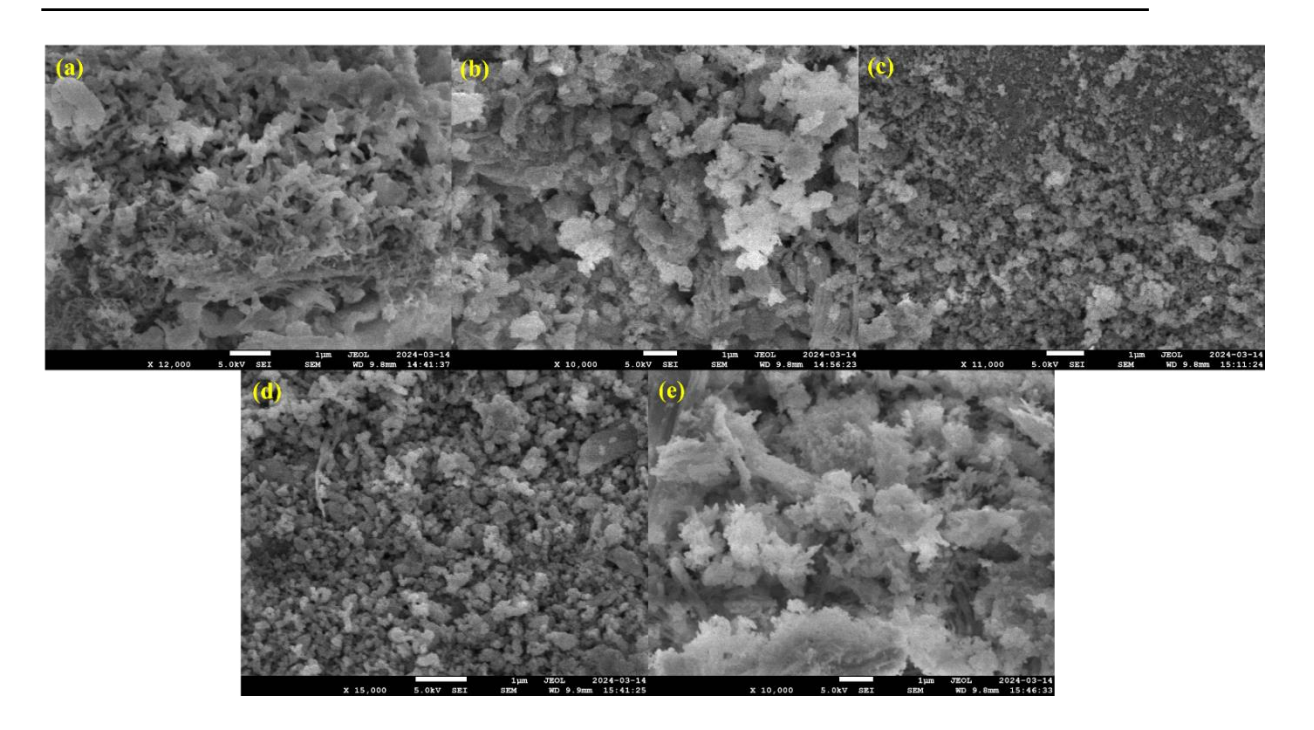


Fig. 6.11 FESEM images of the calcined (a) Cu@MS, (b) Cu@Al-MS, (c) Cu@Sn-MS, (d) Cu@Ti-MS, and (e) Cu@Zr-MS catalysts

Table 6.3 Elemental surface composition of the synthesized Cu supported on pristine and metal-incorporated mesoporous silica catalysts.

Catalyst	Atomic weight % from EDX					
	Si	0	Cu	Metal	Si/Metal Molar Ratio	
Cu@MS	43	51.6	5.4	-	-	
Cu@Al-MS	40.7	50.6	4.7	4	9.67	
Cu@Sn-MS	35.3	44.9	4.7	14.9	10.05	
Cu@Ti-MS	38.7	49.8	4.9	6.6	10	
Cu@Zr-MS	36.4	47	4.8	11.8	10.1	

6.1.9 HRTEM

To gain deeper insights into the morphology of the Cu@Zr-MS catalyst reduced at 300 °C, HRTEM analysis was employed (Fig. 6.12). The analysis revealed a diverse particle morphology, characterized by a somewhat non-uniform shape, in agreement with the XRD analysis which had indicated that the catalyst lacked a regular, well-ordered structure, like that of MCM-41.. Notably, the Cu species appeared to be distributed uniformly across the support surface, indicating efficient loading on the support surface.

Additionally, the images presented challenges in distinguishing between SiO_2 and ZrO_2 , which could imply a well-mixed phase or the successful integration of Zr into the silica matrix. These observations align with the findings from previous characterization analyses, reinforcing the hypothesis that Zr had been successfully incorporated into the SiO_2 framework.

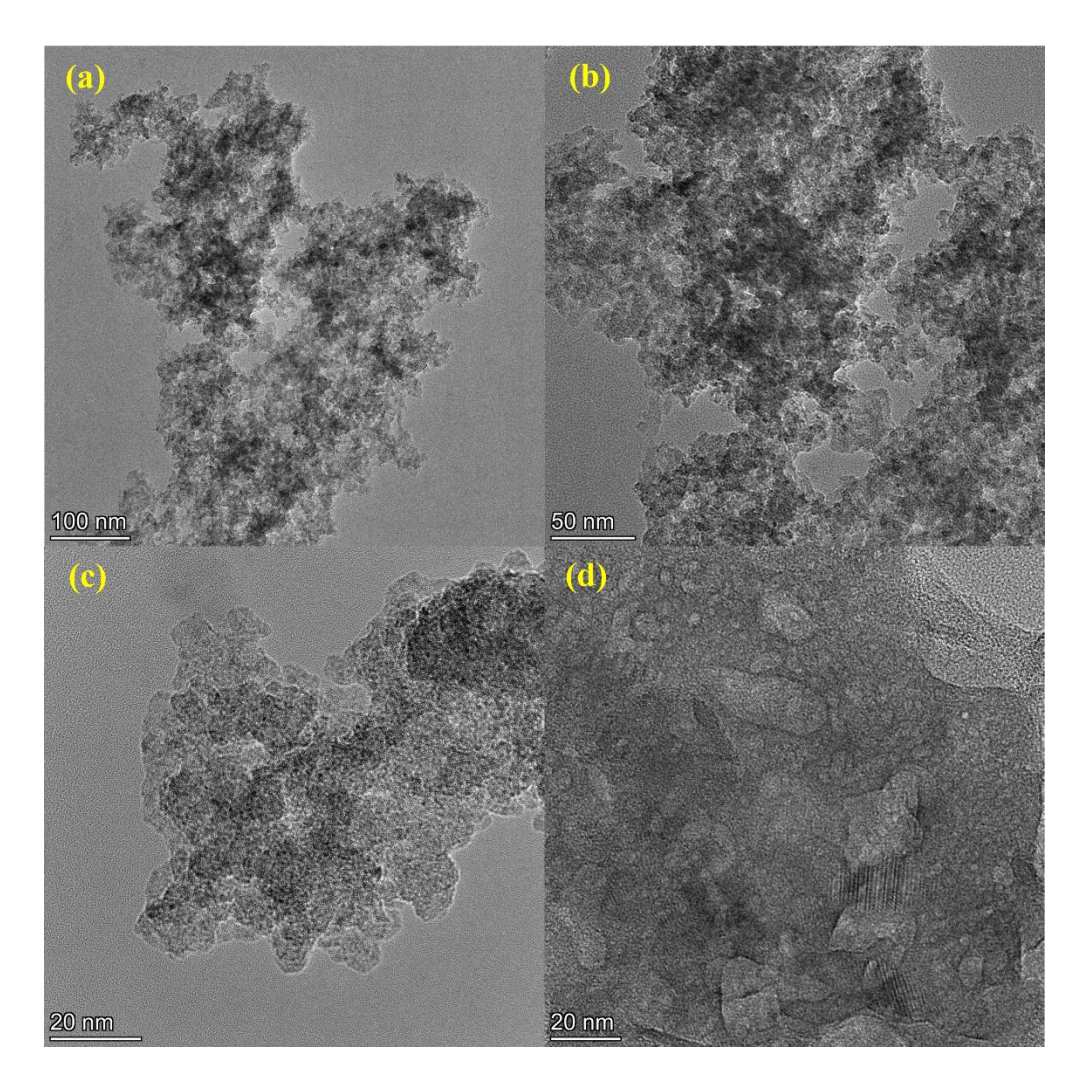


Fig. 6.12 HRTEM images of the reduced Cu@Zr-MS catalyst.

6.2 Evaluation of Catalytic Activity in FFR hydrogenation

6.2.1 Effect of metal incorporation in mesoporous silica support

The evaluation of the catalytic performance of the synthesized catalysts was initiated by assessing the activity of pure and metal-incorporated mesoporous silica supported Cu catalysts in FFR hydrogenation at 180 °C, an H₂ to FFR molar ratio of 10, and a WHSV of 0.5 g_{FFR} g_{catalyst}⁻¹ h⁻¹ (Fig. 6.13). At low loadings values such as the one used

here and low reaction temperatures, Cu catalysts generally exhibit nearly 100% selectivity towards FAL, making selectivity less useful for comparing different Cu catalysts. Instead, yield becomes a more suitable parameter, as it accounts for the amount of product formed relative to the reactant fed and can vary due to differences in conversion rates. Among all the catalysts, the pure mesoporous silica-supported Cu catalyst (Cu@MS) showed the lowest FFR conversion and FAL yield at 29.5% and 27.2%, respectively. The Auger analysis had revealed a high proportion of Cu²⁺ in Cu@MS, which corresponds to weak acidic sites that are less effective in binding the reactant and catalyzing the conversion. Cu@Sn-MS showed slightly better performance, but still underperformed due to its exclusive presence of Cu⁺ species and weak surface acid sites. Although Cu⁺ can act as Lewis acid sites and activate FFR, its inability to activate H₂ limits its effectiveness in hydrogenation. Cu@Al-MS showed improved performance with a conversion of 45.5% and a FAL yield of 44.75%, likely due to the presence of medium acid sites and a high surface area, which would allow for better metal dispersion. However, the presence of only 8.7% Cu^o in Cu@Al-MS implies that H₂ activation is limited and therefore, leading to poorer hydrogenation ability. Despite having a significantly higher number of strong acid sites, the Cu@Ti-MS catalyst achieved only moderate conversion (57.2%) and yield (55.2%) (Fig. 6.13). This performance can be attributed to the fact that, like the Cu@Sn-MS catalyst, Cu@Ti-MS contains only Cu⁺ species, which are less effective at activating hydrogen compared to Cu⁰ species. However, the presence of oxygen vacancies in Cu@Ti-MS provides a crucial advantage, aiding not only in FFR activation but also facilitating H₂ activation, thus compensating for the absence of Cu⁰ species and the exclusive presence of Cu⁺. Additionally, it is important to note that while strong acid sites can enhance catalytic activity, they can also overly bind reactant and product molecules. This can hinder desorption, lower conversion rates, accelerate catalyst deactivation, and lead to the formation of undesired by-products [24]. Cu@Zr-MS demonstrated the highest conversion (74.5%) and yield (72.9%) among all the catalysts, even though it possessed the second lowest surface area. The balanced presence of Cu⁰ and Cu⁺, as revealed by Auger analysis, suggests that Cu@Zr-MS effectively combines the benefits of both active species: Cu⁰ for hydrogen activation and Cu⁺ for reactant activation. Additionally, NH₃-TPD analysis showed an increase in acidic strength post-Zr incorporation, which likely contributes to the improved catalytic activity observed in Cu@Zr-MS. Furthermore, XPS analysis indicated the presence of partially reduced Zr³⁺ species in Cu@Zr-MS, which may contribute to the formation of oxygen vacancies that further enhance catalytic performance by providing additional active sites for both H₂ and FFR activation.

Beyond the factors previously discussed, the role of metal oxophilicity is also pivotal in catalytic performance. Metals with high oxophilicity, such as W, Mo, Zr, and Ti, have a strong affinity for oxygen-containing molecules, which facilitates their activation and conversion. This is especially relevant in processes like hydrodeoxygenation and hydrogenation, where efficient handling of oxygen and hydrogen is crucial. This importance is evident from studies on phenol hydrodeoxygenation using metal oxide-supported Pd catalysts [49]. For instance, Pd@Al₂O₃, despite having the highest number of surface acid sites, did not perform as well as Pd@ZrO₂ and Pd@TiO₂, which showed superior deoxygenation rates due to the higher oxophilicity of Zr and Ti. Similarly, other research on Pd@Zr_xCe_{1-x}O₂ catalysts highlighted that oxophilicity significantly influenced deoxygenation to benzene [50]. In the context of our study, Zr, Ti, and Sn are known for their significant oxophilicity. However, despite its oxophilicity, the Sn-containing catalyst (Cu@Sn-MS) showed poor performance due to its low surface area, weak acidity and the absence of necessary Cu⁰ phase. Similarly, despite Ti's oxophilic nature, the strong acid sites in Cu@Ti-MS and absence of Cu⁰ may have limited FFR conversion due to lower availability of H atoms and by hindering the desorption of reactant and product species. The Cu@Al-MS catalyst exhibited surprisingly low conversion and FAL yield - despite having sufficient number of both weak and medium-strength acid sites and a relatively high surface area - likely due to Al's lower oxophilicity compared to the other metals. Overall, the superior performance of the Cu@Zr-MS catalyst can be attributed to a combination of sufficient acidic sites of appropriate strength, balanced Cu⁰-Cu⁺ proportions, presence of oxygen vacancies and the oxophilic nature of Zr.

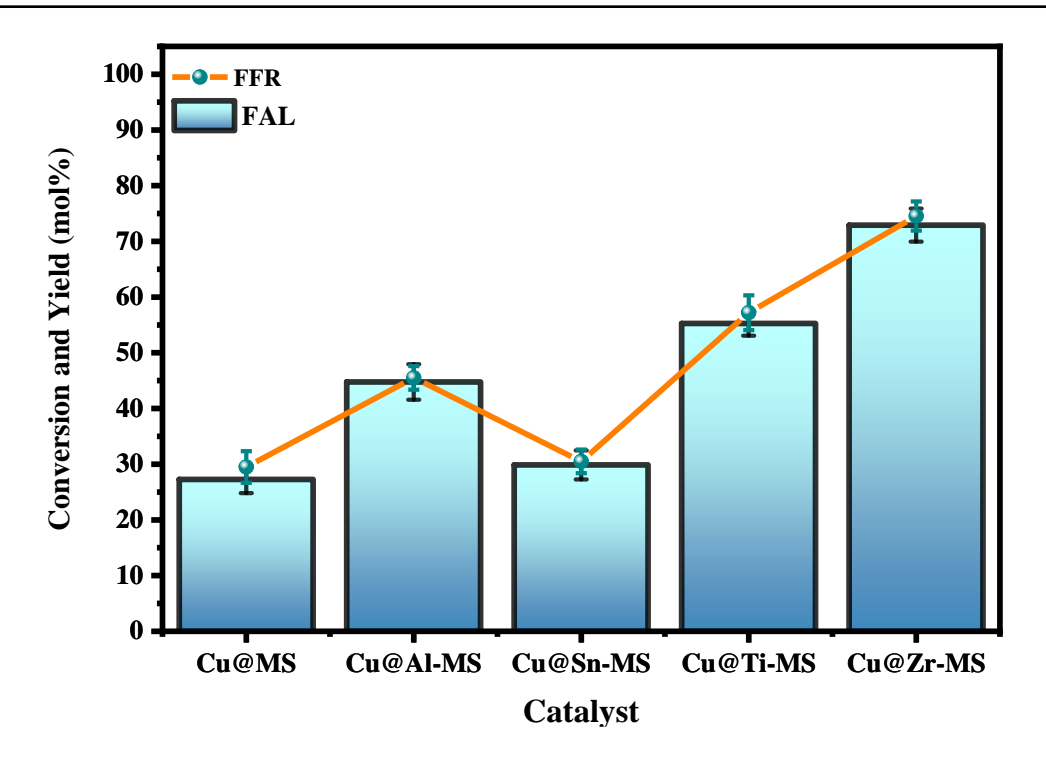


Fig. 6.13 Effect of Metal Incorporation on the conversion and yield during FFR hydrogenation over Cu supported on mesoporous silica catalysts. Feed Flowrate = 5.43 mmol_{FFR} h⁻¹, H₂/FFR = 10, Temperature = 180 °C, WHSV = $1 \text{ g}_{\text{FFR}} \text{ h}^{-1} \text{ g}_{\text{catalyst}}^{-1}$, Pressure = 1 atm.

6.2.2 Effect of Temperature

Fig. 6.14 illustrates how temperature affects FFR conversion and FAL yield over Cu@Zr-MS catalyst. Lowering the temperature from 180 °C to 160 °C caused the conversion to decline from 74.5% to 56.6% and the FAL yield to decrease from 72.9% to 54.5%. This drop in conversion and FAL yield at lower temperatures can be attributed to Cu's limited ability to activate and dissociate hydrogen, coupled with its weaker binding with activated hydrogen atoms adsorbed on the surface, allowing for their easy desorption [51,52]. Notably, no 2-MeF formation was observed at both 160 °C and 180 °C. This is because Cu interacts more strongly with FFR than with FAL. Thus, despite their specificity towards the C=O bond, Cu-based catalysts cannot fully deoxygenate FFR at low temperatures [25,53,54], leading to high FAL selectivity, and negligible 2-MeF selectivity. Also, the Cu loading used was on the lower end, so the hydrogenation ability would also be limited, preventing over-hydrogenation to 2-MeF.

Increasing the temperature to 200 °C resulted in the reactant conversion rising to 90.6%, while the FAL yield increased to 85%. At this temperature, 2-MeF was also observed, with a yield of about 5.2%. Further increasing the temperature to 220 °C

increased conversion to approximately 97%. However, the FAL yield dropped to 76% while the 2-MeF yield soared to 17.5%. The increased conversion at higher temperatures can be attributed to Cu becoming highly active not only in H₂ activation but also in the hydrogenation of the C=O bond in FFR and the hydrogenolysis of the C-O bond in FAL. Consequently, at moderate temperatures, the hydrogenation of the C=O bond increases, yielding more FAL [4,53,54], while higher temperatures promote the hydrogenolysis of the C-O bond in FAL, producing larger quantities of 2-MeF [25].

These trends indicate that the optimal yield observed at 180 °C suggests a delicate balance at this temperature - the catalyst was sufficiently active for the hydrogenation of the C=O bond in FFR but not overly active to cause extensive hydrogenolysis of FAL.

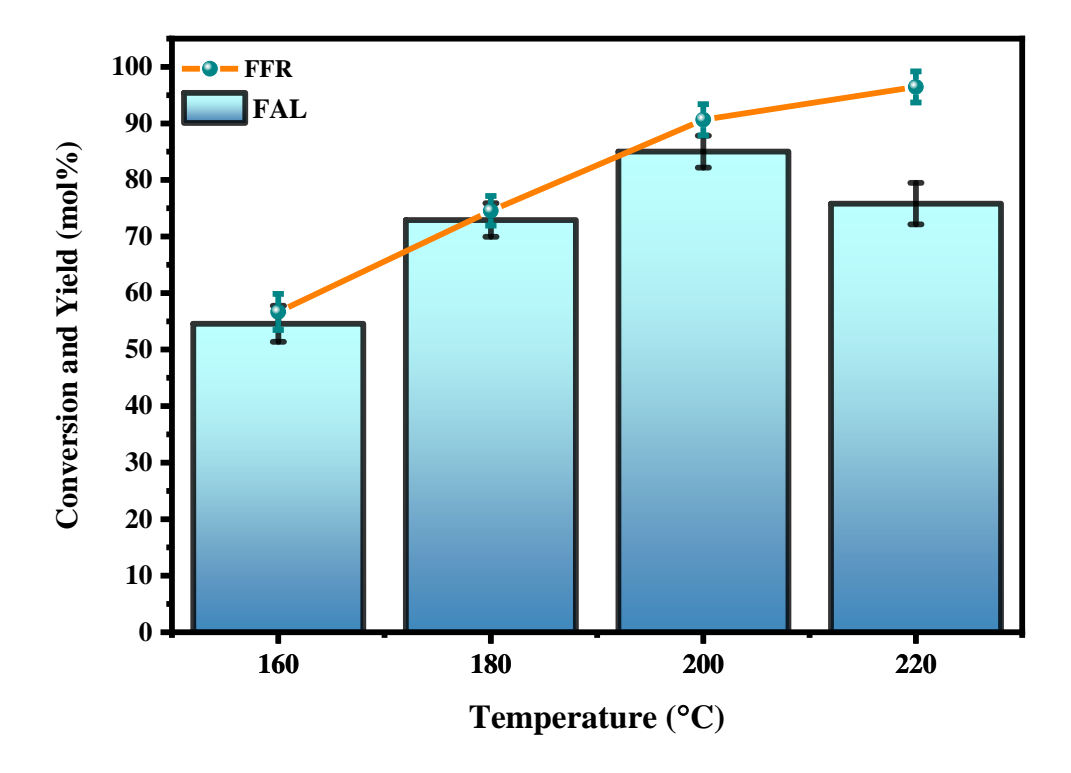


Fig. 6.14 Effect of reaction temperature on the conversion and yield during FFR hydrogenation over Cu@Zr-MS catalyst. Feed Flowrate = $5.43 \text{ mmol}_{FFR} \text{ h}^{-1}$, $\text{H}_2/\text{FFR} = 10$, WHSV = $1 \text{ g}_{FFR} \text{ h}^{-1} \text{ g}_{catalyst}^{-1}$, Pressure = 1 atm.

6.2.3 Effect of WHSV

Figure 6.15 presents the results of investigating the influence of varying WHSV on FAL yield over Cu@Zr-MS catalyst. Previously, during the investigation of the effect of temperature, an optimum yield of 85% was observed at 200 °C while maintaining the space velocity at 1 g_{FFR} h⁻¹ g_{catalyst}-1. To explore the role of WHSV further, additional

experiments were conducted at space velocity values of 0.5, 1, 1.5 and 2 g_{FFR} h⁻¹ g_{catalyst}⁻¹. Decreasing the WHSV from 1 to 0.5 g_{FFR} h⁻¹ g_{catalyst}⁻¹ resulted in a 5% increase in FFR conversion, whereas the FAL yield declined to 79%. 2-MeF yield, on the other hand, jumped to 14.7%. On the other hand, increases in space velocity to 1.5 and 2 g_{FFR} h⁻¹ g_{catalyst}⁻¹ caused the conversion to drop to 79% and 63%, respectively. Similarly, FAL yield declined sharply to 74.7% and 62.6% as the space velocity increased to 1.5 and 2 g_{FFR} h⁻¹ g_{catalyst}⁻¹, respectively. The yield of 2-MeF also mirrored the trend of FAL, dropping to 0% at a WHSV of 2 g_{FFR} h⁻¹ g_{catalyst}⁻¹. The increase in space velocity led to a reduction in residence/contact time, limiting the time available for FFR and/or FAL to undergo conversion [4,25]. Consequently, not only was FFR partially converted, but the FAL and 2-MeF yields also decreased.

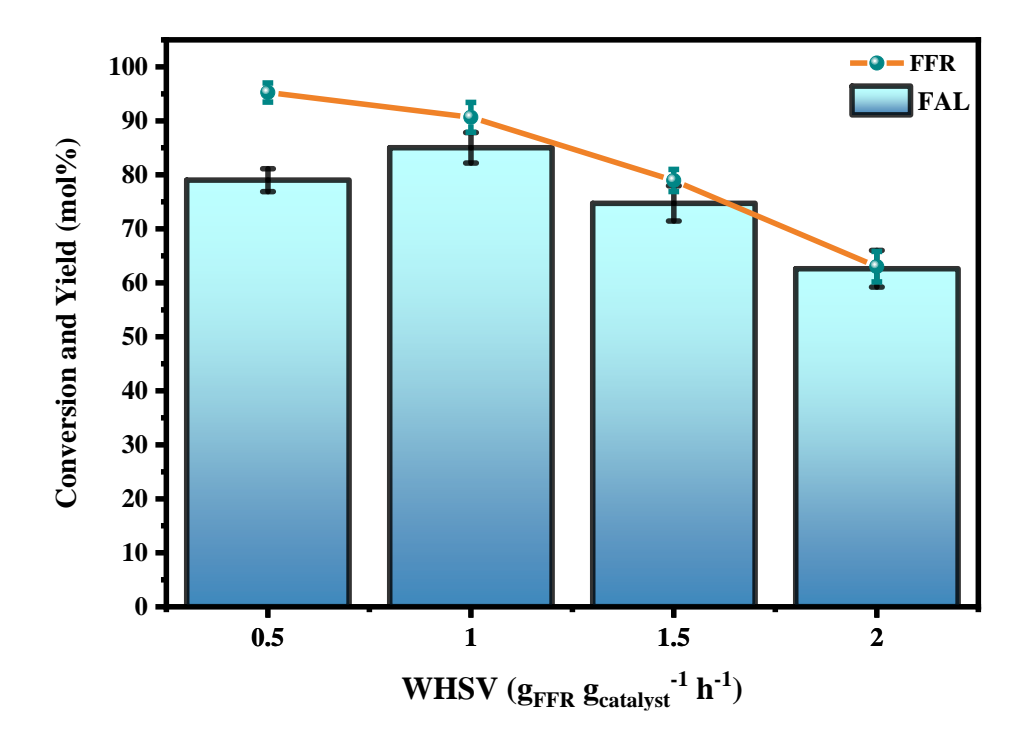


Fig. 6.15 Effect of WHSV on the conversion and yield during FFR hydrogenation over Cu@Zr-MS catalyst. $H_2/FFR=10$, Temperature = 200 °C, Pressure = 1 atm.

6.2.4 Catalyst Stability and Regeneration

To evaluate catalyst stability during extended operation, a extended time-on-stream (TOS) study was conducted (Fig. 6.16). The catalyst maintained a consistent conversion rate of ~90% for the first 18 h after which a gradual decline was observed. After the 24th h, the decline in conversion was more rapid, with the conversion value dropping off steeply to 53.8% at the end of the 30^h h. The FAL yield also mirrored a somewhat

similar trend, where it hovered constantly around a value of around 85% for the first 16 hours. Like conversion, the yield began to decline rapidly after the 24-hour mark, reaching a final value of 51.8% at the end of the 30-hour mark. The results indicate the catalyst was very active in the initial 10 to 12 h, likely due to the high activity of Cu for H₂ activation and the Cu⁺ and oxygen vacancies for activating the C=O bond of FFR. With increasing time-on-stream, it is likely that the active sites were progressively deactivated by deposition of carbonaceous species, which would reduce their capacity to activate H₂ and the reactant and therefore, explain the declining conversion and FAL yield values. Although catalyst deactivation was not explicitly studied, the observed changes in conversion and product yield can be explained by insights from the literature. MacIntosh and Beaumont's study on FFR hydrogenation over supported Ni metal catalysts linked deactivation to the formation of oligomeric and/or polymeric condensation compounds derived from FFR and FAL [55]. Similarly, Du et al. [15], in their investigation of FFR hydrogenation to FAL over silica-supported Cu catalysts, associated deactivation with carbon deposition from the polymerization products of FFR and FAL. Additionally, research by Jiménez-Gómez et al. [4,53,54] supported these findings, attributing the deactivation of their mesoporous silica-supported Cu catalyst to carbonaceous deposits from oligomeric compounds, and also noted that stronger adsorption of FFR and FAL may contribute to deactivation through site blocking. In light of these insights, the likely cause of catalyst deactivation in this study involves the strong adsorption of FFR and FAL and the formation of their oligomerization products, leading to site and/or pore blockage.

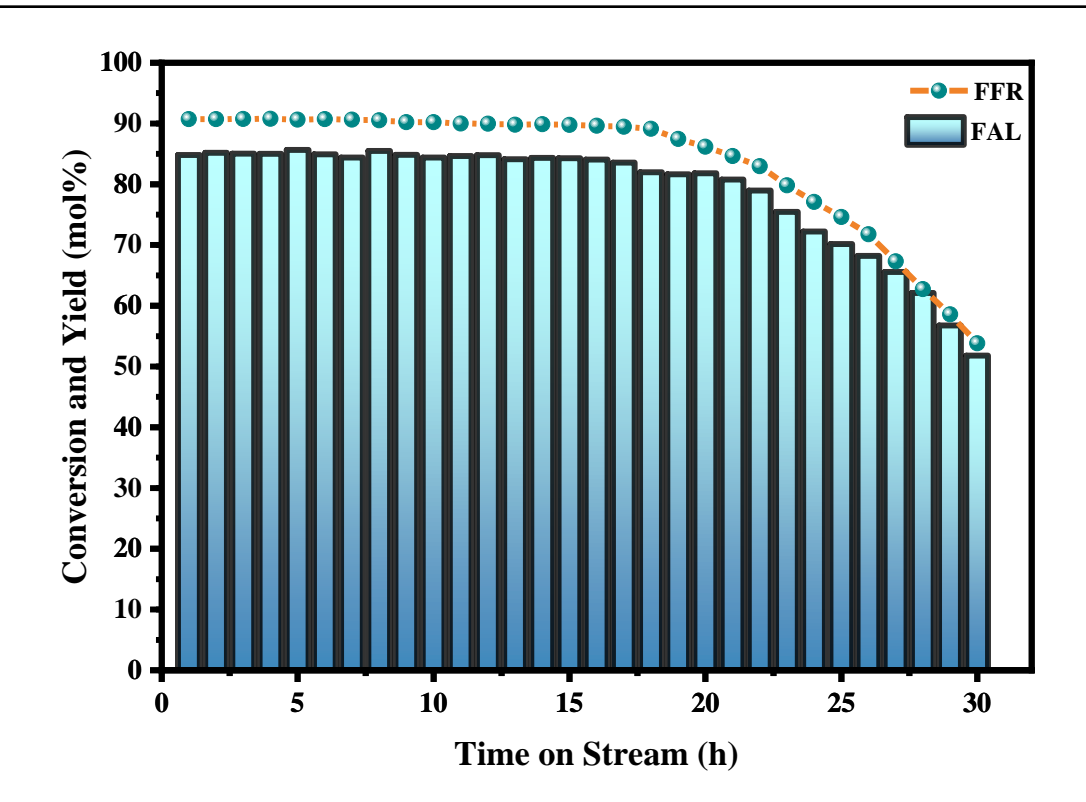


Fig. 6.16 Time-on-Stream (TOS) study for FFR hydrogenation to FAL over Cu@Zr-MS catalyst. Feed Flowrate = $5.43 \text{ mmol}_{FFR} \text{ h}^{-1}$, $\text{H}_2/\text{FFR} = 10$, Temperature = $200 \,^{\circ}\text{C}$, WHSV = $1 \, \text{g}_{FFR} \, \text{h}^{-1} \, \text{g}_{\text{catalyst}}^{-1}$, Pressure = $1 \, \text{atm}$, TOS = $30 \, \text{h}$.

To evaluate the durability and long-term catalytic performance, a regeneration study was conducted following an initial 24-h TOS (time on stream) reaction cycle. The regeneration process involved two steps: first, calcination at 500 °C in air, followed by reactivation in a hydrogen atmosphere, both performed within the fixed-bed reactor. After regeneration, the catalyst underwent a second 24-h TOS cycle to assess its stability and ability to maintain performance across multiple cycles. The results, shown in Fig. 6.17, demonstrate a partial restoration of catalytic activity post-regeneration. The catalyst sustained a conversion rate of nearly 80% for the first 8 h, after which a gradual decline in conversion was observed. This decline became more pronounced after 12 h and accelerated, eventually reaching a final conversion of 56.2%. No changes were observed in the product distribution as FAL remained the dominant product, with a consistent yield of around 74% during the initial 12 h. However, its yield began to decrease after this point, dropping to approximately 52% by the end of the 24-h period. These shifts in catalytic performance may be attributed to sintering caused by prolonged exposure to high temperatures during the reduction, TOS, and calcination steps, potentially altering the catalyst's morphology and impacting its stability over time.

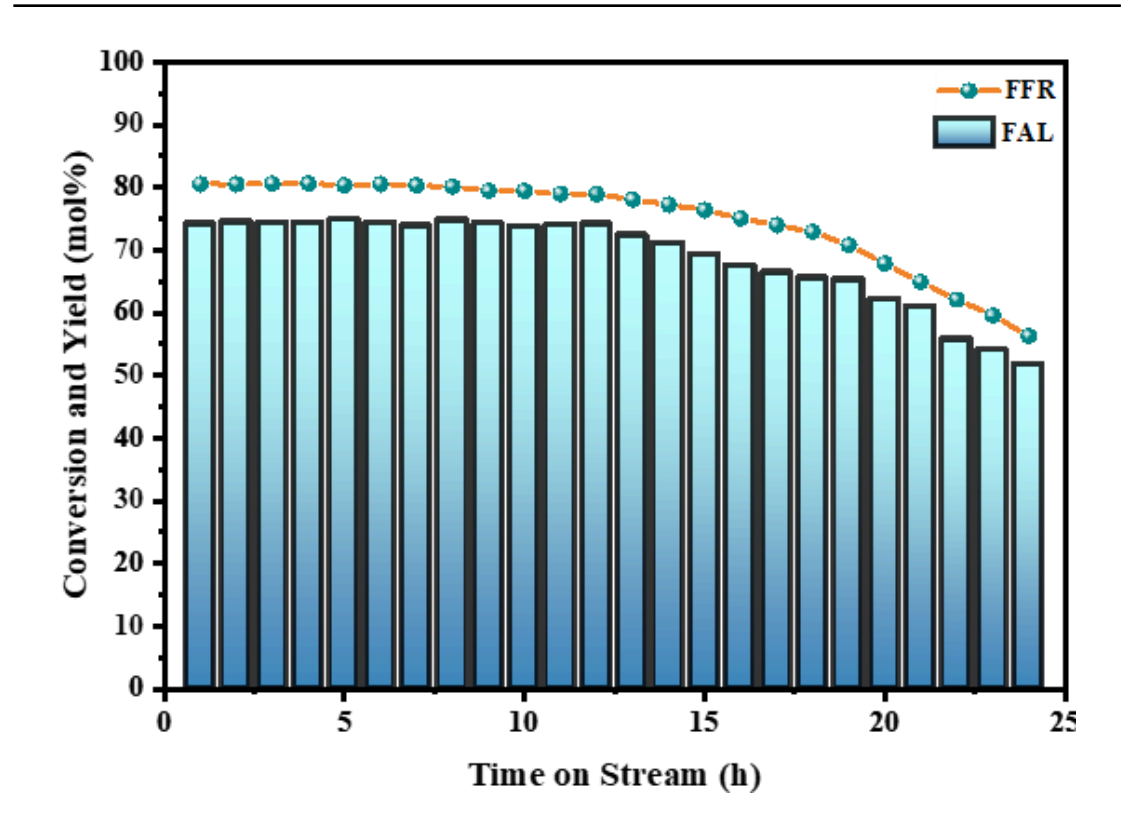


Fig. 6.17 Regeneration study for FFR hydrogenation to FAL over Cu@Zr-MS catalyst. Feed Flowrate = $5.43 \text{ mmol}_{FFR} \text{ h}^{-1}$, H₂/FFR = 10, Temperature = 200 °C, WHSV = $1 \text{ g}_{FFR} \text{ h}^{-1} \text{ g}_{catalyst}^{-1}$, Pressure = 1 atm, TOS = 24 h.

6.2.5 Probable Reaction Mechanism

Based on the comprehensive characterization analyses and process parameter evaluations, a plausible reaction mechanism for the conversion of FFR to FAL over the Cu@Zr-MS catalyst can be outlined (Fig. 6.18). Reduction of the calcined Cu@Zr-MS catalyst at 300 °C in a hydrogen atmosphere results in the reduction of Cu $^{2+}$ to Cu 0 . These newly formed Cu 0 sites play a crucial role in facilitating the reduction of Cu $^{2+}$ O-Zr $^{4+}$ bonds at the Cu and Zr-MS support interface, through spillover to Cu $^{+}$ -O_v-Zr $^{3+}$ bonds, in the process creating oxygen vacancies (O_v).

Upon introducing FFR into the reactor, the Cu^0 sites activate H_2 molecules, dissociating them into atomic hydrogen, which is essential for the hydrogenation step. Concurrently, Cu^+ sites [15] and oxygen vacancies [19], acting as Lewis acid centers, interact with the carbonyl group of FFR, enhancing its adsorption and activation. Additionally, the unreduced Zr^{4+} species, due to their oxophilic nature, facilitate interaction with the carbonyl group of FFR. The hydrogenation of FFR to FAL can then proceed via two possible mechanisms [56]. In the first mechanism, an H atom attacks

the carbon atom of the C=O group, resulting in the formation of an alkoxide intermediate. This intermediate then reacts with another H atom to produce FAL. In the second mechanism, an H atom attacks the carbonyl oxygen, leading to the formation of a hydroxyalkyl intermediate. This intermediate subsequently yields FAL upon the addition of a second hydrogen atom [56]. The second mechanism is generally considered more favourable due to the stabilization provided by the furan ring [56]. When the hydrogen atom first attacks the carbonyl oxygen, it leaves the carbon atom with a lone, unpaired electron. The furan ring stabilizes this unpaired electron through delocalization, thereby lowering the activation energy for this reaction route. This stabilization effect makes the hydrogenation process more efficient and favours the production of FAL. After the reduction of the C=O bond to a C-OH bond and subsequent desorption of the FAL product, the active sites on the catalyst are once again exposed to the reactants. This renewal of active sites allows the catalytic cycle to continue efficiently, facilitating ongoing hydrogenation reactions.

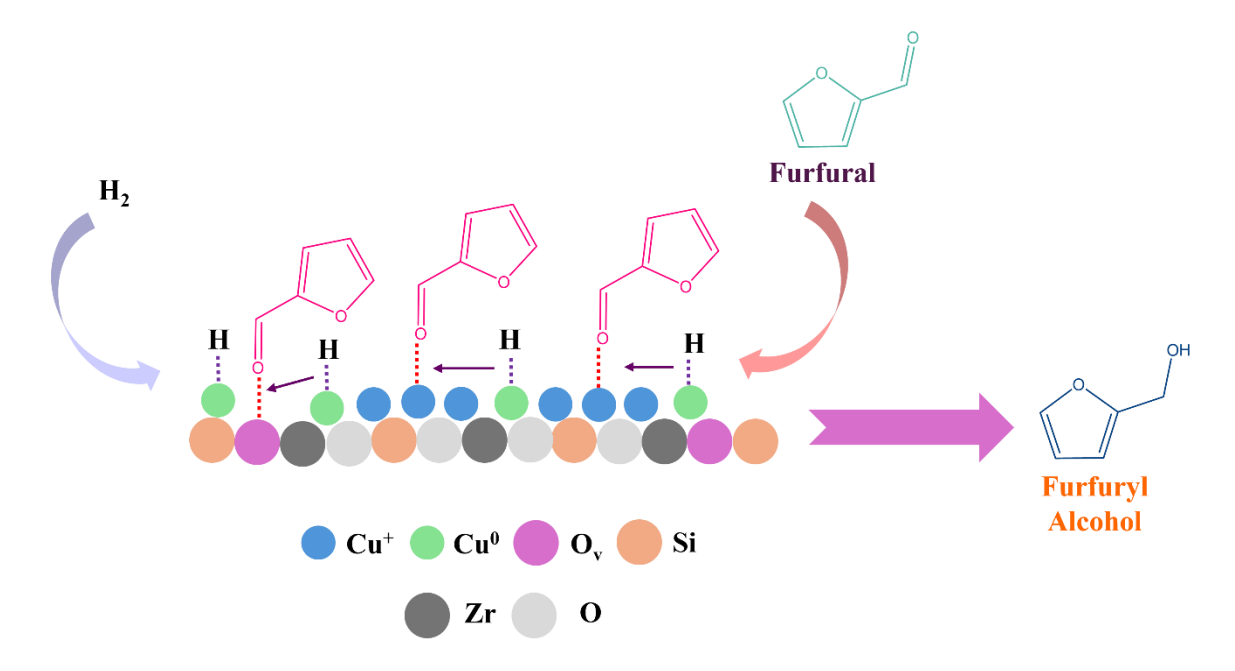


Fig. 6.18 A schematic representation of possible reaction mechanism of FFR hydrogenation over Cu@Zr-MS to FAL

References

- [1] R. Jothi Ramalingam, J.N. Appaturi, T. Pulingam, H.A. Al-Lohedan, D.M. Aldhayan, In-situ incorporation of ruthenium/copper nanoparticles in mesoporous silica derived from rice husk ash for catalytic acetylation of glycerol, Renew. Energy. 160 (2020) 564–574. https://doi.org/10.1016/j.renene.2020.06.095.
- [2] O.O. Fasanya, A.Y. Atta, M.T.Z. Myint, J. Dutta, B.Y. Jibril, Effects of synthesis methods on performance of CuZn/MCM-41 catalysts in methanol steam reforming, Int. J. Hydrogen Energy. 46 (2021) 3539–3553. https://doi.org/10.1016/j.ijhydene.2020.10.181.
- [3] X. Lu, H. Guo, J. Chen, D. Wang, A.F. Lee, X. Gu, Selective Catalytic Transfer Hydrogenation of Lignin to Alkyl Guaiacols Over NiMo/Al-MCM-41, ChemSusChem. 15 (2022). https://doi.org/10.1002/cssc.202200099.
- [4] C.P. Jiménez-Gómez, J.A. Cecilia, R. Moreno-Tost, P. Maireles-Torres, Selective Production of 2-Methylfuran by Gas-Phase Hydrogenation of Furfural on Copper Incorporated by Complexation in Mesoporous Silica Catalysts, ChemSusChem. 10 (2017) 1448–1459. https://doi.org/10.1002/cssc.201700086.
- [5] R.Y. Abrokwah, V.G. Deshmane, D. Kuila, Comparative performance of M-MCM-41 (M: Cu, Co, Ni, Pd, Zn and Sn) catalysts for steam reforming of methanol, J. Mol. Catal. A Chem. 425 (2016) 10–20. https://doi.org/10.1016/j.molcata.2016.09.019.
- [6] Z. Zhan, H.C. Zeng, A catalyst-free approach for sol-gel synthesis of highly mixed ZrO2-SiO2 oxides, J. Non. Cryst. Solids. 243 (1999) 26–38. https://doi.org/10.1016/S0022-3093(98)00810-2.
- [7] S. Suttiruengwong, S. Pivsa-Art, M. Chareonpanich, Hydrophilic and hydrophobic mesoporous silica derived from rice husk ash as a potential drug carrier, Materials (Basel). 11 (2018). https://doi.org/10.3390/ma11071142.
- [8] M. El-Sakhawy, A.M. Adel, M.A. Diab, M. Al-Shemy, Facile methods for the preparation of micro- and mesoporous amorphous silica from rice husk, Biomass Convers. Biorefinery. 12 (2022) 4709–4718. https://doi.org/10.1007/s13399-020-01112-2.
- [9] J.B. Miller, S.E. Rankin, E.I. Ko, Strategies in controlling the homogeneity of zirconia-silica aerogels: Effect of preparation on textural and catalytic properties, J. Catal. 148 (1994) 673–682. https://doi.org/10.1006/jcat.1994.1254.
- [10] P.M. Cuesta Zapata, J.F. Miranda, F. Orellana, E. Gonzo, N.A. Bonini, Synthesis of Cu/SiO2(MCM-41) mesostructured catalysts. Effect of the preparation method on the textural properties and chemical structure, Mater. Chem. Phys. 287 (2022). https://doi.org/10.1016/j.matchemphys.2022.126232.
- [11] S. Shen, J. Chen, R.T. Koodali, Y. Hu, Q. Xiao, J. Zhou, X. Wang, L. Guo, Activation of MCM-41 mesoporous silica by transition-metal incorporation for photocatalytic hydrogen production, Appl. Catal. B Environ. 150–151 (2014) 138–146. https://doi.org/10.1016/j.apcatb.2013.12.014.
- [12] D. Liu, X.Y. Quek, W.N.E. Cheo, R. Lau, A. Borgna, Y. Yang, MCM-41

- supported nickel-based bimetallic catalysts with superior stability during carbon dioxide reforming of methane: Effect of strong metal-support interaction, J. Catal. 266 (2009) 380–390. https://doi.org/10.1016/j.jcat.2009.07.004.
- [13] J. Yu, S. Liu, X. Mu, G. Yang, X. Luo, E. Lester, T. Wu, Cu-ZrO2 catalysts with highly dispersed Cu nanoclusters derived from ZrO2@ HKUST-1 composites for the enhanced CO2 hydrogenation to methanol, Chem. Eng. J. 419 (2021) 129656. https://doi.org/10.1016/j.cej.2021.129656.
- [14] H. Du, X. Ma, M. Jiang, P. Yan, Z. Conrad Zhang, Highly efficient Cu/SiO2 catalyst derived from ethanolamine modification for furfural hydrogenation, Appl. Catal. A Gen. 598 (2020). https://doi.org/10.1016/j.apcata.2020.117598.
- [15] H. Du, X. Ma, P. Yan, M. Jiang, Z. Zhao, Z.C. Zhang, Catalytic furfural hydrogenation to furfuryl alcohol over Cu/SiO2 catalysts: A comparative study of the preparation methods, Fuel Process. Technol. 193 (2019) 221–231. https://doi.org/10.1016/j.fuproc.2019.05.003.
- [16] A. Jaswal, P.P. Singh, A.K. Kar, T. Mondal, R. Srivastava, Production of 2-methyl furan, a promising 2nd generation biofuel, by the vapor phase hydrodeoxygenation of biomass-derived furfural over TiO2 supported Cu[sbnd]Ni bimetallic catalysts, Fuel Process. Technol. 245 (2023). https://doi.org/10.1016/j.fuproc.2023.107726.
- [17] F. Li, B. Cao, R. Ma, J. Liang, H. Song, H. Song, Performance of Cu/TiO2-SiO2 catalysts in hydrogenation of furfural to furfuryl alcohol, Can. J. Chem. Eng. 94 (2016) 1368–1374. https://doi.org/10.1002/cjce.22503.
- [18] K. Rajendran, M. Sharma, A. Jaison, M. Ankitha, A.D. Tiwari, C.P. Vinod, D. Jagadeesan, Oxidation of ethylene by Cu/TiO2: reducibility of Cu2+ in TiO2 as a possible descriptor of catalytic efficiency, Catal. Sci. Technol. 13 (2023) 2330–2339. https://doi.org/10.1039/d2cy02170f.
- [19] Z. Zhang, Z.L. Wang, K. An, J. Wang, S. Zhang, P. Song, Y. Bando, Y. Yamauchi, Y. Liu, Ti3+ Tuning the Ratio of Cu+/Cu0 in the Ultrafine Cu Nanoparticles for Boosting the Hydrogenation Reaction, Small. 17 (2021) 1–10. https://doi.org/10.1002/smll.202008052.
- [20] J. Yu, D. Zhao, X. Xu, X. Wang, N. Zhang, Study on RuO 2/SnO 2: Novel and Active Catalysts for CO and CH 4 Oxidation, ChemCatChem. 4 (2012) 1122–1132. https://doi.org/10.1002/cctc.201200038.
- [21] H. Yamaura, S. Hirao, S. Yamaguchi, H. Yahiro, Investigation on reduction behaviors of SnO2 and SnO2-supported CuO sensor materials by temperature-programmed reduction method combined with resistance measurement, Sensors Mater. 28 (2016) 1203–1210. https://doi.org/10.18494/SAM.2016.1281.
- [22] H. Zhu, Z. Qin, W. Shan, W. Shen, J. Wang, Pd/CeO2-TiO2 catalyst for CO oxidation at low temperature: A TPR study with H2 and CO as reducing agents, J. Catal. 225 (2004) 267–277. https://doi.org/10.1016/j.jcat.2004.04.006.
- [23] G. Cordoba, M. Viniegra, J.L.G. Fierro, R. Arroyo, TPR, ESR, and XPS Study of Cu 2 ½ Ions in Sol Gel-Derived TiO 2, J. Solid State Chem. 6 (1998) 1–6.

- [24] A. Jaswal, V. Garule, A. Pandey, P. Pratap Singh, T. Mondal, P. Biswas, Selective furfural hydrodeoxygenation over Cu-Fe catalysts with In-Situ Cu@Fe3O4 formation, J. Ind. Eng. Chem. (2024). https://doi.org/10.1016/j.jiec.2024.04.011.
- [25] F. Dong, Y. Zhu, H. Zheng, Y. Zhu, X. Li, Y. Li, Cr-free Cu-catalysts for the selective hydrogenation of biomass-derived furfural to 2-methylfuran: The synergistic effect of metal and acid sites, J. Mol. Catal. A Chem. 398 (2015) 140–148. https://doi.org/10.1016/j.molcata.2014.12.001.
- [26] D. Gao, H. Yin, Y. Feng, A. Wang, Coupling reaction between methanol dehydrogenation and maleic anhydride hydrogenation over zeolite-supported copper catalysts, Can. J. Chem. Eng. 93 (2015) 1107–1118. https://doi.org/10.1002/cjce.22185.
- [27] M.A. Díaz-Pérez, J. Moya, J.C. Serrano-Ruiz, J. Faria, Interplay of Support Chemistry and Reaction Conditions on Copper Catalyzed Methanol Steam Reforming, Ind. Eng. Chem. Res. 57 (2018) 15268–15279. https://doi.org/10.1021/acs.iecr.8b02488.
- [28] S. Damyanova, P. Grange, B. Delmon, Surface characterization of zirconia-coated alumina and silica carriers, J. Catal. 168 (1997) 421–430. https://doi.org/10.1006/jcat.1997.1671.
- [29] Y. Wang, R. Wu, Y. Zhao, Effect of ZrO2 promoter on structure and catalytic activity of the Ni/SiO2 catalyst for CO methanation in hydrogen-rich gases, Catal. Today. 158 (2010) 470–474. https://doi.org/10.1016/j.cattod.2010.07.016.
- [30] X. Yu, W. chun Zhu, S. Gao, L. li Chen, H. jing Yuan, J. huan Luo, Z. lü Wang, W. xiang Zhang, Transformation of ethanol to ethyl acetate over Cu/SiO2 catalysts modified by ZrO2, Chem. Res. Chinese Univ. 29 (2013) 986–990. https://doi.org/10.1007/s40242-013-3024-8.
- [31] X. Ma, S. Wang, J. Gong, X. Yang, G. Xu, A comparative study of supported TiO 2 catalysts and activity in ester exchange between dimethyl oxalate and phenol, J. Mol. Catal. A Chem. 222 (2004) 183–187. https://doi.org/10.1016/j.molcata.2004.08.004.
- [32] N. Koivikko, T. Laitinen, A. Mouammine, S. Ojala, R.L. Keiski, Catalytic activity studies of Vanadia/Silica—Titania catalysts in SVOC partial oxidation to formaldehyde: Focus on the catalyst composition, Catalysts. 8 (2018). https://doi.org/10.3390/catal8020056.
- [33] M. Itoh, H. Hattori, K. Tanabe, The acidic properties of TiO2-SiO2 and its catalytic activities for the amination of phenol, the hydration of ethylene and the isomerization of butene, J. Catal. 35 (1974) 225–231. https://doi.org/10.1016/0021-9517(74)90201-2.
- [34] H. Zhang, N. Zhang, J. Man, Y. Du, J. Cui, J. Sun, A sustainable approach from rice husks to P,N-dual doping porous C/SiOx composites for high-performance lithium-ion battery anodes, J. Electroanal. Chem. 904 (2022) 115939. https://doi.org/10.1016/j.jelechem.2021.115939.
- [35] H. Zhang, Z. Yang, N. Zhang, K. Qiao, Y. Liu, W. He, J. Cui, J. Sun, Boron-

- doped rice husk-derived C/SiOx composites as high-property anode for Li-ion batteries, Ionics (Kiel). 28 (2022) 4159–4167. https://doi.org/10.1007/s11581-022-04641-0.
- [36] D. Tharani, M. Ananthasubramanian, Influence of pre-treatment processes on the purity and characteristics of silica extracted from rice husk, Biomass Convers. Biorefinery. 14 (2023) 12517–12529. https://doi.org/10.1007/s13399-022-03728-y.
- [37] H. Chu, Q. Wu, J. Huang, Rice husk derived silicon/carbon and silica/carbon nanocomposites as anodic materials for lithium-ion batteries, Colloids Surfaces A Physicochem. Eng. Asp. 558 (2018) 495–503. https://doi.org/10.1016/j.colsurfa.2018.09.020.
- [38] G. Zheng, Y. Xiang, L. Xu, H. Luo, B. Wang, Y. Liu, X. Han, W. Zhao, S. Chen, H. Chen, Q. Zhang, T. Zhu, Y. Yang, Controlling Surface Oxides in Si/C Nanocomposite Anodes for High-Performance Li-Ion Batteries, Adv. Energy Mater. 8 (2018) 1–12. https://doi.org/10.1002/aenm.201801718.
- [39] P. Lv, H. Zhao, C. Gao, T. Zhang, X. Liu, Highly efficient and scalable synthesis of SiOx/C composite with core-shell nanostructure as high-performance anode material for lithium ion batteries, Electrochim. Acta. 152 (2015) 345–351. https://doi.org/10.1016/j.electacta.2014.11.149.
- [40] G. Singh, T.S. Khan, C. Samanta, R. Bal, A. Bordoloi, Single-step synthesis of 2-pentanone from furfural over Cu–Ni @SBA-15, Biomass and Bioenergy. 156 (2022) 106321. https://doi.org/10.1016/j.biombioe.2021.106321.
- [41] S. Lomate, A. Sultana, T. Fujitani, Vapor Phase Catalytic Transfer Hydrogenation (CTH) of Levulinic Acid to γ-Valerolactone Over Copper Supported Catalysts Using Formic Acid as Hydrogen Source, Catal. Letters. 148 (2018) 348–358. https://doi.org/10.1007/s10562-017-2241-z.
- [42] Y. Zhao, H. Zhang, Y. Xu, S. Wang, Y. Xu, S. Wang, X. Ma, Interface tuning of Cu+/Cu0 by zirconia for dimethyl oxalate hydrogenation to ethylene glycol over Cu/SiO2 catalyst, J. Energy Chem. 49 (2020) 248–256. https://doi.org/10.1016/j.jechem.2020.02.038.
- [43] K. Samson, M. Sliwa, R.P. Socha, K. Góra-Marek, D. Mucha, D. Rutkowska-Zbik, J.F. Paul, M. Ruggiero-Mikoajczyk, R. Grabowski, J. Soczyński, Influence of ZrO2 structure and copper electronic state on activity of Cu/ZrO2 catalysts in methanol synthesis from CO2, ACS Catal. 4 (2014) 3730–3741. https://doi.org/10.1021/cs500979c.
- [44] Z. Li, H. Hao, J. Lu, C. Wu, R. Gao, J. Li, C.L. Liu, W.S. Dong, Role of the Cu-ZrO2 interface in the hydrogenation of levulinic acid to γ-valerolactone, J. Energy Chem. 61 (2021) 446–458. https://doi.org/10.1016/j.jechem.2021.01.046.
- [45] I.C. Freitas, S. Damyanova, D.C. Oliveira, C.M.P. Marques, J.M.C. Bueno, Effect of Cu content on the surface and catalytic properties of Cu/ZrO 2 catalyst for ethanol dehydrogenation, J. Mol. Catal. A Chem. 381 (2014) 26–37. https://doi.org/10.1016/j.molcata.2013.09.038.

- [46] P. Hanyš, P. Janeček, V. Matolín, G. Korotcenkov, V. Nehasil, XPS and TPD study of Rh/SnO2 system Reversible process of substrate oxidation and reduction, Surf. Sci. 600 (2006) 4233–4238. https://doi.org/10.1016/j.susc.2006.01.150.
- [47] C. Ding, Y. Zhang, X. Di, N. Zhang, Y. Zhang, X. Wang, High-density polyethylene composite filled with red mud: effect of coupling agent on mechanical and thermal properties, Environ. Technol. (United Kingdom). 43 (2022) 3283–3294. https://doi.org/10.1080/09593330.2021.1921047.
- [48] S. Kamari, F. Ghorbani, Extraction of highly pure silica from rice husk as an agricultural by-product and its application in the production of magnetic mesoporous silica MCM–41, Biomass Convers. Biorefinery. 11 (2021) 3001–3009. https://doi.org/10.1007/s13399-020-00637-w.
- [49] C.A. Teles, P.M. de Souza, A.H. Braga, R.C. Rabelo-Neto, A. Teran, G. Jacobs, D.E. Resasco, F.B. Noronha, The role of defect sites and oxophilicity of the support on the phenol hydrodeoxygenation reaction, Appl. Catal. B Environ. 249 (2019) 292–305. https://doi.org/10.1016/j.apcatb.2019.02.077.
- [50] P.M. De Souza, R.C. Rabelo-Neto, L.E.P. Borges, G. Jacobs, B.H. Davis, D.E. Resasco, F.B. Noronha, Hydrodeoxygenation of Phenol over Pd Catalysts. Effect of Support on Reaction Mechanism and Catalyst Deactivation, ACS Catal. 7 (2017) 2058–2073. https://doi.org/10.1021/acscatal.6b02022.
- [51] S. Chen, R. Wojcieszak, F. Dumeignil, E. Marceau, S. Royer, How Catalysts and Experimental Conditions Determine the Selective Hydroconversion of Furfural and 5-Hydroxymethylfurfural, Chem. Rev. 118 (2018) 11023–11117. https://doi.org/10.1021/acs.chemrev.8b00134.
- [52] B. Seemala, C.M. Cai, R. Kumar, C.E. Wyman, P. Christopher, Effects of Cu-Ni Bimetallic Catalyst Composition and Support on Activity, Selectivity, and Stability for Furfural Conversion to 2-Methyfuran, ACS Sustain. Chem. Eng. 6 (2018) 2152–2161. https://doi.org/10.1021/acssuschemeng.7b03572.
- [53] C.P. Jiménez-Gómez, J.A. Cecilia, D. Durán-Martín, R. Moreno-Tost, J. Santamaría-González, J. Mérida-Robles, R. Mariscal, P. Maireles-Torres, Gasphase hydrogenation of furfural to furfuryl alcohol over Cu/ZnO catalysts, J. Catal. 336 (2016) 107–115. https://doi.org/10.1016/j.jcat.2016.01.012.
- [54] C.P. Jiménez-Gómez, J.A. Cecilia, I. Márquez-Rodríguez, R. Moreno-Tost, J. Santamaría-González, J. Mérida-Robles, P. Maireles-Torres, Gas-phase hydrogenation of furfural over Cu/CeO2 catalysts, Catal. Today. 279 (2017) 327–338. https://doi.org/10.1016/j.cattod.2016.02.014.
- [55] K.L. MacIntosh, S.K. Beaumont, Nickel-Catalysed Vapour-Phase Hydrogenation of Furfural, Insights into Reactivity and Deactivation, Top. Catal. 63 (2020) 1446–1462. https://doi.org/10.1007/s11244-020-01341-9.
- [56] S. Sitthisa, T. Sooknoi, Y. Ma, P.B. Balbuena, D.E. Resasco, Kinetics and mechanism of hydrogenation of furfural on Cu/SiO2 catalysts, J. Catal. 277 (2011) 1–13. https://doi.org/10.1016/j.jcat.2010.10.005.

lerived and metal-inco	rporated mesopo	rous silica	

Chapter 7: FFR Transfer Hydrogenation to 2-MeF over Mg-Fe mixed oxide catalysts

This chapter investigates Mg-Fe mixed oxide catalysts with varying Mg/Fe molar ratios (1 to 5) synthesized via a co-precipitation method for vapor-phase FFR transfer hydrogenation to 2-MeF. The catalysts were characterized using XRD, NH₃-TPD, CO₂-TPD, N₂ physisorption, FESEM, HRTEM and XPS to gain sights into their properties. Subsequently, a comprehensive evaluation of these catalysts was carried out to assess their catalytic efficacy in the FFR transfer hydrogenation process. This investigation explored the influence of Mg to Fe ratios, reaction temperatures, space velocity and calcination temperatures of the catalysts under atmospheric pressure conditions. Following the conclusion of process parameter optimization, the long-term catalytic activity evaluation was also studied. Later, a rigorous regeneration study, where the catalyst was regenerated after an initial cycle of extended time-on-stream reactions. Here, the catalyst was first calcined at 500 °C in air, and then subjected to a second cycle of TOS reactions.

7.1 Characterization

7.1.1 XRD

Fig. 7.1 illustrates the XRD diffractograms for pure Mg and Fe oxides, along with Mg-Fe mixed oxides at varying Mg/Fe molar ratios. The pure Fe oxide displays peaks at 2θ values of 24.2°, 33.2°, 35.7°, 40.9°, 49.5°, 54.1°, 57.6°, 62.5°, 64.2° and 71.9°, which correspond to the (012), (104), (110), (113), (024), (116), (018), (214), (030), and (10 10) lattice planes of the hexagonal hematite (α-Fe₂O₃) phase [1]. Meanwhile, the pure Mg oxide shows three smaller peaks at 2θ values of 36.9°, 74.7°, and 78.7°, paired with two prominent peaks at 42.9° and 62.3°, characteristic of the cubic periclase MgO phase [2,3]. In the Mg-Fe mixed catalyst with a 1:1 molar ratio, the Fe₂O₃ peaks at 40.9°, 49.5°, 54.1°, and 57.4° lose much of their intensity, leaving only the peaks at 33.1° and 35.6° visible. Additionally, new peaks at 42.8° and 62.1° emerge, with the former potentially correspond to MgO and the latter to both MgO and Fe₂O₃. Increasing the Mg/Fe ratio to 2 results in the disappearance of all Fe₂O₃ peaks except for the (110) lattice plane. The peaks at 42.9° and 62.5° become more pronounced, and a small shoulder at 36.5° likely reflects the (111) phase of periclase MgO. A distinct sharp peak

around 30° may indicate the formation of an MgFe₂O₄ spinel ferrite phase. As the Mg/Fe ratio further increased to 5, these peaks at 42.8° and 62.1° further intensify and shift to lower values, accompanied by the emergence of a new peak corresponding to MgO at 78.7°. Meanwhile, the Fe₂O₃ peaks disappear entirely, and no evidence of the spinel phase is detected, possibly due to the phase being amorphous, or present in quantities below the detection limit of XRD.

The catalysts containing both Mg and Fe show broad XRD peaks, which stand in stark contrast to the sharp peaks observed for the pure MgO sample. This broadening points to a significant structural transformation during the calcination process. It has been observed that the precursors of Mg-Fe catalysts, prepared via the co-precipitation method, exhibit a layered structure akin to brucite (Mg(OH)₂). In this structure, Mg²⁺ or Fe³⁺ cations occupy the centres of octahedra, which share edges to form twodimensional sheets [4]. These sheets stack into a three-dimensional network, held together by hydrogen bonds [4]. Upon calcination, the original layered structure is disrupted, leading to a highly disordered phase [4,5]. This is reflected in the broad XRD peaks observed, which suggest the formation of a Mg-Fe mixed oxide phase with limited long-range order. The shift of XRD peaks towards lower 20 values with increasing Mg/Fe ratios in our study further suggests the incorporation of Fe ions into the MgO lattice, forming a solid ferro-periclase solution. The shift towards lower 20 values is a result of ionic radius of Fe³⁺ (0.65 Å) being smaller as compared to that of Mg²⁺ (0.72 Å). This results in a lattice contraction, supporting the formation of a (Mg(Fe³⁺)-O) mixed oxide phase. Literature reports align with these findings [6–8], indicating that Mg-Fe mixed oxides are formed after calcination at 500 °C from hydrotalcite-type precursors, and adopt a highly disordered structure [7,9]. A similar structural transformation has been observed in other catalyst systems. For example, Takehira and colleagues noted the formation of a periclase-like phase (Mg(Ni²⁺-, Al³⁺)-O) in Ni-Mg-Al catalysts, also synthesized via co-precipitation, where mixed oxides of Mg, Ni, and Al were formed [10,11].

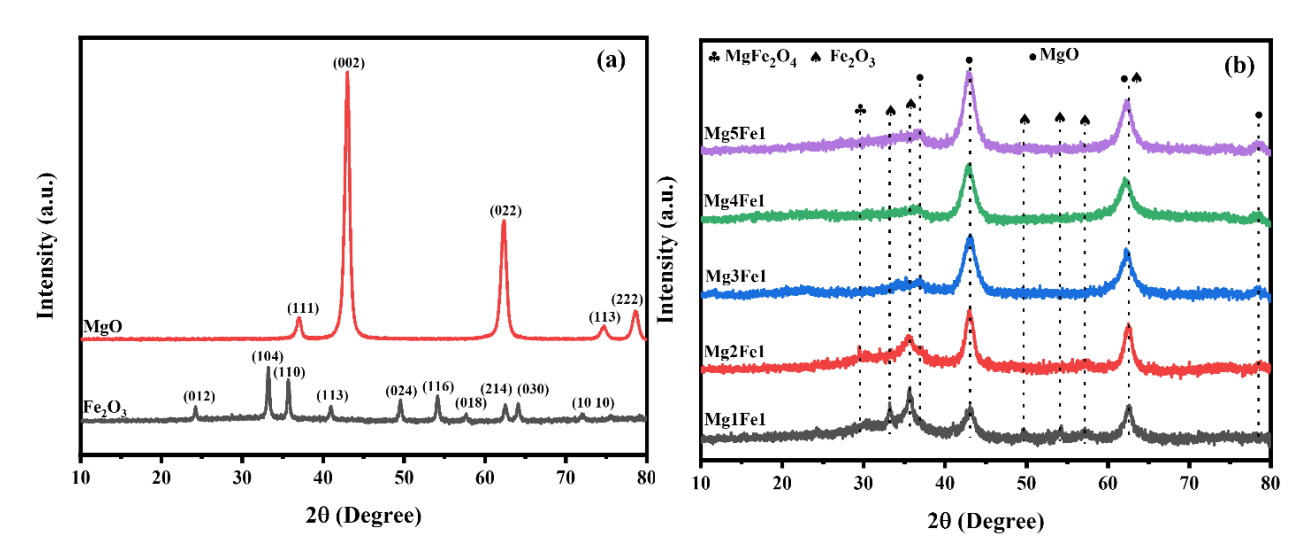


Fig. 7.1 XRD diffraction patterns of (a) Mg0Fe1 and Mg1Fe0 and (b) Mg-Fe mixed oxide catalysts with varying Mg/Fe ratios.

Table 7.1 Physical properties of the synthesized pure and mixed oxide Mg-Fe catalysts.

Surface Area (m²/g)	Pore Volume (cm³/g)	Pore Size (nm)
30.9	0.063	8.16
117.2	0.442	15.1
100.6	0.369	19.5
155.2	0.552	14.2
149	0.621	16.7
152.4	0.355	9.4
201.2	0.47	9.3
	(m ² /g) 30.9 117.2 100.6 155.2 149 152.4	(m²/g) (cm³/g) 30.9 0.063 117.2 0.442 100.6 0.369 155.2 0.552 149 0.621 152.4 0.355

7.1.2 N₂ Physisorption

Table 7.1 presents the results from the N₂ physisorption analysis, detailing specific surface area, pore volume, and pore size distribution of the catalysts studied. The Mg0Fe1 catalyst, which contains only pure iron oxide, exhibited the lowest surface area and pore volume among all the catalysts, consistent with observations reported in the literature [12,13]. This is likely due to the propensity of iron oxide particles to agglomerate.[13,14] For the Mg-Fe mixed catalysts, no distinct trend in surface area and pore volume values was observed. However, the introduction of Mg significantly increased both surface area and pore volume, an effect that could be attributed to the creation of meso- and/or microporosity [3]. Notably, when the Mg/Fe ratio exceeded 3, there was minimal change in the surface area values, and the pore volume also remained

relatively constant beyond this ratio. In terms of pore size distribution, the pure Fe₂O₃ (Mg0Fe1) catalyst exhibited the smallest average pore size among the catalysts. The addition of Mg increased the pore size, with the Mg-Fe mixed oxide catalyst at a Mg/Fe ratio of 2 having the largest pore size. However, as the Mg/Fe ratio continued to increase beyond 2, the average pore size began to decrease. Despite these variations, all Mg-Fe mixed oxide catalysts featured pores sufficiently large to facilitate the diffusion of reactants and products to and from the active sites, thereby minimizing potential diffusion resistance and ensuring efficient catalytic activity.

7.1.3 NH₃-TPD

NH₃-TPD analysis was conducted on the Mg0Fe1, Mg4Fe1, and Mg1Fe0 catalysts to evaluate their surface acidic sites, as illustrated in Fig. 7.2. The desorption temperature of NH₃ categorizes these sites into weak (< 300 °C), medium (300 to 500 °C), and strong (> 500 °C) acidic sites. The Mg0Fe1 catalyst, composed solely of Fe₂O₃, exhibited a broad desorption band from 100 to 400 °C, with a prominent peak around 200 °C, indicating the presence of predominantly weak acidic sites. a broad desorption band was observed between 100 and 400 °C, with a prominent peak around 200 °C, indicating the predominance of weak acidic sites. The band extended beyond 300 °C, showing a minor hump-like peak at approximately 345 °C, which tapered off around 380 °C. This tailing into the medium temperature range, coupled with the small hump, suggests the presence of some medium-strength acidic sites in small amounts. For the Mg1Fe0 catalyst, which contains only Mg, a similar broad band between 100 and 300 °C was observed, peaking at around 180 °C, indicating weak acidic sites. However, the intensity of this peak was weaker than that of the Mg0Fe1 catalyst. Interestingly, a broad band between 300 and 450 °C, peaking near 360 °C, was observed, indicating a significant presence of medium-strength acidic sites. The acidity in the pure MgO catalyst may be attributed to the presence of coordinatively unsaturated Mg²⁺ sites can act as Lewis acid sites, contributing to the observed desorption profile. The Mg4Fe1 catalyst, with a Mg to Fe ratio of 4, showed desorption profiles similar to those of the Mg1Fe0 catalyst, with a broad peak between 100 and 300 °C and another between 300 and 450 °C. The intensity of both the low-temperature and medium-temperature peaks appeared to be greater than that observed in both the Mg0Fe1 and Mg1Fe0 catalysts, suggesting an increased number of both weak and medium-strength acidic sites. These findings are consistent with literature reports on similar systems, such as MgO-SiO₂ [15,16], and MgO-Al₂O₃ [17,18] mixed oxides, and activated carbon-supported MgO catalysts [19], where comparable NH₃-desorption profiles were observed. In these studies, an increase in the intensities of peaks corresponding to weak and medium or strong acidic sites was noted at high Mg contents. The observed increase in the number of acidic sites in the Mg4Fe1 catalyst, relative to the Mg0Fe1 and Mg1Fe0 catalysts, could be attributed to the incorporation of Fe into the MgO lattice. Ramasamy et. al. [18] and Shen et. al. [20] have reported that Lewis acidity in Mg-rich mixed oxides (such as Mg-Al) can be ascribed to the presence of the trivalent metal (Al³⁺ or Fe³⁺ in this case) in the M³⁺-O-Mg²⁺ species. Additionally, there may be some contribution from coordinatively unsaturated Mg²⁺ sites as well, thereby explaining increased strength of acidic sites.

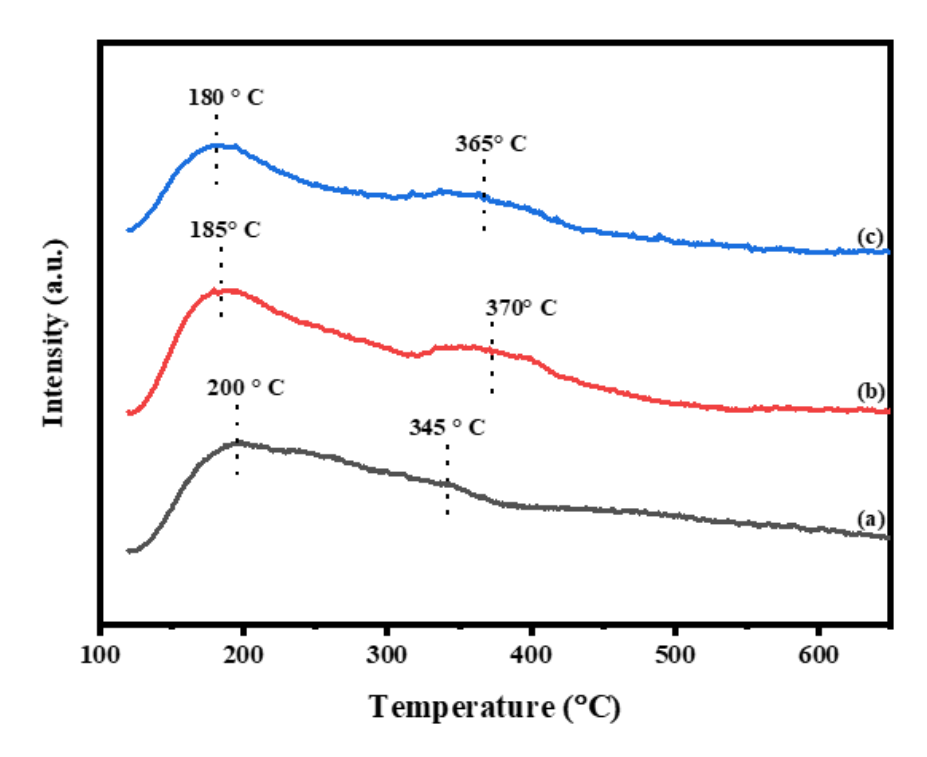


Fig. 7.2 NH₃-TPD profiles of (a) Mg0Fe1, (b) Mg4Fe1 and (c) Mg1Fe0 catalysts. **7.1.4** CO₂-TPD

To evaluate the nature of the basic sites on the surface of the catalysts, CO₂-TPD analysis was performed for Mg0Fe1, Mg4Fe1, and Mg1Fe0 catalysts (Fig. 7.3). Similar to acidic sites, surface basic sites can be categorized as weak, medium, or strong based on the CO₂ desorption temperature. The Mg0Fe1 catalyst, composed of just Fe₂O₃, showed no detectable CO₂ desorption peaks, which is expected since Fe³⁺ species act

Chapter 7| FFR Transfer Hydrogenation to 2-MeF over Mg-Fe mixed oxide catalysts

as Lewis acid sites, capable of accepting electrons. CO₂ binding, however, requires Lewis base sites, which donate electrons. The pure MgO catalyst (Mg1Fe0) displayed a prominent peak between ~250 °C and 370 °C, indicative of weak to moderately strong basic sites. Additionally, it featured two smaller peaks corresponding to strong basic sites at approximately 555 °C and 680 °C. The Mg4Fe1 mixed oxide catalyst, on the other hand, exhibited a broad desorption peak between 300 °C and 400 °C, centered around 360 °C, signifying the presence of medium-strength basic sites. The mediumstrength basic sites are typically attributed to Mg-O pairs, while stronger basic sites are associated with low coordination O²⁻ anions [20,21]. Interestingly, the shift of the medium-strength basic site peak from 300 °C in the pure MgO catalyst to 360 °C in the Mg4Fe1 catalyst suggests a slight increase in the strength of these sites. This enhancement can likely be attributed to the incorporation of Fe³⁺ ions into the MgO lattice, which introduces defects to balance the increased positive charge, leading to adjacent oxygen atoms becoming coordinatively unsaturated. Notably, the peaks corresponding to strong basic sites were absent in the CO₂-TPD profile of the Mg4Fe1 catalyst. This could be due to the presence of Fe reducing the overall basicity of the surface, weakening the stronger basic sites. Shen et. al. [20] had also noted a reduction in the basic strength of surface sites post Al introduction in Mg-rich Mg-Al mixed oxide catalysts, which they attributed to the fact that the O²⁻ anions associated with Al³⁺ species exhibited much weaker basicity as compared to those associated with Mg²⁺ as the nearest neighbours.

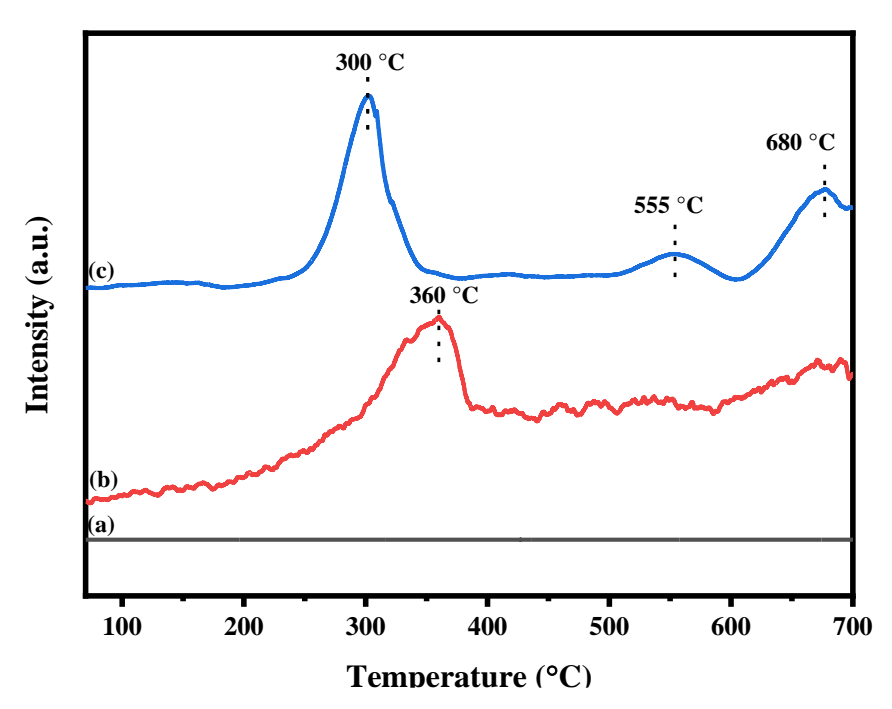


Fig. 7.3 CO_2 -TPD profiles of (a) Mg0Fe1, (b) Mg4Fe1 and (c) Mg1Fe0 catalysts.

7.1.5 FESEM

Fig. 7.4 presents FESEM images of the synthesized Mg-Fe mixed oxide catalysts. The pure Fe₂O₃ sample consisted of roughly spherical particles that appeared agglomerated, consistent with literature describing the tendency of iron oxides to agglomerate [13,14]. Introducing Mg in a 1:1 molar ratio with Fe caused a noticeable morphological change, characterized by the emergence of flake/plate-like structures, as observed in previous studies [13]. Additionally, the Fe₂O₃ spheres became very small, consistent with observations suggesting a reduction in Fe₂O₃ crystallite size due to the presence of oxides of other metals such as Al [22]. The flakes appear to grow around these spheres, suggesting that the spherical Fe₂O₃ particles are dispersed or situated on the surface of the flake-like structures. As the Mg/Fe ratio increased from 1 to 5, the morphology evolved significantly: the spherical Fe₂O₃ particles became less discernible, likely due to the increasing prominence of the large flakes or plate-like structures. This change suggests that at higher Mg/Fe ratios, the flakes or plates may cover or obscure the spherical particles. Moreover, the higher Mg/Fe ratios contribute to enhanced porosity in the catalyst structure, as indicated by the widely distributed plates and their emergence from cavities. This increased porosity is consistent with previous findings [3,13]. Furthermore, the EDX analysis (table 7.2) of the synthesized catalysts found the surface elemental composition to be close to the intended values.

Chapter 7| FFR Transfer Hydrogenation to 2-MeF over Mg-Fe mixed oxide catalysts

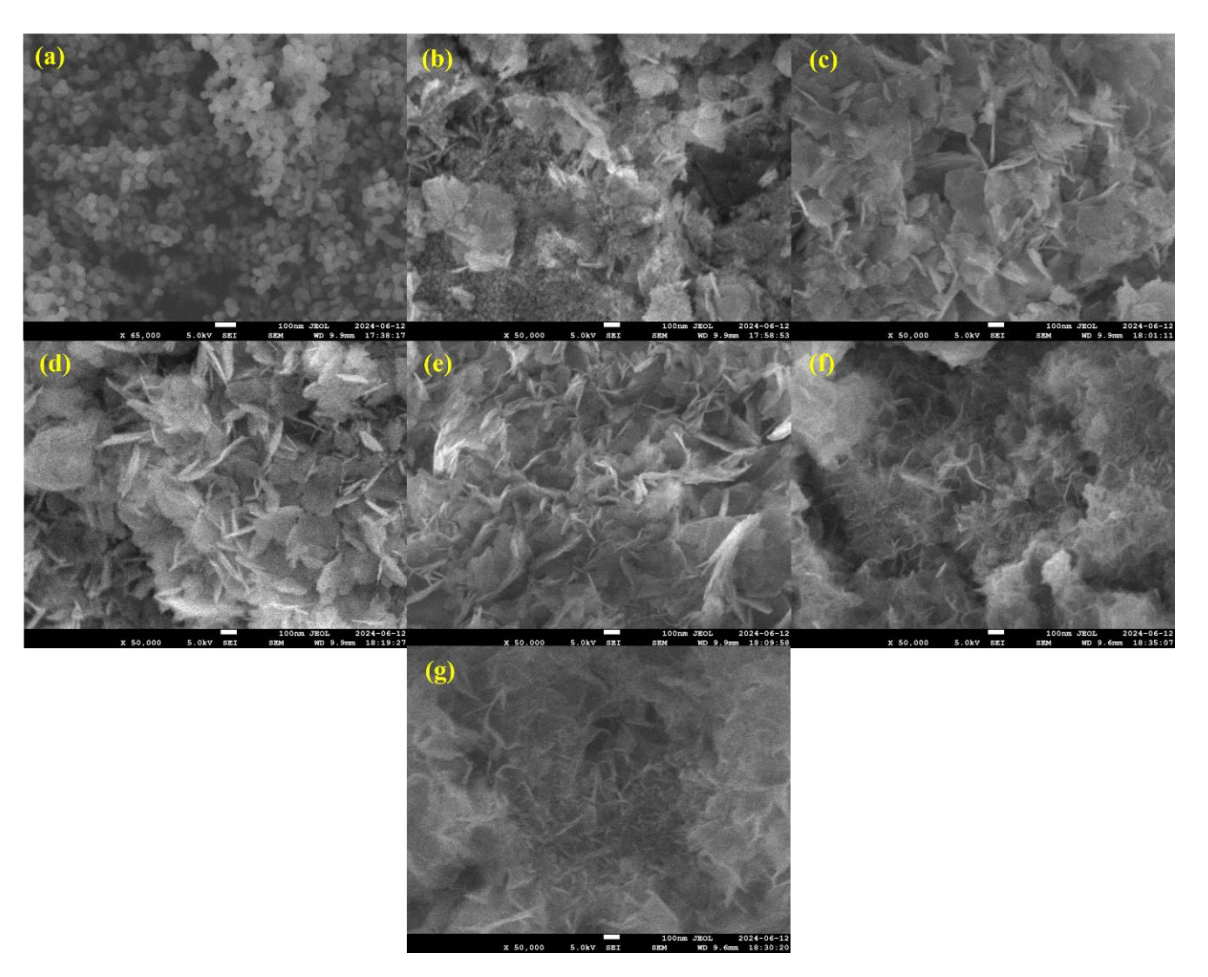


Fig. 7.4 FESEM images of (a) Mg0Fe1, (b) Mg1Fe1, (c) Mg2Fe1, (d) Mg3Fe1, (e) Mg4Fe, (f) Mg5Fe1, and (g) Mg1Fe0 catalysts

Table 7.2 Elemental composition analysis (EDX) of the pristine and Mg-Fe mixed oxide catalysts

Catalyst _	Atomic Weight %			Mg/Fe molar
	Mg	Fe	0	ratio
Mg0Fe1	-	66.6	33.4	-
Mg1Fe1	22	45	33	1.12
Mg2Fe1	30.9	33.9	34	2.09
Mg3Fe1	35.9	27.8	36.3	2.96
Mg4Fe1	40.1	23.1	36.8	4.03
Mg5Fe1	43.2	19.2	37.6	5.17
Mg1Fe0	63.4	-	36.6	-

7.1.6 XPS

To determine the surface oxidation state of Fe in the synthesized catalysts, XPS analysis was performed on MgOFe1, Mg4Fe1, and Mg1Fe catalysts. For the Mg0Fe1 (pure Fe₂O₃) catalyst, the Fe 2p spectrum displayed two main peaks corresponding to Fe 2p_{3/2} and Fe 2p_{1/2} at binding energies of approximately 711 eV and 724.5 eV, respectively as seen in Fig. 7.5 (a). Deconvolution of the Fe 2p_{3/2} peak revealed a multiplet indicative of Fe³⁺ present as bulk α-Fe₂O₃ (hematite) phase [23–25]. Additionally, a higher binding energy surface peak was identified, which likely corresponds to Fe³⁺ in low coordination environments, where reduced electron density necessitates a higher binding energy for photoelectron emission. The spectrum also exhibited two satellite peaks, associated with the Fe $2p_{3/2}$ and Fe $2p_{1/2}$ energy levels, at 719 eV and 732.7 eV, respectively. According to the literature, the doublets in the Fe 2p spectrum typically have a binding energy difference of about 13.4 eV, and the satellite peaks usually appear around 8 eV higher than the main peaks [24]. The observed values closely match those reported, confirming that Fe is present as Fe^{3+} (α -Fe₂O₃) in the Mg0Fe1 catalyst. This aligns with the XRD observations, which identified Fe₂O₃ as the only phase formed. Similarly, the Fe 2p spectrum for the Mg4Fe1 catalyst mirrored that of Mg0Fe1 (Fig. 7.5b), showing peaks exclusively associated with Fe³⁺ species. This finding again aligns with the XRD findings, which showed a shift in peaks to lower 2θ values with increasing Mg/Fe ratios. This shift was attributed to the incorporation of Fe³⁺ into the MgO lattice, where the smaller ionic radius of Fe³⁺ (0.65 Å) compared to Mg²⁺ (0.72 Å) caused lattice contractions and formed a ferro-periclase Mg(Fe³⁺)O solid solution. The consistent results from both XPS and XRD analyses reinforce the conclusion that Fe is present as Fe³⁺ in the Mg4Fe1 catalyst.

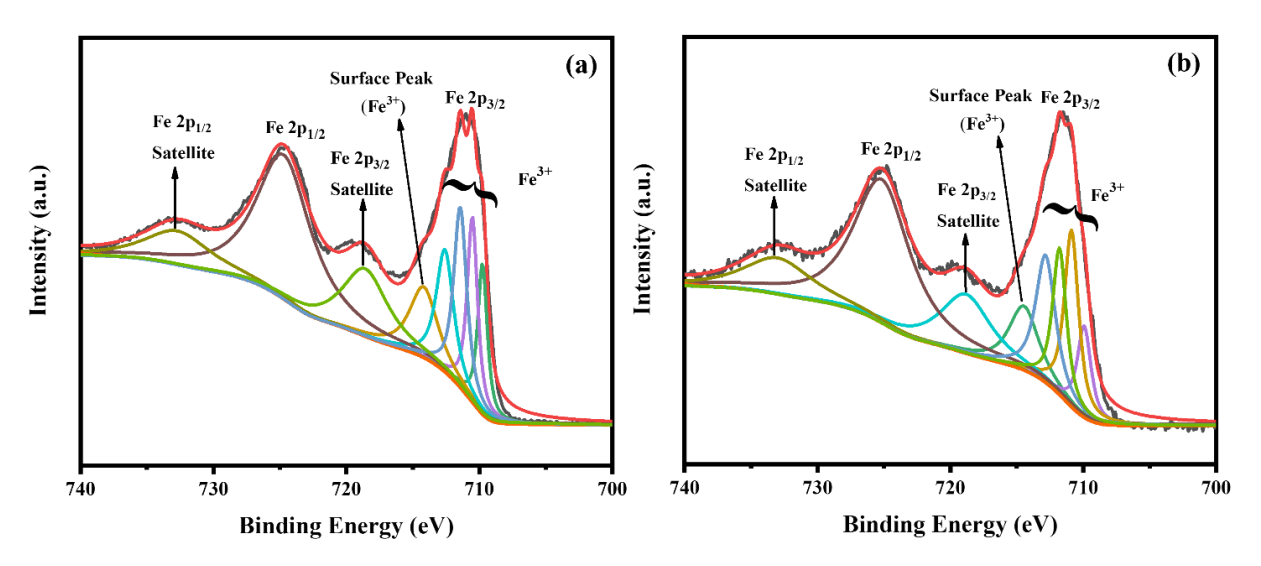


Fig. 7.5 Fe 2p spectra of (a) Mg0Fe1 and (b) Mg4Fe1 catalysts.

7.1.7 HRTEM

The morphology of the catalyst with a Mg/Fe ratio of 4 was further examined using HRTEM. The HRTEM images (shown in Fig. 7.6) confirmed the presence of thin, flake-like or plate-like structures, aligning well with both the FESEM results and prior findings in the literature [3,26]. Additionally, the images revealed that these plates or flakes were distributed in a random, disordered fashion, consistent with the disordered structure observed in the FESEM analysis. This structural disorder is likely attributed to the removal of carbonate and water species from the interlayers of the precursor material, along with dehydroxylation that occurs during the calcination process [3]. This combination of factors during calcination could have disrupted the structural regularity, leading to the observed morphology.

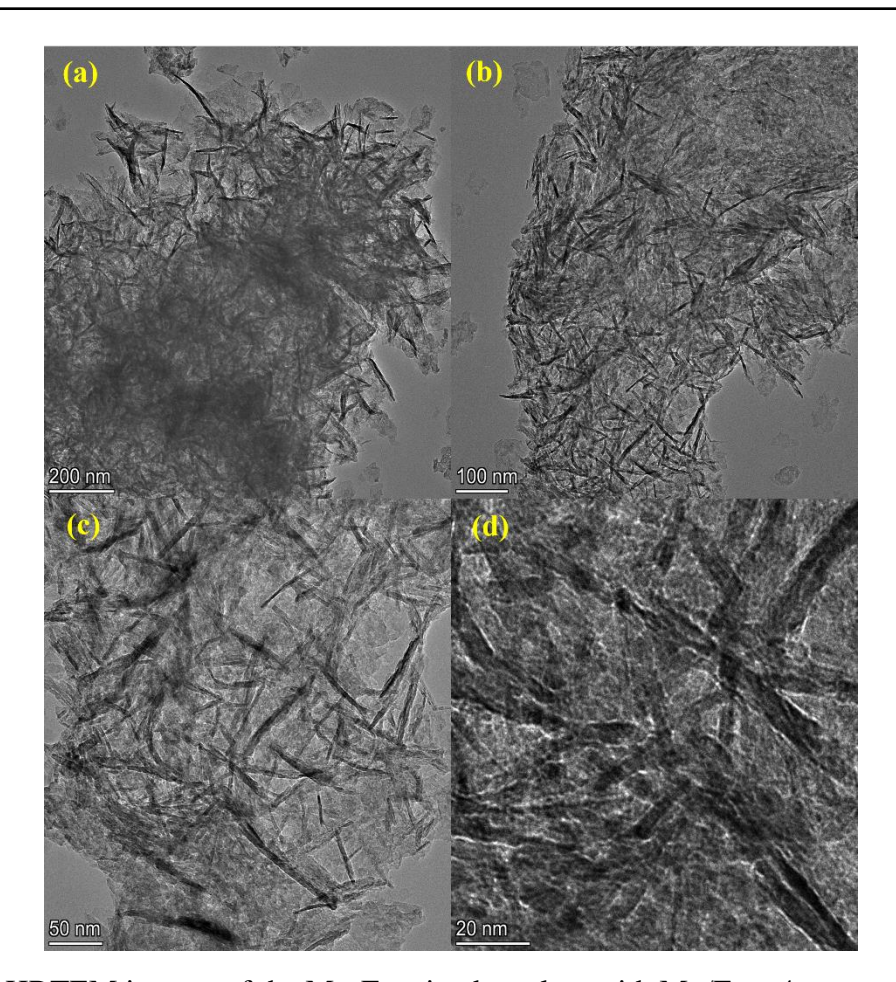


Fig. 7.6 HRTEM images of the Mg-Fe mixed catalyst with Mg/Fe = 4.

7.2 Evaluation of FFR Transfer Hydrogenation Activity

7.2.1 Initial Catalyst Screening

As highlighted in the introduction, Mg-Fe mixed oxides have shown significant potential as catalysts for the transfer hydrogenation of FFR due to the presence of Lewis acid-base pairs essential for the selective hydrogenation of FFR to 2-MeF. To further explore this potential, the catalytic performance of the synthesized Mg-Fe mixed oxide catalysts was evaluated, starting with an examination of pure MgO and Fe₂O₃ catalysts as benchmarks for FFR transfer hydrogenation at 300 °C, with a WHST of 1.43 $g_{catalyst}$ h g_{FFR}^{-1} (WHSV = 0.70 g_{FFR} h⁻¹ $g_{catalyst}^{-1}$).

7.2.1.1 Evaluation of pure Mg and Fe oxide catalysts

As highlighted in the introduction, Mg-Fe mixed oxides have shown significant potential as catalysts for the transfer hydrogenation of FFR due to the presence of Lewis acid-base pairs essential for the selective hydrogenation of FFR to 2-MeF. Building on

these insights, the evaluation of the catalytic performance of the synthesized Mg-Fe mixed oxide catalysts was commenced by examining the effect of varying Mg to Fe molar ratios on the transfer hydrogenation of FFR to 2-MeF at 300 °C, with a WHST of 1.40 $g_{catalyst}$ h g_{FFR}^{-1} (WHSV = 0.70 g_{FFR} h⁻¹ $g_{catalyst}^{-1}$), as shown in Fig. 7.7. When pure Fe₂O₃ was used as the catalyst, the initial FFR conversion was moderate at 57.3% in the 1st h. However, this activity rapidly declined, plummeting to just 18.8% by the 4th h. The deactivation was reflected in the product selectivities, which shifted dramatically over the 4-hour evaluation period. The catalyst started with a moderate selectivity of 60.2% for 2-MeF; however, it dropped sharply by nearly 70% to just 18% by the end of 4th h. Conversely, the selectivity for FAL increased significantly, rising from 35.7% to 76.4% over the same period. These results suggest that while Fe₂O₃ is effective at activating the C=O bond in FFR due to the presence of Lewis acidic Fe³⁺ sites, it lacks the sites capable of effectively activating the alcohol hydrogen donor to generate the necessary hydrogen atoms for efficient deoxygenation. This limitation is evident in the moderate 2-MeF selectivity, indicating suboptimal C-O bond hydrogenolysis activity. The rapid deactivation further underscores this inadequacy, as the catalyst becomes predominantly selective towards FAL formation, indicating a shift from deoxygenation to mere hydrogenation of the carbonyl group. When MgO was employed as the catalyst, it achieved almost complete FFR conversion consistently throughout the 4-hour period. In terms of product distribution, a notable trend emerged: the catalyst exhibited a pronounced preference for FFR hydrogenation over the entire 4 h period. FAL consistently remained the predominant product, with its selectivity maintaining above 60% throughout, and rising to 70.6% towards the end of the assessment period. Conversely, the selectivity for 2-MeF showed a downward trajectory, starting at 35.2% and dropping to 27.2% by the end of the 4th h. This indicates that while MgO may exhibit lower hydrogenolysis activity compared to Fe₂O₃, it demonstrates a superior ability to activate the alcohol donor, allowing it to sustain high catalytic activity with a much milder decline in 2-MeF selectivity over time.

Interestingly, these findings diverge from the observations made by Grazia et al. [2], who also investigated MgO's role in vapor-phase transfer hydrogenation of FFR. They reported limited hydrogenolysis activity of MgO, with FAL being the

Chapter 7| FFR Transfer Hydrogenation to 2-MeF over Mg-Fe mixed oxide catalysts

predominant product up to 400 °C. Their study - one of the very few in this domain showed FFR conversion remained relatively constant at 30-35% between 250 and 350 °C, increasing to 59% only at 500 °C. Even at this elevated temperature, 2-MeF selectivity reached only 35%, while FAL continued to dominate at 32%. In contrast, the current study demonstrated nearly complete FFR conversion with a 2-MeF selectivity of 48.2% in just the 1 h. This superior performance can likely be attributed to the use of IPA as the hydrogen donor instead of methanol, which was used by Grazia's team. Numerous studies have shown that secondary alcohols like IPA have significantly higher hydrogen donation capabilities compared to primary alcohols like methanol [27,28], leading to more efficient C-O bond hydrogenolysis and thus, higher 2-MeF selectivity. Additionally, the higher donor-to-substrate molar ratio (~20) used in this study, along with possible differences in space velocity - which influences the contact time between reactants and the catalyst - may further explain the enhanced conversion and product distribution observed here.

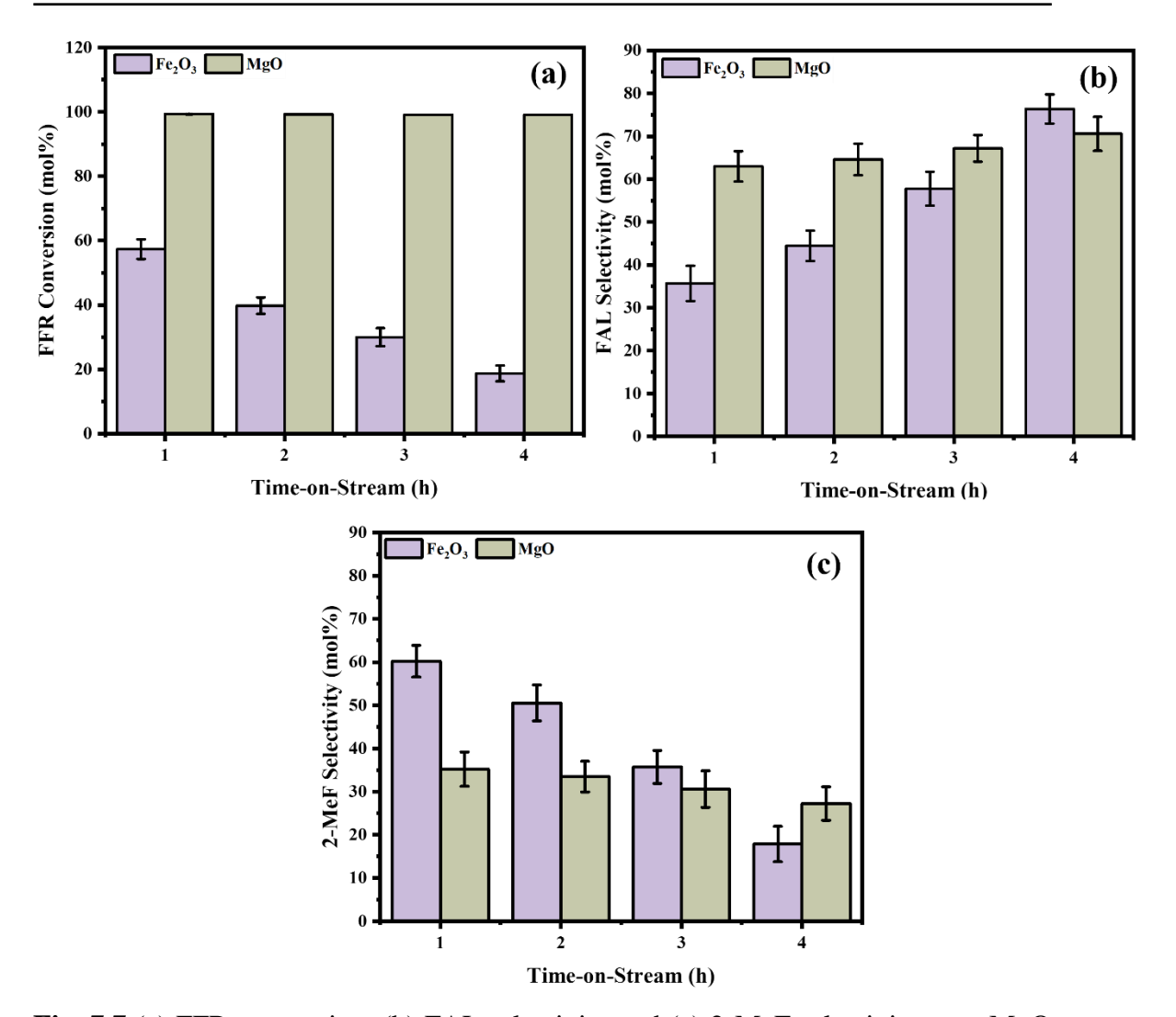


Fig. 7.7 (a) FFR conversion, (b) FAL selectivity and (c) 2-MeF selectivity over MgO and Fe₂O₃ catalysts during FFR CTH. Reaction conditions: feed flowrate = 7.24 mmol_{FFR} h⁻¹, Temperature = 300 °C, WHSV = 0.70 g_{FFR} h⁻¹ g_{catalyst} ⁻¹, Pressure = 1 atm.

7.2.1.2 Evaluation of Mg-Fe mixed oxide catalysts

After evaluating the catalytic performance of MgO and Fe₂O₃ in FFR transfer hydrogenation, the impact of varying Mg to Fe molar ratios was investigated. At 300 °C and a WHST of 1.43 g_{catalyst} h g_{FFR}⁻¹ (WHSV = 0.70 g_{FFR} h⁻¹ g_{catalyst}⁻¹) (Fig. 7.8), the introduction of Mg to Fe in a 1:1 molar ratio increased FFR conversion to 65.2%, compared to the 57.3% achieved with pure Fe₂O₃. Despite this enhancement, the catalyst exhibited relatively rapid deactivation, with a final conversion of 23.4%, still surpassing the 18% conversion seen with Fe₂O₃. Initially, the selectivity towards 2-MeF was 75.2%, about 4% higher than that for Fe₂O₃, while selectivity towards FAL was 20.6%. Over a four-hour period, the catalyst's deactivation was slightly less

pronounced than that of Fe₂O₃, with 2-MeF selectivity decreasing to 22.5% and FAL selectivity increasing to 71.6%.

Increasing the Mg to Fe molar ratio further enhanced both FFR conversion and 2-MeF selectivity, while also mitigating catalyst deactivation. This can be attributed to the fact that increasing amounts of Mg increases basic sites that enhance alcohol donor dehydrogenation, leading to a greater availability of hydrogen atoms for hydrogenolysis and thus higher 2-MeF yields. This observation aligns with literature reports that basic sites are crucial for activating the donor [2,3,12,29,30]. For instance, Maderuelo-Solera et al. [3] observed that increasing the Mg/Fe molar ratio led to higher FFR conversion and furfural alcohol (FAL) yields during FFR transfer hydrogenation. Similarly, López-Asensio et al. [30] reported a significant rise in both FFR conversion and FAL yield as the Mg/Al ratio increased from 1 to 4 in Mg-Al mixed oxide catalysts. Gyngazova et al. demonstrated a correlation between the catalytic activity of alkaline earth metal oxides - SrO, CaO, and MgO - and their basic site strength, with SrO being the most active, followed by CaO and MgO [29].

However, the results also emphasize the necessity of balancing acidic and basic sites for optimal FFR conversion and deoxygenation. Pure Fe₂O₃, possessing only acidic sites as seen from CO₂-TPD analysis (Fig. 7.3), provided moderate selectivity towards 2-MeF but had limited donor activation capability and deactivated quickly. In contrast, MgO, with its basic sites, was effective in donor activation but less efficient in hydrogenolysis. The mixed Mg-Fe catalysts showed improved performance, perhaps due to the surface acidic and basic sites working in tandem to completely deoxygenate FFR. However, it is worth noting that beyond a certain a point, an excess of Mg was not beneficial as it reduced the number of acidic sites, leading to decreased 2-MeF selectivity. The optimal Mg/Fe ratio was found to be 4, where 2-MeF selectivity peaked at 89.2% in the first hour but declined to 59.7% by the end of four hours. Higher Mg/Fe ratios resulted in reduced 2-MeF selectivity, indicating that while basic sites are essential, an excessive Mg ratio limits the availability of acidic sites needed for effective FFR activation. Thus, achieving a balance between acidic and basic sites is crucial for optimizing catalytic performance, ensuring efficient FFR conversion, and maximizing product selectivity.

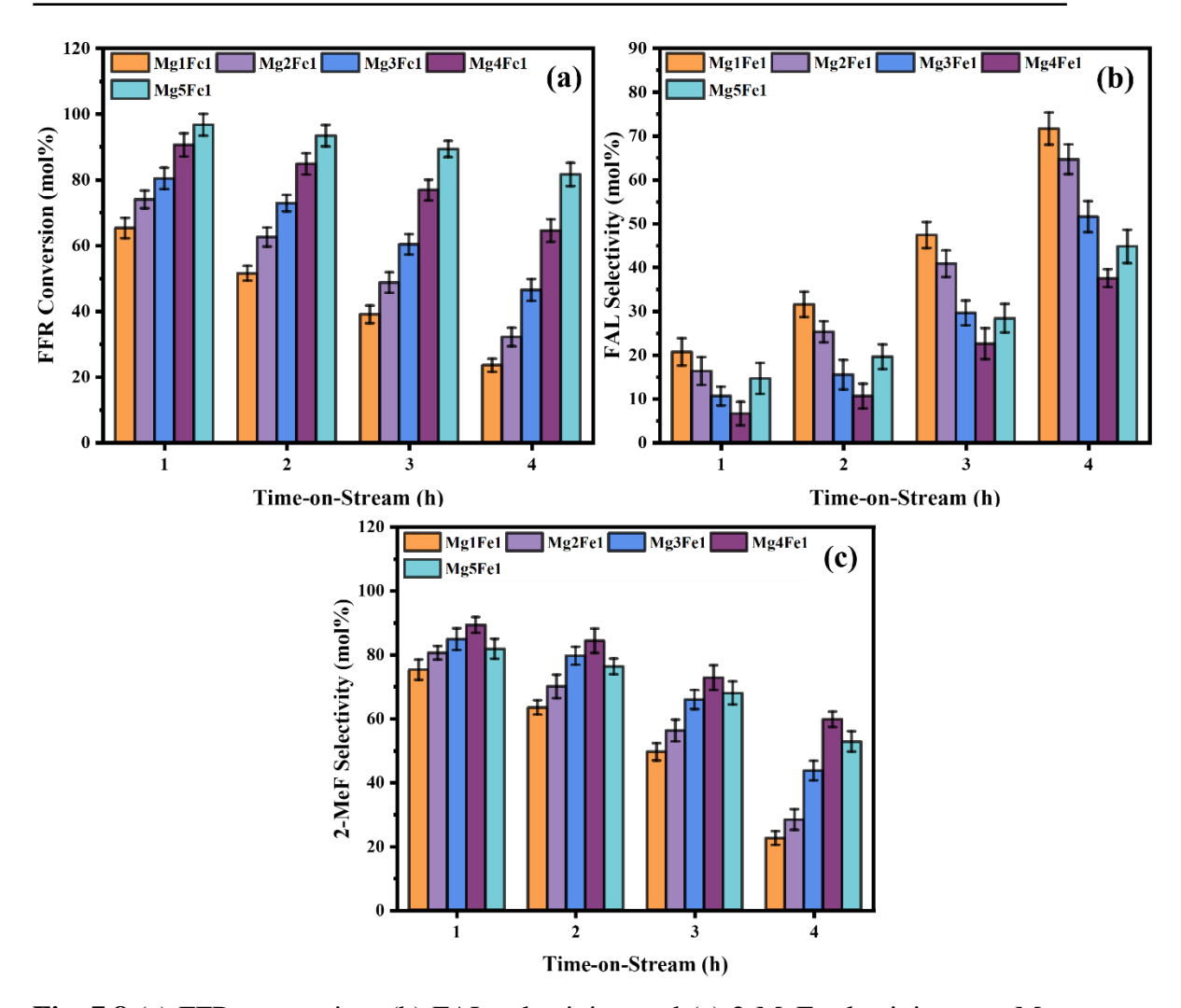


Fig. 7.8 (a) FFR conversion, (b) FAL selectivity, and (c) 2-MeF selectivity over MgFe mixed oxide catalysts with varying Mg/Fe ratios during FFR CTH. Reaction conditions: feed flowrate = $7.24 \text{ mmol}_{FFR} \text{ h}^{-1}$, Temperature = $300 \, ^{\circ}\text{C}$, WHSV = $0.70 \, \text{g}_{FFR} \, \text{h}^{-1} \, \text{g}_{\text{catalyst}}^{-1}$, Pressure = 1 atm.

7.2.2 Effect of Temperature

During the initial catalyst screening, the Mg-Fe mixed oxide catalyst with a Mg/Fe ratio of 4 exhibited strong performance in terms of FFR conversion, 2-MeF selectivity, and stability over the 4-hour period. This promising performance led to its selection for further investigations into how reaction parameters influence the selectivity of the target compound.

Fig. 7.9 illustrates the effect of temperature on FFR conversion and 2-MeF selectivity during FFR CTH. A notable increase in FFR conversion was observed as the reaction temperature was raised from 300 °C to 350 °C and 400 °C, with conversion rates reaching 97.2% and 100%, respectively. In addition to improved conversion,

enhanced catalytic stability was evident, as the reduction in conversion over the 4-hour assessment period was significantly lower at higher temperatures compared to 300 °C. Regarding product distribution, an increase in reaction temperature from 300 °C to 400 °C led to a decrease in FAL selectivity and a corresponding rise in 2-MeF selectivity. At 400 °C, the optimum temperature for 2-MeF selectivity, a high initial value of 92.6% was recorded in the first hour, which slightly declined to 79.8% by the end of the fourth hour. During this same period, FAL selectivity was low, starting at 1.1% in the first hour and increasing to 14.8% by the end of the fourth hour. The improved FFR conversion and target compound selectivity at elevated temperatures suggest that alcohol dehydrogenation became more favourable, leading to a higher availability of hydrogen atoms for C-O bond hydrogenolysis. However, it is worth noting that increasing the reaction temperature from 300 °C to 400 °C also resulted in the formation of some condensation products and heavy molecular weight compounds, likely due to polymerization and/or oligomerization of FFR and intermediate FAL. These heavier molecules remained in the catalyst bed, indicating side reactions that became more prominent at higher temperatures.

Further increasing the temperature to 450 °C, however, led to a decline in both conversion rates and catalyst stability. The catalyst deactivated rapidly, as shown in Figure 7, with conversion dropping from 76.5% at the end of the first hour to just 35% by the end of the 4th h. This decline can be attributed to increased cracking and decomposition reactions at such high temperatures, which likely promoted the formation of heavy molecular weight compounds in greater amounts that block the access to active sites or poison them. Consequently, 2-MeF selectivity also decreased rapidly, falling from 86% at the end of the first hour to 41.3% by the end of the 4th h on stream. The rapid deactivation was accompanied by a significant increase in FAL selectivity, which rose from 4.6% to nearly 50% over the same period. A similar trend was observed when the reaction temperature was reduced from 300 °C to 250 °C. The lower temperature resulted in a decreased conversion rate, starting at 71.8% in the 1st h - 19% lower than that observed at 300 °C during the same period. As the reaction progressed, the catalyst deactivated quickly, with conversion dropping to just 30.2% by the end of the 4th h. 2-MeF selectivity was also much lower than at 300 °C and followed a steep declining trend similar to FFR conversion, indicating that at lower temperatures,

alcohol donor activation slowed down considerably. This reduction in hydrogen availability for hydrogenolysis led to increased FAL formation, which became the dominant product in the latter half of the reaction period. Given FAL's high polymerization tendencies, the rapid deactivation at lower temperatures may also be linked to its increased formation.

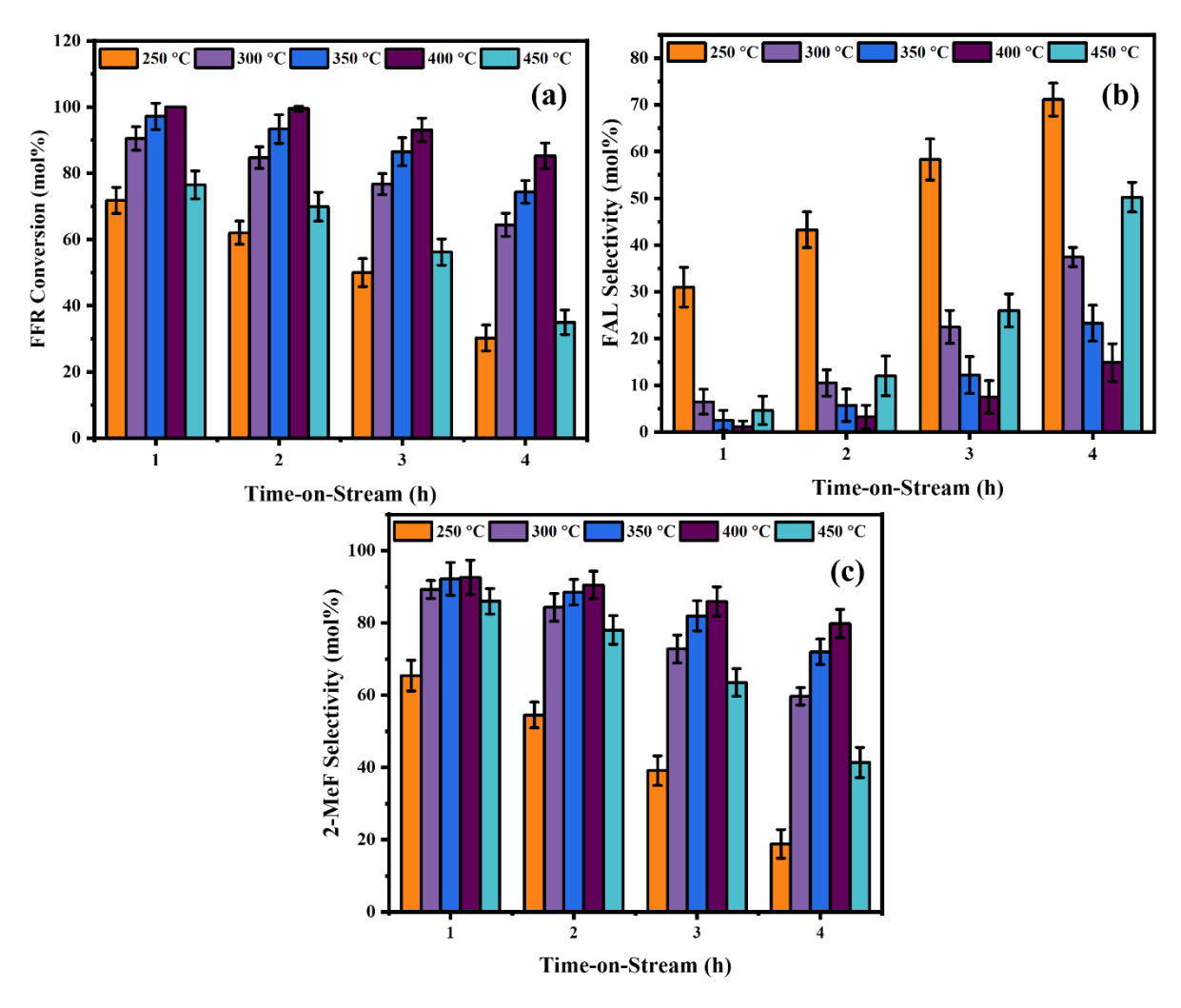


Fig. 7.9 (a) FFR conversion, (b) FAL selectivity, and (c) 2-MeF selectivity over Mg-Fe mixed oxide catalysts with Mg/Fe = 4 during FFR CTH at different temperatures. Reaction conditions: feed flowrate = $7.24 \, \text{mmol}_{\text{FFR}} \, \text{h}^{-1}$, WHSV = $0.70 \, \text{g}_{\text{FFR}} \, \text{h}^{-1} \, \text{g}_{\text{catalyst}}^{-1}$, Pressure = 1 atm.

7.2.3 Effect of WHSV

Fig. 7.10 illustrates the impact of varying space velocity (WHSV) on the selectivity towards 2-MeF during FFR CTH using a Mg-Fe oxide catalyst with a Mg/Fe ratio of 4. In prior experiments examining the effect of temperature, the optimal selectivity was achieved at 400 °C, with the space velocity held constant at = 0.70 g_{FFR} h⁻¹ $g_{catalyst}$ ⁻¹. Now, in order to explore the role of WHSV, additional investigations were carried out

at space velocity values of 0.35, 1.04 and 1.39 g_{FFR} h⁻¹ g_{catalyst} -1. When the space velocity was reduced from 0.7 to 0.35 g_{FFR} h⁻¹ g_{catalyst} -1, the conversion remained nearly constant at 100% in the 1st h. However, as the reaction progressed, the catalyst began to deactivate, leading to a significant drop in conversion to 69.8% by the 4th h. At this lower space velocity, 2-MeF selectivity was slightly lower during the first two hours compared to that observed at the higher space velocity of 0.70 g_{FFR} h⁻¹ g_{catalyst} -1 in the first 2 h. In the final two hours, however, the 2-MeF selectivity decreased significantly, falling well below the values seen at the higher space velocity, finally achieving a value of 62%. At the same time, FAL selectivity rose sharply, from 0.5% to 30.4% over the 4-h period. This behavior can be attributed to the increased contact time between reactant molecules and the catalyst that results from lowering the space velocity. This extended interaction allows FFR and/or the intermediate FAL to undergo polymerization and/or oligomerization reactions, thereby promoting the formation of heavier molecular weight compounds. In the investigation of temperature effects, it was shown that elevated temperatures also facilitate the production of such heavy compounds. By reducing the space velocity, the conditions become even more favourable for these reactions. The greater formation of heavy products likely leads to decreased catalytic stability and lower 2-MeF selectivity, as the active sites on the catalyst become blocked or poisoned. As a result, the number of available active sites diminishes, leading to reduced conversion and diminished selectivity for 2-MeF.

Increasing the same velocity from 0.7 to 1.04 and 1.39 g_{FFR} g_{catalyst}⁻¹ h⁻¹, resulted in a reduction in conversion to 92.2% and 78.5%, respectively, within the 1st h. As the reaction continued, the conversion further declined, falling below the levels observed at 0.7 g_{FFR} g_{catalyst}⁻¹ h⁻¹. This decrease in conversion can be attributed to the reduced contact time between the reactants and the catalyst at higher space velocities. Interestingly, the rate of decline in conversion between successive hours on stream diminished with higher space velocities. This trend suggests that at elevated velocities, reactants spend less time interacting with the catalyst, limiting the opportunity for side reactions. Despite this, the reduced contact time negatively impacted 2-MeF selectivity, which dropped from 79.8% after 4 h on stream for 0.7 g_{FFR} g_{catalyst}⁻¹ h⁻¹ to 72% and 58% at space velocities of 1.04 and 1.39 g_{FFR} g_{catalyst}⁻¹ h⁻¹, respectively. At the same time, selectivity towards FAL increased at higher space velocities. This increase is linked to

the reduced time available for FAL to undergo hydrogenolysis and the decreased activation rate of the hydrogen donor. Consequently, the higher space velocities favoured FAL formation, which in turn reduced 2-MeF production.

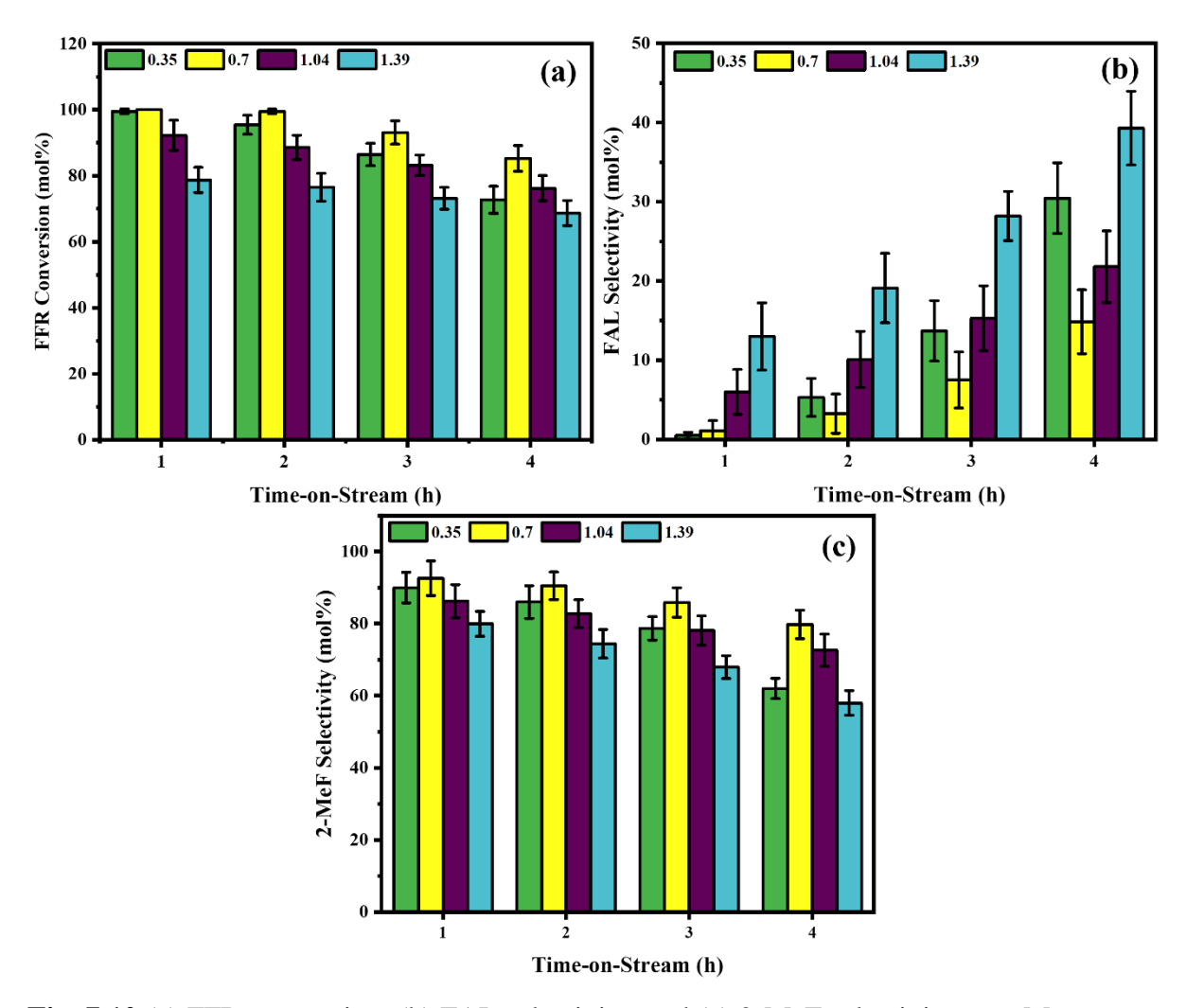


Fig. 7.10 (a) FFR conversion, (b) FAL selectivity, and (c) 2-MeF selectivity over Mg-Fe mixed oxide catalysts with Mg/Fe = 4 during FFR CTH at different space velocity values ($g_{FFR} g_{catalyst}^{-1} h^{-1}$). Reaction conditions: Temperature = 400 °C, Pressure = 1 atm.

7.2.4 Effect of calcination temperature

Calcination temperature is a key factor influencing the structural and chemical properties of catalysts, thereby impacting their performance in catalytic reactions. In the case of Mg-Fe mixed oxide catalysts with a Mg/Fe ratio of 4, previous optimizations of reaction conditions - such as a reaction temperature of 400 °C and a space velocity of 0.7 g_{FFR} g_{catalyst}⁻¹ h⁻¹ - produced the highest FFR conversion and selectivity towards 2-MeF. Here, the catalyst was calcined at 500 °C. To further explore the impact of

calcination temperature, the catalysts were calcined at 400, 600, 700, and 800 °C and the results are shown in Fig. 7.11.

As the calcination temperature increased from 500 °C to 800 °C, a significant decline was observed in both FFR conversion and 2-MeF selectivity. At 500 °C, the catalyst performed optimally, achieving a 100% conversion after the 1st h with a 2-MeF selectivity of 92.6%. However, when the calcination temperature was raised to 600 °C, the conversion dropped to 87.3% in the 1st h, followed by a gradual decline to 70% by the 4th h. Though the initial drop in 2-MeF selectivity was moderate, decreasing to 85.5% in the 1st h at 600 °C, the decline accelerated over time, falling to 66.4% by the end of the 4th h, in contrast to the 79.8% recorded at 500 °C. Further increases in calcination temperature to 700 °C and 800 °C led to sharper reductions in both conversion and selectivity. The catalyst calcined at 700 °C showed a conversion of 72.4% after the 1st h, which dropped steeply to 41% by the 4th h. Similarly, 2-MeF selectivity started at 73.4% and plummeted to 39.1% by the end of the 4th h. The catalyst calcined at 800 °C exhibited even more dramatic losses, with conversion dropping from 60% in the 1st h to just 22% by the 4th h, while 2-MeF selectivity fell from 58.7% to a mere 12.8%. The catalyst calcined at 400 °C, while active, also showed a marked reduction in performance compared to the 500 °C sample. After the 1st h, the conversion was 70.3%, with a 2-MeF selectivity of 80.4%, both considerably lower than the values at 500 °C. As the reaction proceeded, the catalyst's performance degraded rapidly, with conversion dropping to 38.2% and 2-MeF selectivity to 29.8% by the 4th h.

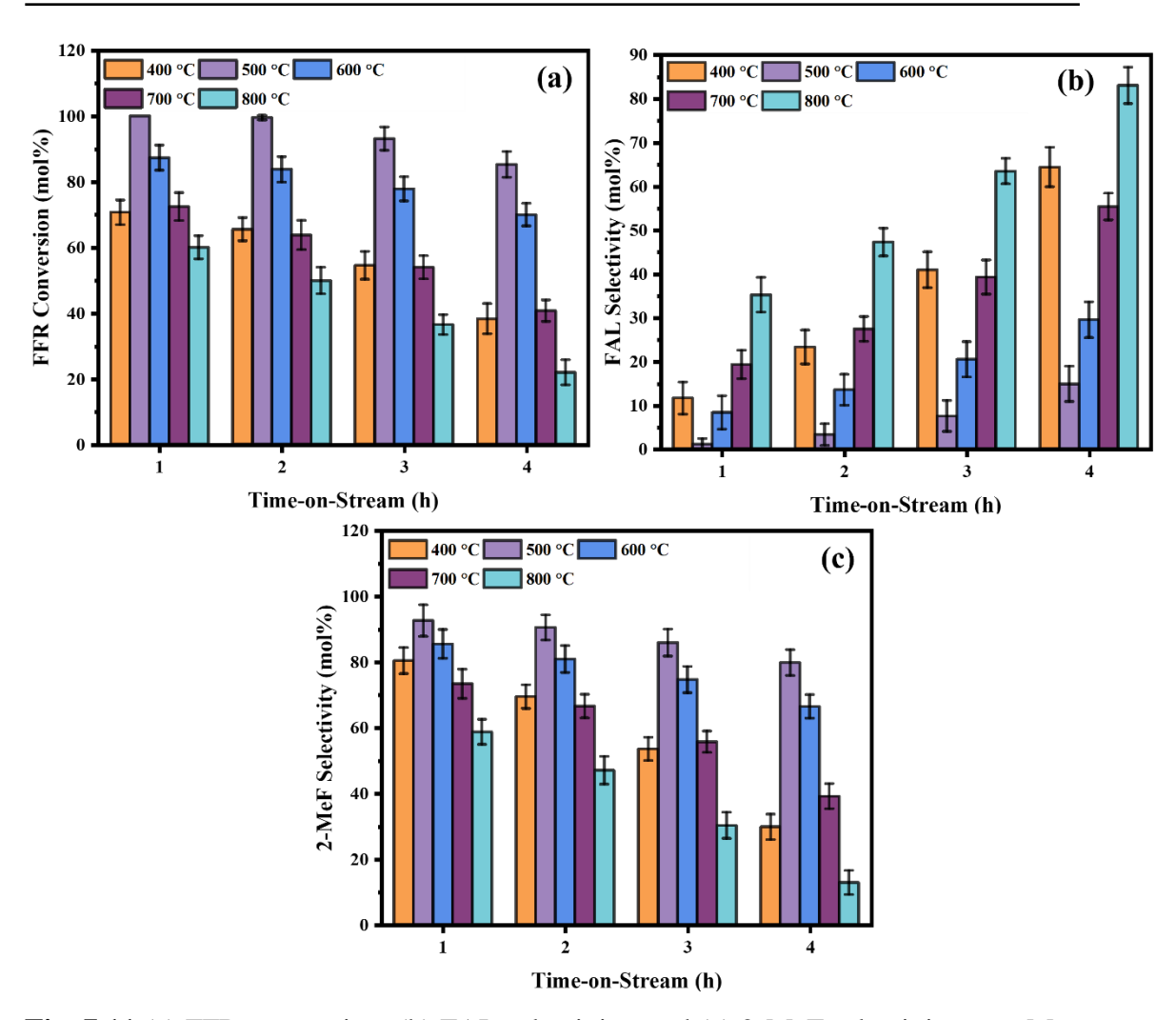


Fig. 7.11 (a) FFR conversion, (b) FAL selectivity, and (c) 2-MeF selectivity over Mg-Fe mixed oxide catalysts with Mg/Fe = 4 calcined at different temperatures during FFR CTH. Reaction conditions: feed flowrate = 7.24 mmol_{FFR} h^{-1} , Temperature = 400 °C, WHSV = 0.70 $g_{FFR} h^{-1} g_{catalyst}^{-1}$, Pressure = 1 atm.

To better understand the variations in FFR conversion and 2-MeF selectivity, it is crucial to consider how the catalysts' properties changed with increasing calcination temperatures, as revealed through various characterization techniques. Calcination temperature is known to have a significant impact on the structural and acid-base characteristics of hydrotalcite-derived catalysts, which directly influence their catalytic activity.

XRD analysis (Fig. 7.12) demonstrated that as the calcination temperature rose above 500 °C, a distinct spinel MgFe₂O₄ phase began to form. The emergence of this phase was first noticeable at 600 °C, accompanied by sharper peaks for MgO, signifying enhanced crystallinity and a larger crystallite size. With further increases to 700 and 800 °C, the intensity of both the MgFe₂O₄ spinel phase and MgO became even more

pronounced, indicating continued growth in crystallite size. In contrast, the sample calcined at 400 °C exhibited broad, weak diffraction peaks, suggesting a largely amorphous structure, likely due to incomplete decomposition of the hydrotalcite precursor. These findings are consistent with observations made by López-Asensio et. al., Ramasamy et. al., and Shen et. al., who reported similar behavior in Mg-Al mixed oxide catalysts prepared via the same co-precipitation method. They reported that when calcination temperatures exceeded 500 °C, a spinel MgAl₂O₄ phase formed, which is known for having lower surface area and pore volume compared to the periclase-type Mg-Al mixed oxides [18,20,30,31].

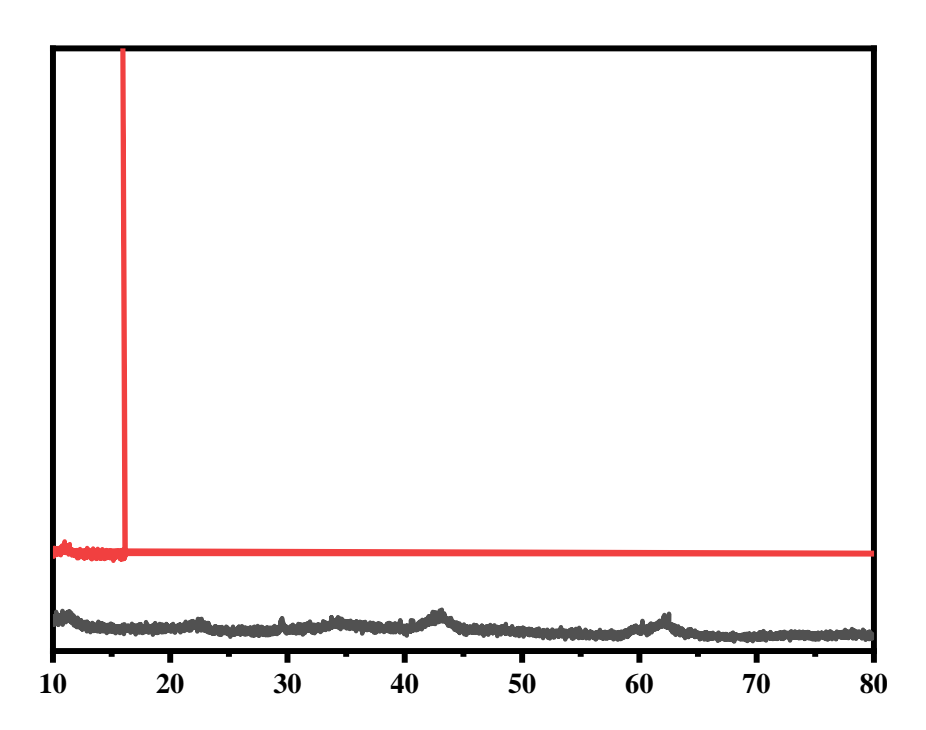


Fig. 7.12 Diffraction patterns of the Mg-Fe mixed oxide catalysts with Mg/Fe = 4 calcined at (a) $400 \, ^{\circ}$ C, (b) $600 \, ^{\circ}$ C, (c) $700 \, ^{\circ}$ C and (d) $800 \, ^{\circ}$ C.

The morphological changes observed via FESEM analysis (Fig. 7.13) align with these XRD findings. The increased calcination temperature led to more densely packed and larger rod-like structures, correlating with reduced porosity and surface area, while lower calcination temperature led to incomplete decomposition of precursors, both of which would impact catalytic performance. It's reasonable to infer that the surface areas and pore volumes of the catalysts calcined at 400 °C and at higher temperatures (600, 700, and 800 °C) were all lower than those of the catalyst treated at 500 °C.

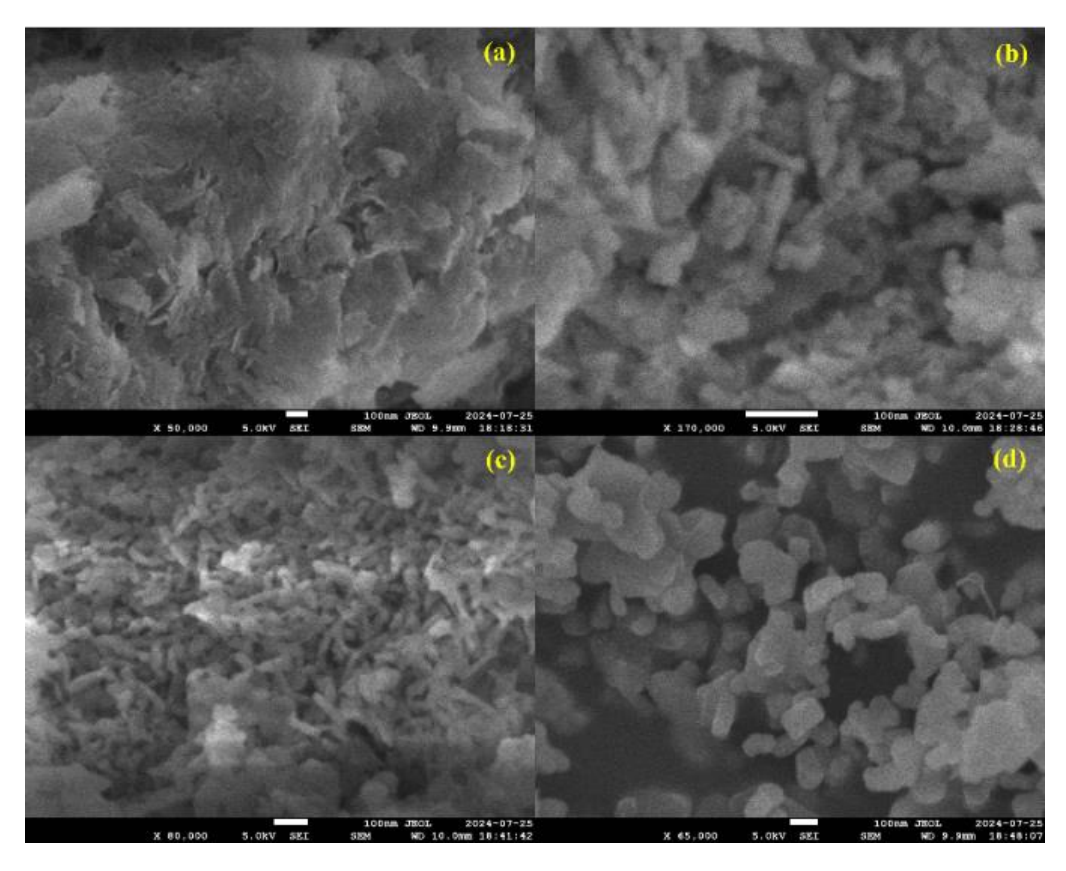


Fig. 7.13 FESEM images of the Mg-Fe mixed oxide catalysts with Mg/Fe = 4 calcined at (a) $400 \,^{\circ}$ C, (b) $600 \,^{\circ}$ C, (c) $700 \,^{\circ}$ C and (d) $800 \,^{\circ}$ C.

CO₂-TPD (Table 7.3) analysis provided further insight into these structural changes. The catalyst calcined at 400 °C showed no detectable CO₂ desorption, indicating an absence of basic sites, likely due to incomplete transformation. As the calcination temperature increased from 500 to 800 °C, there was a notable reduction in CO₂ desorption (table 3), reflecting a decrease in the number of available basic sites. These results are consistent with prior studies by Ramasamy et. al. [18] and Shen et. al. [20], who also observed reduced basic site density as calcination temperatures increased. While NH₃-TPD analysis was not performed in this study, Shen's findings suggest that the strength of acidic sites would similarly decrease as calcination temperature increased, [20] a trend that likely applies to the Mg-Fe catalysts in this investigation.

Table 7.3 CO_2 Desorption Values from CO_2 -TPD Analysis of Mg-Fe Mixed Oxide Catalysts with Mg/Fe = 4 calcined at different temperatures.

Catalyst	CO ₂ desorbed (mmol/g)
Mg4Fe1-400	-
Mg4Fe1-500	6.50
Mg4Fe1-600	4.87
Mg4Fe1-700	3.12
Mg4Fe1-800	1.88

Taken together, the lower surface areas, reduced porosity, higher crystallite size and diminished acidic and basic site densities of the catalysts calcined at 400, 600, 700, and 800 °C provide a clear explanation for the observed decline in FFR conversion and 2-MeF selectivity. With fewer active surface sites to interact with both the reactant FFR and the H donor alcohol molecules, the catalytic efficiency drops significantly, leading to the reduced performance seen at these calcination temperatures.

7.2.5 Catalyst Stability and Regeneration

To assess the catalyst's stability over an extended period, its performance was tracked for 8 h, as shown in Fig. 7.14. During the first two hours, the catalyst maintained an impressive FFR conversion rate close to 100%, with 2-MeF selectivity hovering around 92%. FAL formation was minimal at this stage, with only 1% selectivity in the 1st h and a slight increase to 3.3% by the 2nd h. However, after the 2-h mark, signs of catalyst deactivation began to emerge. Over the next 2 h, FFR conversion gradually dropped to 85.1%, accompanied by a decline in 2-MeF selectivity to 79.5%. In contrast, FAL selectivity spiked, reaching 14.7% within the same timeframe. Beyond the 4-h point, catalyst deactivation became more pronounced. By the end of the 8-h run, FFR conversion had plummeted to 30%, while 2-MeF selectivity dropped sharply to just 16.1%. Meanwhile, FAL selectivity soared, accounting for 78.4% of the product distribution by the final hour. This rapid deactivation over such a relatively short period could be attributed to the buildup of carbonaceous deposits on the catalyst's surface. These deposits, likely formed from the oligomerization or polymerization of FFR or FAL at elevated reaction temperatures, may have poisoned the acidic and basic active sites responsible for activating both FFR and the hydrogen donor, ultimately impairing the catalyst's activity.

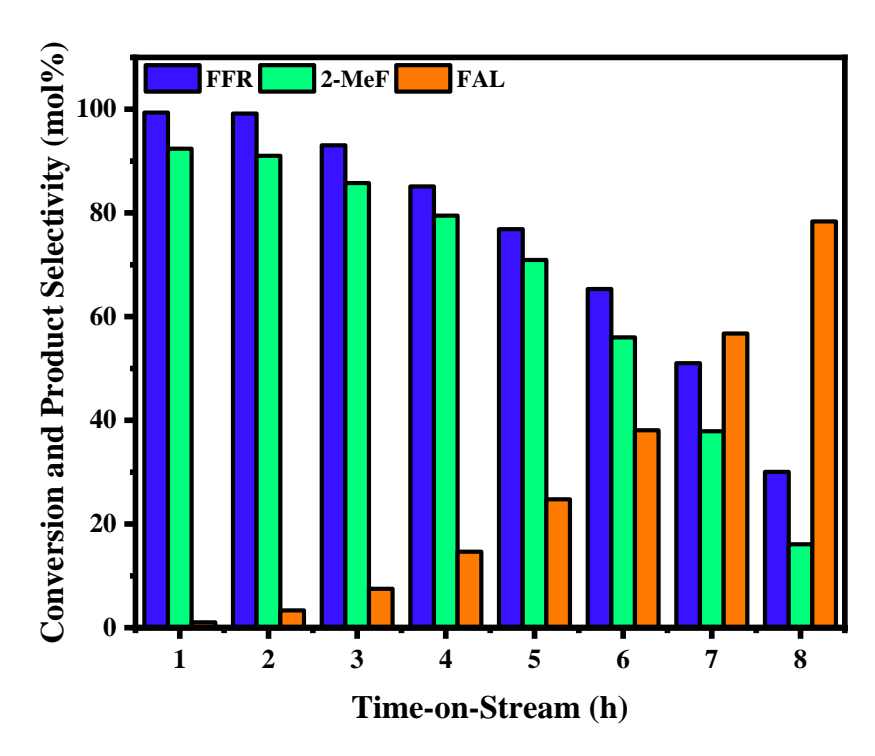


Fig. 7.14 Time-on-stream (TOS) study for FFR CTH over Mg-Fe mixed oxide catalysts with Mg/Fe = 4 calcined at 500 °C. Reaction conditions: feed flowrate = 7.24 mmol_{FFR} h^{-1} , Temperature = 400 °C, WHSV = 0.70 $g_{FFR} h^{-1} g_{catalyst}^{-1}$, Pressure = 1 atm.

To assess the catalyst's durability and potential for repeated use, a regeneration study was conducted following the initial 8-hour TOS run. The spent catalyst was regenerated in-situ through calcination at 500 °C in air for 5 hours, carried out within the fixed-bed reactor. After this regeneration process, the catalyst was tested in a second 8-hour TOS cycle to gauge its stability and reusability across multiple cycles. As depicted in Fig. 7.15, the regenerated catalyst showed only a partial recovery in performance. A notable shift was observed in both conversion rates and product selectivity. In the first hour, the catalyst achieved a conversion of 90.6%, but this time, the decline began right after the first hour. While the drop in conversion was gradual over the first 4 h, the values were consistently lower compared to the fresh catalyst during the same timeframe. Similarly, 2-MeF selectivity followed a comparable trend. It started at 88.1% in the first hour slightly below that achieved by the fresh catalyst - and continued to decrease over time. By the end of the 4th h, 2-MeF selectivity had dropped to 75.8%, while FAL selectivity had increased to 17.3%. After the 4-h mark, both conversion and 2-MeF selectivity declined more sharply than they had with the fresh catalyst. By the 8th h, conversion had plummeted to 22%, and 2-MeF selectivity fell drastically to just 6.3%. These figures were significantly lower than those obtained with the fresh catalyst, highlighting more severe deactivation in the regenerated catalyst. During this period, FAL selectivity surged to nearly 88%, indicating a shift in product distribution. The incomplete recovery and faster deactivation observed in the regenerated catalyst may be due to incomplete removal of carbonaceous species during in-situ calcination, or potential sintering caused by prolonged exposure to high temperatures. These factors likely altered the catalyst's structure, compromising its stability and overall effectiveness over time.

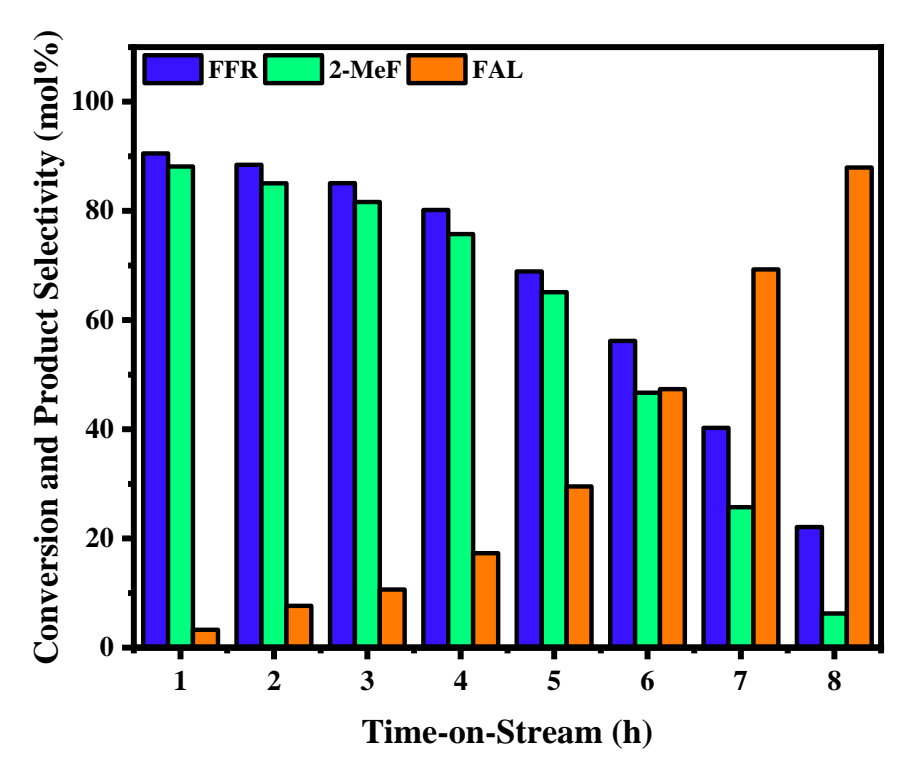


Fig. 7.15 Regeneration study for FFR CTH over Mg-Fe mixed oxide catalysts with Mg/Fe = 4 calcined at 500 °C. Reaction conditions: feed flowrate = 7.24 mmol_{FFR} h⁻¹, Temperature = 400 °C, WHSV = 0.70 g_{FFR} h⁻¹ g_{catalyst} ⁻¹, Pressure = 1 atm.

7.2.6 Probable Reaction Mechanism

The mechanism behind the transfer hydrogenation process typically follows one of two well-established pathways: the metal hydride route or the direct hydrogen transfer route [32–34]. In the case of heterogeneous catalysts containing both acidic and basic sites, such as the Mg-Al mixed oxides reported in the literature and the Mg-Fe mixed oxides synthesized in this study, the process is more likely to proceed via the direct hydrogen transfer route [32,33]. This is primarily because the formation of metal hydrides on such catalysts is challenging, making the metal hydride route less feasible [32].

The direct hydrogen transfer mechanism, also known as the Meerwein-Ponndorf-Verley (MPV) mechanism, requires the presence of both Lewis acidic and basic sites to facilitate the reduction reaction. In this mechanism, the Lewis acidic site act as an electron-deficient centers that bind to the electron-rich oxygen atoms of both the hydrogen donor and the reactant [32,34–36]. At the same time, the adjacent basic site plays a critical role by attracting the proton from the O-H bond of the alcohol donor [32,34–36]. The strength of the interaction between the hydroxyl oxygen in the alcohol and the Lewis acid site directly influences the acidity of the hydrogen atom in the donor [32]. The more acidic the hydrogen, the easier it becomes for the basic site to abstract it [32]. On the flip side, if the basic site is sufficiently strong, it can efficiently pull the hydrogen from the alcohol's hydroxyl group, forming a species that binds to the adjacent Lewis acid site [32]. This setup creates an ideal environment for the hydride transfer to occur, driving the reduction reaction forward.

In this study (Fig. 7.16), the Lewis acid centers $-Mg^{2+}$ and Fe^{3+} - play a key role in activating both the hydrogen donor alcohol (IPA) and the reactant (FFR) by interacting with the lone pairs of oxygen in their hydroxyl (-OH) and carbonyl (-C=O) groups, respectively. Simultaneously, an adjacent basic site (O²-) engages with the hydrogen atom of the hydroxyl group in IPA, weakening the O-H bond. As this occurs, the αhydrogen atom attached to the α-carbon of the adsorbed IPA molecule attacks the carbonyl group of the FFR molecule, which is adsorbed on a nearby Lewis acid site. This interaction leads to the formation of a six-membered transition state ring. The process concludes with the formation of an FAL molecule, while IPA is converted to acetone, which gets desorbed off the surface. The reaction continues in a similar fashion: the newly formed FAL molecule adsorbs onto a Lewis acid site through the oxygen atom in its hydroxyl group, positioning itself near another IPA molecule adsorbed on a similar site. Again, the α-hydrogen from the IPA is transferred to the hydroxyl group of FAL, with the adjacent basic site facilitating the removal of the hydrogen atom from IPA's hydroxyl group. This cycle ultimately results in the production of 2-MeF and a water molecule, both of which desorb from the catalyst surface, allowing the process to repeat.

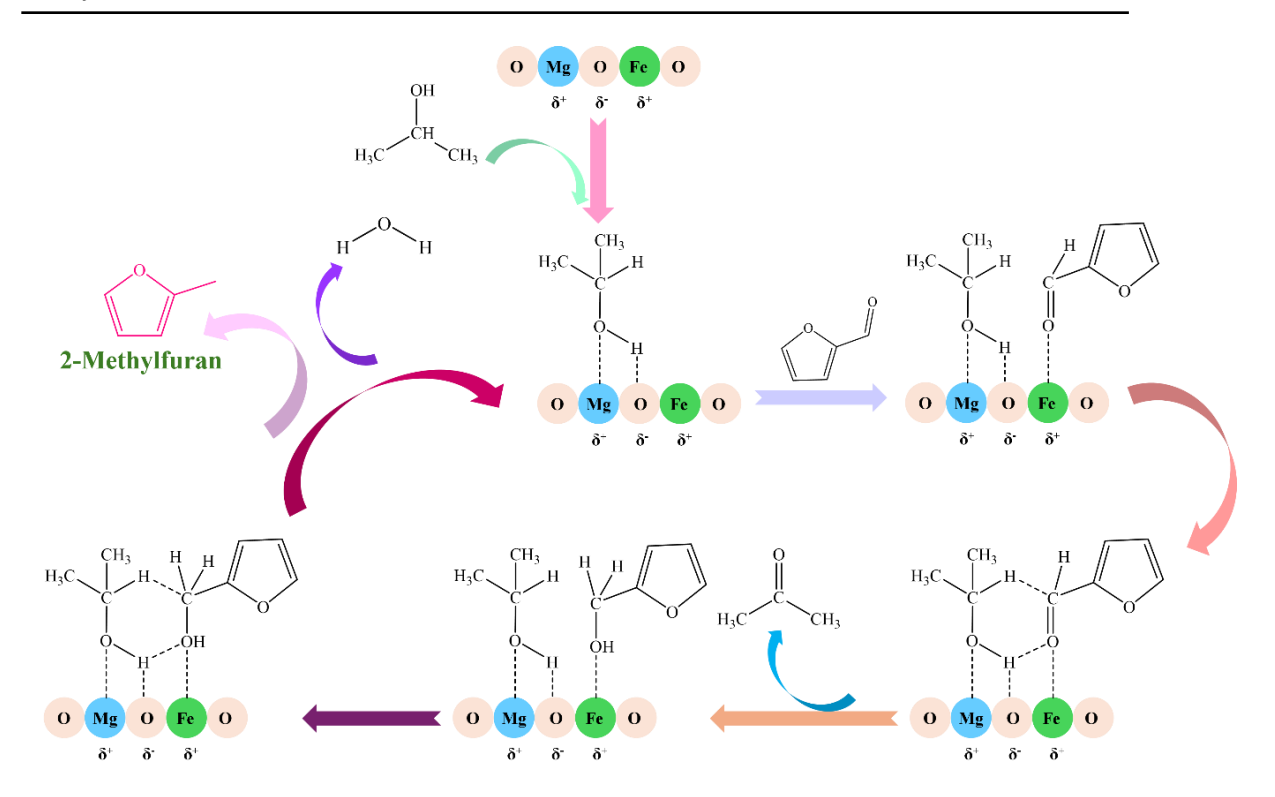


Fig. 7.16 Probable reaction of FFR CTH to 2-MeF over Mg-Fe mixed catalyst with Mg/Fe = 4.

References

- [1] Y. Liu, T. Zhang, S. Li, K. Zhang, X. Wang, Y. Zhan, Y. Zheng, L. Jiang, Geometric and electronic modification of the active Fe3+ sites of α-Fe2O3 for highly efficient toluene combustion, J. Hazard. Mater. 398 (2020). https://doi.org/10.1016/j.jhazmat.2020.123233.
- [2] L. Grazia, A. Lolli, F. Folco, Y. Zhang, S. Albonetti, F. Cavani, Gas-phase cascade upgrading of furfural to 2-methylfuran using methanol as a H-transfer reactant and MgO based catalysts, Catal. Sci. Technol. 6 (2016) 4418–4427. https://doi.org/10.1039/c5cy02021b.
- [3] R. Maderuelo-Solera, R. López-Asensio, J.A. Cecilia, C.P. Jiménez-Gómez, C. García-Sancho, R. Moreno-Tost, P. Maireles-Torres, Catalytic transfer hydrogenation of furfural to furfuryl alcohol over calcined MgFe hydrotalcites, Appl. Clay Sci. 183 (2019) 105351. https://doi.org/10.1016/j.clay.2019.105351.
- [4] D. Kang, X. Yu, S. Tong, M. Ge, J. Zuo, C. Cao, W. Song, Performance and mechanism of Mg/Fe layered double hydroxides for fluoride and arsenate removal from aqueous solution, Chem. Eng. J. 228 (2013) 731–740. https://doi.org/10.1016/j.cej.2013.05.041.
- [5] F. Peng, T. Luo, Y. Yuan, Controllable synthesis of Mg-Fe layered double hydroxide nanoplates with specific Mg/Fe ratios and their effect on adsorption of As(v) from water, New J. Chem. 38 (2014) 4427–4433. https://doi.org/10.1039/c4nj00548a.
- [6] M. Hájek, J. Kocík, K. Frolich, A. Vávra, Mg-Fe mixed oxides and their rehydrated mixed oxides as catalysts for transesterification, J. Clean. Prod. 161 (2017) 1423–1431. https://doi.org/10.1016/j.jclepro.2017.05.199.
- [7] M. Tu, J. Shen, Y. Chen, Microcalorimetric Studies of Surface Acid/Base Properties of Magnesium Iron Catalysts Prepared from Hydrotalcite-Type Precursors, J. Solid State Chem. 128 (1997) 73–79. https://doi.org/10.1006/jssc.1996.7151.
- [8] P.S. Kumbhar, J. Sanchez-Valente, J.M.M. Millet, F. Figueras, Mg-Fe Hydrotalcite as a Catalyst for the Reduction of Aromatic Nitro Compounds with Hydrazine Hydrate, J. Catal. 191 (2000) 467–473. https://doi.org/10.1006/jcat.2000.2827.
- [9] Y. Ohishi, T. Kawabata, T. Shishido, K. Takaki, Q. Zhang, Y. Wang, K. Nomura, K. Takehira, Mg-Fe-Al mixed oxides with mesoporous properties prepared from hydrotalcite as precursors: Catalytic behavior in ethylbenzene dehydrogenation, Appl. Catal. A Gen. 288 (2005) 220–231. https://doi.org/10.1016/j.apcata.2005.04.033.
- [10] K. Takehira, T. Shishido, P. Wang, T. Kosaka, K. Takaki, Autothermal reforming of CH4 over supported Ni catalysts prepared from Mg-Al hydrotalcite-like anionic clay, J. Catal. 221 (2004) 43–54. https://doi.org/10.1016/j.jcat.2003.07.001.
- [11] K. Takehira, T. Shishido, P. Wang, T. Kosaka, K. Takaki, Steam reforming of CH4 over supported Ni catalysts prepared from a Mg-Al hydrotalcite-like

- anionic clay, Phys. Chem. Chem. Phys. 5 (2003) 3801–3810. https://doi.org/10.1039/b304261h.
- [12] C. Lucarelli, D. Bonincontro, Y. Zhang, L. Grazia, M. Renom-Carrasco, C. Thieuleux, E.A. Quadrelli, N. Dimitratos, F. Cavani, S. Albonetti, Tandem hydrogenation/hydrogenolysis of furfural to 2-methylfuran over a Fe/Mg/O catalyst: Structure–activity relationship, Catalysts. 9 (2019). https://doi.org/10.3390/catal9110895.
- [13] L. Xu, S. Niu, C. Lu, D. Wang, K. Zhang, J. Li, NH3-SCR performance and characterization over magnetic iron-magnesium mixed oxide catalysts, Korean J. Chem. Eng. 34 (2017) 1576–1583. https://doi.org/10.1007/s11814-017-0044y.
- [14] A. Azhari, M. Sharif Sh., F. Golestanifard, A. Saberi, Phase evolution in Fe2O3/MgO nanocomposite prepared via a simple precipitation method, Mater. Chem. Phys. 124 (2010) 658–663. https://doi.org/10.1016/j.matchemphys.2010.07.030.
- [15] X. Huang, Y. Men, J. Wang, W. An, Y. Wang, Highly active and selective binary MgO-SiO2 catalysts for the production of 1,3-butadiene from ethanol, Catal. Sci. Technol. 7 (2017) 168–180. https://doi.org/10.1039/c6cy02091g.
- [16] C. Angelici, M.E.Z. Velthoen, B.M. Weckhuysen, P.C.A. Bruijnincx, Influence of acid-base properties on the Lebedev ethanol-to-butadiene process catalyzed by SiO2-MgO materials, Catal. Sci. Technol. 5 (2015) 2869–2879. https://doi.org/10.1039/c5cy00200a.
- [17] M. Gao, M. Zhang, Y. Li, Investigation into 1,3-butadiene and other bulk chemicals' formation from bioethanol over Mg-Al catalysts, RSC Adv. 7 (2017) 11929–11937. https://doi.org/10.1039/c6ra27610e.
- [18] K.K. Ramasamy, M. Gray, H. Job, D. Santosa, X.S. Li, A. Devaraj, A. Karkamkar, Y. Wang, Role of Calcination Temperature on the Hydrotalcite Derived MgO-Al2O3 in Converting Ethanol to Butanol, Top. Catal. 59 (2016) 46–54. https://doi.org/10.1007/s11244-015-0504-8.
- [19] J.H. Park, H. Ur Rasheed, K.H. Cho, H.C. Yoon, K.B. Yi, Effects of magnesium loading on ammonia capacity and thermal stability of activated carbons, Korean J. Chem. Eng. 37 (2020) 1029–1035. https://doi.org/10.1007/s11814-020-0508-3.
- [20] J. Shen, M. Tu, C. Hu, Structural and Surface Acid/Base Properties of Hydrotalcite-Derived MgAlO Oxides Calcined at Varying Temperatures, J. Solid State Chem. 137 (1998) 295–301. https://doi.org/10.1006/jssc.1997.7739.
- [21] M. Xu, E. Iglesia, C.R. Apestegu, D.I. Cosimo, E.T. Al, Structure and Surface and Catalytic Properties of Mg-Al Basic Oxides, J. Catal. 178 (1998) 499–510.
- [22] M. do C. Rangel, F.M. Mayer, S.J. de Oliveira, S.G. Marchetti, F.L. Faita, D. Ruiz, G. Saboia, M.K. Dagostini, J. Morais, M. do C. Martins Alves, Dehydrogenation of ethylbenzene to styrene over magnesium-doped hematite catalysts, Appl. Catal. A Gen. 669 (2024). https://doi.org/10.1016/j.apcata.2023.119514.

- [23] A.P. Grosvenor, B.A. Kobe, M.C. Biesinger, N.S. McIntyre, Investigation of multiplet splitting of Fe 2p XPS spectra and bonding in iron compounds, Surf. Interface Anal. 36 (2004) 1564–1574. https://doi.org/10.1002/sia.1984.
- [24] M. Omran, T. Fabritius, A.M. Elmahdy, N.A. Abdel-Khalek, M. El-Aref, A.E.H. Elmanawi, XPS and FTIR spectroscopic study on microwave treated high phosphorus iron ore, Appl. Surf. Sci. 345 (2015) 127–140. https://doi.org/10.1016/j.apsusc.2015.03.209.
- [25] M. Synowiec, D. Zákutná, A. Trenczek-Zajac, M. Radecka, The impact of nanometric Fe2O3 on the magnetic, electronic, and photocatalytic behavior of TiO2@Fe2O3 heterostructures, Appl. Surf. Sci. 608 (2023) 0–11. https://doi.org/10.1016/j.apsusc.2022.155186.
- [26] S. Kannan, R. Vir Jasra, Microwave assisted rapid crystallization of Mg-M(III) hydrotalcite where M(III)=Al, Fe or Cr, J. Mater. Chem. 10 (2000) 2311–2314. https://doi.org/10.1039/b004219f.
- [27] P. Panagiotopoulou, N. Martin, D.G. Vlachos, Effect of hydrogen donor on liquid phase catalytic transfer hydrogenation of furfural over a Ru/RuO2/C catalyst, J. Mol. Catal. A Chem. 392 (2014) 223–228. https://doi.org/10.1016/j.molcata.2014.05.016.
- [28] H. Niu, J. Luo, C. Li, B. Wang, C. Liang, Transfer Hydrogenation of Biomass-Derived Furfural to 2-Methylfuran over CuZnAl Catalysts, Ind. Eng. Chem. Res. 58 (2019) 6298–6308. https://doi.org/10.1021/acs.iecr.9b00408.
- [29] M.S. Gyngazova, L. Grazia, A. Lolli, G. Innocenti, T. Tabanelli, M. Mella, S. Albonetti, F. Cavani, Mechanistic insights into the catalytic transfer hydrogenation of furfural with methanol and alkaline earth oxides, J. Catal. 372 (2019) 61–73. https://doi.org/10.1016/j.jcat.2019.02.020.
- [30] R. López-Asensio, J.A. Cecilia-Buenestado, C. Herrera-Delgado, M.Á. Larrubia-Vargas, C. García-Sancho, P.J. Maireles-Torres, R. Moreno-Tost, Mixed Oxides Derived from Hydrotalcites Mg/Al Active in the Catalytic Transfer Hydrogenation of Furfural to Furfuryl Alcohol, Catalysts. 13 (2023). https://doi.org/10.3390/catal13010045.
- [31] S.A. Bocanegra, A.D. Ballarini, O.A. Scelza, S.R. de Miguel, The influence of the synthesis routes of MgAl2O4 on its properties and behavior as support of dehydrogenation catalysts, Mater. Chem. Phys. 111 (2008) 534–541. https://doi.org/10.1016/j.matchemphys.2008.05.002.
- [32] M.J. Gilkey, B. Xu, Heterogeneous Catalytic Transfer Hydrogenation as an Effective Pathway in Biomass Upgrading, ACS Catal. 6 (2016) 1420–1436. https://doi.org/10.1021/acscatal.5b02171.
- [33] J.S.M. Samec, J.E. Bäckvall, P.G. Andersson, P. Brandt, Mechanistic aspects of transition metal-catalyzed hydrogen transfer reactions, Chem. Soc. Rev. 35 (2006) 237–248. https://doi.org/10.1039/b515269k.
- [34] G.S. More, A. Shivhare, S.P. Kaur, T.J. Dhilip Kumar, R. Srivastava, Catalytic interplay of metal ions (Cu2+, Ni2+, and Fe2+) in MFe2O4 inverse spinel catalysts for enhancing the activity and selectivity during selective transfer

- hydrogenation of furfural into 2-methylfuran, Catal. Sci. Technol. 12 (2022) 4857–4870. https://doi.org/10.1039/d2cy00970f.
- [35] C. Jiménez-Sanchidrián, J.M. Hidalgo, J.R. Ruiz, Reduction of heterocyclic carboxaldehydes via Meerwein-Ponndorf-Verley reaction, Appl. Catal. A Gen. 303 (2006) 23–28. https://doi.org/10.1016/j.apcata.2006.01.035.
- [36] M.A. Aramendía, V. Borau, C. Jiménez, J.M. Marinas, J.R. Ruiz, F.J. Urbano, Catalytic transfer hydrogenation of citral on calcined layered double hydroxides, Appl. Catal. A Gen. 206 (2001) 95–101. https://doi.org/10.1016/S0926-860X(00)00588-3.

talysts			

Chapter 8: Conclusion and Future Recommendations

In a world increasingly defined by the need for sustainable solutions, the production of chemicals and fuels from renewable resources is no longer a distant goal but a pressing necessity. Chemicals and fuels are the lifeblood of modern society, powering everything from transportation to the production of everyday materials. However, the heavy reliance on fossil fuels has left an undeniable mark on our environment. The challenge before us is clear: we must transition to greener alternatives that can deliver the same essential products without depleting our planet's finite resources.

Biomass stands at the forefront of this transformation, offering a renewable feedstock capable of replacing fossil fuels in the production of high-value chemicals as well as high volume fuels. At the heart of this shift is the concept of platform chemicals, which serve as building blocks for a vast range of industrial applications. Among these, furfural (FFR) - a versatile compound derived from agricultural residues - has emerged as a key player. Its potential to be converted into valuable products like 2-methylfuran (2-MeF) and furfuryl alcohol (FAL) positions it as a cornerstone of the bio-based economy.

This thesis systematically explored and optimized catalytic systems for FFR valorization by investigating both conventional molecular hydrogen (H₂)-based methods and the innovative transfer hydrogenation route. By tackling these two distinct pathways, this thesis seeks to offer a holistic perspective on FFR conversion. The molecular H₂ route, being well-established, provided deeper insights into catalyst performance in traditional hydrogenation processes, while the emerging transfer hydrogenation approach, utilizing alternative hydrogen donors, represents a more sustainable, energy-efficient method. Together, these strategies expand the available methods for producing valuable chemicals like 2-MeF and FAL, paving the way for cleaner and more versatile processes in biomass conversion.

Through the investigation of diverse catalytic systems - including bimetallic catalysts, mixed metal oxides, and supported metal catalysts - this thesis has aimed to unlock more efficient, selective, and sustainable pathways for FFR valorization. The insights gathered not only advance the scientific understanding of catalytic biomass conversion

but also contribute meaningfully to the broader goal of creating a greener, more resilient future.

8.1 Conclusion

Building on these advancements, a series of critical insights were gathered through a comprehensive and systematic evaluation of catalytic systems, aimed at optimizing the sustainable conversion of FFR into valuable products.

Chapter 4 focuses on the catalytic HDO of FFR to produce 2-MeF using TiO₂-supported mono and bimetallic Cu-Ni catalysts in a fixed-bed reactor at ambient H₂ pressures. Catalysts were synthesized with a fixed Cu content of 10 wt.% and varying Ni content (0-20 wt.%) through a wet impregnation method. Characterization techniques such as XRD, TPR, and SEM revealed that increasing Ni content enhanced the dispersion and reducibility of Cu, likely due to strong interactions between CuO and NiO species, as well as improved surface area and porosity. The catalytic performance highlighted that both monometallic Cu and Ni catalysts achieved over 90% conversion, with the Cu catalyst demonstrating a modest 55% selectivity towards 2-MeF. Increasing the Ni content led to complete FFR conversions and an increase in 2-MeF selectivity. Notably, the Cu-Ni bimetallic catalyst with 10% Ni content achieved the highest selectivity of 84.5% at 200 °C and a WHSV of 0.87 g_{FFR} h⁻¹ g_{catalyst}⁻¹. However, increasing Ni to 20% negatively impacted selectivity, leading to unwanted over-hydrogenation products like THFA and 2-MeTHF. Temperature played a crucial role in product distribution; temperatures below 200 °C favored FAL formation, while higher temperatures promoted the formation of C₄ and C₅ ring-opening products. A similar trend was observed with varying contact times, where shorter times increased FAL production and longer times favored by-products such as 2-MeTHF. Furthermore, the long-term stability tests demonstrated that the catalyst maintained near-complete FFR conversions and stable selectivity for 2-MeF over a 12-hour duration.

Chapter 5 explores the synthesis and evaluation of Cu-Fe mixed oxide catalysts with varying Cu/Fe molar ratios from 0.5 to 2, utilizing a straightforward sol-gel method for the HDO of FFR in a fixed-bed reactor under ambient H₂ pressures. Key findings from characterization analyses indicate that the Cu/Fe ratio significantly influences the dispersion and reducibility of the catalysts. Notably, a Cu/Fe ratio of 1 enhances CuO dispersion and reducibility due to strong Cu-Fe interactions. As the Cu/Fe ratio

increases, Fe's reducibility improves, while Cu's reducibility declines due to the formation of more stable bulk oxides. The catalytic evaluation demonstrated that low Cu/Fe ratios produced acidic sites with insufficient strength and limited hydrogen availability, resulting in moderate conversion and 2-MeF selectivity. Conversely, catalysts with high Cu/Fe ratios exhibited similar trends due to excess Cu increasing acidity but reducing H availability. The optimal performance was achieved with an equimolar Cu and Fe catalyst, attaining a value of 90% selectivity at an H₂/FFR ratio of 10, 230 °C, and a WHSV of 0.5 g_{FFR} h⁻¹ g_{catalyst}⁻¹. Temperature was found to be critical in product distribution, favoring FAL formation below 230 °C while promoting C₅ opening reactions at higher temperatures. A similar trend was noted with WHSV, where lower contact times enhanced FAL production. Investigating the H₂/FFR molar ratios revealed that a ratio of 10 or higher was optimal for achieving excellent conversion and 2-MeF selectivity, highlighting the importance of H availability. The study also identified 350 °C as the ideal reduction temperature, as higher temperatures diminished conversion and selectivity by fully reducing essential acidic sites. The TOS study indicated initial conversions exceeding 99%, gradually declining to 93.7% over 24 hours. Selectivity for 2-MeF remained stable at 90% for the first 12 hours but dropped to 55% by the end. Regeneration studies showed partial recovery, with 85% conversion maintained for the first 10 hours, eventually declining to 68%. Similarly, 2-MeF selectivity fell from 86% to 46.5% by the 24-hour mark.

Chapter 6 investigates the innovative use of rice husk ash as a sustainable and cost-effective silica source for the development of mesoporous silica supports. Metals such as Al, Ti, Zr, and Sn were incorporated into the silica framework and the catalytic efficacy of these metal-modified mesoporous silica materials, loaded with Cu catalysts, was assessed for FFR hydrogenation FAL in a fixed-bed reactor under atmospheric H₂ pressures. Characterization analyses revealed that the pristine mesoporous silica lacked the typical MCM-41 hexagonal structure, with further disruptions observed after metal integration. Successful metal incorporation led to significant reductions in surface area and pore volume, correlated with the incorporated metals' mass and size. Additionally, strong metal-support interactions were confirmed, enhancing the reducibility of CuO species through more reducible Cu²⁺-O-M^{δ+} bonds at the metal-support interface. Characterization analyses also indicated a shift toward higher acidic strength with metal integration, particularly in the Cu@Ti-MS catalyst. Catalytic activity at 160 °C

revealed that Cu@MS had the lowest FFR conversion and FAL yield due to weak acidic site strength, while Zr incorporation achieved the best results, with FFR conversion and FAL yield of 74.5% and 72.9%, respectively. Optimization revealed peak performance for Cu@Zr-MS at H₂/FFR = 10, 200 °C, and WHSV = 1 g_{FFR} h⁻¹ g_{catalyst}⁻¹, achieving conversion and yield rates of 90.6% and 85%, respectively. Prolonged assessments showed stable conversion around 90% for the first 18 hours, maintaining FAL yields of approximately 85% for about 16 hours. However, both metrics declined after 24 hours, dropping to 53.8% and 51.8% by the end of the 30-hour period. The regeneration study indicated a partial restoration of catalytic activity, with nearly 80% conversion for the first 8 hours and a consistent FAL yield of around 74% during this period. However, both conversion and yield gradually declined, falling to 56.2% and 52% respectively, at the end of the 24 h period.

Chapter 7 investigates the synthesis and catalytic performance of Mg-Fe mixed oxide catalysts with varying Mg/Fe ratios (1 to 5), produced via a co-precipitation method. These catalysts were tested for the vapor-phase FFR transfer hydrogenation to 2-MeF at atmospheric pressure in a fixed-bed reactor at ambient pressures and under inert atmosphere. As the Mg/Fe ratio increased, Fe was integrated into the MgO lattice and the increased surface area and pore volume increased. The analyses revealed a balanced distribution of weak and medium-strength acidic and basic sites across the catalysts as well as a disordered morphology characterized by thin, flaky plates that changed to thick rod-like structures at higher calcination temperatures. In catalytic performance tests, the Fe₂O₃ catalyst showcased selectivity for 2-MeF, but exhibited low conversion and rapid deactivation. In contrast, MgO achieved full FFR conversion but yielded equal amounts of both FAL and 2-MeF. When combined, the Mg-Fe catalysts significantly enhanced conversion rates and 2-MeF selectivity, especially with higher Mg/Fe ratios, which slowed deactivation over a 4-hour period. However, excessive Mg tipped the balance, reducing 2-MeF selectivity and increasing FAL production. The standout performer was the Mg-Fe catalyst with a Mg/Fe ratio of 4 calcined at 500 °C, achieving 85.2% conversion and 79.8% selectivity for 2-MeF at 400°C, alongside a space-time yield of 0.7 g_{FFR} g_{catalyst} h⁻¹ after 4 h on stream. Temperature proved crucial: lower temperatures hindered hydrogen donor activation and hydrogenolysis, leading to rapid deactivation. Conversely, raising the temperature to 400°C dramatically enhanced conversion and selectivity, though excessively high temperatures caused unwanted cracking and carbonaceous deposits, resulting in faster deactivation. WHSV also played a significant role; shorter contact times decreased FFR conversion and increased FAL yield, while longer times led to reduced conversion and quicker deactivation. The optimal calcination temperature was determined to be 500°C, as deviations resulted in diminished FFR conversion and 2-MeF selectivity. TOS studies revealed that while initial conversion exceeded 99%, it declined to 85.2% by the 4th h and sharply dropped to 30% by the 8th h. 2-MeF selectivity followed a similar pattern, remaining steady at 92% for the first 2 h before falling to 79.8% after 4 h and plummeting to just 16.1% by the 8th h. Regeneration studies indicated that the catalyst could recover some activity, reaching ~90% conversion shortly after regeneration, but this performance quickly deteriorated, with conversion dropping to 22% after 8 h. A comparable decline in 2-MeF selectivity was noted, starting at 75.8% after regeneration and dropping to 6.1% after 8 h.

8.2 Future Recommendations

- 1. Future research should prioritize investigating the mechanisms of catalyst deactivation in the context of furfural hydrogenation. While this thesis focused on the development and optimization of catalytic systems for converting FFR to high-value chemicals, understanding deactivation pathways is crucial for enhancing long-term catalyst stability and performance. By integrating insights from existing literature with experimental studies, future work can elucidate the factors contributing to catalyst deactivation, paving the way for the design of more robust and resilient catalytic systems tailored for continuous biomass conversion processes.
- 2. A valuable future direction stemming from our investigation of Cu-Ni bimetallic catalysts supported on titania could involve exploring alternative supports with distinct acidic or basic properties, such as ceria, zirconia, alumina, or silica. This approach would allow for the evaluation of how these different supports influence the catalytic behavior and overall effectiveness of the bimetallic catalysts, potentially leading to improved performance in various reactions.
- 3. From our work on Cu-Fe mixed oxide catalysts, a promising future direction could be to explore the use of various high surface area supports, such as activated carbon, or silica. This approach may enhance catalyst performance by improving the dispersion

and accessibility of active sites, offering valuable insights into the impact of different supports on the properties and efficacy of the catalysts.

- 4. Building on our exploration of Cu catalysts supported on mesoporous silicas derived from rice husk ash, future research could delve into the use of various templating methods to create different silica structures, such as MCM-41 and SBA-15. Another approach could be to systematically vary the silicon-to-metal molar ratio during metal incorporation, revealing how these structural differences influence catalytic performance in FFR hydrogenation.
- 5. Building on our exploration of Mg-Fe catalysts for furfural transfer hydrogenation, a promising future direction could involve substituting Fe with metals like Al, Ti, or Zr to investigate new catalyst compositions while retaining similar acid-base properties. Additionally, Mg could be replaced with Ca or Zn, opening avenues for further enhancing catalytic performance through varied metal combinations. Exploring the addition of a metal such as Cu could also provide valuable insights into how this influences catalytic activity. Furthermore, experimenting with various synthesis methods for these mixed metal oxides could shed light on how different approaches affect catalyst performance, paving the way for innovative solutions in catalytic systems and potentially enhancing the activity of the Mg-Fe systems synthesized here.
- 5. Future research should prioritize conducting scale-up studies to evaluate the practical applicability of catalytic systems developed at bench-scale in industrial settings. These studies will assess catalyst performance and stability under realistic operational conditions, enhancing the understanding of their scalability and efficiency for biomass-derived processes. Additionally, exploring the economic feasibility and lifecycle analysis of these catalytic systems will provide valuable insights into their potential for real-world applications, ultimately facilitating the transition from laboratory-scale experiments to large-scale production.
- 6. A critical avenue for future research is the in-depth investigation of catalyst deactivation mechanisms. While this thesis focused on identifying and optimizing catalytic systems for efficient FFR conversion, understanding how and why catalysts deactivate over time is essential for their long-term success. Unravelling the pathways of deactivation under realistic operating conditions would not only result in extended catalyst lifespans but also unlock the potential for more reliable, sustainable biomass

conversion processes. Addressing these challenges head-on will be key to transforming laboratory-scale innovations into robust, high-performance catalysts that meet the demands of industrial applications.

Appendix

Fixed bed reactor unit with Gas Chromatograph



List of Publications

Journal Publications

- 1. **A. Jaswal**, V. Garule, A. Pandey, P.P. Singh, T. Mondal, P. Biswas, Selective furfural hydrodeoxygenation over Cu-Fe catalysts with In-Situ Cu@Fe₃O₄ formation, Journal of Industrial and Engineering Chemistry 138 (2024) 338-349.
- 2. **A. Jaswal**, P.P. Singh, A.K. Kar, T. Mondal, R. Srivastava, Production of 2-methyl furan, a promising 2nd generation biofuel, by the vapor phase hydrodeoxygenation of biomass-derived furfural over TiO₂ supported Cu Ni bimetallic catalysts, Fuel Processing Technology 245 (2023) 107726.
- 3. **A. Jaswal**, P.P. Singh, T. Mondal, Furfural-a versatile, biomass-derived platform chemical for the production of renewable chemicals, Green Chemistry 24 (2022) 510–551.
- 4. **A. Jaswal**, V. Garule, T. Mondal, Transforming Waste into Wealth: Cu Catalysts Supported on Metal-Incorporated Mesoporous Silica Derived from Rice Husk Ash for Furfural Hydrogenation (**Manuscript under revision**)
- 5. **A. Jaswal**, V. Garule, O. Singh, P.P. Singh, T. Mondal, Sustainable Chemistry in Action: Harnessing Earth-Abundant Mg-Fe Mixed Oxide Catalysts for Vapor Phase Furfural Transfer Hydrogenation (**Manuscript under review**)
- 6. **A. Jaswal**, R. Goswami, P.P. Singh, T. Mondal, Enhancing Pine Needle Valorization: The Impact of Pre-Treatment on Pyrolysis and Bio-Oil Characteristics (**Manuscript under review**).
- 7. P.P. Singh, **A. Jaswal**, A. Singh, T. Mondal. From Waste to Clean Energy: An Integrated Pyrolysis and Catalytic Steam Reforming Process for Green Hydrogen Production From Agricultural Crop Residues. ACS Sustainable Chemistry & Engineering 12 (2024) 2058-2069.
- 8. P.P. Singh, **A. Jaswal**, R. Singh, T. Mondal, K.K. Pant. Green hydrogen production from biomass A thermodynamic assessment of the potential of conventional and advanced bio-oil steam reforming processes, International Journal of Hydrogen Energy 50 (2024) 627-639.

- 9. P.P. Singh, **A. Jaswal**, N. Nirmalkar, T. Mondal, Synergistic effect of transition metals substitution on the catalytic activity of $LaNi_{0.5}M_{0.5}O_3$ (M = Co, Cu, and Fe) perovskite catalyst for steam reforming of simulated bio-oil for green hydrogen production, Renewable Energy 207 (2023) 575–587.
- 10. P.P. Singh, **A. Jaswal**, T. Mondal, Refining the Reforming Process: Optimization Strategies for Hydrogen Production from Phenol (**Manuscript under preparation**).

Book Chapters

- 1. **A. Jaswal**, P.P. Singh, S. Lande, T. Mondal, Agro-forestry waste as a Potential Resource for Climate Change Mitigation. In Clean Energy Transition-via-Biomass Resource Utilization: A Way to Mitigate Climate, pp. 59-78, 2024, Springer Nature Singapore.
- 2. H.K. Tirumaladasu, P.P. Singh, **A. Jaswal**, T. Mondal, Slow Pyrolysis of Rice Husk in a Lab-Scale Batch Reactor: Influence of Temperature on the Products Yield and Bio-oil Composition (Conference paper). In Recent Advances in Bio-Energy Research (ICRABR-2022), pp. 199-2013, 2023, Springer Proceedings in Energy

Conference Presentations

- 1. A. Jaswal, P.P. Singh, T. Mondal, Furfural vapor phase hydrodeoxygenation to 2-methylfuran, a 2nd generation biofuel, over TiO₂ supported Cu-Ni bimetallic catalysts, *Conference on Advances on Catalysis for Enegy and Environment" (CACEE 2022)*, Tata Institute of Fundamental Research, Mumbai, October 2022.
- 2. A. Jaswal, P.P. Singh, T. Mondal, Vapor phase hydrodeoxygenation of biomass derived furfural to 2-methylfuran over a series of TiO₂ supported mono and bimetallic Cu and Ni catalysts, *ACS Spring 2023: Crossroads of Chemistry*
- 3. A. Jaswal, P.P. Singh, T. Mondal, Selective Furfural Hydrodeoxygenation Through In-Situ Cu@Fe₃O₄ Formation in Cu-Fe Mixed Oxide Catalysts, *ACS Spring 2024: Many Flavors of Chemistry*.

4. A. Jaswal, T. Mondal, A vapor phase route for the production of 2-methylfuran, a 2 generation biofuel, from biomass-derived furfural, *The 10th UK catalysis conference*, Loughborough, UK, January 2024.

5. A. Jaswal, V. Garule, T. Mondal, Enhanced Selectivity in Furfural Hydrodeoxygenation via In-Situ Cu@Fe₃O₄ Generation within Cu-Fe Mixed Oxide Catalysts, *International Conference on Catalysis for Clean Energy Technologies and Sustainable Development*, Panjab University Chandigarh, April 2024.

Biodata

Anurag Jaswal

Education:

M.Tech: Chemical Engineering from Dr. S.S.B. UICET, Panjab University,

Chandigarh, India (2019)

Performance/CGPA: 6.67/10

B.Tech: Chemical Engineering from Chandigarh University, Panjab, India (2017)

Performance/CGPA: 8.77/10

Research interest:

- ✓ Heterogeneous catalysis
- ✓ Biomass conversion to value-added chemicals and fuels
- ✓ Techno-economic evaluation of biomass conversion processes
- ✓ Waste water treatment

Technical skills:

Handling and analysing the data using the following sophisticated analytical instruments:

- ✓ FTIR
- ✓ Gas Chromatography with MS, FID and TCD
- ✓ TGA

Softwares: ASPEN+, Origin, X'pert-Plus HighScore etc.